Vibration Isolation and Shock Protection for MEMS

by

Sang Won Yoon

A dissertation submitted in partial fulfillment
of the requirements for the degree of
Doctor of Philosophy
(Electrical Engineering)
in The University of Michigan
2009

Doctoral Committee:

Professor Khalil Najafi, Co-Chair
Professor Noel C. Perkins, Co-Chair
Professor Karl Grosh
Professor Kensall D. Wise
Associate Professor Euisik Yoon
Research Scientist Sangwoo Lee

DEDICATION

To my family

With thankfulness and love

ACKNOWLEDGMENTS

During the period I studied at the University of Michigan (U-M), the U-M clean room had several different names: Solid-State Electronics Laboratory (SSEL), MNF (Michigan Nano Facility), and LNF (Lurie Nanofabrication Facility). This long time greatly enriched my life with many memories and I hope to dedicate this acknowledgment to many people that I hope to express my thankfulness. I feel very lucky to be with these great people.

First and foremost, I would like to express my great appreciation for my advisors, Prof. Khalil Najafi and Prof. Noel C. Perkins, for their guidance and encouragement throughout my graduate study. I learned many things from them other than just technical knowledge. I learned how to define and solve problems, how to have a vision, how to mange stress and encourage myself, and how to enjoy (or even love) research.

I would also like to appreciate my committee members, Prof. Kensall D. Wise, Prof. Karl Grosh, Prof. Euisik Yoon, and Dr. Sangwoo Lee, for their encouragement and critical reviews of my dissertation. Especially, Dr. Lee played a role as another co-advisor since 2006 and always opened to discuss with me. Also, I would like to appreciate my prelim committee members, Prof. Yogesh Gianchandani and Prof. Michel Maharbiz, who could not attend my defense because of critical time conflicts.

I hope to thank to previous and present my buddies in the SSEL and MNF/LNF and in the Center of Wireless Integrated MicroSystems (WIMS). We together spent many times at the lab (or sometimes at restaurants/bars) and shared tons of memories that I will never forget. I especially appreciate Dr. Hanseup Kim who first introduced MEMS to me. I also thanks to many friends who I met in U-M. Owe to them, I could refresh my mind and enthusiasm to finalize my graduate study.

Finally, I hope to thank to my family, Jin-San Yoon, Mal-Nam Kim, Hye Jung Yoon, and Young-Ah Lim. My father, Dr. Jin-San Yoon, was and is always my hero. For my mother, Dr. Mal-Nam Kim, I cannot be who I am now without her love and support. My sister, Hye Jung, was and is always my best friend. I give

my best wishes for your study to be another doctor in my family. My wife, Young-Ah, is one of the greatest successes I made in U-M. Thank you for all the encouragements, supports, understanding, and amusements you provided me.

TABLE OF CONTENTS

LIST OF FIGURES

LIST OF TABLES

LIST OF APPENDICES

APPENDICE

Abstract

Forces arising from environmental sources have profound influence on the functioning of microelectromechanical (MEMS) devices. Two examples include mechanical vibration and shock, which can significantly degrade the performance and reliability of MEMS. Mechanical vibrations can generate unwanted device output, and shock loads can permanently damage device structures. Thus, there is strong motivation to understand and to mitigate the adverse effects of shock and vibration on MEMS devices.

The effects of mechanical vibrations and the means to mitigate them are not well understood. Herein, we present detailed analyses that identify how vibration degrades device performance, especially for MEMS gyroscopes. Two classes of gyroscopes are studied and modeled in detail: Tuning fork gyroscopes (TFG) and vibrating ring gyroscopes (VRG). Despite their differential operation, all capacitive TFGs are affected by vibration due to nonlinear characteristics of their capacitive drive/sense electrodes, while some TFG designs are shown to be more vibration-tolerant than others by >99%. By contrast, VRGs remain immune to vibration effects due to the decoupling of vibration excited modes and sensing modes. Overall, vibration effects in gyroscopes and other MEMS can also be reduced by integrating a vibration-isolation platform, and TFG's vibration sensitivity is improved by >99% using a properly-designed platform.

Prior shock protection in MEMS has utilized two strategies: optimizing device-dimensions and hard shock stops. While both strategies afford protection, they also incur a trade-off in shock versus device performance. Two new shock protection technologies are developed herein: (1) nonlinear-spring shock stops and (2) soft-coating shock stops. The nonlinear springs form compliant motion-limiting stops that reduce impact. Similarly, soft coating stops utilize a soft thin-film layer on an otherwise hard surface to increase the surface compliance and energy dissipation. Both solutions decrease the impact forces generated between the device mass and the shock stops, and enable wafer-level, batch fabrication processes compatible with microfabrication techniques. Simulation and experimental results clearly demonstrate that both solutions offer superior shock protection compared to conventional hard shock stops. Following testing of more than 70 devices, we observe a twenty fold increase in device-

survival rate for devices protected either by silicon nonlinear-spring stop or by Parylene soft-coating stops.

CHAPTER 1

INTRODUCTION

Since their introduction in the 1960s in the form of resonating gate transistors, Micro-Electro-Mechanical-Systems (MEMS) have made enormous advances. MEMS manufacturing technologies have led to many new classes of devices which continue to replace their macro-scale counterparts due to their miniature size, low cost, reduced power consumption, and convenient integration with semiconductors/IC fabrication techniques.

This transition from macro-scale to micro-scale devices is reflected by the large increase of the MEMS market. Currently MEMS devices are widely employed in applications ranging from consumer products (including automotive components, mobile phones, gaming devices and toys) to specialized markets for extreme environments (such as in military and mining/oil production applications). Moreover, the MEMS market, which was already valued at more than eight billion in 2005, is expected to triple by 2015 [1].

This dramatic expansion of the MEMS market is due in part to the successful transfer of this technology from the laboratory to the commercial sector. In the commercial sector, the devices are challenged by uncertain and frequently changing environments which may significantly impact device performance and reliability. For successful commercialization, one must ensure that device performance remain robust.

Mechanical vibration and shock are two major environmental influences that potentially degrade device performance. These effects are frequently more significant in MEMS devices than in ICs because MEMS employ mechanical structures that are susceptible to mechanical vibration and shock. The mechanically-induced vibration and shock experienced by moving MEMS micro-structures may deteriorate device reliability and promote degraded performance and/or structural damage.

These undesirable effects are reported in several experimental observations [2-5]. In short, vibration is known to produce unwanted device output while shock may produce permanent structural damage As discussed in more detail in Sections 1.1 and 1.2, these influences are difficult to control by electronics [6] and may ultimately reduce

the service life of the device [4].

Therefore, there is considerable interest in developing technologies to protect the MEMS devices from vibration and shock. Much effort, especially in MEMS packaging, has been already devoted to the challenge of developing protection technologies against vibration and shock [2, 4, 7-9]. This protection becomes even more critical for high-performance devices or devices considered for harsh environment applications. High-performance designs often involve delicate device structures and/or sensitive interface electronics, which are highly susceptible to mechanical excitation. Devices in harsh environments also require greater reliability than devices employed in less severe applications..

This dissertation has three major objectives. First, we will analyze a number of mechanisms which produce the undesirable effects due to vibration or shock. The analyses will be performed for individual classes of devices and potential applications. Second, using these analyses, we will identify which devices and applications are most sensitive to vibration or shock and thus require protection. Third, we will design and develop technologies that provide vibration isolation and/or shock protection. The resulting technologies are designed to be easily integrated with many MEMS devices using conventional microfabrication techniques. Moreover, the performance improvements by the proposed technologies will be demonstrated by simulations and/or by experiments. Also, design trade-offs and the relative advantages/disadvantages of the proposed technologies will be highlighted.

In the remainder of this chapter, we will review shock and vibration effects on MEMS and the associated methods of protection in Sections 1.1 and 1.2, respectively. Specifically, Section 1.1.1 reviews shock conditions in several applications while Section 1.1.2 details how shock affects MEMS devices. Section 1.1.3 surveys available shock protection methods and their pros/cons and Section 1.1.4 introduces our new shock-protection technologies and highlights their advantages. Concerning vibration, Section 1.2.1 reviews vibration conditions by application and Section 1.2.2 discusses the associated effects on devices. Section 1.2.3 describes available vibration isolation/suppression techniques. Section 1.3 highlights the overall contributions of this dissertation. Finally, this chapter closes in Section 1.4 with the outline of the dissertation.

1.1. Shock Protection for MEMS

1.1.1. Shock from Environment

Mechanical shock develops from a large force over a very short time relative to the settling time or the natural period of a device [10]. Shock is thus characterized by large amplitude, short-duration, impulse-like loads. Shock loads are not easy to quantify due to their wide amplitude range (20g to 100,000g or larger), their wide range of duration (50 to 6000 μsec) [11], and their largely unknown and unrepeatable 'shape' (pulse, half-sine, etc) [12].

Shock from the environment, despite some uncertainties, can be roughly classified by application. Among the three characteristics that define shock (amplitude, duration, and shape), the pulse shape is least understood and varies considerably by event and application. Shock duration is often related to shock amplitude, as shown in many applications [11], and higher shock amplitude generally (but not always) accompanies shorter shock duration.

Table 1.1 summarizes the shock amplitudes arising in various environments. In everyday/common applications such as free fall, an object experiences 1-g acceleration until it impacts a surface. When impacting hard surfaces, an object may experience substantial (~2000 g) shock when dropped from a mere 1-m (e.g., from a table) and significantly greater (~7000 g) shock when dropped from 25m (e.g., from a building). In automotive applications, airbag sensors are required to operate in 20-50 g [13, 14] shock environments and knock sensors in 1000 g [13] shock environments. Other automotive applications require device survival following shock amplitudes of 3000 g [15]. Even higher shock amplitudes are realized in harsh environments. Sensors for oil and gas exploration are required to survive 20,000 g shock. In laboratory experiments, shock tests using Hopkinson bars often produce shock ranging from 5,000 to 150,000 g [4, 16, 17]. In military applications, large shock amplitudes ranging from 10,000 to 100,000 g are generated during launching munitions [18, 19] while the munition itself experiences much lower shock amplitude (<20 g) during flight.

Table 1.1. Shock amplitudes realized in various environments

Application		Shock Amplitude	Reference
Everyday/common applications			
Free fall under gravity	Free fall before contacting surface	1 g	Elementary physics
	Fall from a 1-m table to hard surface	~2,000 g	calculation
	Fall from a 25-m height building to hard surface	~7,000 g	[20]
Automotive	Operation range of accelerometers for airbag	50 g	[13, 14]
	Operation range of knocking sensor	1,000 g	[13]
	Requirement in sensors for automotive applications	< 3,000 g	[15]
Harsh environment applications			
Exploration	Oil and gas prospecting	20,000 g	[21]
Shock tests	Hopkinson bar	5,000-150,000 g	[4, 16, 17]
Military	Gunfire	23,000 g	[19]
	Munitions launching from tank, artillery, and mortar	10,000-100,000 g	[18, 22]
	Munitions flight after the launch from tank, artillery, and mortar	0.5-20 g	[22]

1.1.2. Shock Effects on MEMS

The most serious shock effect on MEMS is structural damage to the device. MEMS devices that utilize delicate mechanical structures are therefore susceptible to shock loads, and are damaged by initiation and propagation of cracks [23, 24], complete fracture of device structures [4, 5, 16, 20, 25], and generation of debris [4].

Even though the damage mechanism is not always understood [26], the damage ultimately results when a device structure cannot sustain the high stress induced by shock. The maximum sustainable stress in MEMS structures follows from the fracture stress for brittle materials and the yield stress for ductile materials [27]. In MEMS, the fracture stress is more commonly considered because most MEMS devices are made of brittle materials such as silicon, polysilicon, and oxide/nitride. Even though the fracture stress varies depending on test conditions [5], shock loading tests using silicon-

based MEMS structures lead to a commonly accepted range of fracture stress of 0.8-1G Pa [4, 20] as explained in detail in Chapter 5.

One of the processes leading to the damage is referred to as brittle fracture [26]. As shown in Figure 1.1, an initial crack propagates through a wafer due to localized, elevated stress leading ultimately to wafer fracture.

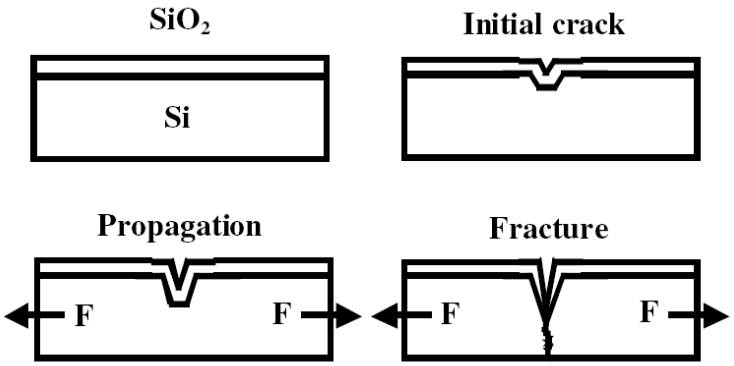

Figure 1.1. MEMS damage by brittle fracture [26].

The damage produced by shock loading has been observed in many MEMS devices [4, 16, 20, 25]. For example, polysilicon microengines having complex structures were subjected to various shock amplitudes from 500 g to 40,000 g [4]. The microengine is composed of several linear comb-drive actuators mechanically connected by linkage beams to a rotating gear that is anchored to a substrate, as shown in Figure 1.2a. In this experiment, the delivered shock spans across many of the application ranges described in Section 1.1.1 and was applied to the top, bottom, and sides of the microengines. Various engine components were damaged including gears detached from the substrate, broken/lost linkage beams, broken joints at the gear/linkage beam connection, and fractured rear-guide beams for the actuators. Because of the complexity of the test structures, the individual damage mechanisms are hard to analyze.

Follow-up experiments using simpler test devices [16] have helped identify damage mechanisms. For example, the test devices included in [16] are an array of cantilever beams and simple comb-drive resonators (Figure 1.2b) which were fabricated using two fabrication processes, namely SUMMiT^{TM} and Cronos MUMPs. After several high-g shocks (5,000 g to 200,000 g) delivered via a Hopkinson bar, many of the cantilever beams and the resonators were damaged at their anchor points. These damages were consistent and identical regardless of fabrication methods.

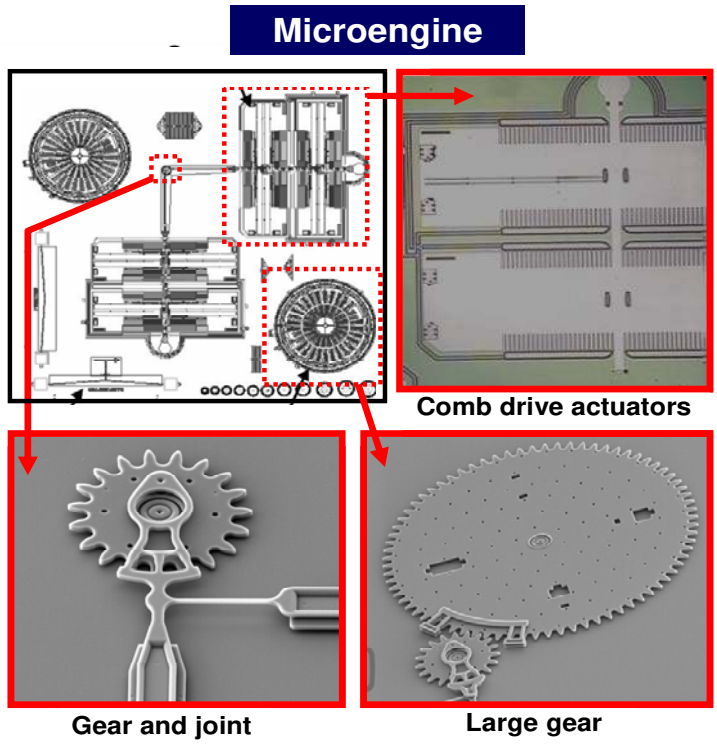

Figure 1.2. (a) Complex microengine used in shock tests [4] and (b) shock-induced damage in simple comb-drive actuator (top) and an array of micro-cantilever beams (bottom) [16].

Shock-induced damage is also reported in several other devices. For example, MEMS magnetometers subjected to ~7000 g shock exhibited fracture of supporting torsion beams upon dropping from a 25-m high building [20]. The magnetometers consisted of a ferromagnetic material covering a silicon structure with a flat surface supported by torsion beams. Another example is an array of cantilever beams having small tip masses [25]. The cantilever beams, 1-7 mm long and 50-200 μm wide, were fabricated using a silicon wafer thinned down to 100 μm by KOH etching and patterned by deep RIE. Shocks of 10,000-40,000 g were applied in the lateral direction resulting in fracture at the beam anchor points due to high bending stress. Fracture surfaces aligned with the (111) crystal plane of the silicon where the surface energy to resist fracture is minimum [5, 28]. Interestingly, a high speed camera was used to monitor the real-time fracture processes of the cantilevers.

In contrast, well-designed MEMS devices are able to survive high shock tests. SiC resonators, for example, survived high shock tests up to 10,000 g [29] and partially met the military requirements shown in Section 1.1.1. An overview of shock effects and shock test processes designed for MEMS is provided in [11].

In summary, the above survey of shock testing of MEMS devices leads to the following main conclusions: (1) fracture of micro structures can be induced by excessive shock amplitude, (2) fracture often occurs at anchor points due to elevated bending stresses, and (3) the shock durability of structures is mainly determined by structural dimensions, material properties, and shock amplitude. Shock-induced damage becomes an even more significant concern for high performance devices composed of more flexible micro-structures and in harsh environment applications where higher shock amplitude are encountered.

1.1.3. Shock Protection for MEMS

Limiting the maximum stress is imperative in shock-protection technologies. As the dominant stress in many microstructures derives from bending, it is therefore important to limit displacements/deformations that induce significant bending. This objective can be accomplished by limiting the excessive displacement of the device proof mass.

These ideas are illustrated nicely in the simple MEMS design of Figure 1.3 that is

composed of a single proof mass supported by two beams. The beams employed in this surface micro-machined device are 2 μm thick and 3 μm wide. A range of beam lengths is considered that yield device resonant (or natural) frequencies ranging from 100 Hz to 500k Hz. The shock-induced bending stress and methods to prevent the bending-induced fracture are further discussed in the latter part of this section and Chapter 4. We compute the maximum bending stress at the base of the beams when subjected to two shock loads, 2000 g and 7000 g. The lower shock load is consistent with requirements for automotive applications and the higher shock load is consistent with a drop from a 25-m building; refer to Section 1.1.1. A fracture stress of 0.8G Pa is selected as the design criteria for determining the likelihood of failure; refer to Section 1.1.2.

In the Figure 1.3, notice that the bending stress decreases with increasing device resonant frequency. This is expected since increasing resonant frequency implies a stiffer device, smaller deflections of the proof mass, and thus smaller bending stress at the base of the beam. The bending stress computed at 7000-g shock loading (blue dash-dot line) predicts that the device will survive if its resonant frequency exceeds ~200k Hz. Therefore, devices having high resonant frequencies may not require shock protection even at reasonably large shock loading. Such "high-frequency" devices may include time-reference resonators and disk gyroscopes whose resonant frequencies range from 100k Hz to several Mega Hz [30-34]. However, other MEMS devices are likely to be susceptible to shock such as accelerometers (resonant frequencies 0.5 to 5.5k Hz) [35-38], several micro-mirrors (0.3-2k Hz) [39, 40], or devices having mid-range 1st mode resonant frequencies (4.5k to 15k Hz) such as non-degenerate gyroscopes or ring gyroscopes [14, 41-45].

The results of Figure 1.3 also confirm the obvious conclusion that a device that sustains fracture under high-g shock loading may readily survive under low-g shock loading. For example, a device having a resonant frequency from ~10k Hz to ~200k Hz will be damaged when dropped from a tall building (7000-g shock, blue dash-dot line) but will survive when used in automotive applications (2000-g shock, black solid line).

A conceptually simple strategy to provide shock protection is to design device structures that never sustain stresses that exceed the fracture stress. Relative to Figure 1.3, this strategy is tantamount to increasing the device resonant frequency. Other examples include the improved shock resistance of a magnetometer by adjusting the length of the device-beam [20], a high-impact (1200-g) gyroscope with optimized

device structure [3], micromachined actuators [4], and a SiC resonator with high resonant frequency [29].

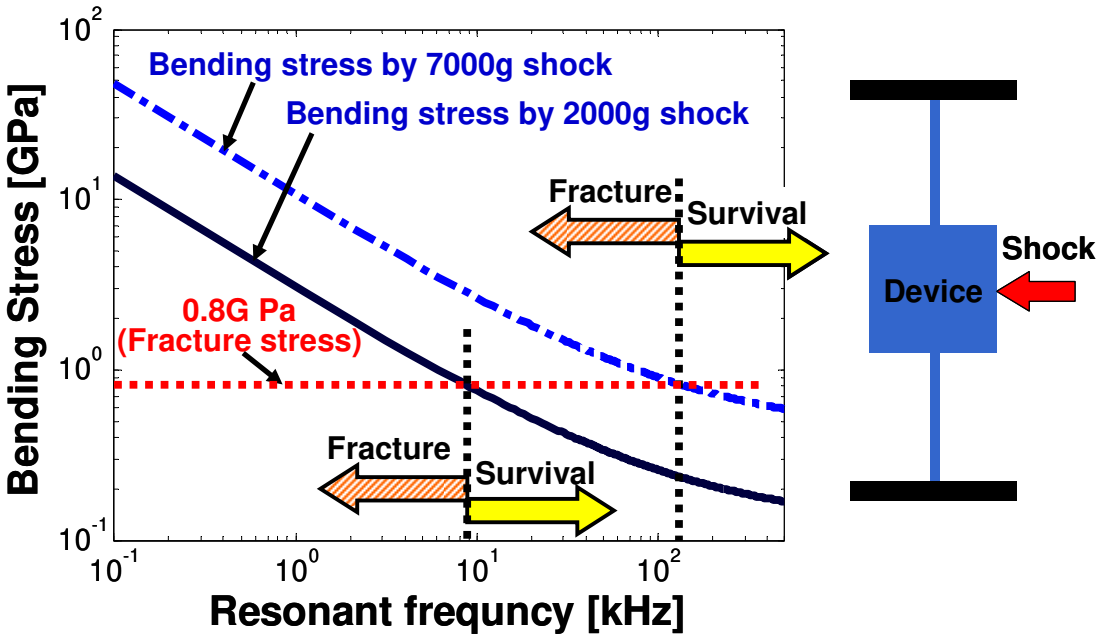

Figure 1.3. Computed bending stress as the function of the resonant frequency (or stiffness of support beams) and shock amplitude.

The above concept of re-sizing structural elements to avoid shock damage is attractive, because no additional treatments are required and shock performance can be conveniently optimized by layout-level design adjustments. However, this shock protection is often achieved at the expense of device performance, including resolution or sensitivity. The increased resonant frequency is not acceptable in devices such as high performance accelerometers which require low resonant frequencies [14, 35]. In addition, this method is limited to specific applications because it depends on known shock amplitudes.

These disadvantages can be mitigated by a second strategy; the use of hard shock stops (Figure 1.4). This strategy is based on the assumption that the critical stress develops when the device beam bends, and that the bending stress is maximized at critical points such as beam anchors. This method seeks to restrict the maximum bending stress by employing motion-limiting hard shock stops which limit the travel of the device's microstructure. The introduction of 'stops' decouples the device design from the shock-protection design, thus enabling superior device performance. Hard shock stops may not be achievable for devices having very high resonant frequencies

because of fabrication limitations. For example, a MEMS resonator whose resonant frequency is 150 kHz may achieve bending stresses that exceed the fracture stress when it bends by only ~0.1 μm when subjected to a shock loading of 10,000 g.

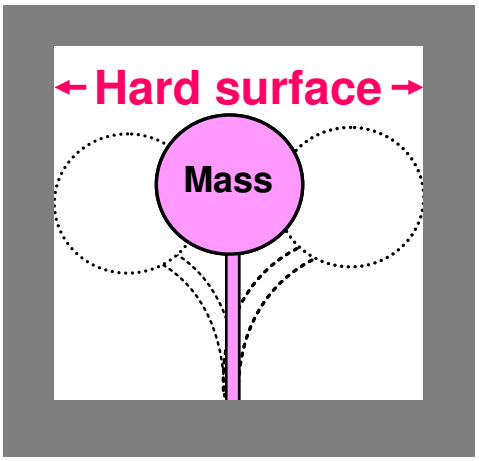

Figure 1.4. Conceptual design of hard shock stops.

Hard stops have been adopted in many applications. An encapsulated capacitive accelerometer, which utilizes out-of-plane over-range shock stops made of an encapsulation and a substrate wafer, survived up to 10,000 g shock [46]. The rim (or framework) of a piezoresisitive accelerometer functions as in-plane over-range stop, which is defined simultaneously with the accelerometer, and thus, no modification of fabrication or device design was required for shock protection purpose [47].

Several clever modifications of the shock stop concept have also been reported. A teeter-totter structure was designed to make the substrate wafer function as both up and down directional shock stops [8]. This design, though used on specific devices, eliminates the capsulation wafer needed in the typical up-direction shock stop [46]. Mushroom-shape hard stops, which are surface micromachined on their substrate, were adopted to limit the movement of an accelerometer to all three (x, y, and z) directions [7]. The accelerometer survived shocks exceeding 2000 g along all three axes with no damage or performance shift and met requirements for automotive applications. For more precise control of the gap between the device mass and its stops, a capacitive accelerometer used one set of finger electrodes as in-plane shock stops [48]. Also, to reduce the gap in the vertical direction, out-of-plane shock stops were defined using CVD film released after removing a thin sacrificial layer underneath the film [34, 49].

Note that the impact on a shock stop can generate a secondary source of shock

(e.g., impact force) that may result in fracture, debris, performance shifts, or residual oscillation of the device [27, 50-52]. The additional stresses due to impact on a shock stop may lead to fracture even though the stop is meant to limit the maximum bending stress at the anchor. This potential problem increases with the more delicate microstructures used in higher performance devices. Therefore, effective shock protection technologies must also limit secondary impact forces in addition to limiting the overall deflections of the microstructure.

Some efforts have already been devoted to implementing this dual strategy. A curved surface shock stop was suggested as one means to reduce the impact force by distributing the contact force over a larger contact area [53]. However, the impact force reduction was relatively minor, and it is also not easy to fabricate a curved surface in the manner to equally distribute impact force. Increasing the damping imparted to the device mass is another method to reduce the impact force. An encapsulated accelerometer was vented to improve shock resistance [54], but this solution is not possible in high-Q MEMS devices like gyroscopes, resonators, or oscillators. The impact force can be reduced by decreasing the gap between the device and its stops. However, as the impact force scales with the square of the gap, the ultimate reduction is small yet the fabrication complexity can be large.

1.1.4. New Shock Protection Technologies for MEMS

In this dissertation, we propose two new shock protection technologies that address the shortcomings noted above. Our solutions basically employ the shock stop idea to decouple the device design and the shock-protection design, and are specialized to reduce the impact force, which is the potential problem of hard shock stops.

Our two solutions utilize one or both of the two ways to reduce the impact force. Figure 1.5 shows conceptual views of the solutions. Our first concept is nonlinear spring shock stops and utilizes a nonlinear spring formed either by a single microbeam or by a cascade of closely spaced microbeams. The compliance of these beam structures increases the contact time between the device and stops, and thus reduces the impact force delivered to the device as it impacts the shock stop. In addition, the nonlinear hardening stiffness afforded by these structures leads to rapid (nonlinear) increases in the restoring force, leading to decreased travel of the device's mass.

However, impulse reduction by this concept is minor because of minor damping effect from the stops.

Our second concept is soft coating shock stops and utilizes a thin-film layer of a soft material on an otherwise hard surface, and relies both on the increased surface compliance and energy dissipation. The increased compliance extends the contact time, and the increased dissipation reduces the impulse by the smaller coefficient of restitution (COR). Thus, the impact force decreases with a soft coating. Also, the 'softer' coating dissipates more energy during impact, and this serves to reduce both the number of impacts as well as the settling time following shocks. This energy absorption at the impact site becomes more attractive especially in the case of vacuum-packaged MEMS, when we cannot increase the damping of the device mass. However, this concept has smaller impact force reduction compared with nonlinear spring shock stops.

Both of our two concepts showed (1) superior shock protection compared with conventional hard shock stops, (2) convenient integration with many MEMS devices, and (3) wafer-level, batch fabrication process compatible with conventional microfabrication techniques except the deposition of soft-coating materials such as polymers. The nonlinear spring and soft coating shock stops will be further discussed in Chapters 4 and 5.

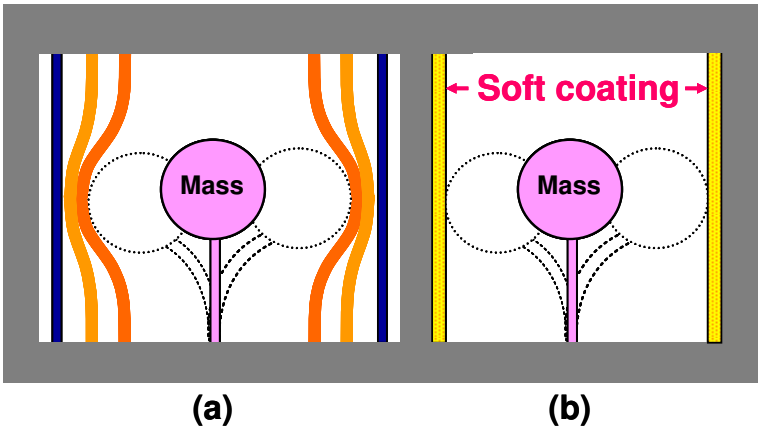

Figure 1.5. Conceptual views of our two novel shock protection technologies. (a) Nonlinear spring shock stops and (b) soft coating shock stops.

1.2. Vibration Isolation for MEMS

In this section, we will characterize the vibration environment experienced by MEMS devices in various applications (Section 1.2.1), note how these vibrations may degrade device performance (Section 1.2.2), and report methods to suppress vibration (Section 1.2.3) in MEMS device design. Finally, we provide a short preview of the vibration analysis and isolation systems developed further in this dissertation.

1.2.1. Characterizing Vibration Environments

Mechanical vibration refers to sustained oscillatory motion over a reasonably long time relative to the settling time of a device [12]. Vibration can manifest itself in narrow-band response, as is observed in the simple harmonic response of rotating machinery [55], all the way to wide-band (or broad-band) response as that may follow shortly after an impact event [3, 12].

Table 1.2 summarizes the dominant vibration frequencies often considered in a wide range of applications. The dominant frequency ranges listed correspond to the those needed to define the acceleration power spectrum. Everyday/common applications include the vibration environments produced in land vehicles, in factories, and in vibration testing and these environments typically produce modest vibrations from near DC to perhaps of a few kHz.

By contrast, significantly larger amplitude vibrations are experienced in harsh environments, particularly those associated with space flight or military applications. While a spacecraft in stationary orbit experiences very small and low frequency (< 3 Hz) vibrations, it may experience large vibrations over a large bandwidth (10k Hz) during launch. Military applications, including aircraft and missile launch and flight, similarly produce very large vibrations and large bandwidths (e.g., up to 50k Hz).

Vibration can also be generated from incident impact (or shock). As briefly described in Section 1.1.2, impacts in MEMS devices produce broad-band excitation and generate subsequent dynamic response of device structures. Each frequency of those shocks has a distinct amplitude [56, 57]. Shock-induced vibration is also commonly used in vibration-performance testing for MEMS [3, 58].

Table 1.2. Dominant Vibration Frequencies in Various Environments

Application		Dominant vibration frequency spectrum	Reference
Everyday/common applications			
Land vehicles	Car on normal road	0-400 Hz	[59]
	Ambulance	2-500 Hz	[60]
	Amtrack train	1-1000 Hz	[60]
	Requirement for several automotive sensors	100-2000 Hz	[15]
Factory	Rotating machinery (motors, fans)	<1000 Hz	[55]
Vibration tests	Shaker table	10-20,000 Hz	[61]
Harsh environment applications			
Spacecraft	Spacecraft in orbit	0.1-3 Hz	[62-65]
	Spacecraft during launch	Transient: <60 Hz Random vibration: 20-20,00Hz Pyrotechnic shock: 10-10,000 Hz	[66]
Military	Military aircraft (flight)	100-2000 Hz	[67]
	Missile	0-50,000 Hz	[68]

1.2.2. Vibration Effects on MEMS

Mechanical vibrations in MEMS can degrade device performance because performance frequently relies on the displacements of or stress in microstructures [57, 69]. The undesirable dynamics generates errors in the device output.

Such output errors (also referred to as "vibration sensitivity") have been observed in many devices and can be categorized as: (1) false output, or (2) sensitivity change. False outputs arise when a MEMS device responds to vibration by generating output even in the absence of any target input. A commercial MEMS vibratory gyroscope generates false output errors when subject solely to impact and subsequent vibration and no rotation [58, 69]. In this instance, an impact of 100-g was applied along the sense-axis of the gyro and produced a false output of ~3.5 deg/sec even though no rotation was applied. However, anther impact-like vibration of 1200-g amplitude generated smaller false output of ~1.6 deg/sec when applied along with the rotation axis of the gyro. Another MEMS gyroscope exhibited distinct vibration sensitivities when operated in common mode (gyroscope employs single mode of vibration of proof mass) versus differential mode (gyroscope employs two modes of vibration of proof mass) [70]. In particular, the gyro operating in common-mode exhibited more than four

times the vibration-induced false output compared to differential mode.

In contrast, the sensitivity change (also referred to as "scale-factor change") occurs in the presence of the target input. The total output of the device is that due to the target input plus that due to the unwanted vibration. For example, thin-film piezoelectric pressure sensors showed significant sensitivity change (10-12%) when simultaneously subjected to 10 g vibration [71]. Similarly, a MEMS gyro experienced a change in rotation-rate sensitivity when both a rotational and a sense-axis vibration were applied [69]. MEMS silicon resonators were reported to produce phase noise of ~10 ppb/g because their resonant frequency changed by vibration-induced structural stress or displacement [72, 73]. This phase noise was a bit higher than that of quartz resonators, which also suffered vibration-induced frequency shifts because the vibration alters the orientation of the quartz molecules [74].

These errors immediately appear at the device output, and therefore, we call them output errors. The output errors can generate critical systemic problem in sensor systems [65] because they are unpredictable and hard to be compensated using electronics.

Another problem associated with vibration is accelerated device fatigue it may produce. Vibration-induced fatigue may manifest itself in the same physical damage including microstructure cracks, debris, bonding area cracks, and/or detachment of bonding wires. Fatigue is more likely under the "high-cycle" conditions produced during long-term testing as is required by many industrial and military standards. Therefore, we call them as long-term fatigue-accelerated physical damage. This problem, although not handled in detail in this thesis, can be mitigated by employing an effective vibration-isolation system originally designed to suppress output errors induced by sustained vibrations.

1.2.3. Vibration Suppression for MEMS

Many strategies exist to reduce vibrations within engineering including designing a classical vibration isolation system in the form of a "soft suspension." However, vibration isolation technologies for MEMS are challenged by many limitations due to the constraints imposed by physical size, material selection, fabrication methods, and integration methods. For example, it would be impractical to fabricate a soft

suspension to eliminate low frequency vibrations in a bandwidth below 100 Hz because small device masses and relatively stiff suspension components (e.g. cantilever beams) in MEMS devices yield natural frequencies often in the kHz range and above. Another potential solution is to substantially increase damping by resorting to fluid-filled devices. However, current micro-fabrication techniques do not provide the means to accommodate sealed fluid cavities in a reliable and repeatable manner.

Despite these limitations, several techniques to suppress vibrations in MEMS devices have been reported. Potential techniques to suppress vibration are illustrated in Figure 1.6. For example, one can suppress vibration either by optimizing the device itself (i.e., design a "vibration-insensitive" device) or by isolating the device from vibrations (i.e., integrating the device with a vibration isolator). The micromachined vibration isolators may not have sufficiently low natural frequencies, but they are effective for MEMS devices that are susceptible to high frequency vibrations, such as gyroscopes. Interface electronics, such as electronic filters or active vibration control, may also be used for vibration suppression. But there are few examples of this in the MEMS literature.

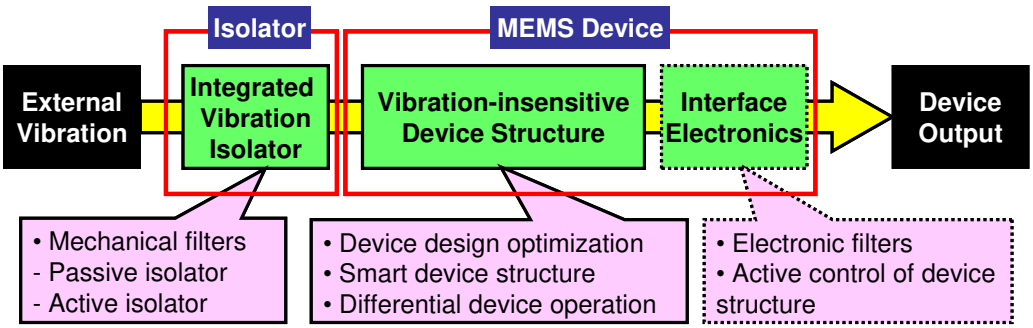

Figure 1.6. Concepts for vibration suppression in MEMS.

1.2.3.1. Optimized Device Structures

In some applications, it may be possible to design a device to be insensitive to vibrations by making it unresponsive to mechanical inputs or by canceling the unwanted effects of vibration. While this strategy appears attractive, a design optimized for superior vibration response may well be inferior from the standpoint primary device performance (e.g. have unacceptable sensitivity).

Vibration suppression through the optimized device design can be realized by several approaches. One approach involves optimizing the physical dimensions to

increase the resonant frequency of the device so that it lies well above the frequency spectrum of the environmental excitation. This is particularly important for resonators, which are especially susceptible to environmental excitation having frequencies at/near the resonant frequencies of the device [57]. The increased resonant frequency follows from stiffening the device which renders it less susceptible to vibration-induced output (errors). Damping can also be used advantageously to reduce vibration as demonstrated in [12, 54]. However, in many applications, the stiffened structure may yield less sensitivity and/or resolution for the device. This approach is often employed in MEMS vibratory gyroscopes which are especially sensitive to environmental vibrations. As a result, it is generally advised that the resonant frequency for MEMS gyros be several times larger than the environmental excitation frequencies [42, 75, 76]. Also, a cubic structure made of piezoelectric material (PZT) was operated at its 29^{th} resonance mode (>100k Hz) and was used as a gyroscope [77]. This high resonant frequency makes the device less sensitive to external vibration as explained above.

A second approach follows from utilizing a vibration mode for the device operation that is largely immune to environmental excitation due to its mode shape, properly located read-out electrodes, or added electrical filters. This approach is often employed in degenerate-mode MEMS vibratory gyroscopes such as ring gyroscopes [42, 78, 79]. Ring gyros detect rotation rates using a pair of ring bending modes. However environmental excitation largely induces translation (not bending) of the ring structure. For instance, the bending modes of a ring gyroscope were measured to have a resonant frequency (~30 kHz) approximately 1.5 times that of the translation mode (~20k Hz) [42]. Some gyroscopes employ torsional mode shapes, that are also largely immune to environmental excitation as they are hard to excite [80].

Another promising approach is to cancel vibration effects using differential operation modes. Differential operation employs two identical sensors that operate out-of-phase and the outputs of the two sensors are subtracted to amplify sensor signal and to cancel out common-mode noise. In this context, environmental vibration is essentially noise that generates undesirable motion of a common mode shape in the two device structures, and is effectively cancelled using differential read-out. This is fundamentally a variation on the approach above since differential operation and common-mode operation reply on distinct mode shapes. This “common-mode rejection” is employed in tuning fork gyroscopes which have two single-mass gyroscopes operating out-of-phase [57, 81]; refer to detailed discussions in Chapter 2.

For example, a tuning fork gyroscope using common-mode rejection exhibited a greater than 75% reduction in output error when it was excited by wide-band vibration, compared to that when operated in common mode [70]. Another example is an accelerometer that uses two vibrating micro-beams operated in differential mode to achieve common-mode rejection [82]. This approach has been extended to multiple tuning fork gyros to achieve a more symmetric operation and to minimize frequency mismatch due to fabrication errors [83, 84]. Thus, a major challenge with this approach overall is to achieve perfect matching of the resonant frequencies of the component devices.

Yet another approach is to control unwanted vibration using interface electronics that either actively control vibration or filter vibration. Electrical filters or frequency demodulators at the terminal output of the device output are used to filter unwanted, out-of-band signals that derive from environmental excitation. Micromachined mechanical filters can also be used as reported in [33, 85]. However, such filters cannot distinguish in-band signal from in-band noise in several. Active vibration control of MEMS devices has not yet become common. One example though is a micro-cantilever beam (width 30 μm, length 500 μm and thickness of 2 μm) [86] which, at least in a design stage, did not demonstrate performance improvements.

1.2.3.2. Addition of Vibration Isolators

Another vibration-suppression method is integrating a separate vibration isolator structure with MEMS devices. Classical vibration isolators serve as mechanical low pass filters and essentially attenuate high frequency environmental excitation. Excitation that is not well above the resonant frequency of the isolation/device, however, may not be attenuated and can even be amplified. Thus, isolation system design [87] requires good understandings of (1) the frequency spectrum of the environmental excitation, (2) how this excitation will impact device performance, and (3) the potential adverse effects of introducing an isolator.

Vibration isolation using "soft suspensions" is well-known in macro-scale applications as in the example of a vehicle suspension system and there is therefore considerable literature providing extensive descriptions of concepts, designs, fabrication methods and test results. In addition to the classical (passive) isolation introduced above, there are also active vibration isolators as shown conceptually in Figure 1.7.

As mentioned above, the basic passive isolator serves as a mechanical low-pass filter. In our present discussion of MEMS devices, the isolator would be inserted between a device and the environment and it filters higher frequency vibrations so that they do not adversely affect the device. While, this strategy is simple and its performance can be easily adjusted by simple design changes, it also has limitations in both operation and performance. Passive low-pass-filters (LPF) and notch filters (NF) have been developed, but vibration isolators operating as high-pass-filters (HPF) or band-pass-filters (BPF) have not been reported using passive components. Moreover, vibration isolators often require delicate and compliant structures which are then susceptible to overload and damage from shock.

These problems may be resolved by employing active vibration isolators. An active isolator consists of a passive isolator, vibration sensor, actuator, and feedback control electronics (Figure 1.7). Adequate design of these components improves the vibration-isolating performance and also introduces novel filter operation. However active isolators require more complex structures, harder fabrication/integration, larger power consumption and more volume compared to passive isolators [12].

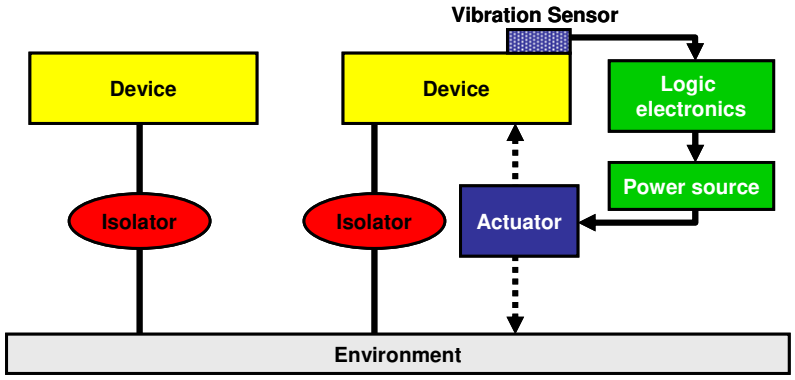

Figure 1.7. Conceptual views of a passive vibration isolator (left) and an active vibration isolator (right).

The basic passive mechanical low-pass-filter (LPF) simply consists of a set (or multiple sets) of a mass-spring-damper combination mounted between the base of the package (environment) and the device itself as shown in Figure 1.8a. The spring-mass-damper combination can be fabricated either (1) by using mechanical structures or (2) by exploiting the viscoelastic properties of materials [12]. This filter attenuates the effects of vibrations that have frequencies larger than the filter's resonant frequency (f_L). This attenuation level is determined by f_L and by the filter's damping properties which

also determine the filter's peak amplitude, and the slope after f_L. The details of mounting a device on an isolator can also influence isolation performance. For example, vibration effects on quartz resonators were greatly reduced when the resonators were attached to a vibration isolator using a minimum number of symmetrically arranged attachments [74].

Passive mechanical notch filters are traditionally referred to vibration 'absorbers' in the literature in mechanical vibrations. They 'absorb' vibrations over a small range of frequencies centered about the resonant frequency of the absorber [12]. The absorber consists of a second mass-spring-damper mounted to a device mass as shown in Figure 1.8b. At the absorber resonant frequency, the absorber oscillated out of phase with the device and when properly tuned can significantly reduce the device oscillations within a narrow bandwidth. However, there are several problems with this strategy. First, the effects of vibrations having frequencies even modestly different from the absorber resonant frequency may not be attenuated and in fact may even become amplified. Second, it can be a challenge to match the absorber resonant frequency to the dominant excitation frequency/ies in a changing and often unknown environment. Third, the absorber should ideally be attached to the device mass and the additional absorber mass may generate unexpected influence on device performance including shifting the resonant frequency and reducing the quality factor.

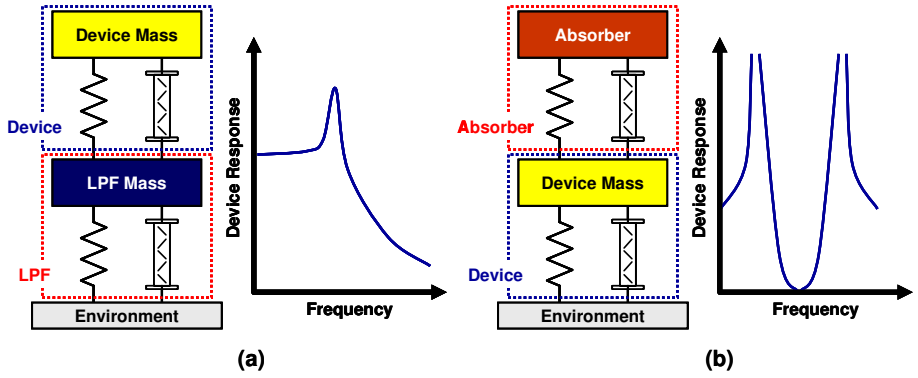

Figure 1.8. Conceptual views of (a) a mechanical low-pass-filter (LPF) and (b) a mechanical notch filter (NF, i.e. a vibration absorber).

Few published works address vibration effects specifically for MEMS devices or their vibration isolation. Of course, it may be somewhat artificial to separate vibration isolators used for macro-scale versus MEMS-scale devices. Nevertheless this distinction is important due to the disparate manufacturing methods and materials that

are available to construct effective vibration isolators. Here, we shall focus on vibration isolators that can be produced using micromachining technologies and the available materials for MEMS fabrication.

Prior studies consider low-pass filters composed of silicon micro-beams because low-pass filters are the easiest to fabricate and to integrate with devices. For example, a micromachined vibration isolator integrated with a surface transverse wave (STW) resonator was reported [9, 88]. This isolator is composed of silicon micro-beams fabricated by KOH etching and bonded with a commercial quartz STW resonator using a conductive epoxy. As reviewed above, the isolator functions as a low-pass-filter and successfully attenuates vibrations having frequencies higher than the filter's bandwidth (1.2 kHz). This bandwidth was sufficiently small, considering the very high natural frequency of the device (1 GHz), and the resulting vibration sensitivity was measured to be $1.8*10^{-8}$/g, which also agrees with FEM predictions ($1.3*10^{-8}$/g). However, adding the isolator integration also resulted in unintended additional vibration modes. Because of the bonding epoxy used in the integration of the isolator, a gap of 20-25 μm was created between the resonator and the isolator. This gap was sufficient to enable the excitation of additional vibration mode that distorted the frequency response of the resonator.

Aside from micromachined vibration isolators, other designs employed viscoelastic materials to attenuate vibration energy. Rubber was used to isolate MEMS acoustic sensors from vibration [89] and an isolator made of oil and air was also investigated [90]. Another design employed an active vibration isolator [91]. This design was composed of a clamped-clamped silicon beam structure with a center mass, which yielded a passive isolator, and an active isolator formed by PZT actuators and sensors. However, all of the above studies were for the conceptual design stage and none demonstrated device performance improvement via experiments.

1.3. Principal Contributions

The major contributions resulting from this dissertation are summarized below.

Concerning shock protection in MEMS devices, we

1. develop two novel shock protection concepts in the form of nonlinear springs

and soft coating shock stops,

2. demonstrate the superior shock protection afforded by these two concepts (shock survival improved at least 20 times over that with conventional hard stops),
3. identify a new fracture mechanism induced by impact between the device mass and its motion-limiting (hard) shock stops,
4. demonstrate experimentally the nature of this fracture mechanism.

Concerning vibration isolation for MEMS devices, we

1. analyze and compare the vibration sensitivities of MEMS devices, including two common designs for MEMS angular rate gyros (tuning fork design and ring design) that are known to be relatively immune to environmental vibration,
2. achieve partial suppression of vibration-induced effects by altering the device design,
3. quantitatively demonstrate vibration suppression by integrating a vibration isolator for MEMS and provide guidelines for MEMS isolator design.

1.4. Organization of Dissertation

This dissertation consists of six chapters and appendices. Chapter 1 introduces the topics of shock and vibration of MEMS devices by reviewing how these environmental influences arise in applications, the problems they create, and previous solutions and their limitations. Chapter 2 presents a careful analysis of vibration effects in MEMS devices with a focus on MEMS gyros. Chapter 3 then demonstrates how these vibration effects are minimized using integrated vibration isolators. Chapter 4 presents two novel shock protection concepts that minimize the impact of the device mass with motion-limiting stops. Chapter 5 summarizes the fabrication of these shock protection concepts and the associated experimental results from shock tests. Finally, Chapter 6 concludes the dissertation by reviewing the principal contributions and future research opportunities.

References

[1] J. Bryzek, S. Roundy, B. Bircumshaw, C. Chung, K. Castellino, J. R. Stetter, and M. Vestel, "Marvelous MEMS," *Circuits and Devices Magazine, IEEE,* vol. 22, pp. 8-28, 2006.

[2] D. M. Tanner, J. A. Walraven, K. S. Helgesen, L. W. Irwin, D. L. Gregory, J. R. Stake, and N. F. Smith, "MEMS reliability in a vibration environment," in the Proceeding of *IEEE International Reliability Physics Symposium*, 2000, pp. 139-145.

[3] J. A. Geen, S. J. Sherman, J. F. Chang, and S. R. Lewis, "Single-chip surface micromachined integrated gyroscope with 50/spl deg//h Allan deviation," *IEEE Journal of Solid-State Circuits,* vol. 37, pp. 1860-1866, 2002.

[4] D. M. Tanner, J. A. Walraven, K. Helgesen, L. W. Irwin, F. Brown, N. F. Smith, and N. Masters, "MEMS reliability in shock environments," in the Proceeding of *IEEE International Reliability Physics Symposium*, 2000, pp. 129-138.

[5] C. J. Wilson and P. A. Beck, "Fracture testing of bulk silicon microcantilever beams subjected to a side load," *Journal of Microelectromechanical Systems,* vol. 5, pp. 142-150, 1996.

[6] D. S. Steinberg, *Vibration Analysis for Electronic Equipment* 3rd ed.: Wiley-Interscience, 2000.

[7] G. J. O'Brien, J. Hammond, G. Li, D. Koury, and D. J. Monk, "Outrigger: solid outer frame lateral accelerometer design," in the Proceeding of *International Conference on Solid-State Sensors, Actuators and Microsystems (TRANSDUCERS)*, 2005, pp. 176-179 Vol. 1.

[8] A. Selvakumar and K. Najafi, "A high-sensitivity z-axis capacitive silicon microaccelerometer with a torsional suspension," *Journal of Microelectromechanical Systems,* vol. 7, pp. 192-200, 1998.

[9] J. R. Reid, V. M. Bright, and J. A. Kosinski, "A micromachined vibration isolation system for reducing the vibration sensitivity of surface transverse wave resonators," *Ultrasonics, Ferroelectrics and Frequency Control, IEEE Transactions on,* vol. 45, pp. 528-534, 1998.

[10] J. T. Broch, *Mechanical vibration and shock measurements*. Naerum: Bruel & Kjaer, 1980.

[11] V. T. Srikar and S. D. Senturia, "The reliability of microelectromechanical systems (MEMS) in shock environments," *Journal of Microelectromechanical Systems,* vol. 11, pp. 206-214, 2002.

[12] D. J. Inman, *Engineering Vibration*, 2 ed.: Prentice Hall, 2000.

[13] J. D. Turner and A. L. Austin, "Sensors for automotive telematics," *Measurement Science and Technology,* vol. 11, pp. R58-R79, 2000.

[14] N. Yazdi, F. Ayazi, and K. Najafi, "Micromachined inertial sensors," *Proceedings of the IEEE,* vol. 86, pp. 1640-1659, 1998.

[15] D. R. Sparks, "Application of MEMS technology in automotive sensors and actuators," in the Proceeding of *Micromechatronics and Human Science, 1998. MHS '98. Proceedings of the 1998 International Symposium on*, 1998, pp. 9-15.

[16] M. A. Duesterhaus, V. I. Bateman, and D. A. Hoke, "Shock testing of surface micromachined MEMS devices," in the Proceeding of *Auunual Fuze Conference*, New Orleans, LA, USA, 2003.

[17] AACS Shock Calibrator, Model 2973A (ENDEVCO)

[18] T. G. Brown, B. Davis, D. Hepner, J. Faust, C. Myers, C. Muller, T. Harkins, M. Holis, and B. Placzankis, "Strap-down microelectromechanical (MEMS) sensors for high-g munition applications," *Magnetics, IEEE Transactions on,* vol. 37, pp. 336-342, 2001.

[19] I. W. Scaysbrook, S. J. Cooper, and E. T. Whitley, "A miniature, gun-hard MEMS IMU for guided projectiles, rockets and missiles," in the Proceeding of *Position Location and Navigation Symposium, 2004. PLANS 2004*, 2004, pp. 26-34.

[20] J. K. Yee, H. H. Yang, and J. W. Judy, "Shock resistance of ferromagnetic micromechanical magnetometers," *Sensors and Actuators A: Physical,* vol. 103, pp. 242-252, 2003.

[21] S. Jean-Michel, "Current Capabilities of MEMS Capacitive Accelerometers in a Harsh Environment," *Aerospace and Electronic Systems Magazine, IEEE,* vol. 21, pp. 29-32, 2006.

[22] T. G. Brown, "Harsh military environments and microelectromechanical (MEMS) devices," in the Proceeding of *Sensors, 2003. Proceedings of IEEE*, 2003, pp. 753-760 Vol.2.

[23] C. L. Muhlstein, S. B. Brown, and R. O. Ritchie, "High-cycle fatigue of single-crystal silicon thin films," *Journal of Microelectromechanical Systems,* vol. 10, pp. 593-600, 2001.

[24] D. M. Tanner, "Reliability of surface micromachined MicroElectroMechanical actuators," in the Proceeding of *International Conference on Microelectronics*, Nis, France, 2000, pp. 97-104 vol.1.

[25] M. Sheehy, M. Reid, J. Punch, S. Goyal, and G. Kelly, "The failure mechanisms of micro-scale cantilevers in shock and vibration Stimuli," in the Proceeding of *Symposium on Design, Test, Integration and Packaging of MEMS & MOEMS*, 2008.

[26] W. Merlijn van Spengen, "MEMS reliability from a failure mechanisms perspective," *Microelectronics Reliability,* vol. 43, pp. 1049-1060, 2003.

[27] S. W. Yoon, N. Yazdi, N. C. Perkins, and K. Najafi, "Micromachined integrated shock protection for MEMS," *Sensors and Actuators A: Physical,* vol. 130-131, pp. 166-175, 2006.

[28] T. Ando, K. Sato, M. Shikida, T. Yoshioka, Y. Yoshikawa, and T. Kawabata, "Orientation-dependent fracture strain in single-crystal silicon beams under uniaxial tensile conditions," in the Proceeding of *International Symposium on Micromechatronics and Human Science*, 1997, pp. 55-60.

[29] R. G. Azevedo, J. G. Debbie, A. V. Jog, J. Babak, D. R. Myers, C. Li, X.-a. Fu, M. Mehregany, W. B. J. Muthu, and A. P. Pisano, "A SiC MEMS Resonant Strain Sensor for Harsh Environment Applications," *Sensors Journal, IEEE,* vol. 7, pp. 568-576, 2007.

[30] Y. Xie, S.-S. Li, Y.-W. Lin, Z. Ren, and C. T. C. Nguyen, "Spurious mode suppression in UHF micromechanical extensional wine-glass ring resonators," in the Proceeding of *IEEE International Conference on Micro Electro Mechanical Systems (MEMS)*, 2005, pp. 219-222.

[31] J. Wang, Z. Ren, and C. T. C. Nguyen, "1.156-GHz self-aligned vibrating micromechanical disk resonator," *Ultrasonics, Ferroelectrics and Frequency Control, IEEE Transactions on,* vol. 51, pp. 1607-1628, 2004.

[32] Y.-W. Lin, S. Lee, S.-S. Li, Y. Xie, Z. Ren, and C. T. C. Nguyen, "Series-resonant VHF micromechanical resonator reference oscillators," *IEEE Journal of Solid-State Circuits,* vol. 39, pp. 2477-2491, 2004.

[33] S.-S. Li, Y.-W. Lin, Z. Ren, and N. C. T. C., "Disk-Array Design for Suppression of Unwanted Modes in Micromechanical Composite-Array Filters," in the Proceeding of *Micro Electro Mechanical Systems (MEMS)*, 2006, pp. 866-869.

[34] H. Johari and F. Ayazi, "High-frequency capacitive disk gyroscopes in (100) and (111) silicon," in the Proceeding of *Micro Electro Mechanical Systems, 2007. MEMS. IEEE 20th International Conference on*, 2007, pp. 47-50.

[35] N. Yazdi and K. Najafi, "An all-silicon single-wafer micro-g accelerometer with a combined surface and bulk micromachining process," *Microelectromechanical Systems, Journal of,* vol. 9, pp. 544-550, 2000.

[36] J. Chae, H. Kulah, and K. Najafi, "A monolithic three-axis micro-g micromachined silicon capacitive accelerometer," *Microelectromechanical Systems, Journal of,* vol. 14, pp. 235-242, 2005.

[37] ADXL330 (Analog Devices Inc.)

[38] K. Ishihara, Y. Chi-Fan, A. A. Ayon, and M. A. Schmidt, "Inertial sensor technology using DRIE and wafer bonding with connecting capability," *Microelectromechanical Systems, Journal of,* vol. 8, pp. 403-408, 1999.

[39] H. Xie, Y. Pan, and G. K. Fedder, "A CMOS-MEMS mirror with curled-hinge comb drives," *Microelectromechanical Systems, Journal of,* vol. 12, pp. 450-457, 2003.

[40] P. F. Van Kessel, L. J. Hornbeck, R. E. Meier, and M. R. Douglass, "A MEMS-based projection display," *Proceedings of the IEEE,* vol. 86, pp. 1687-1704, 1998.

[41] M. C. Lee, S. J. Kang, K. D. Jung, S.-H. Choa, and Y. C. Cho, "A high yield rate MEMS gyroscope with a packaged SiOG process," *Journal of Micromechanics and Microengineering,* vol. 15, pp. 2003-2010, 2005.

[42] M. W. Putty, "A Micromachined Vibrating Ring Gyroscope," Ph.D. Thesis, University of Michigan, 1995

[43] M. F. Zaman, A. Sharma, and F. Ayazi, "High Performance Matched-Mode Tuning Fork Gyroscope," in the Proceeding of *IEEE International Conference on Micro Electro Mechanical Systems*, Istanbul, Turkey 2006, pp. 66-69.

[44] T. K. Tang, R. C. Gutierrez, C. B. Stell, V. Vorperian, G. A. Arakaki, J. T. Rice, W. J. Li, I. Chakraborty, K. Shcheglov, J. Z. Wilcox, and W. J. Kaiser, "A packaged silicon MEMS vibratory gyroscope for microspacecraft," in the Proceeding of *Micro Electro Mechanical Systems, 1997. MEMS '97, Proceedings, IEEE., Tenth Annual International Workshop on*, 1997, pp. 500-505.

[45] S. Lee, S. Park, J. Kim, S. Lee, and D.-I. Cho, "Surface/bulk micromachined single-crystalline-silicon micro-gyroscope," *Journal of Microelectromechanical Systems,* vol. 9, pp. 557-567, 2000.

[46] L. B. Wilner, "A high performance, variable capacitance accelerometer," *IEEE Transactions on Instrumentation and Measurement,* vol. 37, pp. 569-571, 1988.

[47] S. Huang, X. Li, Y. Wang, J. Jiao, X. Ge, D. Lu, L. Che, K. Zhang, and B. Xiong, "A piezoresistive accelerometer with axially stressed tiny beams for both much increased sensitivity and much broadened frequency bandwidth," in the Proceeding of *International Conference on Solid-State Sensors, Actuators and Microsystems (TRANSDUCERS)*, 2003, pp. 91-94 vol.1.

[48] J. M. Tsai and G. K. Fedder, "Mechanical noise-limited CMOS-MEMS accelerometers," in the Proceeding of *IEEE International Conference on Micro Electro Mechanical Systems (MEMS)*, 2005, pp. 630-633.

[49] J. A. Geen and D. W. Carow, "Micromachined devices with stop members," in *United States Patent*. vol. US 6,487,908B2, I. Analog Devices, Ed., 2002.

[50] S. W. Yoon, N. Yazdi, N. C. Perkins, and K. Najafi, "Novel integrated shock protection for MEMS," in the Proceeding of *International Conference on Actuators and Microsystems Solid-State Sensors (TRANSDUCERS)*, 2005, pp. 396-400 Vol. 1.

[51] S. W. Yoon, N. Yazdi, J. Chae, N. C. Perkins, and K. Najafi, "Shock protection using integrated nonlinear spring shock stops," in the Proceeding of *IEEE International Conference on Micro Electro Mechanical Systems (MEMS)*, Istanbul, Turkey, 2006, pp. 702-705.

[52] S. W. Yoon, S. Lee, N. C. Perkins, and K. Najafi, "Shock protectiong using soft coating as shock stops," in the Proceeding of *A Solid State Sensors, Actuators and Microsystems Workshop (Hilton Head)*, Hilton Head Island, SC, USA, 2006, pp. 396-399.

[53] J. Dong, X. Li, Y. Wang, D. Lu, and S. Ahat, "Silicon micromachined high-shock accelerometers with a curved-surface-application structure for over-range stop protection and free-mode-resonance depression," *Journal of Micromechanics and Microengineering,* vol. 12, pp. 742-746, 2002.

[54] W.-T. Park, A. Partridge, R. N. Candler, V. Ayanoor-Vitikkate, G. Yama, M. Lutz, and T. W. Kenny, "Encapsulated submillimeter piezoresistive accelerometers," *Journal of Microelectromechanical Systems,* vol. 15, pp. 507-514, 2006.

[55] L. A. Sievers and A. H. von Flotow, "Linear control design for active vibration isolation of narrow band disturbances," in the Proceeding of *Decision and Control, 1988., Proceedings of the 27th IEEE Conference on*, 1988, pp. 1032-1037 vol.2.

[56] A. V. Oppenheim, A. S. Willsky, and S. H. Nawab, *Signals and Systems* Prentice Hall, 1996.

[57] S. W. Yoon, S. W. Lee, N. C. Perkins, and K. Najafi, "Vibration Sensitivity of MEMS Tuning Fork Gyroscopes," in the Proceeding of *IEEE SENSORS 2007 Conference* Atlanta, Georgia, USA, 2007, pp. 115-119.

[58] ADXRS150/300 (Analog Device, Inc.)

[59] J. Y. Wong, *Theory of ground vehicles*, 2 ed.: John Wiley & Sons, 1993.

[60] J. Wu, R. R. Zhang, Q. Wu, and K. K. Stevens, "Environmental vibration assessment and its applications in accelerated tests for medical devices," *Journal of Sound and Vibration,* vol. 267,

pp. 371-383, 2003.

[61] Type 4809 (Bruel & Kjaer)

[62] A. J. Butterfield and S. E. Woodard, "Measured spacecraft instrument and structural interactions " *Journal of Spacecraft and Rockets* vol. 33, pp. 556-562, 1996.

[63] S. E. Woodard, D. A. Gell, and R. R. Lay, "Measured spacecraft dynamic effects on atmospheric science instruments," *Geoscience and Remote Sensing, IEEE Transactions on,* vol. 36, pp. 359-367, 1998.

[64] Y. Zhao and J. Alexander, "Effects of G-jitter on Experiments Conducted in Low-Earth Orbit: A Review " in the Proceeding of *Aerospace Sciences Meeting and Exhibit*, Reno, Nevada, USA, 2003.

[65] S. J. C. Dyne, D. E. L. Tunbridge, and P. P. Collins, "The vibration environment on a satellite in orbit," in the Proceeding of *High Accuracy Platform Control in Space, IEE Colloquium on*, London, UK, 1993, pp. 12/1-12/6.

[66] P. Wilke, C. Johnson, P. Grosserode, and D. Sciulli, "Whole-spacecraft vibration isolation for broadband attenuation," in the Proceeding of *Aerospace Conference Proceedings, 2000 IEEE*, 2000, pp. 315-321 vol.4.

[67] E. Veilleux, "Vibration Control of Printed-Circuit Boards in a Dynamic Environment," *Parts, Materials and Packaging, IEEE Transactions on,* vol. 6, pp. 100-105, 1970.

[68] R. D. Weglein, "The Vibration Sensitivity of VHF Quartz Crystals for Missile Applications," in the Proceeding of *38th Annual Symposium on Frequency Control. 1984*, 1984, pp. 73-79.

[69] J. A. Geen, "Progress in integrated gyroscopes," in the Proceeding of *Position Location and Navigation Symposium (PLANS)*, Monterey, CA, USA, 2004, pp. 1-6.

[70] A. R. Schofield, A. A. Trusov, and A. M. Shkel, "Multi-Degree of Freedom Tuning Fork Gyroscope Demonstrating Shock Rejection," in the Proceeding of *IEEE Sensors*, 2007, pp. 120-123.

[71] A. A. Kazaryan, "A Thin-Film Piezoelectric Pressure Sensor " *Measurement Techniques,* vol. 45, pp. 515-518, 2002.

[72] M. Agarwal, K. K. Park, M. Hopcroft, S. Chandorkar, R. N. Candler, B. Kim, R. Melamud, G. Yama, B. Murmann, and T. W. Kenny, "Effects of Mechanical Vibrations and Bias Voltage Noise on Phase Noise of MEMS Resonator Based Oscillators," in the Proceeding of *19th IEEE International Conference on Micro Electro Mechanical Systems*, Istanbul, Turkey, 2006, pp. 154-157.

[73] R. Kazinczi, J. R. Mollinger, and A. Bossche, "Environment-induced failure modes of thin film resonators," *Journal of Microlithography, Microfabrication, and Microsystems,* vol. 1, pp. 63-69, 2002.

[74] R. L. Filler, "The acceleration sensitivity of quartz crystal oscillators: a review," *Ultrasonics, Ferroelectrics and Frequency Control, IEEE Transactions on,* vol. 35, pp. 297-305, 1988.

[75] C. Jeong, S. Seok, B. Lee, H. Kim, and K. Chun, "A study on resonant frequency and Q factor

tunings for MEMS vibratory gyroscopes," *Journal of Micromechanics and Microengineering,* vol. 14, pp. 1530-1536, 2004.

[76] G. J. O'Brien, D. J. Monk, and K. Najafi, "Angular rate gyroscope with dual anchor support," in the Proceeding of *A Solid State Sensors, Actuators and Microsystems Workshop (Hilton Head)*, Hilton Head, SC, 2002, pp. 285–288.

[77] K. Maenaka, H. Kohara, M. Nishimura, T. Fujita, and Y. Takayama, "Novel Solid Micro-Gyroscope," in the Proceeding of *Micro Electro Mechanical Systems, 2006. MEMS 2006 Istanbul. 19th IEEE International Conference on*, 2006, pp. 634-637.

[78] F. Ayazi and K. Najafi, "A HARPSS polysilicon vibrating ring gyroscope," *Microelectromechanical Systems, Journal of,* vol. 10, pp. 169-179, 2001.

[79] G. He and K. Najafi, "A single-crystal silicon vibrating ring gyroscope," in the Proceeding of *A Solid State Sensors, Actuators and Microsystems Workshop (Hilton Head 2006)*, 2002, pp. 718-721.

[80] N. Hedenstierna, S. Habibi, S. M. Nilsen, T. Kvisteroy, and G. U. Jensen, "Bulk micromachined angular rate sensor based on the `butterfly'-gyro structure," in the Proceeding of *Micro Electro Mechanical Systems, 2001. MEMS 2001. The 14th IEEE International Conference on*, 2001, pp. 178-181.

[81] H. Xie and G. K. Fedder, "Integrated Microelectromechanical Gyroscopes," *Journal of Aerospace Engineering,* vol. 16, pp. 65-75 2003.

[82] B. Le Foulgoc, O. Le Traon, A. Parent, T. Bourouina, F. Marty, A. Bosseboeuf, and H. Mathias, "Concepts and limits for the miniaturization of silicon differential vibrating inertial micro-beam accelerometer," in the Proceeding of *IEEE Sensors Conference*, 2007, pp. 103-106.

[83] J. A. Geen, "Very low cost gyroscopes," in the Proceeding of *IEEE Sensors*, 2005, pp. 537-540.

[84] S. Kim, B. Lee, J. Lee, and K. Chun, "A gyroscope array with linked-beam structure," in the Proceeding of *Micro Electro Mechanical Systems, 2001. MEMS 2001. The 14th IEEE International Conference on*, 2001, pp. 30-33.

[85] M. U. Demirci and C. T. C. Nguyen, "A low impedance VHF micromechanical filter using coupled-array composite resonators," in the Proceeding of *The 13th International Conference on Solid-State Sensors, Actuators and Microsystems (TRANSDUCERS)*, 2005, pp. 2131-2134 Vol. 2.

[86] W. Zhang, G. Meng, and H. Li, "Adaptive vibration control of micro-cantilever beam with piezoelectric actuator in MEMS " *The International Journal of Advanced Manufacturing Technology,* vol. 28, pp. 321-327, 2006.

[87] T. Braman and O. Grossman, "Designing Vibration and Shock Isolation Systems for Micro Electrical Machined Based Inertial Measurement Units," in the Proceeding of *IEEE/ION Position, Location, And Navigation Symposium (PLANS)*, 2006, pp. 400-404.

[88] J. R. Reid, V. M. Bright, and J. A. Kosinski, "A micromachined vibration isolation system for a 1 GHz STW resonator," in the Proceeding of *IEEE International Frequency Control Symposium*,

1997, pp. 783-790.

[89] J. Yin, G. Lu, C. Gong, X. Liu, and Q. Lei, "Study on optimizing material parameters in the acoustic-vibration sensors isolation packaging system," in the Proceeding of *Electronic Packaging Technology, 2005 6th International Conference on*, 2005, pp. 632-634.

[90] Y. Ping and L. Fuyun, "Design and analysis of a novel oil-air vibration isolator for microelectromechanical systems manufacturing platform " *Proceedings of the I MECH E Part C Journal of Mechanical Engineering Science,* vol. 221, pp. 195-201, 2007.

[91] Y. Meyer, T. Verdot, M. Collet, J. Baborowski, and P. Muralt, "Active isolation of electronic micro-components with piezoelectrically transduced silicon MEMS devices," *Smart Materials and Structures,* vol. 16, pp. 128-134 2007.

CHAPTER 2

VIBRATION EFFECTS ON MEMS

This chapter analyzes vibration effects on MEMS devices, especially MEMS gyroscopes. We have three goals to achieve in this chapter. First, we analyze the mechanisms by which vibration produces errors in the output of MEMS devices, especially gyroscopes. Second, we compare the error-generation mechanisms of several gyroscope designs. Third, we investigate the effectiveness and fundamental limitations of the device-level vibration-suppression methods, which were introduced in Chapter 1.

Section 2.1 outlines the mechanisms producing vibration-induced errors in MEMS and explains why MEMS vibratory gyroscopes are selected for our study. Section 2.2 classifies reported MEMS gyroscopes by vibration phenomena. Vibration effects on non-degenerate gyroscopes, especially non-tuning fork gyroscopes and tuning fork gyroscopes, are analyzed in Sections 2.3 and 2.4, respectively. Section 2.5 presents vibration effects on ring gyroscopes, one of the most common degenerate gyroscopes. Finally, this chapter closes in Section 2.6 by summarizing our findings of vibration effects on the various MEMS gyroscopes.

2.1. Vibration Effects on MEMS Devices and Selection of Gyroscopes

Vibration can create short-lived output errors. Output errors in MEMS devices are generated because the operation of many MEMS devices relies on the dynamic displacement of device structures. Undesired displacements induced by vibration result in unpredictable false outputs that cannot be compensated with electronics and they generate critical and systemic problems [1].

Vibration-induced output errors, also called vibration sensitivity, have been reported for various MEMS devices. We selected MEMS gyroscopes for our study for two reasons. First, MEMS gyroscopes, because of their high quality factor (Q-factor), are known to be susceptible to vibration. Many MEMS gyroscopes require high Q ranging from 45 (in air) to tens of thousands (in vacuum). The high Q is beneficial in

improving gyro performance, including resolution and sensitivity. However, the high Q-factor also amplifies vibration amplitudes at certain frequencies and increases output signal distortions. One method of minimizing the vibration sensitivity is to increase the resonant frequency of a gyroscopes by orders of magnitude larger than the frequencies present in the environmental vibration [2]. However, this method has fundamental limitations because the increased resonant frequency also reduces the sense-direction displacement due to the Coriolis force.

The second consideration in our selection of gyroscopes is their complex structure and operation. The analysis of complex devices is advantageous because once a complex one is understood, less complex designs are easy to analyze. A MEMS gyroscope can be modeled as a combination of a resonator (driving mass) and an accelerometer (sensing mass). This two-device-combination makes analyzing the vibration effects on gyroscopes suitably challenging.

Vibration effects on MEMS accelerometers are not handled in this thesis because vibration is the target input that accelerometers are designed to measure.

2.2. Classification of MEMS Gyroscopes by Vibration Phenomena

To understand vibration effects on MEMS gyroscopes, we classify them into several categories. The results are depicted in Figure 2.1 as a genealogical tree of reported MEMS vibratory gyroscopes that is divided into branches by vibration phenomena. Vibratory gyroscopes can be broadly divided into angle gyros (whole-angle mode) measuring the absolute angle rotation and rate gyros (open-loop or force-to-balance modes) measuring the angular rate [2-4]. A few micromachined angle-gyro designs were reported [4-6], but none have demonstrated reasonable device performance.

Almost all micromachined gyroscopes are vibratory gyroscopes, which employ the Coriolis-force-induced energy transfer between the two vibration modes of the gyroscope [2]. The two vibration modes, i.e., the sense and drive modes, can be either a degenerate pair or a non-degenerate pair, depending on the nature of the operating modes of the gyroscopes [2, 5, 7]. Physically, the degenerate pair refers to a pair of vibration modes that have identical resonant frequencies [8], while the non-degenerate pair refers to a vibration-mode pair having distinct resonant frequencies. Vibrating shell and solid gyroscopes are typical degenerate types [2, 3, 7, 9, 10] whereas all other

vibratory gyroscopes are the non-degenerate types [5, 11]. The non-degenerate types can be mostly modeled as a so-called Coriolis accelerometer, which consists of an accelerometer (sense mass) and a resonator (drive mass). These two devices can have identical (matched-mode) or similar (split-mode) resonant frequencies. The matched-mode design is predominantly used because the Coriolis force is amplified by the high Q, resulting in higher sensitivity and resolution with lower drift [12, 13]. Ideally, these two masses should also be completely decoupled to minimize quadrature error [13, 14]. However, because of design limitations, several coupled or partially-decoupled designs have been proposed [14, 15]. A conceptual sketch of these designs is shown in Figure 2.2. The first class is a design that has coupled sense and drive masses (CP type) [12]. The second class is a design that has decoupled sense and drive masses with an anchored sense mass (DS type) [16, 17]. The third class is a design that has decoupled sense and drive masses with an anchored drive mass (DD type) [18-20]. A doubly decoupled design is also reported [13, 14, 21].

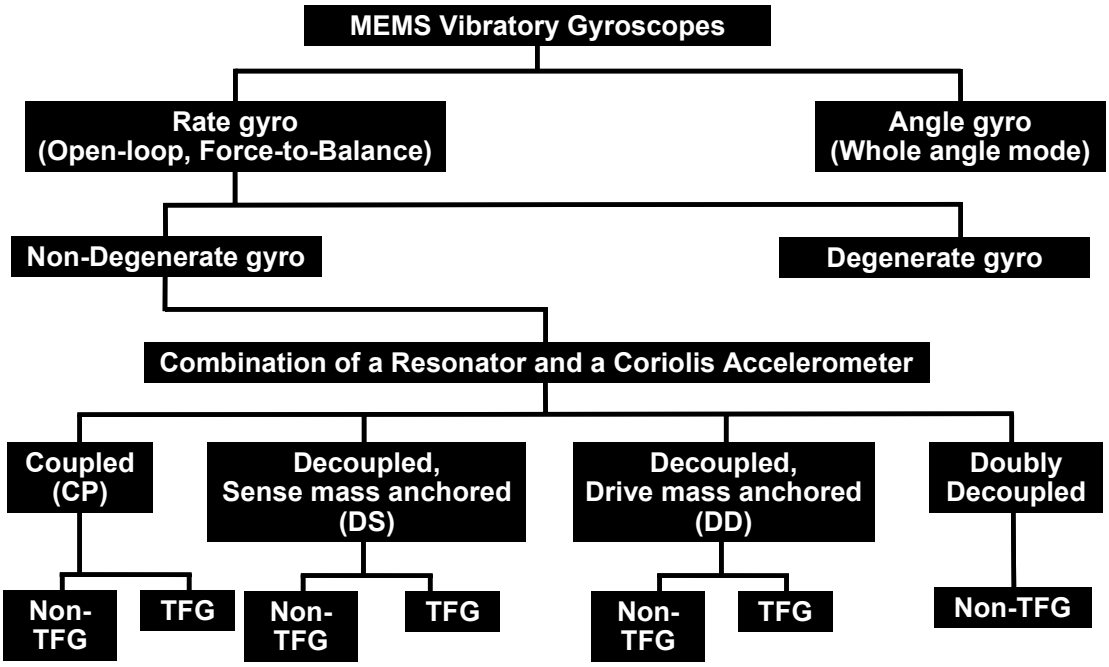

Figure 2.1. Genealogical tree of MEMS vibratory gyroscopes.

Tuning fork gyroscopes (TFG) consist of two such gyroscopes, as depicted in Figure 2.2, and they are designed to vibrate out of phase. Figure 2.3 illustrates detailed views of the three major TFG designs, i.e., CP, DS, and DD types. The doubly decoupled design is considered as a non-TFG (in Section 2.3) but not as a TFG

(in Section 2.4) in this thesis because the design has not been applied to tuning fork gyroscopes. All three TFG types will be analyzed. Of course, each TFG design can also be operated as a non-TFG if the TFG consists of two non-TFGs. Table 2.1 summarizes the reported gyroscopes classified by our classifications explained above.

These structures generally employ comb-drive electrodes for large and stabilized actuation, and capacitance parallel-plate sensing for maximum sensitivity. These actuation and/or sensing mechanisms can also introduce vibration-induced errors that occur because of asymmetric side-effects or nonlinearities, not because of the dynamics of the structure. However, because of the differential operation of the TFG, these errors arise only in particular situations, as discussed below. Also, we consider only linear beam gyroscopes even though torsion beams are used in several gyroscopes [3, 22, 23] because the torsion beam designs can be covered by the same analysis.

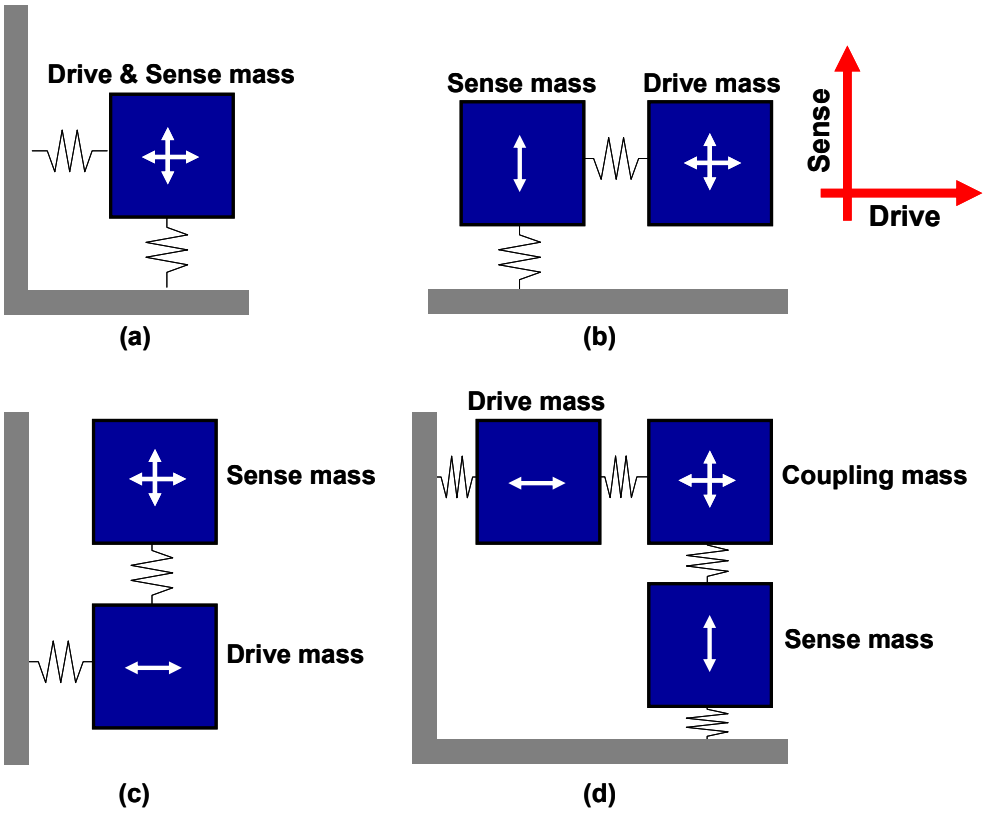

Figure 2.2. Classification of non-degenerate gyroscopes. (a) a design that has coupled sense and drive masses (CP type), (b) a design that has decoupled sense and drive masses with an anchored sense mass (DS type), (c) a design that has decoupled sense and drive masses with an anchored drive mass (DD type), and (d) a doubly decoupled design that has completely decoupled sense and drive masses with one coupling (or connecting) mass.

Table 2.1. Summary of our classification of reported gyroscopes

Degenerate	Relation between sense/drive masses	TFG/Non-TFG	References
Non-degenerate	CP	TFG	[12, 24]
		Non-TFG	[25]
	DS	TFG	[16, 17, 26]
		Non-TFG	[15, 27, 28]
	DD	TFG	[19, 20, 29]
		Non-TFG	[18, 30-36]
	Doubly decoupled	Non-TFG	[13, 14, 21, 37, 38]
Degenerate			[2, 3, 7, 9, 10, 39]

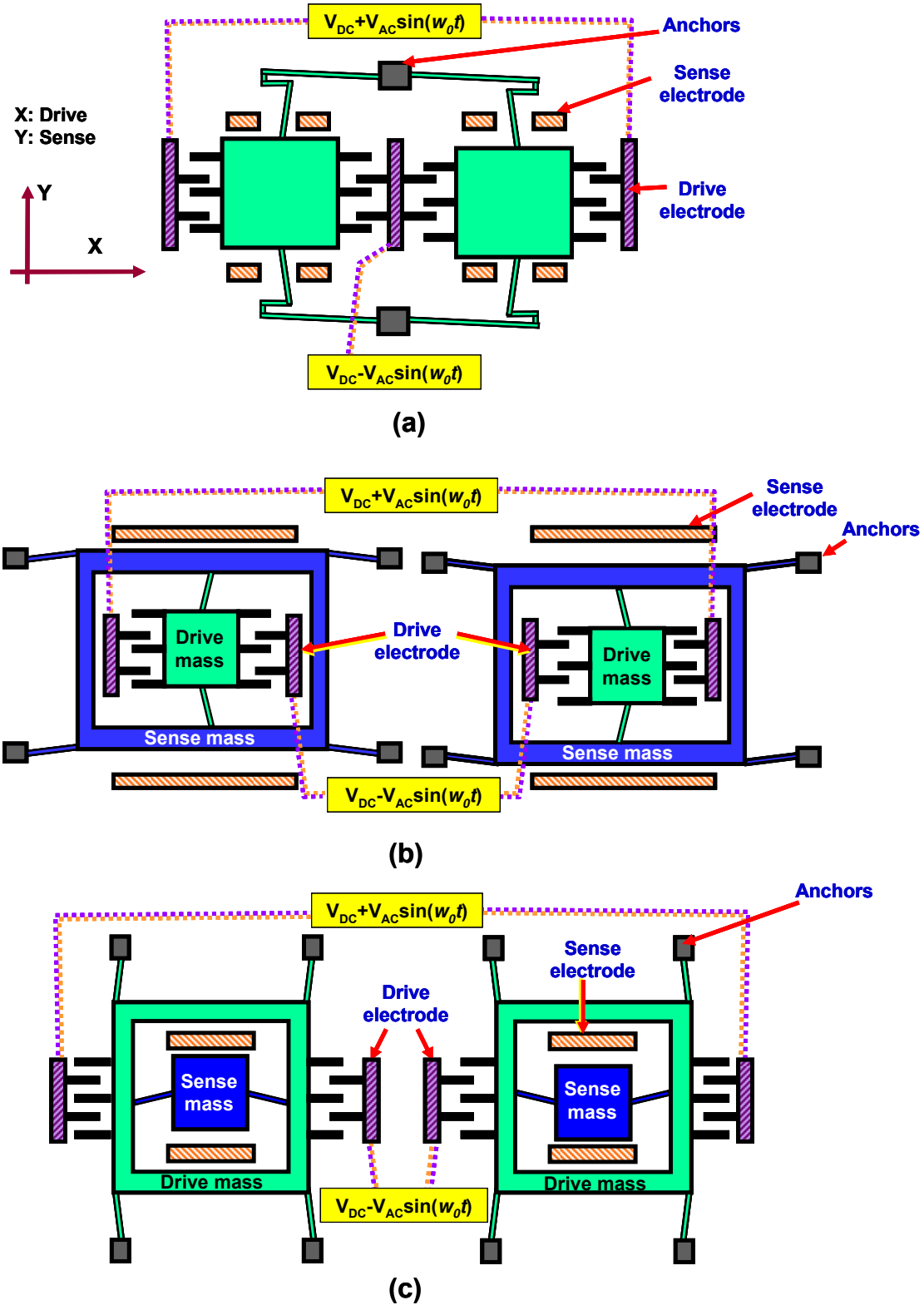

Figure 2.3. Detailed view of the three major designs of tuning fork gyroscopes. (a) CP design, (b) DS design, (c) DD design.

2.3. Vibration Effects on Non-Degenerate Gyroscopes I - Non-Tuning Fork Gyroscopes

Vibratory gyroscopes have three principal axes: (1) the driving axis (direction of v_d), (2) the sensing axis (direction of Coriolis force, F_C), and (3) the rotation axis (direction of Ω). For convenience, we will denote the driving axis as the x-axis, the sensing axis as the y-axis, and rotation axis as the z-axis. The Coriolis force is given by: $F_C = (2m_d v_d)\mathrm{x}(\Omega)$ where m_d is the mass of the resonator, v_d is the response (driving) velocity, and Ω is the angular velocity to be measured. Vibration effects will be analyzed based on their directions and frequencies.

Vibration effects on non-tuning fork gyroscopes are primarily produced from the dynamic behavior of the mechanical structures of the gyroscopes. Our analysis shows that vibrations in the sensing direction are, as expected, the most influential. There are several reasons for this. First, z-axis vibrations have negligible effects because gyroscopes, which are designed to be stiff in that direction, undergo negligible z-axis displacement. Second, x-axis vibrations are less significant than y-axis vibrations when the rotation velocity (Ω) is small. The reason is that a gyro's sense circuitry is designed to read displacements only in the sensing axis, and thus, x-axis vibrations must be converted to y-axis displacement through the Coriolis force ($F_C = 2m_d v_d \Omega$) to be read by the sense circuitry. But for small Ω, especially when it is close to the resolution of the gyroscope, F_C is much smaller than the y-direction force ($F_y = ma_y$) induced by y-axis vibration (a_y). If Ω=0, the x-axis vibration cannot distort the gyroscope's output.

Vibrations having frequencies close to the resonant frequency of the gyroscope are most problematic. Most MEMS gyroscopes are designed to have a very high Q-factor so that their displacements induced by Coriolis forces can be amplified. But the high Q-factor also amplifies environmental vibrations near the device resonance.

As an example, we used the physical dimensions derived from an example gyroscope [48]. The gyroscope has a resonant frequency of 15 kHz and a Q of 40,000. We found several interesting observations. First, the drive-axis (a_x) and the sense-axis (a_y) vibrations are compared. Both vibrations are assumed to have the same amplitude and frequency. The y-direction force produced by a_y (i.e., F_y) has an amplitude $>10^3$ times larger than the additional Coriolis force induced by a_x when Ω=1 deg/sec. Thus,

any sense-axis vibration is far more influential in producing errors than drive-axis vibration as expected.

Second, low frequency vibrations and vibrations having frequencies at/near the gyro's resonance frequency (f_0) are compared. We assumed that the high-frequency (at/near f_0) and low-frequency vibrations have identical amplitude and that their amplitudes are small enough to ensure that the vibration-induced displacement remains smaller than the gap of sense electrodes. Also, because the outputs of the gyroscope's read-out circuit go through a band pass filter, we can measure only capacitive outputs having frequencies near the gyro's resonant frequency.

The differential capacitive read-out obeys

$$\Delta C_{out} = \varepsilon_0 A_s \left(\frac{1}{g_s - y} - \frac{1}{g_s + y} \right) \cong C_0 \left(\frac{y}{g_s} \right) + C_0 \left(\frac{y}{g_s} \right)^3, \quad C_0 = \frac{2\varepsilon_0 A_s}{g_s} \tag{2.1}$$

where A_S is the area of sensing electrodes, g_s is the initial gap between sense electrodes, and y is the displacement of the sense mass along the sense direction. Higher order terms are ignored in this approximation because they have minor influence. The displacement y consists of the desired displacement by due to the Coriolis force and the unwanted displacement due to vibration. Assuming a very slow rotation, this total displacement is given by

$$\begin{aligned} \frac{y}{g_s} &= \frac{D_0}{2} \sin\left[(w_0 + w_r) t \right] + \frac{D_0}{2} \sin\left[(w_0 - w_r) t \right] + D_v \sin(w_v t) \\ &\cong D_0 \sin(w_0 t) + D_v \sin(w_v t) \end{aligned} \tag{2.2}$$

where w_0 is the resonant frequency of the gyroscope, w_r is the rotation rate, and w_v is the vibration frequency. As we assumed a very slow rotation, w_r is assumed to be zero. D_0 is the amplitude of the displacement of the sense mass generated by the Coriolis force, and D_v is the amplitude of the displacement of the sense mass generated by the sense-axis vibration. Substituting equation (2.2) into (2.1) yields

$$\Delta C_{out,1st} = C_0 \left(\frac{y}{g_s} \right) = C_0 \left[D_0 \sin(w_0 t) + D_v \sin(w_v t) \right] \tag{2.3}$$

$$\begin{aligned}
&\Delta C_{out,2nd} = C_0\left[D_0\sin\left(w_0t\right)+D_v\sin(w_vt)\right]^3 \\
&= C_0\left[-\frac{D_0^3}{4}\sin\left(3w_0t\right)+\frac{3}{4}D_0^3\sin\left(w_0t\right)\right] \\
&+C_0\left[\begin{array}{l}
-\frac{D_v^3}{4}\sin\left(3w_vt\right)+\frac{3}{4}D_v^3\sin\left(w_vt\right)+3D_0^2D_v\sin\left(w_vt\right)+3D_0D_v^2\sin\left(w_0t\right) \\
-\frac{3}{4}D_0^2D_v\left\{\sin(2w_0+w_v)t-\sin(2w_0-w_v)t\right\} \\
-\frac{3}{4}D_0D_v^2\left\{\sin(w_0+2w_v)t+\sin(w_0-2w_v)t\right\}
\end{array}\right]
\end{aligned} \tag{2.4}$$

From these equations, we can extract the following terms that derive from vibration

$$\Delta C_{out,1st,vib} = C_0D_v\cdot\sin(w_vt) \tag{2.5}$$

$$\Delta C_{out,2nd,vib} = C_0\left[\begin{array}{l}
-\frac{D_v^3}{4}\sin\left(3w_vt\right)+\frac{3}{4}D_v^3\sin\left(w_vt\right) \\
+3D_0^2D_v\sin\left(w_vt\right)+3D_0D_v^2\sin\left(w_0t\right) \\
-\frac{3}{4}D_0^2D_v\left\{\sin(2w_0+w_v)t-\sin(2w_0-w_v)t\right\} \\
-\frac{3}{4}D_0D_v^2\left\{\sin(w_0+2w_v)t+\sin(w_0-2w_v)t\right\}
\end{array}\right] \tag{2.6}$$

The term (2.5) that is first order in the (small) displacement D_v is much larger than the terms (2.6) that are all third order in the displacements D_v and D_o. Vibrations having frequencies at/near the gyro's resonant frequency still exist in both expressions (2.5) and (2.6), while vibrations having low frequencies (order of magnitude lower than the resonant frequency) exist only in equation (2.6), after the gyro outputs are band-pass-filtered. Therefore, vibration having frequencies at/near the resonant frequency of the gyroscope are dominant because they arise in both equations and because the amplitude D_v is amplified by the high Q. Calculations using the example gyroscope [12] show that vibration at the gyroscope's resonant frequency (15 kHz) will yield $>10^{10}$ times larger output distortion than low frequency vibrations (10-100 Hz) because of the high Q (40k) of this gyroscope.

2.4. Vibration Effects on Non-Degenerate Gyroscopes II - Tuning Fork Gyroscopes

To counter vibration-induced errors, tuning fork gyroscopes (TFGs) employ two

masses that vibrate out of phase. This differential operation cancels common-mode errors and also doubles the amplitude of the output signal. Therefore, TFGs are believed to be insensitive to vibrations [2, 15, 17, 40]. However, TFGs can still experience vibration-induced errors from two sources: differential-mode vibrations and common-mode vibrations.

Differential-mode vibrations arise when the two masses of a TFG experience different vibration amplitudes. This difference creates an imbalance in the operation of the two masses of a TFG, and thus, the vibration effects no longer cancel. One cause of differential-mode vibration is the unavoidable detuning of the two masses during fabrication leading to differences in gyro mass, stiffness, Q-factor, and/or sense/drive gaps. Another cause arises from rotational vibrations producing different vibration-induced displacement of each mass in a TFG [17], but it is not dealt in this thesis..

By contrast, common-mode vibrations occur when the two masses of a TFG experience the same vibration. Common-mode vibration can be more critical than differential-mode vibration because it may arise even for an ideally-tuned gyroscope. Although a TFG operates differentially, detailed analysis reveals that even a perfectly-tuned ideal TFG cannot completely eliminate linear vibrations in several special situations.

Some of the situations have been qualitatively explained by means of static analysis using one TFG design made of two DS-type gyroscopes [17]. However, a more comprehensive understanding of common-mode vibrations is still needed. We present an extensive analysis of the vibration-induced errors in most of the reported tuning fork gyroscopes. The vibration-induced error sources are analyzed for each TFG class (explained in Section 2.2) using nonlinear dynamic models. The models are simulated to permit comparison of vibration sensitivities among the TGF classes. Finally, we determine the dominant vibration-induced error source of each design and determine whether vibration effects can be suppressed by structure-level design changes.

2.4.1. Modeling

To numerically analyze vibration-induced errors, we conducted simulations using MATLAB and SIMULINK. The model represents a real tuning fork gyroscope, and it is schematically depicted in Figure 2.4.

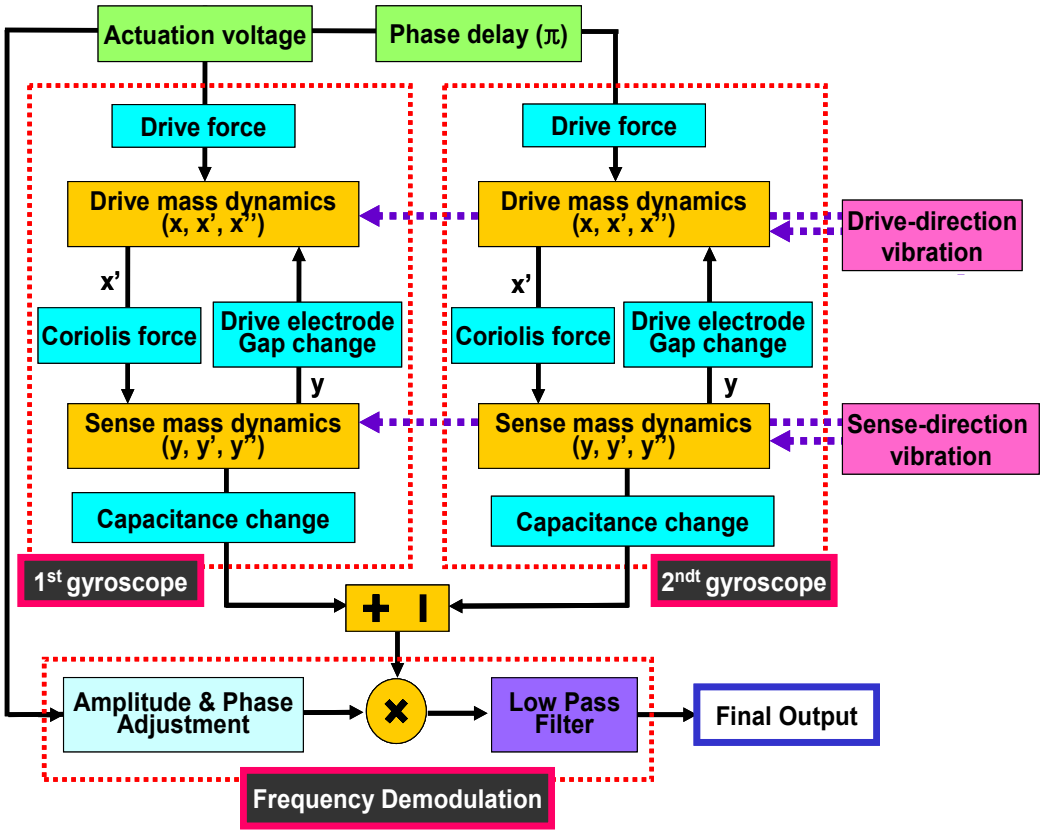

Figure 2.4. Block diagram of the simulation model built using MATLAB and SIMULINK.

This model consists of (1) the equations of motion representing the dynamics of the sense and drive masses of a TFG, (2) the vibration sources and vibration-induced forces, (3) the actuation voltage, (4) the differential capacitive read-out, and (5) the frequency demodulation. The equations of motion are a set of four nonlinear differential equations in four unknown coordinates representing the drive and sense direction displacements of each gyroscope in a TFG; refer to Section 2.4.1.1. The equations are solved numerically using the ODE45 solver in MATLAB. The frequency demodulation will recover only output signals whose frequencies are at/near the gyro's resonant frequency, as in the case of matched-mode gyroscopes [12, 28].

2.4.1.1. Equations of Motion

The notation used in Section 2.4 is defined as follows.

- x_{left}/y_{left}, x_{right}/y_{right}: Drive/sense direction displacement of the left and

right gyros of a TFG

- m_d/m_s, b_d/b_s, k_d/k_s: Mass, damping coefficient and stiffness of drive/sense masses
- $F_{d,left}$, $F_{d,right}$: Drive direction actuating force at drive electrodes of the left/right gyros of a TFG
- $F_{ed,left}$, $F_{ed,right}$: Sense direction electrostatic force at drive electrodes of the left/right gyros of a TFG
- $F_{c,left}$, $F_{c,right}$: Coriolis force of the left/right gyros of a TFG
- a_x/a_y: Vibrations along drive/sense direction
- V_{DC}/V_{AC}: DC/AC actuation voltages at drive electrodes
- $C_d(x, y)$: The capacitance of drive electrodes
- w_0: Resonant frequency of a gyroscope
- Φ_{AC}(Electrode): The phase of AC actuation voltages at each drive electrode. The left and right gyros of a TFG operate anti-phase.
- Ψ_{ed}(Electrode): Sign of F_{ed} at each drive electrode of the left/right gyros of a TFG
- Ω: Rotation rate

The dynamics of the drive masses of left/right gyroscopes are governed by:

$$\text{Left gyro:}\quad m_d\ddot{x}_{left} + b_d\dot{x}_{left} + k_d x_{left} = F_{d,left} - m_d a_x \tag{2.7}$$

$$\text{Right gyro:}\quad m_d\ddot{x}_{right} + b_d\dot{x}_{right} + k_d x_{right} = F_{d,right} - m_d a_x \tag{2.8}$$

where the $F_{d,left}$ and $F_{d,right}$ are given by:

$$F_{d,left} = \sum_{left,right\ electrodes} \frac{1}{2}\left[V_{DC} + V_{AC}\sin(w_0 t + \Phi_{AC}(Electrode))\right]^2 \frac{\partial C_d(x_{left}, y_{left})}{\partial x_{left}} \tag{2.9}$$

$$F_{d,right} = \sum_{left,right\ electrodes} \frac{1}{2}\left[V_{DC} + V_{AC}\sin(w_0 t + \Phi_{AC}(Electrode))\right]^2 \frac{\partial C_d(x_{right}, y_{right})}{\partial x_{right}} \tag{2.10}$$

The dynamics of the sense masses of left/right gyroscopes are governed by:

$$\text{Left gyro:}\quad m_s\ddot{y}_{left} + b_s\dot{y}_{left} + k_s y_{left} = F_{c,left} - m_s a_y + F_{ed,left} \tag{2.11}$$

Right gyro: $m_s \ddot{y}_{right} + b_s \dot{y}_{right} + k_s y_{right} = F_{c,right} - m_s a_y + F_{ed,right}$ (2.12)

where the $F_{c,left}$//$F_{c,right}$ and $F_{ed,left}$//$F_{ed,right}$ are given by:

$$F_{ed,left} = \sum_{left,right\ electrodes} \Psi_{ed}(Electrode) \cdot \frac{1}{2}\left[V_{DC} + V_{AC}\sin(w_0 t + \Phi_{AC}(Electrode))\right]^2 \frac{\partial C_d(x_{left}, y_{left})}{\partial y_{left}} \quad (2.13)$$

$$F_{ed,right} = \sum_{left,right\ electrodes} \Psi_{ed}(Electrode) \cdot \frac{1}{2}\left[V_{DC} + V_{AC}\sin(w_0 t + \Phi_{AC}(Electrode))\right]^2 \frac{\partial C_d(x_{right}, y_{right})}{\partial y_{right}} \quad (2.14)$$

$$F_{c,left} = 2m_d \dot{x}_{left} \times \Omega \quad (2.15)$$

$$F_{c,right} = 2m_d \dot{x}_{right} \times \Omega \quad (2.16)$$

2.4.1.2. Model Parameters

The model parameters, derived from either high-volume commercial gyroscopes [16, 17, 41] or from typical designs, are listed in Table 2.2.

Table 2.2. Model parameters

Model parameters			
Parameters	**Value**	**Parameters**	**Value**
Resonant frequency	14 kHz	Comb-drive finger overlapping length	5 μm
Q-factor	45	Sensing voltage	1.5 V_{DC}
Driving amplitude	~2 μm	Initial sensing capacitance	~11 fF

To be conservative, a relatively low Q-factor of 45 was selected from among the reported gyroscopes [18], because a higher Q-factor would generate much lager vibration-induced error. To achieve a fair comparison, all types of gyros are assumed to have the same parameters except drive and sense masses. The drive masses of Type-DS (corresponding to the sense masses of Type-DD) are smaller than the sense masses (corresponding to the drive mass of Type-DD) because of the nature of this design. However, the drive and sense masses of Type-CP gyroscopes are the same. In our simulations, the drive/sense masses of a Type-CP gyro, the sense mass of a Type-DS gyro, and the drive mass of a Type-DD gyro are identical.

All gyroscope designs are then subjected to the same impulsive impact that

induces transient response. The impact (shown in Figure 2.5) generates wide-band vibration similar to that produced in many applications [41]. As the figure shows, the impact used in a real vibration experiment and that used in our simulations are of similar shape. The impact initiates unwanted dynamic response of the gyroscope structure leading to vibration-induced errors that are also design dependent. We compute and compare the maximum output response (i.e., transient response) following the impact.

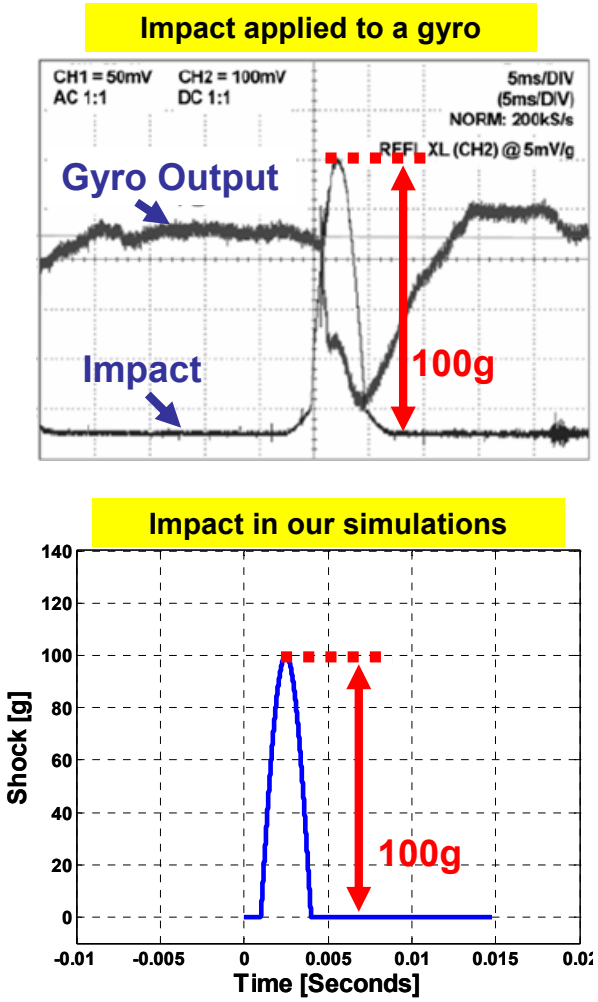

Figure 2.5. Impact shape observed in vibration testing of gyroscopes [41] (top) and impact shape used in our simulations (bottom).

2.4.2. Simulation Results

Figure 2.6 shows typical time records of the calculated output responses from Type-CP, Type-DS, and Type-DD gyroscopes (shown in Figure 2.3) both before and after impact. Figure 2.6a shows the responses with superimposed rotation while

Figure 2.6b illustrates the responses without superimposed rotation. For Figure 2.6a, a rotation rate (100 deg/sec) was suddenly applied at 0.05 seconds and the rectangular impact was suddenly applied at 0.12 seconds after the gyroscope's output was stabilized. This example and realistic impact [41] is defined by a 100g acceleration amplitude and 3 ms duration and it is applied in both the drive and sense directions simultaneously.

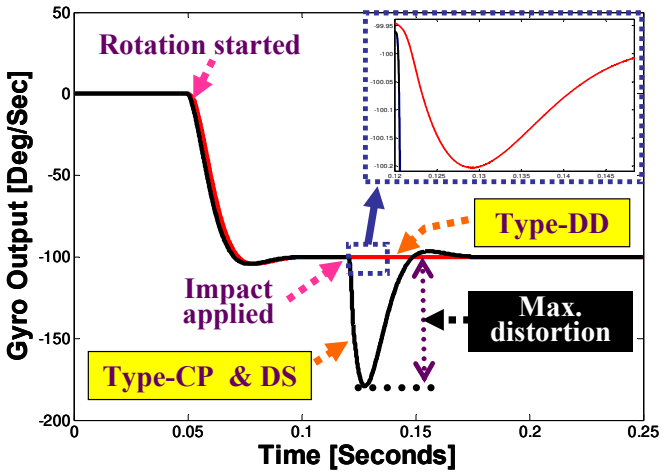

(a) With rotation signal

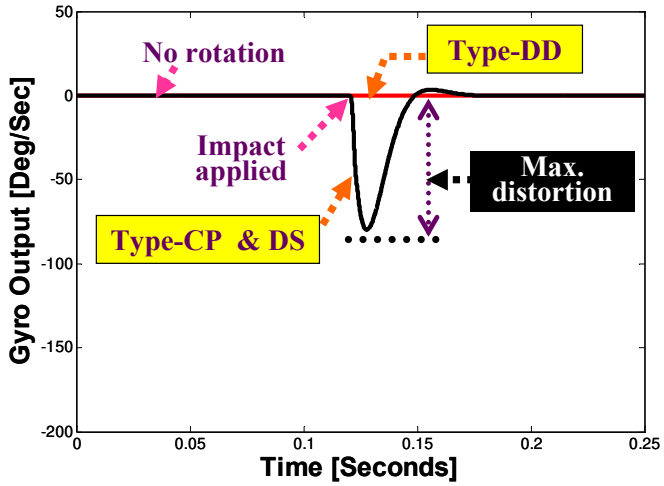

(b) Without rotation signal

Figure 2.6. Simulated outputs for Type-CP, Type-DS, and Type-DD gyroscopes after subjected to the impact shown in Figure 2.5. The impact has 100g amplitude and 3 ms duration.

The simulation results demonstrate that the outputs of all three gyroscopes are distorted by the applied impact/vibration. Type-CP and Type-DS gyroscopes suffer much (orders of magnitude) greater, vibration-induced errors than Type-DD gyroscopes both with and without superimposed rotation. In particular, the maximum transient

response of a Type-DD gyroscope in Figure 2.6a is less than 1% of that of a Type-DS gyroscope in this example. This reduction also depends upon the time when the impact is applied and the phase of the gyroscope's actuating signal. Moreover, the results of Figure 2.6b show that a Type-DD gyroscope does not generate any output error relative to the large output error produced by a Type-CP and Type-DS gyroscope in keeping with the results of Figure 2.6a. These simulations clearly demonstrate that gyros with Type-DD structure are far less sensitive to vibration-induced errors than those with Type-CP and/or Type-DS structures. This rather marked distinction derives from the fact at each design has a different dominant error source as shown next.

2.4.3. Vibration-induced Error Sources in Tuning Fork Gyroscopes

Ideal TFGs have three major sources of vibration-induced errors. One error comes from the capacitive nonlinearity at the sense electrodes, and the other two errors come from the capacitive nonlinearity at the drive electrodes. Table 2.3 summarizes these error sources and vibration conditions that cause them. It is interesting to note that Type-CP and Type-DS gyros have far greater potential to generate vibration-induced output errors than Type-DD gyros for the reasons discussed below. Moreover, sense-direction vibration is the dominant environmental condition because it is involved in every vibration-induced error. Therefore, if we design an integrated vibration-isolator (which will be described in Chapter 3), it is essential to integrate the isolator along the sense direction. Non-ideal effects in gyroscopes, like quadrature errors, are not included in this analysis. Rather, our objective is to discuss the fundamental limits of ideally fabricated gyroscopes and the possibility of vibration suppression by device-level design changes.

2.4.3.1. Error Source I - Capacitive Nonlinearity at Sense Electrodes

The parallel-plate sensing mechanism contributes a nonlinear behavior between sense capacitance and sense axis displacement. This nonlinearity is negligible in normal operation because the displacement produced by the Coriolis force is small. However, larger displacements can be readily generated by vibration, and these displacements are subject to capacitive nonlinearity. This nonlinearity-induced error will cancel except when a Coriolis force and vibration along the sense direction arise simultaneously. In addition, this nonlinearity-induced error arises in all types of

tuning fork gyroscopes.

Table 2.3. Conditions leading to vibration-induced errors. F_C denotes Coriolis force (due to rotation), A_X denotes vibration along drive direction, and A_Y denotes vibration along sense direction.

Error mechanisms		Condition generating vibration-induced errors					
Electrodes	Specific Error Sources	Type-CP & Type-DS			Type-DD		
		F_C	A_X	A_Y	F_C	A_X	A_Y
Sense	Capacitive nonlinearity	Yes	-	Yes	Yes	-	Yes
Drive	Asymmetric sense-direction electrostatic force	-	Yes	Yes	Does not exist		
	Asymmetric change of drive capacitance	Yes	-	Yes	Does not exist		

The effect of this nonlinearity can be explained as follows. Let y be the displacement of the sense mass along the sense axis. Then, per equation (2.1), the differential capacitive read-out is given by

$$C_s = \varepsilon A_s \left[\frac{2d}{g_s^2 - y^2} \right] \cong \frac{2\varepsilon A_s}{g_s^2} \left[y + \frac{y^3}{g_s^2} + \frac{y^5}{g_s^4} \right] \tag{2.17}$$

Where higher order (smaller) terms are neglected. Let d_0 denote the displacement of the sense mass along the sense direction by the Coriolis force and d_v denote the associated displacement due to the sense direction vibration. Because of the differential operation of TFGs, the total displacement of the left gyro is d_0+d_v whereas that of the right gyro is $-d_0+d_v$. Assuming a very slow rotation, let $d_0= D_0\sin(w_0t)$ and $d_v=D_v\sin(w_vt)$, then the sense direction displacement of the left gyroscope (d_L) and that of the right gyro (d_R) are

$$\begin{aligned} d_L &= d_0 + d_v = \frac{D_0}{2}\sin\left(w_0 + w_r\right)t + \frac{D_0}{2}\sin\left(w_0 - w_r\right)t + D_v \sin w_v t \\ &\cong D_0 \sin w_0 t + D_v \sin w_v t \end{aligned} \tag{2.18}$$

$$\begin{aligned} d_R &= -d_0 + d_v = -\frac{D_0}{2}\sin\left(w_0 + w_r\right)t - \frac{D_0}{2}\sin\left(w_0 - w_r\right)t + D_v \sin w_v t \\ &\cong -D_0 \sin w_0 t + D_v \sin w_v t \end{aligned} \tag{2.19}$$

where D_0 and D_v are the amplitudes of the displacement by the Coriolis force and by vibration, respectively, and w_0, w_r and w_v are the gyroscope's resonant frequency, rotation rate and vibration frequency, respectively. By substituting (2.18) and (2.19) into (2.17), we can calculate the capacitance of the left gyro (C_L) and the right gyro (C_R). Subtracting C_L from $C_{R,}$ we arrive at the output of a TFG (C_{final})

$$C_{final} = C_L - C_R = 4\frac{\varepsilon A_s}{g_s^2}\left[d_0 + \frac{d_0^3}{g_s^2} + \frac{d_0^5}{g_s^4}\right] + 4\frac{\varepsilon A_s}{g_s^2}\left[\frac{3d_0 d_v^2}{g_s^2} + \frac{5d_0 d_v^4 + 10d_0^3 d_v^2}{g_s^4}\right] \tag{2.20}$$

In this equation, the terms in the first bracket derive solely from the Coriolis force. However, the terms in the second bracket, which are denoted as $C_{vibration,all}$ represent vibration-induced errors and they derive from both rotation and vibration simultaneously. This latter term,

$$C_{vibration,all} = 4\frac{\varepsilon A_s}{g_s^2}\left[\frac{3d_0 d_v^2}{g_s^2} + \frac{5d_0 d_v^4 + 10d_0^3 d_v^2}{g_s^4}\right] \tag{2.21}$$

which does not contain any linear terms, is produced by the capacitive nonlinearity. The first and the second terms of $C_{vibration,all}$ are further analyzed by substituting (2.18) and (2.19) into (2.21).

$$\begin{aligned} C_{vibration,1st} &= 12\frac{\varepsilon A_s}{g_s^4} d_0 d_v^2 = 12\frac{\varepsilon A_s}{g_s^4} D_0 D_v^2 \sin w_0 t \cdot \sin^2 w_v t \\ &= \left[6\frac{\varepsilon A_s}{g_s^4}\left(D_0 D_v^2\right)\sin w_0 t\right] - \left[6\frac{\varepsilon A_s}{g_s^4}\left(D_0 D_v^2\right)\{\sin(w_0 + 2w_v)t + \sin(w_0 - 2w_v)t\}\right] \end{aligned} \tag{2.22}$$

$$\begin{aligned} C_{vibration,2nd} &= 20\frac{\varepsilon A_s}{g_s^6}\left(d_0 d_v^4 + 2d_0^3 d_v^2\right) \cong 20\frac{\varepsilon A_s}{g_s^6} d_0 d_v^4 \\ &= 20\frac{\varepsilon A_s}{g_s^6}\left[D_0 D_v^4 \sin w_0 t \cdot \sin^4 w_v t\right] \\ &= 20\frac{\varepsilon A_s}{g_s^6}\left(D_0 D_v^4\right)\left[\frac{3}{8}\sin w_0 t - \frac{1}{2}\sin w_0 t \cdot \sin 2w_v t + \frac{1}{8}\sin w_0 t \cdot \sin 4w_v t\right] \end{aligned} \tag{2.23}$$

The second term of $C_{vibration,2nd}$ is ignored because it is negligibly small compared to $C_{vibration,1st}$ in most situations. Note that vibration-induced errors shown in equations (2.22) and (2.23) are not filtered out by the frequency demodulation in several situations.

From the last two equations, we can observe several interesting points. The terms in the first bracket and the second bracket of equation (2.22) are detailedly below

in expressions (2.24) and (2.25), respectively. Note that the $D_0(w_0)D_v^2(w_v)$ term in equations (2.24) and (2.25) depends on w_0 and w_v. Note also that the expression (2.24) is non-zero regardless of the vibration frequency (w_v), that D_v^2 is maximized when $w_v \approx w_0$ and the maximum value of $D_0D_v^2$ increases in proportion to Q^3. Whereas, terms in equation (2.25) will be filtered out by frequency demodulation except when $w_v \approx 0$ because of, and therefore, the $D_0D_v^2$ term increases in proportion to Q. Because of the high Q of the gyroscope, the $D_0D_v^2$ term of expression (2.24) has much larger amplitude than that of (2.25).

$$6\frac{\varepsilon A_s}{g_s^4}\left[D_0(w_0)D_v^2(w_v)\right]\sin w_0 t \tag{2.24}$$

$$6\frac{\varepsilon A_s}{g_s^4}\left[D_0(w_0)D_v^2(w_v)\right]\left[\sin(w_0+2w_v)t+\sin(w_0-2w_v)t\right] \tag{2.25}$$

The terms in (2.23) are generally smaller than those in (2.22) because $D_0D_v^4/g_s^6$ is smaller than $D_0D_v^2/g_s^4$ in normal situations. However, as shown in equation (2.26), they become comparatively large when D_v becomes large. This phenomenon occurs when the gyroscope's Q increases because the first term in equation (2.23) is maximized when $w_v \approx w_0$ and increases in proportion to Q^5 because of the $D_0D_v^5$ term.

$$\max\left(\frac{C_{\text{vibration,2nd}}}{C_{\text{vibration,1st}}}\right) \cong \frac{5}{3}\frac{D_v^2}{g_s^2} \tag{2.26}$$

Another interesting observation is the performance criterion representing the ratio of the gyro's rotation sensitivity (C_{rotation}) over the gyro's vibration sensitivity ($C_{\text{vibration}}$). This criterion is expressed by equation (2.27), which is derived using the maximum amplitude of the first term (the d_0 term) of the first bracket in equation (2.20) and that of the term in equation (2.24).

$$\frac{\text{Rotation Sensitivity}}{\text{Vibration Sensitivity}} = \max\left(\frac{C_{\text{rotation}}}{C_{\text{vibration}}}\right) \cong \frac{4\frac{\varepsilon A_s}{g_s^2}D_0}{6\frac{\varepsilon A_s}{g_s^4}\left(D_0D_v^2\right)} = \frac{2}{3}\frac{g_s^2}{D_v^2} \tag{2.27}$$

We can maximize this criterion either by decreasing D_v or by increasing g_s. Increasing g_s is more convenient because we need to decrease the gyroscope's Q to decrease D_v. To maintain the same rotation sensitivity while increasing the g_s, we

need to increase A_s, and therefore, the size of the gyroscope increases.

2.4.3.2. Error Source II – Capacitive Nonlinearity at Drive Electrodes 1: Asymmetric Electrostatic Force along Sense Direction at Drive Electrodes

Vibration can asymmetrically affect the two gyroscopes of a TFG. The asymmetry stems from the incomplete decoupling of sense and drive masses as explained in Section 2.2, and this can be problematic for the comb-drive electrodes in two ways.

One problem is induced by asymmetric sense-direction electrostatic forces. The gaps in the comb-drive fingers of the drive electrodes change with displacement along the sense direction. This gap change mostly originates from the Coriolis force or by the sense-direction vibration. This gap change leads to an electrostatic force on the comb fingers that depends on displacement in the sense direction. However, in the sense direction, the displacement and the electrostatic force have a nonlinear relationship, and therefore, the electrostatic force becomes asymmetric between the two gyroscopes of a TFG and accelerates the masses of the gyroscopes in one direction. This error is similar to quadrature error [42], but it is generated by vibration, not by non-ideal operation or by any mismatch of the two gyros of a TFG during fabrication.

As shown in Figure 2.3, this effect develops in Type-CP and Type-DS gyroscopes but not in Type-DD gyroscopes, which maintain a constant gap for the drive electrodes. For Type-CP and Type-DS gyros, this unwanted force component serves to accelerate the drive and sense masses along the sense direction, thereby producing an output error.

However, these forces acting on both gyroscopes of a TFG will cancel except in particular situations when both the drive-direction and sense-direction vibrations co-exist [17]. When a drive-direction vibration is also applied to the gyroscopes in Figure 2.3a or b, the overlapping areas of the comb fingers at the left electrodes will decrease, whereas those at the right will increase. This is the same for the left and right gyroscopes. The left electrode of the left gyro is actuated by a positive AC voltage ($V_{DC}+V_{AC}$), while the left electrode of the right gyro is actuated by a negative AC voltage ($V_{DC}-V_{AC}$). Therefore, the sense-directional electrostatic forces of the left and right gyros are unequal and thus they no longer cancel. This error is independent of the existence of the Coriolis force.

The sense-direction electrostatic force can also be generated at sense electrodes but

it is not influential because only a DC voltage is applied to the sense electrodes.

The electrostatic-force-induced error is maximized when vibration is applied at 45 degrees from the drive axis because this error depends on the occurrence of vibration along both drive and sense directions. Figure 2.7 demonstrates that the error induced by asymmetric electrostatic force at drive electrodes is the largest when $\theta=45^0$ and smallest when $\theta=0^0$ or 90^0.

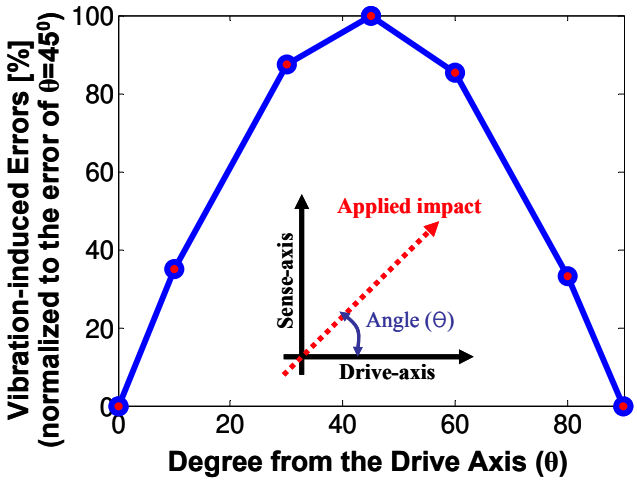

Figure 2.7. Vibration-angle dependency of the errors induced by the asymmetric electrostatic force at drive electrodes.

2.4.3.3. Error Source III – Capacitive Nonlinearity at Drive Electrodes 2: Asymmetric Change of Comb-Drive Capacitance at Drive Electrodes

As described above, the drive electrode gap can change because of vibration along the sense axis. This gap change will modify the capacitance of the comb-drive electrode and thus alter the driving force, Coriolis force, and consequently, the gyroscope's scale factor [17]. This capacitance modification of two gyroscopes of a TFG becomes asymmetric only if the Coriolis force and vibration along the sense axis co-exist. This situation arises because the sense-direction displacements of the two gyros are the same when induced by sense-direction vibration, but opposite when induced by the Coriolis force. However, the asymmetry is independent of any vibration along the drive axis. As before, this error source arises only in Type-CP and Type-DS gyroscopes because Type-DD gyroscopes enforce a constant comb finger gap for the drive electrodes.

2.4.3.4. Summary of Error Sources in the Three TFG Designs

As discussed above, vibration-induced errors in Type-DD gyros arise only from capacitance nonlinearity along the sense axis. By contrast, Type-CP and Type-DS gyroscopes experience all three error sources listed in Table 2.3 because of changing comb-drive gap. In addition, sense-direction vibration is a more detrimental than the Coriolis force or drive-direction vibration because it is involved in all error sources.

2.4.4. Dominant Error Source in Each Tuning Fork Gyroscope Design

2.4.4.1. Dominant Error Source in Type-DD Gyroscopes

Vibration-induced errors in Type-DD gyroscopes mainly arise from the capacitance nonlinearity along the sense direction. The characteristics of this nonlinearity-induced error are illustrated in Figure 2.8. The error amplitude depends on the vibration amplitude (Figure 2.8a), and the existence (Figure 2.8a versus b), and magnitude of the rotation (Figure 2.8c). However, this error mechanism is unaffected by vibration along the drive axis.

2.4.4.2. Dominant Error Source in Type-CP and Type-DS Gyroscopes

Errors in Type-CP and Type-DS gyroscopes are dominated by asymmetry in the sense-directional electrostatic force at the drive electrodes. This error characteristic is illustrated in Figure 2.9. This error may arise if vibrations exist in both the drive and sense directions regardless of any rotation speed (Figure 2.9a). In addition, this error increases with increased vibration amplitude (Figure 2.9b). The other error mechanisms (described in Section 2.4.3) are also observable in the simulations, but their effects are negligible compared to the effect of the asymmetric electrostatic force. The dominant error exceeds all other sources by 99% in our simulations.

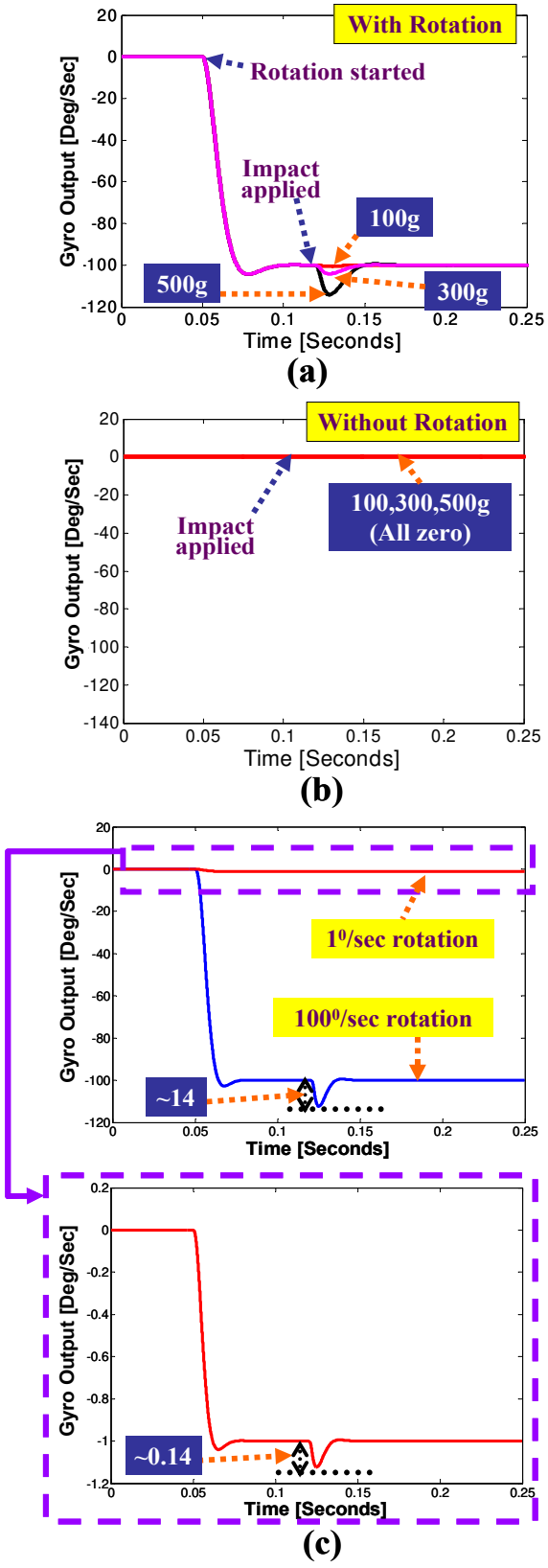

Figure 2.8. Simulated output of Type-DD gyroscopes. During rotation (a), vibration-induced errors occur and increase with larger vibration amplitude (100, 300, 500g). However, when no rotation exists (b), no error is observed. Moreover, the errors are proportional to rotation speed (c).

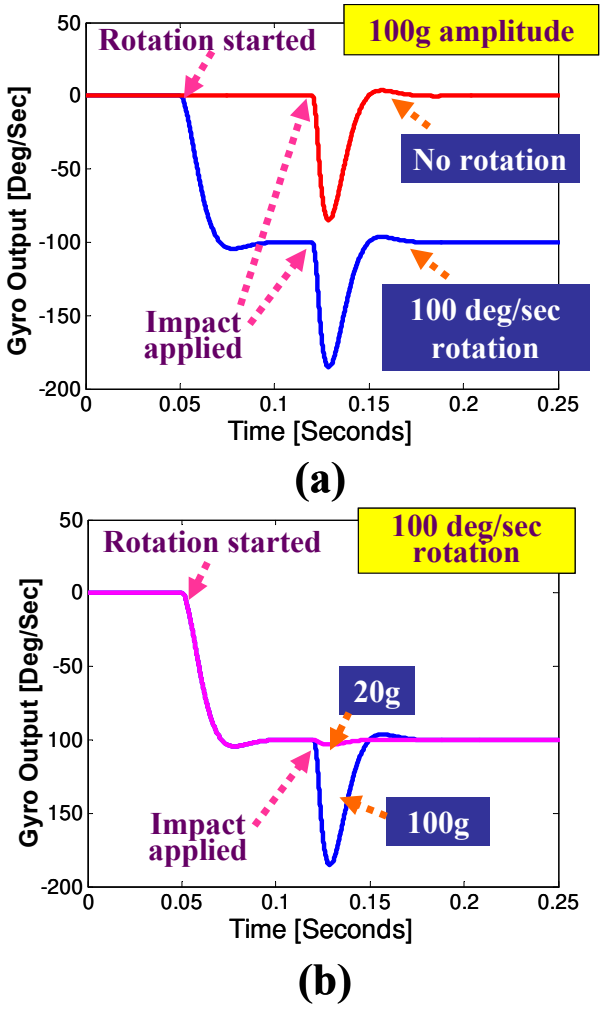

Figure 2.9. Simulated output of Type-DS gyroscopes. The dominant vibration-induced errors in Type-DS are almost independent of rotation speed (a). The vibration-induced errors depend on the vibration amplitude (b). The simulated outputs of Type-CP gyroscopes are almost identical.

2.5. Vibration Effects on Degenerate Gyroscopes - Ring Gyroscopes

Most degenerate gyroscopes rely on the wine-glass mode of a vibrating structure. This mode is also called the flexural mode of shell structures, and we can decouple this mode excited by the gyro's operation (i.e., by Coriolis force) from those excited by environmental vibration. The wine-glass mode includes several design variations, but the most well-known MEMS degenerate gyroscope is the ring gyroscope [2, 9, 10]. Some design variations are also reported [7, 10] but the basic concept remains identical.

Figure 2.10 depicts the conceptual view of a ring gyroscope. A vibratory ring

gyroscope consists of a ring structure, support-spring structures, and electrodes surrounding the ring structure. The electrodes are used for drive, sense, or control of the gyro. The operation of the ring gyroscope relies on two elliptically shaped vibration modes, named the primary and secondary flexural modes, which are also called the drive and sense modes, respectively. The two flexural modes have identical resonant frequency because of the symmetry of the ring structure.

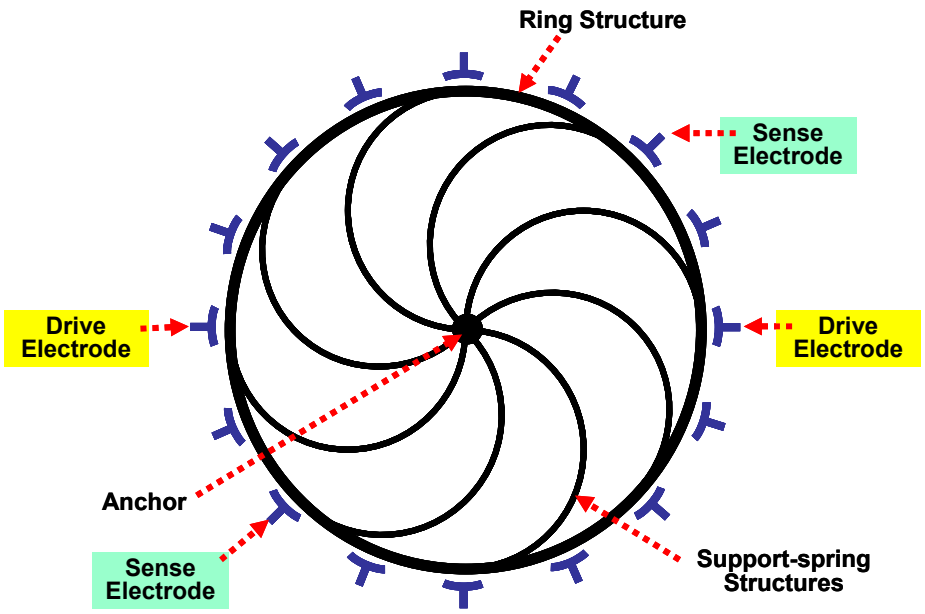

Figure 2.10. Conceptual view of a ring gyroscope.

The ring gyroscope functions as follows. First the electrostatic drive is used to excite the primary flexural (drive) mode in resonance. When the device is rotated, a portion of the vibration energy is transferred from the primary flexural mode to the secondary flexural (sense) mode. The amplitude of the radial displacement of the secondary flexural mode is proportional to the rotation rate and thus serves as the means to detect that rate.

The support-spring structure in this illustrated design utilizes eight semicircular springs that attach the ring structure to its substrate at the center of the ring. The eight-spring design plays an important role in suspending the ring structure, in assuring balanced and symmetric operation of the ring gyroscope, and in allowing the two flexural modes to have identical resonant frequency. The necessity for the eight springs is discussed in previous work [2, 9].

Unlike non-degenerate gyroscopes, ring gyroscopes cannot be analyzed using

simple lumped models because the mass and the stiffness of the ring gyro are distributed within the ring. We represent the ring as a continuum (beam). By contrast, the mass of the support-beam structure is small by comparison and so we treat them as discrete springs that support the ring.

Several studies were conducted to explain the operation of the ring gyroscope under vibration [2, 43, 44]. However, none of them provided a complete model including each ring gyro component and all four vibration modes needed to describe vibration-induced errors. This study presents this complete model including the ring structure, the support-beam structure, and drive electrodes.

2.5.1. Normal Mode Model

Vibrating structures such as ring gyroscopes can be analyzed by the normal mode method. This method assumes that any general vibration-induced displacement of an elastic body ($\vec{u}$) can be expressed by the linear combination of its normal vibration modes per

$$\vec{u} = \sum_{i=1}^{\infty} \Phi_i(p) q_i(t) \tag{2.28}$$

where p is the independent position coordinate(s) which can be expressed by Cartesian coordinates (i.e., x and y) or by cylindrical coordinates (i.e., radial and tangential coordinates). The equation includes generalized (modal) coordinates (i.e., $q_i(t)$) and mode shape functions (i.e., $\Phi_i(p)$). The generalized coordinates are the time-dependent amplitudes of the vibration modes. Relevant derivatives of the quantities, needed later, are given by

$$\Phi_i'(p) = \frac{d\Phi_i}{dp}, \Phi_i''(p) = \frac{d^2\Phi_i}{dp^2} \tag{2.29}$$
$$\dot{q}_i(t) = \frac{dq_i}{dt}, \ddot{q}_i(t) = \frac{d^2q_i}{dt^2}$$

Previous studies indicated that the vibration modes utilized during device operation (i.e., excited by the Coriolis force) are distinct from those excited by environmental vibration [2, 43]. Therefore, to capture both vibration-induced and gyro-operation-induced modes, we include four vibration modes in the following model; two describing vibration-induced effects and two more describing the gyro-

operation. Figure 2.11 shows these four vibration modes.

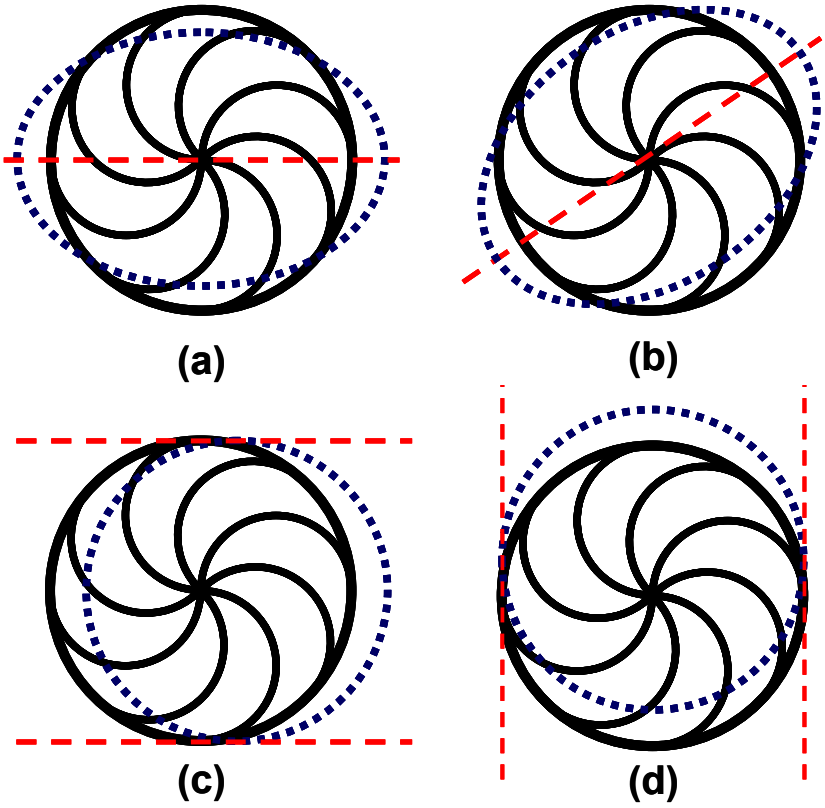

Figure 2.11. Four important vibration modes of a ring gyroscope. (a) mode for drive operation, (b) mode for sense operation, (c) mode for x-axis external excitation, (d) mode for y-axis external excitation.

The four modes are (1) two flexural modes representing drive and sense operation of the ring gyroscope ($\vec{u}_1^F$ and $\vec{u}_2^F$), and (2) two translation modes induced by external excitation in x and y directions ($\vec{u}_1^T$ and $\vec{u}_2^T$). In the translation modes, the center of the ring translates along the x or y direction while the ring does not bend. The stiffness for these modes derives from bending of the supporting semi-circular beams. By contrast, in the flexural modes, the ring structure deforms in the approximate shape of an ellipse while the center of the ring does not translate. The stiffness for these modes derives from the bending of both the ring and the semi-circular beams.

The total displacement of the ring structure is given by

$$\vec{u} = \Phi_1^T q_1^T + \Phi_2^T q_2^T + \Phi_1^F q_1^F + \Phi_2^F q_2^F \tag{2.30}$$

In Cartesian coordinates, the scalar components of equation (2.30) are

$$u_x = \Phi^T_{x1} q^T_1 + \Phi^T_{x2} q^T_2 + \Phi^F_{x1} q^F_1 + \Phi^F_{x2} q^F_2 \tag{2.31}$$

$$u_y = \Phi^T_{y1} q^T_1 + \Phi^T_{y2} q^T_2 + \Phi^F_{y1} q^F_1 + \Phi^F_{y2} q^F_2 \tag{2.32}$$

In cylindrical coordinates, the scalar components of equation (2.30) are

$$u_r = \Phi^T_{r1} q^T_1 + \Phi^T_{r2} q^T_2 + \Phi^F_{r1} q^F_1 + \Phi^F_{r2} q^F_2 \tag{2.33}$$

$$u_\theta = \Phi^T_{\theta 1} q^T_1 + \Phi^T_{\theta 2} q^T_2 + \Phi^F_{\theta 1} q^F_1 + \Phi^F_{\theta 2} q^F_2 \tag{2.34}$$

We employ Lagrange's equation to derive the normal mode model for the operation of the ring gyroscope and its response to environmental vibration. To this end, we must formulate the kinetic energy, potential energy, and work done by dissipative forces for this four degree-of-freedom dynamical system. Note that the potential energy includes that due to bending of the ring structure, bending of the support springs, and the potential energy from the electrostatic forces of drive electrodes. These energies will be derived in following sections. We ignore several non-ideal conditions in ring gyroscopes because of the significant complexity that is added to the analysis/modeling without providing the necessary insight that would be useful for the reader. Although non-idealities in ring gyroscopes (such as non-uniform mass, unbalanced support springs, etc.) increase sensitivity to external vibration because of the coupling between the flexural modes and translation modes [2], the outcome of the analysis presented here will no change significantly.

2.5.2. Mode Shapes

The mode shapes of a vibrating ring are well known [45, 46] and can also be derived using simple calculations because of the symmetry of the ring structure. The first two modes are translation modes in the x and y directions, and their radial/tangential components are

$$\text{X-axis translation mode: } \Phi^T_{r,1}(\theta) = \cos(\theta),\ \Phi^T_{\theta,1}(\theta) = -\sin(\theta) \tag{2.35}$$

$$\text{Y-axis translation mode: } \Phi^T_{r,2}(\theta) = \sin(\theta),\ \Phi^T_{\theta,2}(\theta) = \cos(\theta) \tag{2.36}$$

where θ is an independent spatial coordinate (angle) describing position around the

ring. The second two modes are elliptical-shaped flexural modes and their radial/tangential components are

$$\text{Drive-axis flexural mode: } \Phi^{F}_{r,1}(\theta) = \cos(2\theta),\ \Phi^{F}_{\theta,1}(\theta) = -\frac{1}{2}\sin(2\theta) \tag{2.37}$$

$$\text{Sense-axis flexural mode: } \Phi^{F}_{r,1}(\theta) = \sin(2\theta),\ \Phi^{F}_{\theta,1}(\theta) = \frac{1}{2}\cos(2\theta) \tag{2.38}$$

These mode shapes are orthogonal. The radial and tangential mode shapes, of course, have arbitrary amplitude and therefore they are sometimes reported as multiples of the expressions above. For example, the radial and tangential mode shapes of the drive-axis flexural mode in equation (2.37) is also written as [2, 45, 46]:

$$\Phi^{F}_{r,1}(\theta) = 2\cos(2\theta),\ \Phi^{F}_{\theta,1}(\theta) = -\sin(2\theta) \tag{2.39}$$

The cylindrical coordinates and corresponding Cartesian coordinates are shown in Figure 2.12. Point P is given by:

$$x_p = R_{ring}\cos(\theta),\ y_p = R_{ring}\sin(\theta) \tag{2.40}$$

where R_{ring} is the radius of the ring structure. The cylindrical coordinates can be transformed to Cartesian coordinates using (i=1 or 2).

$$\begin{bmatrix} \Phi^{T}_{x,i}(\theta) \\ \Phi^{T}_{y,i}(\theta) \end{bmatrix} = \begin{bmatrix} \cos(-\theta) & \sin(-\theta) \\ -\sin(-\theta) & \cos(-\theta) \end{bmatrix},\quad \begin{bmatrix} \Phi^{T}_{r,i}(\theta) \\ \Phi^{T}_{\theta,i}(\theta) \end{bmatrix} = \begin{bmatrix} \cos(\theta)\Phi^{T}_{r,i} - \sin(\theta)\Phi^{T}_{\theta,i} \\ \sin(\theta)\Phi^{T}_{r,i} + \cos(\theta)\Phi^{T}_{\theta,i} \end{bmatrix} \tag{2.41}$$

$$\begin{bmatrix} \Phi^{F}_{x,i}(\theta) \\ \Phi^{F}_{y,i}(\theta) \end{bmatrix} = \begin{bmatrix} \cos(-\theta) & \sin(-\theta) \\ -\sin(-\theta) & \cos(-\theta) \end{bmatrix},\quad \begin{bmatrix} \Phi^{F}_{r,i}(\theta) \\ \Phi^{F}_{\theta,i}(\theta) \end{bmatrix} = \begin{bmatrix} \cos(\theta)\Phi^{F}_{r,i} - \sin(\theta)\Phi^{F}_{\theta,i} \\ \sin(\theta)\Phi^{F}_{r,i} + \cos(\theta)\Phi^{F}_{\theta,i} \end{bmatrix} \tag{2.42}$$

These transformations provide the mode shapes in Cartesian coordinates:

$$\text{(1) X-axis translation mode: } \Phi^{T}_{x,1}(\theta) = 1,\ \Phi^{T}_{y,1}(\theta) = 0 \tag{2.43}$$

$$\text{(2) Y-axis translation mode: } \Phi^{T}_{x,2}(\theta) = 0,\ \Phi^{T}_{y,2}(\theta) = 1 \tag{2.44}$$

(3) Drive-axis flexural mode:

$$\Phi^{F}_{x,1}(\theta) = \left[\frac{1}{4}\cos(3\theta) + \frac{3}{4}\cos(\theta)\right] \qquad (2.45)$$

$$\Phi^{F}_{y,1}(\theta) = \left[\frac{1}{4}\sin(3\theta) - \frac{3}{4}\sin(\theta)\right]$$

(4) Sense-axis flexural mode:

$$\Phi^{F}_{x,2}(\theta) = \left[\frac{1}{4}\sin(3\theta) + \frac{3}{4}\sin(\theta)\right] \qquad (2.46)$$

$$\Phi^{F}_{y,2}(\theta) = \left[-\frac{1}{4}\cos(3\theta) + \frac{3}{4}\cos(\theta)\right]$$

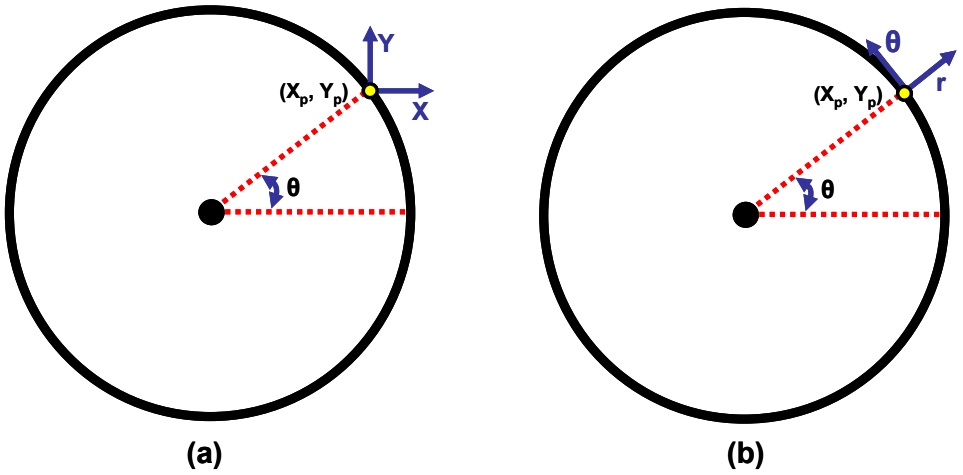

Figure 2.12. Ring structure and coordinates of point P (X_P, Y_p). (a) Cartesian coordinates x and y constructed at point P and (b) cylindrical coordinates radial (r) and tangential (θ) constructed at point P.

2.5.3. Assumptions

We assumed that

(1) The ring gyroscope is ideally fabricated.

(2) The major axis of the first flexural mode is aligned along the drive axis of the ring gyroscope.

From (1) and (2), we assume that the drive electrode is symmetrically located at the positions $\theta=0^0$ and 180^0 on the ring structure. Real ring gyroscopes [2, 9] have a single-ended drive electrode to accommodate the shift of the primary flexural vibration modes, but we excluded this effect to simplify our analysis. A design of the symmetric electrode set was discussed in simple terms in [2].

2.5.4. Kinetic Energy

To calculate the kinetic energy, we use the frames of reference illustrated in Figure 2.13. The quantities appearing in this figure include:

- $X_0Y_0Z_0$: Inertial frame of reference.
- XYZ: Translating and rotating (non-inertial) frame of reference. The origin of this frame is the original center of the ring structure (prior to any translation or this structure).
- $\vec{r}_0$: Position vector from the origin of the inertial frame to the origin of the non-inertial frame (XYZ).
- $\vec{u}^T$: Displacement of the center of the ring structure due to translation.
- $\vec{r}_p$: Position vector from the center of the ring structure to a point on the undeformed ring
- $\vec{u}^F$: Displacement of a point on the ring structure due to flexure.
- $\vec{u}$: Total displacement of a point on the ring structure due to translation and flexure, $\vec{u} = \vec{u}^T + \vec{u}^F$
- $\vec{U}_{arb}$: Position of a point on the ring structure relative to the inertial frame $X_0Y_0Z_0$ (shown as U in Figure 2.13b)

In reference to Figure 2.13,

$$\vec{U}_{arb} = \vec{r}_0 + \vec{u}^T + \vec{r}_p + \vec{u}^F = \vec{r}_0 + \vec{r}_p + \vec{u} \tag{2.47}$$

From a derivation based on infinitesimal rotation [47], the velocity of point P is given by:

$$\vec{v} = \vec{v}_0 + \dot{\vec{u}} + \vec{\Omega} \times (\vec{r}_p + \vec{u}) \tag{2.48}$$

The non-inertial frame XYZ possesses an angular velocity

$$\vec{\Omega} = \Omega_x \mathbf{i} + \Omega_y \mathbf{j} + \Omega_z \mathbf{k} \tag{2.49}$$

and a linear velocity

$$\vec{v}_0 = \frac{d(\vec{r}_0)}{dt} = v_{ox}\mathbf{i} + v_{oy}\mathbf{j} + v_{oz}\mathbf{k} \tag{2.50}$$

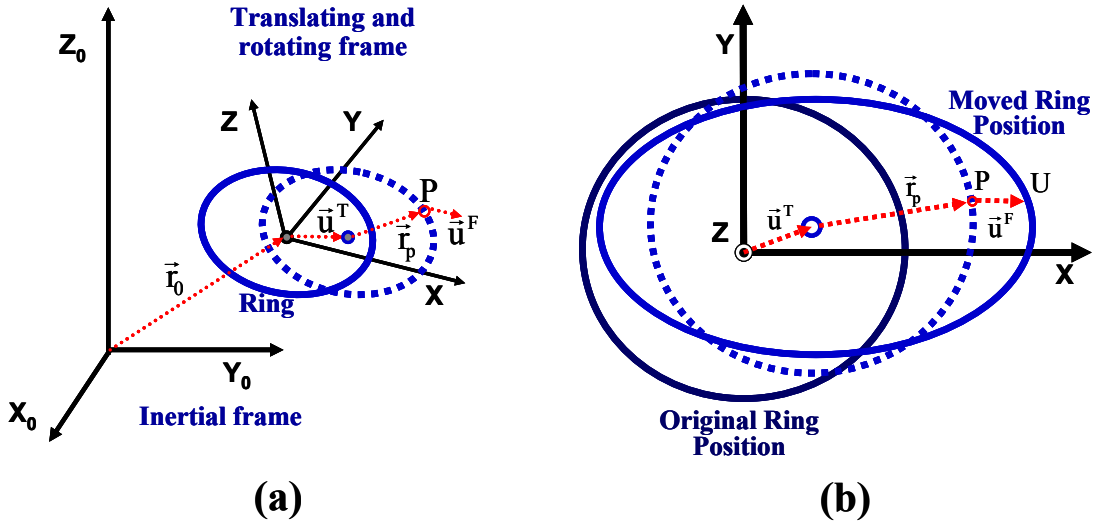

Figure 2.13. Coordinate system used to calculate kinetic energy. (a) the overview of the inertial and translating/rotating frames, (b) the detailed top view of the translating/rotating frame and the deformed ring structure.

Thus, the velocity of an arbitrary point on the ring is given by

$$\begin{aligned}\vec{v} &= \vec{v}_0 + \dot{\vec{u}} + \vec{\Omega}\times(\vec{r}_p + \vec{u}) \\ &= \mathbf{i}\left[v_{ox} + \dot{u}_x - y_p\Omega_z - u_y\Omega_z\right] + \mathbf{j}\left[v_{oy} + \dot{u}_y + x_p\Omega_z + u_x\Omega_z\right] \\ &+\mathbf{k}\left[v_{oz} + y_p\Omega_x + u_y\Omega_x - x_p\Omega_y - u_x\Omega_y\right]\end{aligned} \tag{2.51}$$

The square of the magnitude of this velocity is

$$\begin{aligned}|\vec{v}|^2 &= \left[v_{ox} + \dot{u}_x - y_p\Omega_z - u_y\Omega_z\right]^2 + \left[v_{oy} + \dot{u}_y + x_p\Omega_z + u_x\Omega_z\right]^2 \\ &+\left[v_{oz} + y_p\Omega_x + u_y\Omega_x - x_p\Omega_y - u_x\Omega_y\right]^2\end{aligned} \tag{2.52}$$

where $\vec{r}_p = (x_p, y_p) = \left(R_{ring}\cos\theta, R_{ring}\sin\theta\right)$.

Terms in (2.52) that are independent of the unknown $\vec{u}$ will not contribute to the equations of motion (developed by Lagrange's method) and are therefore eliminated in advance. The remaining terms are re-written as

$$
\begin{aligned}
|\vec{v}|^2 &= \left[\left(\dot{u}_x\right)^2+\left(\dot{u}_y\right)^2\right]+\left[2\Omega_z\left(u_x\dot{u}_y-\dot{u}_x u_y\right)\right] \\
&+\left[\left(u_x\right)^2\left(\Omega_y^2+\Omega_z^2\right)\right]+\left[\left(u_y\right)^2\left(\Omega_x^2+\Omega_z^2\right)\right] \\
&+\left[u_x u_y\left(-2\Omega_x\Omega_y\right)\right] \\
&+\left[u_x x_p\left(2\Omega_y^2+2\Omega_z^2\right)+u_x y_p\left(-2\Omega_x\Omega_y\right)+u_y y_p\left(2\Omega_x^2+2\Omega_z^2\right)+u_y x_p\left(-2\Omega_x\Omega_y\right)\right] \\
&+\left[u_x\left(2v_{oy}\Omega_z-2v_{oz}\Omega_y\right)+u_y\left(-2v_{ox}\Omega_z+2v_{oz}\Omega_x\right)+\dot{u}_x\left(2v_{ox}\right)+\dot{u}_y\left(2v_{oy}\right)\right] \\
&+\left[\dot{u}_x y_p\left(-2\Omega_z\right)+\dot{u}_y x_p\left(2\Omega_z\right)\right]
\end{aligned}
\tag{2.53}
$$

Now, we will replace $\vec{u}^T$ and $\vec{u}^F$ with two term modal expansions using the mode shapes of Section 2.5.1 to yield a 4 degree-of-freedom (discrete) model for the ring. The mode shapes are given in equations (2.43)-(2.46).

The resulting expression for the kinetic energy, though complex, contains many terms that ultimately integrate to zero. These terms vanish due to the orthogonality of the mode shapes and because of the symmetry of the ring structure and the mode shapes. The detailed derivation is given in Appendix D.

The kinetic energy of the system ($T_{kinetic}$) is found by integrating per

$$
T_{kinetic} = \frac{1}{2}\int_V \rho|\vec{v}|^2\,dV \tag{2.54}
$$

Evaluating this integral and noting the terms that vanish yields the following expression for the kinetic energy as a function of the four generalized coordinates.

$$
\begin{aligned}
T_{kinetic} &= \frac{1}{2}M_1^T\left(\dot{q}_1^T\right)^2+\frac{1}{2}M_2^T\left(\dot{q}_2^T\right)^2+\frac{1}{2}M_1^F\left(\dot{q}_1^F\right)^2+\frac{1}{2}M_2^F\left(\dot{q}_2^F\right)^2 \\
&+\Omega_z\left[\gamma^T\left(q_1^T\dot{q}_2^T-\dot{q}_1^T q_2^T\right)+\gamma_1^F\left(q_1^F\dot{q}_2^F-\dot{q}_1^F q_2^F\right)\right] \\
&+\frac{1}{2}\left(\Omega_y^2+\Omega_z^2\right)\alpha_1^T\left(q_1^T\right)^2+\frac{1}{2}\left(\Omega_x^2+\Omega_z^2\right)\beta_2^T\left(q_2^T\right)^2 \\
&+\frac{1}{2}\left(\Omega_x^2\beta_1^F+\Omega_z^2\alpha_1^F+\Omega_z^2\mu_1^F\right)\left(q_1^F\right)^2+\frac{1}{2}\left(\Omega_x^2\beta_2^F+\Omega_y^2\alpha_2^F+\Omega_z^2\mu_2^F\right)\left(q_2^F\right)^2 \\
&-\left(\Omega_x\Omega_y\right)\left[\gamma^T\left(q_1^T q_2^T\right)+\gamma_2^F\left(q_1^F q_2^F\right)\right] \\
&+\left[\left(\Omega_y^2+\Omega_z^2\right)\delta_{x1}^F-\left(\Omega_x\Omega_y\right)\delta_{y1}^F\right]q_1^F+\left[\left(\Omega_x^2+\Omega_z^2\right)\delta_{y2}^F-\left(\Omega_x\Omega_y\right)\delta_{x2}^F\right]q_2^F \\
&+\Omega_z\left(\delta_{x2}^F+\delta_{y2}^F\right)\dot{q}_2^F+\left(v_{oy}\Omega_z-v_{oz}\Omega_y\right)\eta_1^T q_1^T+\left(-v_{ox}\Omega_z+v_{oz}\Omega_x\right)\eta_2^T q_2^T \\
&+\left(v_{ox}\right)\eta_1^T\dot{q}_1^T+\left(v_{oy}\right)\eta_2^T\dot{q}_2^T
\end{aligned}
\tag{2.55}
$$

The equation can be further simplified by assuming that the ring structure experiences angular velocity solely about the out-of-plane z-axis (Ω_z) exists and by removing terms

that are expressed as non-homogenous terms after applying Lagrange method. The non-homogenous terms are removed because they will not excite the ring structure at the resonant frequency. For detailed derivations, refer to Appendix D. These simplifications result in

$$\begin{aligned} T_{kinetic} &= \frac{1}{2}M_1^T\left(\dot{q}_1^T\right)^2+\frac{1}{2}M_2^T\left(\dot{q}_2^T\right)^2+\frac{1}{2}M_1^F\left(\dot{q}_1^F\right)^2+\frac{1}{2}M_2^F\left(\dot{q}_2^F\right)^2 \\ &+\Omega_z\left[\gamma^T\left(q_1^T\dot{q}_2^T-\dot{q}_1^Tq_2^T\right)+\gamma_1^F\left(q_1^F\dot{q}_2^F-\dot{q}_1^Fq_2^F\right)\right] \\ &+\frac{1}{2}\Omega_z^2\alpha_1^T\left(q_1^T\right)^2+\frac{1}{2}\Omega_z^2\beta_2^T\left(q_2^T\right)^2+\frac{1}{2}\Omega_z^2\mu_1^F\left(q_1^F\right)^2+\frac{1}{2}\Omega_z^2\mu_2^F\left(q_2^F\right)^2 \\ &+\left(v_{oy}\Omega_z\right)\eta_1^Tq_1^T-\left(v_{ox}\Omega_z\right)\eta_2^Tq_2^T+\left(v_{ox}\right)\eta_1^T\dot{q}_1^T+\left(v_{oy}\right)\eta_2^T\dot{q}_2^T \end{aligned} \tag{2.56}$$

where

$$M_1^T=\int_V\rho\left[\left(\Phi_{x1}^T\right)^2+\left(\Phi_{y1}^T\right)^2\right]dV=\int_V\rho\left[\left(\Phi_{r1}^T\right)^2+\left(\Phi_{\theta1}^T\right)^2\right]dV \tag{2.57}$$

$$M_2^T=\int_V\rho\left[\left(\Phi_{x2}^T\right)^2+\left(\Phi_{y2}^T\right)^2\right]dV=\int_V\rho\left[\left(\Phi_{r2}^T\right)^2+\left(\Phi_{\theta2}^T\right)^2\right]dV \tag{2.58}$$

$$M_1^F=\int_V\rho\left[\left(\Phi_{x1}^F\right)^2+\left(\Phi_{y1}^F\right)^2\right]dV=\int_V\rho\left[\left(\Phi_{r1}^F\right)^2+\left(\Phi_{\theta1}^F\right)^2\right]dV \tag{2.59}$$

$$M_2^F=\int_V\rho\left[\left(\Phi_{x2}^F\right)^2+\left(\Phi_{y2}^F\right)^2\right]dV=\int_V\rho\left[\left(\Phi_{r2}^F\right)^2+\left(\Phi_{\theta2}^F\right)^2\right]dV \tag{2.60}$$

$$\gamma^T=\int_V\rho\left[\Phi_{x1}^T\Phi_{y1}^T\right]dV,\ \gamma_1^F=\int_V\rho\left[\Phi_{x1}^F\Phi_{y2}^F-\Phi_{x2}^F\Phi_{y1}^F\right]dV \tag{2.61}$$

$$\alpha_1^T=\int_V\rho\left(\Phi_{x1}^T\right)^2dV,\ \beta_2^T=\int_V\rho\left(\Phi_{y2}^T\right)^2dV \tag{2.62}$$

$$\mu_1^F=\int_V\rho\left[\left(\Phi_{x1}^F\right)^2+\left(\Phi_{y1}^F\right)^2\right]dV=M_1^F,\ \mu_2^F=\int_V\rho\left[\left(\Phi_{x2}^F\right)^2+\left(\Phi_{y2}^F\right)^2\right]dV=M_2^F \tag{2.63}$$

$$\eta_1^T=\int_V\rho\left[\Phi_{x1}^T\right]dV,\ \eta_2^T=\int_V\rho\left[\Phi_{y2}^T\right]dV \tag{2.64}$$

2.5.5. Potential Energy I – Ring Structure

The potential energy of the ring gyroscope originates from three sources: (1) the

flexure of the ring structure, (2) the flexure of the support-spring structure, and (3) the electrostatic potential of the electrodes. For an assumed inextensible ring, the potential energy of bending over all the ring elements is given by [46]:

$$U_{m,ring} = \int_V \frac{1}{2} EI \left[\frac{1}{r+\Delta r} - \frac{1}{r} \right]^2 ds \tag{2.65}$$

where the change in curvature of a differential ring element due to bending is given by

$$\frac{1}{r+\Delta r} - \frac{1}{r} \tag{2.66}$$

and E and I are Young's modulus and the moment of inertia of the ring cross section, respectively. When the ring vibrates, a differential element of the ring is displaced to

$$x = x_p + u_x^F, \quad y = y_p + u_y^F \tag{2.67}$$

The differential arc length of a ring element is then given by:

$$ds = \sqrt{x'^2 + y'^2}\, dp \qquad x' = \frac{dx}{dp}, \quad y' = \frac{dy}{dp} \tag{2.68}$$

Assuming no elongation, the curvature of a ring element is given by [48].

$$\frac{1}{r} = \frac{x'y'' - y'x''}{\left(x'^2 + y'^2\right)^{3/2}} \tag{2.69}$$

Therefore, the potential energy due to bending of the ring is given by

$$\begin{aligned} U_{m,ring} &= \int_p \frac{1}{2} EI \left[\frac{x'_p u_y^{F''} - y'_p u_x^{F''} + y''_p u_x^{F'} - x''_p u_y^{F'}}{\left(x'^2_p + y'^2_p\right)^{3/2}} \right]^2 \sqrt{x'^2_p + y'^2_p}\, dp \\ &= \int_p \frac{1}{2} EI \frac{\left[x'_p u_y^{F''} - y'_p u_x^{F''} + y''_p u_x^{F'} - x''_p u_y^{F'} \right]^2}{\left(x'^2_p + y'^2_p\right)^{5/2}} dp \end{aligned} \tag{2.70}$$

Substituting in this result the modal expansion for the displacement due to bending yields the simple quadratic form

$$U_{m,ring} = \frac{1}{2} K_1^R \left(q_1^F \right)^2 + \frac{1}{2} K_2^R \left(q_2^F \right)^2 \tag{2.71}$$

where

$$K_1^R = EI \int_p \frac{\left[x_p' \Phi_{y1}^{F\,''} - y_p' \Phi_{x1}^{F\,''} + y_p'' \Phi_{x1}^{F\,'} - x_p'' \Phi_{y1}^{F\,'} \right]^2}{\left(x_p'^{\,2} + y_p'^{\,2} \right)^{5/2}} dp \tag{2.72}$$

$$K_2^R = EI \int_p \frac{\left[x_p' \Phi_{y2}^{F\,''} - y_p' \Phi_{x2}^{F\,''} + y_p'' \Phi_{x2}^{F\,'} - x_p'' \Phi_{y2}^{F\,'} \right]^2}{\left(x_p'^{\,2} + y_p'^{\,2} \right)^{5/2}} dp \tag{2.73}$$

A detailed derivation of these steps is also provided in [2].

2.5.6. Potential Energy II – Support Beam Structure

The eight semicircular support springs are analyzed using a lumped model. Figure 2.14 illustrates the deflection of the support springs due to the ring translation modes and flexure modes. The figure clearly shows that the stiffness of the support-spring structure is different for the translation modes and the flexural modes. In the translation modes, all eight springs are active. By contrast, in the flexural modes, the four springs attached to the four anti-nodes (located at 0^0, 90^0, 180^0, 270^0 in the figure) are active but the remaining four springs attached to the four nodes (located at 45^0, 135^0, 225^0, 315^0 in the figure) are inactive.

From Figure 2.14, we observe find that we need three principal stiffnesses of a semicircular beam into three directions, as shown in Figure 2.15. They are the horizontal stiffness (K_{HA}), the vertical stiffness (K_{VA}), and the stiffness along to the 45^0 direction (K_{45}). These stiffnesses follow from an analysis of a semicircular spring is having one end fixed and one end allowed to deflect in these principal directions. Using force-deflection equations basic equations provided in reference [49], all three stiffnesses were calculated as follows below:

$$\frac{1}{K_{HA}} = \frac{r_{spring}^{\,3}}{EI_{spring}} \left[-\frac{4}{\pi} + \frac{\pi}{2} \right] \tag{2.74}$$

$$\frac{1}{K_{VA}} = \frac{r_{spring}^{\ 3}}{EI_{spring}}\left[\frac{\pi}{2}\right] \tag{2.75}$$

$$\frac{1}{K_{45}} = \frac{r_{spring}^{\ 3}}{EI_{spring}}\left[-\frac{4}{\pi}+\frac{\pi}{2}\right]\left[\frac{1}{1-8\sin^2(45^0)/\pi^2}\right] = \frac{r_{spring}^{\ 3}}{EI_{spring}}\left[-\frac{4}{\pi}+\frac{\pi}{2}\right]\left[\frac{1}{1-4/\pi^2}\right] \tag{2.76}$$

From Figure 2.14, the translation mode stiffness (K^T) and flexural mode stiffness (K^F) are given by

$$K^T = 2K_{HA} + 2K_{VA} + 4K_{45} \tag{2.77}$$

$$K^F = 4K_{HA} \tag{2.78}$$

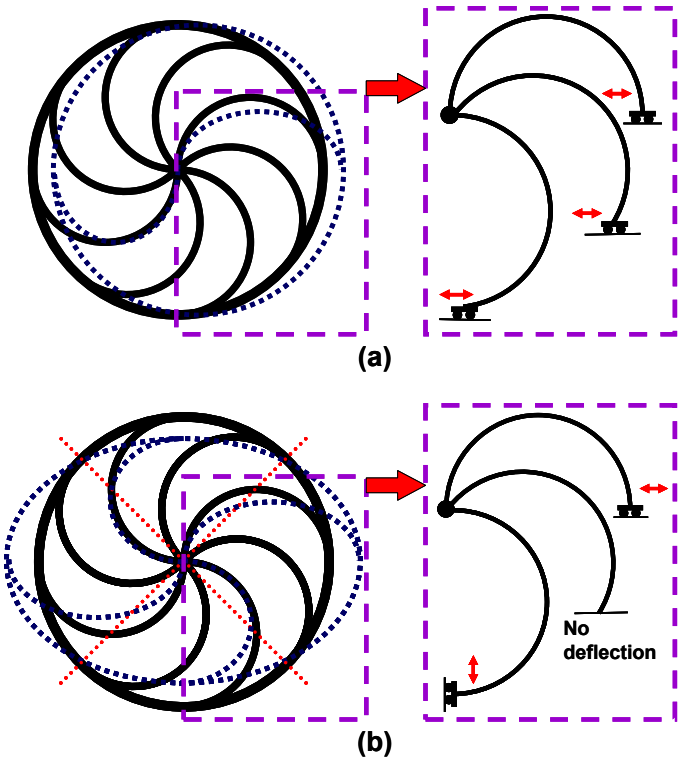

Figure 2.14. Deflections of support springs induced by the (a) translation modes and (b) in flexural modes.

Using parameters for a nickel ring gyroscope (r_{spring}=235μm) [2] and material properties of electroplated nickel (E_{Ni}=190 GPa, ν_{Ni}=0.28 [50]), we calculated K^T = 84 N/m and K^F = 70 N/m. Using the mass of the ring gyro (4.7×10^{-9}kg) [2], we further calculated the resonant frequency of the translation modes to be ~21 kHz. This simple

estimate is quite close to prediction from FEM ~20 kHz and from measurements ~22 kHz as reported in [2].

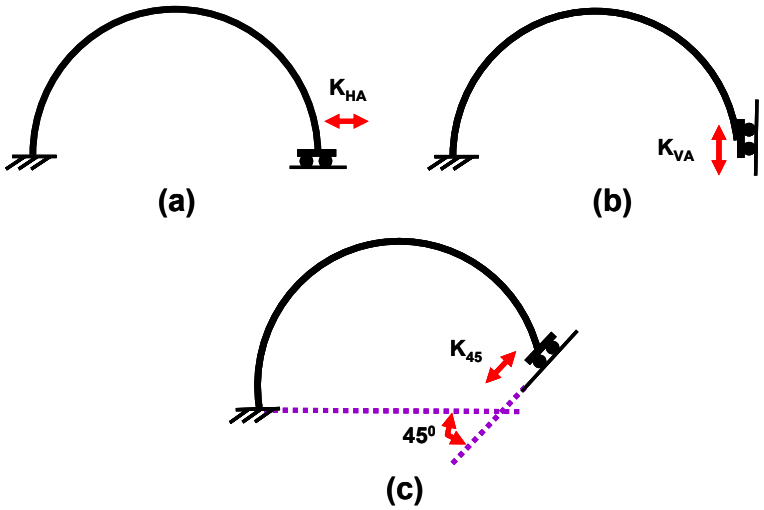

Figure 2.15. Stiffnesses of a semicircular spring in three directions. (a) Horizontal stiffness (K_{HA}), (b) vertical stiffness (K_{VA}), (c) stiffness along 45^0 direction (K_{45}).

Therefore, the potential energy for the support springs follows from

$$U_{m,spring} = \frac{1}{2}K^T\left(q_1^T\right)^2 + \frac{1}{2}K^F\left(q_2^T\right)^2 + \frac{1}{2}K^F\left(q_1^F\right)^2 + \frac{1}{2}K^F\left(q_2^F\right)^2 \qquad (2.79)$$

2.5.7. Potential Energy III – Electrical Potential

The electrodes located on the circumference of the ring, as shown in Figure 2.10, contribute to the electrical potential of the device. One ring-gyro design employs thirty two electrodes [2] and another design employs sixteen [9]. To simplify our modeling, we decided to include only the drive electrodes because they are the only electrodes at which AC voltage is applied to actuate the gyroscope at its resonant frequency. A DC voltage is applied to other electrodes, such as the sense electrodes, to maintain balance across the ring and prevent actuation of the ring through these other electrodes.

We also employed a symmetric electrode set as shown in Figure 2.16. Two drive electrodes, located at $\theta_n=0^0$ and 180^0, are actuated in-phase to activate the drive-axis flexural mode and to suppress the x-axis translation mode.

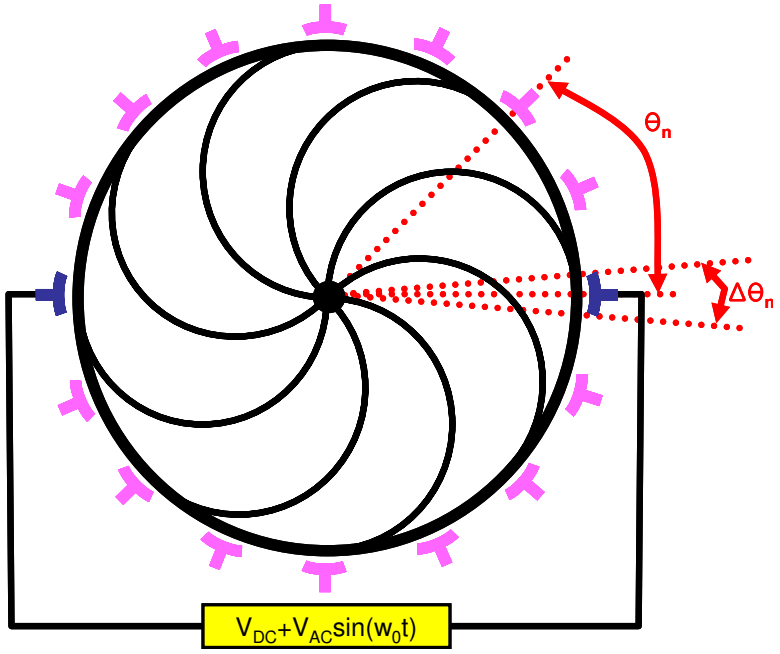

Figure 2.16. Symmetric set of drive electrodes. Two drive electrodes are located at $\theta_n=0^0$ and 180^0 and they are actuated in-phase.

A detailed derivation of the electrical potential energy of the drive electrodes was presented in [2] using the two flexural modes. The capacitance of each electrode in the ring gyroscope is given by

$$C_n = \int_{\theta_n-\Delta\theta_n/2}^{\theta_n+\Delta\theta_n/2} \frac{\varepsilon R_{ring} h_{ring}}{g_0 - \Delta d} d\theta \qquad (2.80)$$

$$\cong \frac{\varepsilon R_{ring} h_{ring}}{g_0} \int_{\theta_n-\Delta\theta_n/2}^{\theta_n+\Delta\theta_n/2} d\theta + \frac{\varepsilon R_{ring} h_{ring}}{g_0^2} \int_{\theta_n-\Delta\theta_n/2}^{\theta_n+\Delta\theta_n/2} (\Delta d) d\theta + \frac{\varepsilon R_{ring} h_{ring}}{g_0^3} \int_{\theta_n-\Delta\theta_n/2}^{\theta_n+\Delta\theta_n/2} (\Delta d)^2 d\theta$$

where g_0 is the equilibrium gap spacing, Δd is the change of the gap spacing due to vibration, and R_{ring} and h_{ring} are the radius and thickness of the ring structure. θ_n and $\Delta\theta_n$ (shown in Figure 2.16) are the location of each electrode and the arc of the electrode, respectively. In cylindrical coordinates, Δd, the vibration displacement of the ring structure, is given by:

$$\Delta d = \Phi_{r1}^T q_1^T + \Phi_{r2}^T q_2^T + \Phi_{r1}^F q_1^F + \Phi_{r2}^F q_2^F \qquad (2.81)$$

Using this relationship, C_n becomes:

$$
\begin{aligned}
C_n &= \frac{\varepsilon R_{ring} h_{ring}}{g_0}\left[\int_{\theta_n-\Delta\theta_n/2}^{\theta_n+\Delta\theta_n/2} d\theta\right] \\
&+\frac{\varepsilon R_{ring} h_{ring}}{g_0^2}\left[\int_{\theta_n-\Delta\theta_n/2}^{\theta_n+\Delta\theta_n/2}\left(\Phi_{r1}^T q_1^T\right)d\theta+\int_{\theta_n-\Delta\theta_n/2}^{\theta_n+\Delta\theta_n/2}\left(\Phi_{r2}^T q_2^T\right)d\theta+\int_{\theta_n-\Delta\theta_n/2}^{\theta_n+\Delta\theta_n/2}\left(\Phi_{r1}^F q_1^F\right)d\theta+\int_{\theta_n-\Delta\theta_n/2}^{\theta_n+\Delta\theta_n/2}\left(\Phi_{r2}^F q_2^F\right)d\theta\right] \\
&+\frac{\varepsilon R_{ring} h_{ring}}{g_0^3}\left[\begin{array}{l}
\left(q_1^T\right)^2\int_{\theta_n-\Delta\theta_n/2}^{\theta_n+\Delta\theta_n/2}\left(\Phi_{r1}^T\right)^2 d\theta+\left(q_2^T\right)^2\int_{\theta_n-\Delta\theta_n/2}^{\theta_n+\Delta\theta_n/2}\left(\Phi_{r2}^T\right)^2 d\theta+\left(q_1^F\right)^2\int_{\theta_n-\Delta\theta_n/2}^{\theta_n+\Delta\theta_n/2}\left(\Phi_{r1}^F\right)^2 d\theta+\left(q_2^F\right)^2\int_{\theta_n-\Delta\theta_n/2}^{\theta_n+\Delta\theta_n/2}\left(\Phi_{r2}^F\right)^2 d\theta \\
+\left(q_1^T q_2^T\right)\int_{\theta_n-\Delta\theta_n/2}^{\theta_n+\Delta\theta_n/2}\left(2\Phi_{r1}^T\Phi_{r2}^T\right)d\theta+\left(q_1^T q_1^F\right)\int_{\theta_n-\Delta\theta_n/2}^{\theta_n+\Delta\theta_n/2}\left(2\Phi_{r1}^T\Phi_{r1}^F\right)d\theta+\left(q_1^T q_2^F\right)\int_{\theta_n-\Delta\theta_n/2}^{\theta_n+\Delta\theta_n/2}\left(2\Phi_{r1}^T\Phi_{r2}^F\right)d\theta \\
+\left(q_2^T q_1^F\right)\int_{\theta_n-\Delta\theta_n/2}^{\theta_n+\Delta\theta_n/2}\left(2\Phi_{r2}^T\Phi_{r1}^F\right)d\theta+\left(q_2^T q_2^F\right)\int_{\theta_n-\Delta\theta_n/2}^{\theta_n+\Delta\theta_n/2}\left(2\Phi_{r2}^T\Phi_{r2}^F\right)d\theta+\left(q_1^F q_2^F\right)\int_{\theta_n-\Delta\theta_n/2}^{\theta_n+\Delta\theta_n/2}\left(2\Phi_{r1}^F\Phi_{r2}^F\right)d\theta
\end{array}\right]
\end{aligned}
\tag{2.82}
$$

The electrical potential energy from the drive electrodes is given by:

$$
U_{drive} = -\sum_{\theta_n=0,180^0}\frac{1}{2}\left[V_{DC}-V_{AC}\sin(w_0 t)\right]^2 C_n \tag{2.83}
$$

This equation, though complex, can be simplified using the following observations:

- The mode shapes (i.e., Φ_{r1}^T, Φ_{r2}^T, Φ_{r1}^F, Φ_{r2}^F) are given by a linear combination of cosθ, sinθ, cos2θ, sin2θ terms. Because θ_n of the drive electrodes are 0 and 180^0, many terms in C_n vanish.
- Terms that do not involve any of the modal coordinates (i.e., q_1^T, q_2^T, q_1^F, q_2^F) are ignored immediately as they will not contribute to the equations of motion (via application of Lagrange's equation).
- Several terms that produce non-homogeneous terms in the equations of motion are ignored because they do not excite the ring at the resonant frequency.
- All other terms in the equations of motion that cannot excite the ring at the flexural resonant frequency are ignored because they will be filtered out.

Upon using the observations above, one can simplify the electrical potential energy to

$$
\begin{aligned}
U_{drive} &= \left(V_{DC}V_{AC}\right)\left(4\chi_{g1}\chi_{d1}\right)\sin(w_0 t)\left(q_1^F\right) \\
&-\frac{1}{2}\left(V_{DC}^2+V_{AC}^2/2\right)\left[\begin{array}{l}
\chi_{g2}\left(\chi_{d3}+\chi_{d1}\right)\left(q_1^T\right)^2+\chi_{g2}\left(\chi_{d3}-\chi_{d1}\right)\left(q_2^T\right)^2 \\
+\chi_{g2}\left(4\chi_{d3}+2\chi_{d2}\right)\left(q_1^F\right)^2+\chi_{g2}\left(4\chi_{d3}-2\chi_{d2}\right)\left(q_2^F\right)^2
\end{array}\right]
\end{aligned}
\tag{2.84}
$$

where

$$\chi_{g1} = \frac{\varepsilon R_{ring} h_{ring}}{g_0^2},\ \chi_{g2} = \frac{\varepsilon R_{ring} h_{ring}}{g_0^3} \tag{2.85}$$
$$\chi_{d1} = \sin(\Delta\theta_n),\ \chi_{d2} = \sin(2\Delta\theta_n),\ \chi_{d3} = \Delta\theta_n$$

Detailed derivation is shown in Appendix E. Note that these can be also expressed by multiple of the expressions depending on the selection of mode shapes, as explained using equations (2.39) and (2.41).

2.5.8. Energy Lost by Viscous Damping

The energy lost due to viscous damping is modeled below as simple modal damping for each mode. Therefore, the damping coefficient from [2] can be simplified to

X-axis translation mode: $$-\frac{1}{2}C_1^T\left(\dot{q}_1^T\right)^2 \tag{2.86}$$

Y-axis translation mode: $$-\frac{1}{2}C_2^T\left(\dot{q}_2^T\right)^2 \tag{2.87}$$

Drive-axis flexural mode: $$-\frac{1}{2}C_1^F\left(\dot{q}_1^F\right)^2 \tag{2.88}$$

Sense-axis flexural mode: $$-\frac{1}{2}C_2^F\left(\dot{q}_2^F\right)^2 \tag{2.89}$$

where $C_1^T, C_2^T, C_1^F, C_2^F$ are damping coefficients for each of the four modes used in this model. Therefore, energy lost by (or work done by) the damping is given by:

$$W_{damping} = -\frac{1}{2}C_1^T\left(\dot{q}_1^T\right)^2 - \frac{1}{2}C_2^T\left(\dot{q}_2^T\right)^2 - \frac{1}{2}C_1^F\left(\dot{q}_1^F\right)^2 - \frac{1}{2}C_2^F\left(\dot{q}_2^F\right)^2 \tag{2.90}$$

2.5.9. Lagrange's Equation

The above expressions for the kinetic energy, potential energy, and dissipation can now be employed in Lagrange's equation to yield the desired 4 degree-of-freedom model as follows

$$\frac{d}{dt}\frac{\partial T_{kinetic}}{\partial \dot{q}_1^T}-\frac{\partial T_{kinetic}}{\partial q_1^T}+\frac{\partial U_{total}}{\partial q_1^T}=\frac{\partial W_{damping}}{\partial \dot{q}_1^T} \tag{2.91}$$

$$\frac{d}{dt}\frac{\partial T_{kinetic}}{\partial \dot{q}_2^T}-\frac{\partial T_{kinetic}}{\partial q_2^T}+\frac{\partial U_{total}}{\partial q_2^T}=\frac{\partial W_{damping}}{\partial \dot{q}_2^T} \tag{2.92}$$

$$\frac{d}{dt}\frac{\partial T_{kinetic}}{\partial \dot{q}_1^F}-\frac{\partial T_{kinetic}}{\partial q_1^F}+\frac{\partial U_{total}}{\partial q_1^F}=\frac{\partial W_{damping}}{\partial \dot{q}_1^F} \tag{2.93}$$

$$\frac{d}{dt}\frac{\partial T_{kinetic}}{\partial \dot{q}_2^F}-\frac{\partial T_{kinetic}}{\partial q_2^F}+\frac{\partial U_{total}}{\partial q_2^F}=\frac{\partial W_{damping}}{\partial \dot{q}_2^F} \tag{2.94}$$

This process yields the following equations of motion

$$\begin{aligned}
&\begin{bmatrix} M_1^T & 0 & 0 & 0 \\ 0 & M_2^T & 0 & 0 \\ 0 & 0 & M_1^F & 0 \\ 0 & 0 & 0 & M_2^F \end{bmatrix}\begin{bmatrix} \ddot{q}_1^T \\ \ddot{q}_2^T \\ \ddot{q}_1^F \\ \ddot{q}_2^F \end{bmatrix}+\begin{bmatrix} C_1^T & 0 & 0 & 0 \\ 0 & C_2^T & 0 & 0 \\ 0 & 0 & C_1^F & 0 \\ 0 & 0 & 0 & C_2^F \end{bmatrix}\begin{bmatrix} \dot{q}_1^T \\ \dot{q}_2^T \\ \dot{q}_1^F \\ \dot{q}_2^F \end{bmatrix}+\begin{bmatrix} k^T & 0 & 0 & 0 \\ 0 & k^T & 0 & 0 \\ 0 & 0 & k_1^R+k^F & 0 \\ 0 & 0 & 0 & k_1^R+k^F \end{bmatrix}\begin{bmatrix} q_1^T \\ q_2^T \\ q_1^F \\ q_2^F \end{bmatrix} \\
&+2\Omega_z\begin{bmatrix} 0 & -\gamma^T & 0 & 0 \\ \gamma^T & 0 & 0 & 0 \\ 0 & 0 & 0 & -\gamma_1^F \\ 0 & 0 & \gamma_1^F & 0 \end{bmatrix}\begin{bmatrix} \dot{q}_1^T \\ \dot{q}_2^T \\ \dot{q}_1^F \\ \dot{q}_2^F \end{bmatrix}+\dot{\Omega}_z\begin{bmatrix} 0 & -\gamma^T & 0 & 0 \\ \gamma^T & 0 & 0 & 0 \\ 0 & 0 & 0 & -\gamma_1^F \\ 0 & 0 & \gamma_1^F & 0 \end{bmatrix}\begin{bmatrix} q_1^T \\ q_2^T \\ q_1^F \\ q_2^F \end{bmatrix} \\
&+\Omega_z^2\begin{bmatrix} -\alpha_1^T & 0 & 0 & 0 \\ 0 & -\beta_2^F & 0 & 0 \\ 0 & 0 & -\mu_1^F & 0 \\ 0 & 0 & 0 & -\mu_2^F \end{bmatrix}\begin{bmatrix} q_1^T \\ q_2^T \\ q_1^F \\ q_2^F \end{bmatrix}+\begin{bmatrix} \chi_1 & 0 & 0 & 0 \\ 0 & \chi_2 & 0 & 0 \\ 0 & 0 & \chi_3 & 0 \\ 0 & 0 & 0 & \chi_4 \end{bmatrix}\begin{bmatrix} q_1^T \\ q_2^T \\ q_1^F \\ q_2^F \end{bmatrix} \\
&=\begin{bmatrix} -\eta_1^T & 0 & 0 & 0 \\ 0 & -\eta_2^T & 0 & 0 \\ 0 & 0 & 0 & 0 \\ 0 & 0 & 0 & 0 \end{bmatrix}\begin{bmatrix} \dot{v}_{ox}(t) \\ \dot{v}_{oy}(t) \\ 0 \\ 0 \end{bmatrix}+\begin{bmatrix} \eta_1^T\Omega_z & 0 & 0 & 0 \\ 0 & \eta_2^T\Omega_z & 0 & 0 \\ 0 & 0 & 0 & 0 \\ 0 & 0 & 0 & 0 \end{bmatrix}\begin{bmatrix} v_{ox}(t) \\ v_{oy}(t) \\ 0 \\ 0 \end{bmatrix} \\
&+\begin{bmatrix} 0 \\ 0 \\ -\xi_d \sin(w_0 t) \\ 0 \end{bmatrix}
\end{aligned} \tag{2.95}$$

The terms in these equations of motion fall into the following five categories. (1) The expression (2.96) contains terms representing the modal mass, damping, and stiffness of the ring gyro mechanical structure; (2) the expression (2.97) contains modal coupling terms induced by the Coriolis forces and by angular acceleration; (3) the expression (2.98) contains additional stiffness terms that arise from centripetal acceleration and electrostatic effects, (4) the expression (2.99) contains the terms

representing the environmental excitation, and (5) the expression (2.100) contains a term from the electrostatic actuation.

$$\begin{bmatrix} M_1^T & 0 & 0 & 0 \\ 0 & M_2^T & 0 & 0 \\ 0 & 0 & M_1^F & 0 \\ 0 & 0 & 0 & M_2^F \end{bmatrix} \begin{bmatrix} \ddot{q}_1^T \\ \ddot{q}_2^T \\ \ddot{q}_1^F \\ \ddot{q}_2^F \end{bmatrix} + \begin{bmatrix} C_1^T & 0 & 0 & 0 \\ 0 & C_2^T & 0 & 0 \\ 0 & 0 & C_1^F & 0 \\ 0 & 0 & 0 & C_2^F \end{bmatrix} \begin{bmatrix} \dot{q}_1^T \\ \dot{q}_2^T \\ \dot{q}_1^F \\ \dot{q}_2^F \end{bmatrix} + \begin{bmatrix} k^T & 0 & 0 & 0 \\ 0 & k^T & 0 & 0 \\ 0 & 0 & k_1^R + k^F & 0 \\ 0 & 0 & 0 & k_1^R + k^F \end{bmatrix} \begin{bmatrix} q_1^T \\ q_2^T \\ q_1^F \\ q_2^F \end{bmatrix} \tag{2.96}$$

$$2\Omega_z \begin{bmatrix} 0 & -\gamma^T & 0 & 0 \\ \gamma^T & 0 & 0 & 0 \\ 0 & 0 & 0 & -\gamma_1^F \\ 0 & 0 & \gamma_1^F & 0 \end{bmatrix} \begin{bmatrix} \dot{q}_1^T \\ \dot{q}_2^T \\ \dot{q}_1^F \\ \dot{q}_2^F \end{bmatrix} + \dot{\Omega}_z \begin{bmatrix} 0 & -\gamma^T & 0 & 0 \\ \gamma^T & 0 & 0 & 0 \\ 0 & 0 & 0 & -\gamma_1^F \\ 0 & 0 & \gamma_1^F & 0 \end{bmatrix} \begin{bmatrix} q_1^T \\ q_2^T \\ q_1^F \\ q_2^F \end{bmatrix} \tag{2.97}$$

$$\Omega_z^2 \begin{bmatrix} -\alpha_1^T & 0 & 0 & 0 \\ 0 & -\beta_2^F & 0 & 0 \\ 0 & 0 & -\mu_1^F & 0 \\ 0 & 0 & 0 & -\mu_2^F \end{bmatrix} \begin{bmatrix} q_1^T \\ q_2^T \\ q_1^F \\ q_2^F \end{bmatrix} + \begin{bmatrix} \chi_1 & 0 & 0 & 0 \\ 0 & \chi_2 & 0 & 0 \\ 0 & 0 & \chi_3 & 0 \\ 0 & 0 & 0 & \chi_4 \end{bmatrix} \begin{bmatrix} q_1^T \\ q_2^T \\ q_1^F \\ q_2^F \end{bmatrix} \tag{2.98}$$

$$\begin{bmatrix} -\eta_1^T & 0 & 0 & 0 \\ 0 & -\eta_2^T & 0 & 0 \\ 0 & 0 & 0 & 0 \\ 0 & 0 & 0 & 0 \end{bmatrix} \begin{bmatrix} \dot{v}_{ox}(t) \\ \dot{v}_{oy}(t) \\ 0 \\ 0 \end{bmatrix} + \begin{bmatrix} \eta_1^T \Omega_z & 0 & 0 & 0 \\ 0 & \eta_2^T \Omega_z & 0 & 0 \\ 0 & 0 & 0 & 0 \\ 0 & 0 & 0 & 0 \end{bmatrix} \begin{bmatrix} v_{ox}(t) \\ v_{oy}(t) \\ 0 \\ 0 \end{bmatrix} \tag{2.99}$$

$$\begin{bmatrix} 0 \\ 0 \\ -\xi_2 \sin(w_0 t) \\ 0 \end{bmatrix} \tag{2.100}$$

where

$$\chi_1 = -\left(V_{DC}^2 + V_{AC}^2/2\right)\left[\chi_{g2}\left(\chi_{d3} + \chi_{d1}\right)\right],\ \chi_2 = -\left(V_{DC}^2 + V_{AC}^2/2\right)\left[\chi_{g2}\left(\chi_{d3} - \chi_{d1}\right)\right], \tag{2.101}$$
$$\chi_3 = -\left(V_{DC}^2 + V_{AC}^2/2\right)\left[\chi_{g1}\left(4\chi_{d3} + 2\chi_{d1}\right)\right],\ \chi_4 = -\left(V_{DC}^2 + V_{AC}^2/2\right)\left[\chi_{g1}\left(4\chi_{d3} - 2\chi_{d1}\right)\right],$$

$$\xi_2 = 8\left(V_{DC} V_{AC}\right)\left(\chi_{g1}\chi_{d1}\right) \tag{2.102}$$

All other quantities appearing in the equations of motion above are defined in previous sections.

Note that the four equations of motion (2.95) form two decoupled sets of equations which independently govern the translation and flexural modes. These decoupled sets are

$$\begin{bmatrix} M_1^T & 0 \\ 0 & M_2^T \end{bmatrix}\begin{bmatrix} \ddot{q}_1^T \\ \ddot{q}_2^T \end{bmatrix}+\begin{bmatrix} C_1^T & 0 \\ 0 & C_2^T \end{bmatrix}\begin{bmatrix} \dot{q}_1^T \\ \dot{q}_2^T \end{bmatrix}+\begin{bmatrix} k^T & 0 \\ 0 & k^T \end{bmatrix}\begin{bmatrix} q_1^T \\ q_2^T \end{bmatrix}+2\Omega_z\begin{bmatrix} 0 & -\gamma^T \\ \gamma^T & 0 \end{bmatrix}\begin{bmatrix} \dot{q}_1^T \\ \dot{q}_2^T \end{bmatrix} \tag{2.103}$$
$$+\dot{\Omega}_z\begin{bmatrix} 0 & -\gamma^T \\ \gamma^T & 0 \end{bmatrix}\begin{bmatrix} q_1^T \\ q_2^T \end{bmatrix}+\Omega_z^2\begin{bmatrix} -\alpha_1^T & 0 \\ 0 & -\beta_2^F \end{bmatrix}\begin{bmatrix} q_1^T \\ q_2^T \end{bmatrix}+\begin{bmatrix} \chi_1 & 0 \\ 0 & \chi_2 \end{bmatrix}\begin{bmatrix} q_1^T \\ q_2^T \end{bmatrix}$$
$$=\begin{bmatrix} -\eta_1^T & 0 \\ 0 & -\eta_2^T \end{bmatrix}\begin{bmatrix} \dot{v}_{ox}(t) \\ \dot{v}_{oy}(t) \end{bmatrix}+\begin{bmatrix} \eta_1^T\Omega_z & 0 \\ 0 & \eta_2^T\Omega_z \end{bmatrix}\begin{bmatrix} v_{ox}(t) \\ v_{oy}(t) \end{bmatrix}+\begin{bmatrix} 0 \\ 0 \end{bmatrix}$$

$$\begin{bmatrix} M_1^F & 0 \\ 0 & M_2^F \end{bmatrix}\begin{bmatrix} \ddot{q}_1^F \\ \ddot{q}_2^F \end{bmatrix}+\begin{bmatrix} C_1^F & 0 \\ 0 & C_2^F \end{bmatrix}\begin{bmatrix} \dot{q}_1^F \\ \dot{q}_2^F \end{bmatrix}+\begin{bmatrix} k_1^R+k^F & 0 \\ 0 & k_1^R+k^F \end{bmatrix}\begin{bmatrix} q_1^T \\ q_2^T \end{bmatrix}+2\Omega_z\begin{bmatrix} 0 & -\gamma_1^F \\ \gamma_1^F & 0 \end{bmatrix}\begin{bmatrix} \dot{q}_1^T \\ \dot{q}_2^T \end{bmatrix} \tag{2.104}$$
$$+\dot{\Omega}_z\begin{bmatrix} 0 & -\gamma_1^F \\ \gamma_1^F & 0 \end{bmatrix}\begin{bmatrix} q_1^T \\ q_2^T \end{bmatrix}+\Omega_z^2\begin{bmatrix} -\mu_1^F & 0 \\ 0 & -\mu_2^F \end{bmatrix}\begin{bmatrix} q_1^T \\ q_2^T \end{bmatrix}+\begin{bmatrix} \chi_3 & 0 \\ 0 & \chi_4 \end{bmatrix}\begin{bmatrix} q_1^T \\ q_2^T \end{bmatrix}$$
$$=\begin{bmatrix} 0 & 0 \\ 0 & 0 \end{bmatrix}\begin{bmatrix} \dot{v}_{ox}(t) \\ \dot{v}_{oy}(t) \end{bmatrix}+\begin{bmatrix} 0 & 0 \\ 0 & 0 \end{bmatrix}\begin{bmatrix} v_{ox}(t) \\ v_{oy}(t) \end{bmatrix}+\begin{bmatrix} -\xi_2\sin(w_0t) \\ 0 \end{bmatrix}$$

Therefore, the flexural modes, which are excited by the operation of the ring gyroscope, are not influenced by the translation modes which are excited by the environmental vibration. Thus, the flexural modes are not influenced by environmental vibration. In other words, a ring gyroscope is vibration-insensitive because its sensing modes which are excited by Coriolis forces remain decoupled from the (translation) modes excited by vibration.

2.5.10. Vibration-induced Errors due to Nonlinearity of the Sense Electrodes

One of the vibration-induced error sources in tuning fork gyroscopes derives from the capacitive nonlinearity at sense electrodes which was neglected in the simplified model above. The same phenomenon might also arise in ring gyroscopes and so we provide an analysis here. Figure 2.17 shows a single-ended sense electrode used in ring gyroscopes [2, 9].

The output of a single-ended parallel-plate sensing electrode, when both Coriolis forces and sense-direction vibration exist, is given by

$$\begin{aligned}\Delta C_1 = C_0\left[1+\frac{1}{g_0}\left\{D_0\sin(w_0t)\right\}+\frac{1}{g_0^2}\left\{D_0^2\sin^2(w_0t)\right\}\right] \\ +C_0\left[\frac{1}{g_0}\left\{D_v\sin(w_vt)\right\}+\frac{1}{g_0^2}\left\{2D_0D_v\sin(w_0t)\sin(w_vt)+d_v^2\sin^2(w_vt)\right\}\right]\end{aligned} \tag{2.105}$$

where C_0 is a constant and g_0 is the gap of electrodes in equilibrium; D_0 and w_0 are the maximum (Coriolis force induced) displacement of the ring structure along the sense direction (i.e., radial displacement along the q_2^F direction) and the flexural resonant

frequency of the ring structure, respectively; D_v and w_v are the maximum vibration-induced displacement of the ring structure along the sense direction and the translational resonant frequency of the ring structure, respectively. As we did in Sections 2.3 and 2.4.3.1, we assumed a very slow rotation to simply derivation. In this equation, the terms in the first bracket are produced solely by the Coriolis force, while the terms in the second bracket are induced from both the Coriolis force and the environmental vibration. Therefore, the vibration-induced capacitive output is given by

$$\Delta C_{vibration} = C_0\left[\frac{1}{g_0}\left\{D_v \sin\left(w_v t\right)\right\} + \frac{1}{g_0^2}\left\{2D_0 D_v \sin\left(w_0 t\right)\sin\left(w_v t\right) + D_v^2 \sin^2\left(w_v t\right)\right\}\right] \quad (2.106)$$

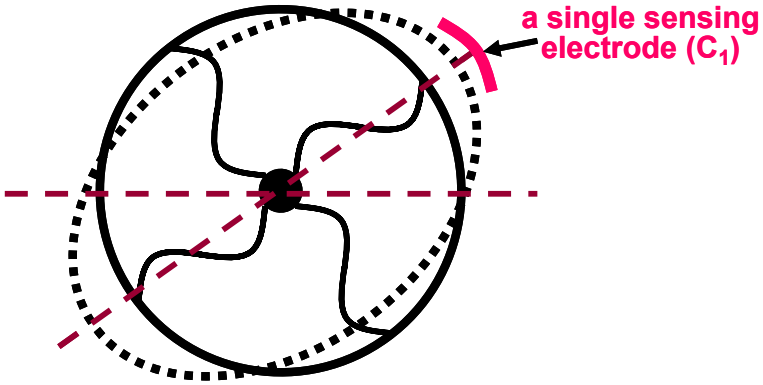

Figure 2.17. Single-ended sensing electrode in a ring gyroscope.

Note that the signals produced from the capacitive read-outs will be filtered out except for those signals having frequencies at or near the resonant frequency of the gyroscope because of the frequency demodulation system explained in Section 2.4.1. Therefore, the three terms in equation (2.106) are filtered except in the following situations:

$$C_0\left[\frac{1}{g_0}\left\{D_v \sin\left(w_v t\right)\right\}\right] = 0 \quad \text{except } w_0 \cong w_v \quad (2.107)$$

$$C_0\left[\frac{1}{g_0^2} 2D_0 D_v \sin\left(w_0 t\right)\sin\left(w_v t\right)\right] = 0 \quad \text{except } w_v \cong 0 \quad (2.108)$$

$$C_0\left[\frac{1}{g_0^2} d_v^2 \sin^2\left(w_v t\right)\right] = 0 \quad \text{except } w_v \cong w_0/2 \quad (2.109)$$

All of these three terms cannot be filtered out in tuning fork gyroscopes, as discussed in Section 2.4. However, all are filtered out in ring gyroscopes because of the decoupled resonant frequencies between the translation modes (~20 kHz) and the flexural modes (~30 kHz). Therefore, even capacitive nonlinearity at the sense electrodes cannot introduce errors in ring gyroscopes due to environmental excitation.

2.6. Summary of Vibration Effects on MEMS Gyroscopes

We selected MEMS vibratory gyroscopes because of their high vibration sensitivity and complex structures. We first classified MEMS gyroscopes into major categories and analyzed and compared the vibration-induced errors in each class. Table 2.4 summarizes our findings which are as follows.

Vibration-induced errors arise from three sources: (1) dynamic response of the mechanical structure of gyroscopes, (2) capacitive nonlinearity at drive electrodes (including asymmetric electrostatic force along the sense direction and asymmetric change of drive capacitance), and (3) capacitive nonlinearity at sense electrodes. The non-TFGs are affected by all three error sources and the dominant error source in this design is the dynamics of the mechanical structure. We also demonstrated that the most important vibrations are those having frequencies at/near the gyro's resonant frequency and those applied along the sense direction. TFGs are affected by the nonlinearity at drive and sense electrodes because their differential operation cancels the dynamic response. Type-CP and Type-DS gyroscopes experience vibration-induced errors originating from both drive and sense electrodes, but Type-DD gyroscopes experience errors originating from only sense electrodes because these gyros enforce a constant gap for the drive electrodes. This is the reason that Type-CP and Type-DS gyros exhibit much larger (>99%) vibration-induced errors than Type-DD gyros in our simulations. The errors in Type-CP and Type-DS gyros arise mainly from the asymmetry in the sense-direction electrostatic force at the drive electrodes, while the far more modest vibration-induced errors for Type-DD gyros arise largely from the capacitance nonlinearity of the sense electrodes. By contrast, ring gyroscopes do not experience errors from any of the three sources because the vibration modes produced by the Coriolis force and those excited by environmental vibration are decoupled.

Table 2.4. Summary of vibration-induced error sources in major classes of gyros. The dominant error source is highlighted.

Gyro Type	Vibration Error Sources		
	Dynamics of Mechanical Structures	Capacitive Nonlinearity at	
		Drive Electrode	Sense Electrode
Non-TFG	**Errors exist**	Errors exist	Errors exist
TFG (CP and DS)	Errors do not exist	**Errors exist**	Errors exist
TFG (DD)	Errors do not exist	Errors do not exist	**Errors exist**
Ring	Errors do not exist	Errors do not exist	Errors do not exist

Although vibration sensitivity is an important factor in evaluating the performance of gyroscopes, some gyroscopes might employ a structure that has higher vibration sensitivity but meet other desirable performance characteristics. For example, the DS-type gyroscope, which is more sensitive to vibration than the DD-type, is in production because it can achieve smaller quadrature error [16]. In this case if good vibration performance is also required of the gyroscope, a vibration isolator, which will be discussed in Chapter 3, will have to be added to the structure.

References

[1] S. J. C. Dyne, D. E. L. Tunbridge, and P. P. Collins, "The vibration environment on a satellite in orbit," in the Proceeding of *High Accuracy Platform Control in Space, IEE Colloquium on*, London, UK, 1993, pp. 12/1-12/6.

[2] M. W. Putty, "A Micromachined Vibrating Ring Gyroscope," Ph.D. Thesis, University of Michigan, 1995

[3] G. J. O'Brien, "Design and Fabrication of MEMS Angular Rate and Angular Acceleration Sensors with CMOS Switched Capacitor Signal Conditioning," Doctor of Philosophy Thesis, Electrical Engineering, University of Michigan, 2004

[4] C. Painter and A. Shkel, "Experimental Evaluation of a Control System for an Absolute Angle Measuring Micromachined Gyroscope," in the Proceeding of *IEEE Sensors Conference*, Irvine, CA, USA 2005, pp. 1084-1087.

[5] A. M. Shkel, "Type I and Type II Micromachined Vibratory Gyroscopes," in the Proceeding of *2006 IEEE/ION Position, Location, And Navigation Symposium*, 2006, pp. 586-593.

[6] D. Piyabongkarn, R. Rajamani, and M. Greminger, "The development of a MEMS gyroscope

for absolute angle measurement," *IEEE Transactions on Control Systems Technology,* vol. 13, pp. 185 - 195, 2005.

[7] M. F. Zaman, A. Sharma, B. V. Amini, and F. Ayazi, "The resonating star gyroscope," in the Proceeding of *Micro Electro Mechanical Systems, 2005. MEMS 2005. 18th IEEE International Conference on*, 2005, pp. 355-358.

[8] C.-O. Chang, G.-E. Chang, C.-S. Chou, W.-T. C. Chien, and P.-C. Chen, "In-plane free vibration of a single-crystal silicon ring," *International Journal of Solids and Structures,* vol. 45, pp. 6114-6132, 2008.

[9] F. Ayazi and K. Najafi, "A HARPSS polysilicon vibrating ring gyroscope," *Microelectromechanical Systems, Journal of,* vol. 10, pp. 169-179, 2001.

[10] G. He and K. Najafi, "A single-crystal silicon vibrating ring gyroscope," in the Proceeding of *A Solid State Sensors, Actuators and Microsystems Workshop (Hilton Head 2006)*, 2002, pp. 718-721.

[11] N. Yazdi, F. Ayazi, and K. Najafi, "Micromachined inertial sensors," *Proceedings of the IEEE,* vol. 86, pp. 1640-1659, 1998.

[12] M. F. Zaman, A. Sharma, and F. Ayazi, "High Performance Matched-Mode Tuning Fork Gyroscope," in the Proceeding of *19th IEEE International Conference on Micro Electro Mechanical Systems*, Istanbul, Turkey 2006, pp. 66-69.

[13] S. E. Alper and T. Akin, "Symmetrical and decoupled nickel microgyroscope on insulating substrate," *Sensors and Actuators A: Physical,* vol. 115, pp. 336-350, 2004.

[14] W. Geiger, W. U. Butt, A. Gai?r, J. Frech, M. Braxmaier, T. Link, A. Kohne, P. Nommensen, H. Sandmaier, W. Lang, and H. Sandmaier, "Decoupled microgyros and the design principle DAVED," *Sensors and Actuators A: Physical,* vol. 95, pp. 239-249, 2002.

[15] H. Xie and G. K. Fedder, "Integrated Microelectromechanical Gyroscopes," *Journal of Aerospace Engineering,* vol. 16, pp. 65-75 2003.

[16] J. A. Geen, S. J. Sherman, J. F. Chang, and S. R. Lewis, "Single-chip surface micromachined integrated gyroscope with 50/spl deg//h Allan deviation," *IEEE Journal of Solid-State Circuits,* vol. 37, pp. 1860-1866, 2002.

[17] J. A. Geen, "Progress in integrated gyroscopes," in the Proceeding of *Position Location and Navigation Symposium (PLANS)*, Monterey, CA, USA, 2004, pp. 1-6.

[18] C. Jeong, S. Seok, B. Lee, H. Kim, and K. Chun, "A study on resonant frequency and Q factor tunings for MEMS vibratory gyroscopes," *Journal of Micromechanics and Microengineering,* vol. 14, pp. 1530-1536, 2004.

[19] A. Scheurle, T. Fuchs, K. Kehr, C. Leinenbach, S. Kronmuller, A. Arias, J. Ceballos, M. A. Lagos, J. M. Mora, J. M. Munoz, A. Ragel, J. Ramos, S. Van Aerde, J. Spengler, A. Mehta, A. Verbist, B. Du Bois, and A. Witvrouw, "A 10 um thick poly-SiGe gyroscope processed above 0.35 um CMOS," in the Proceeding of *Micro Electro Mechanical Systems, 2007. MEMS. IEEE 20th International Conference on*, 2007, pp. 39-42.

[20] T. Jiang, A. Wang, J. Jiao, and G. Liu, "Detection capacitance analysis method for tuning fork micromachined gyroscope based on elastic body model," *Sensors and Actuators A: Physical,* vol. 128, pp. 52-59, 2006.

[21] J.-Y. Lee, S.-H. Jeon, H.-K. Jung, H.-K. Chang, and Y.-K. Kim, "Vacuum packaged single crystal silicon gyroscope with sub mdeg/s//spl radic/Hz resolution," in the Proceeding of *13th International Conference on Solid-State Sensors, Actuators and Microsystems*, 2005, pp. 531-534 Vol. 1.

[22] T. Juneau, A. P. Pisano, and J. H. Smith, "Dual axis operation of a micromachined rate gyroscope," in the Proceeding of *International Conference on Solid State Sensors and Actuators (TRANSDUCERS)*, 1997, pp. 883-886 vol.2.

[23] J. Bernstein, S. Cho, A. T. King, A. Kourepenis, P. Maciel, and M. Weinberg, "A micromachined comb-drive tuning fork rate gyroscope," in the Proceeding of *Micro Electro Mechanical Systems, 1993, MEMS '93, Proceedings An Investigation of Micro Structures, Sensors, Actuators, Machines and Systems. IEEE.*, Fort Lauderdale, FL, USA, 1993, pp. 143-148.

[24] J. Bernstein, S. Cho, A. T. King, A. Kourepenis, P. Maciel, and M. S. Weinberg, "A micromachined comb-drive tuning fork rate gyroscope," in the Proceeding of *Micro Electro Mechanical Systems (MEMS '93), IEEE Proceedings An Investigation of Micro Structures, Sensors, Actuators, Machines and Systems.* , Fort Lauderdale, FL, USA, 1993.

[25] T. Tsuchiya, Y. Kageyama, H. Funabashi, and J. Sakata, "Polysilicon vibrating gyroscope vacuum-encapsulated in an on-chip micro chamber," *Sensors and Actuators A: Physical,* vol. 90, pp. 49-55, 2001.

[26] H. Yan, "Phase-locked mechanical resonator pair and its application in micromachined vibration gyroscope." vol. US 6,938,483, 2005.

[27] S. A. Bhave, J. I. Seeger, J. Xuesong, B. E. Boser, R. T. Howe, and J. Yasaitis, "An integrated, vertical-drive, in-plane-sense microgyroscope," in the Proceeding of *12th International Conference on Solid-State Sensors, Actuators and Microsystems (TRANSDUCERS)*, 2003, pp. 171-174 vol.1.

[28] A. A. Seshia, "Integrated Micromechanical Resonant Sensors for Inertial Measurement Systems," Doctor of Philosophy Thesis, Electrical Engineering and Computer Science, University of California at Berkeley 2002

[29] A. S. Phani, A. A. Seshia, M. Palaniapan, R. T. Howe, and J. Yasaitis, "Modal Coupling in Micromechanical Vibratory Rate Gyroscopes," *Sensors Journal, IEEE,* vol. 6, pp. 1144-1152, 2006.

[30] Y. W. Hsu, "Multi-element Micro Gyro." vol. 6,089,089 Unite State, 2000.

[31] M. C. Lee, S. J. Kang, K. D. Jung, S.-H. Choa, and Y. C. Cho, "A high yield rate MEMS gyroscope with a packaged SiOG process," *Journal of Micromechanics and Microengineering,* vol. 15, pp. 2003-2010, 2005.

[32] K. Schumacher, O. Krömer, U. Wallrabe, J. Mohr, and V. Saile., "Micromechanical LIGA-Gyroscope," in the Proceeding of *Transducers*, 1999.

[33] H. Song, Y. S. Oh, I. S. Song, S. J. Kang, S. O. Choi, H. C. Kim, B. J. Ha, S. S. Baek, and C. M. Song, "Wafer level vacuum packaged de-coupled vertical gyroscope by a new fabrication process," in the Proceeding of *Annual International Conference on Micro Electro Mechanical Systems (MEMS)*, Miyazaki, Japan, 2000, pp. 520-524.

[34] M. Palaniapan, R. T. Howe, and J. Yasaitis, "Performance comparison of integrated z-axis frame microgyroscopes," in the Proceeding of *IEEE The Sixteenth Annual International Conference on Micro Electro Mechanical Systems(MEMS)*, Kyoto, Japan, 2003, pp. 482-485.

[35] J. Kim, S. Park, D. Kwak, H. Ko, and D.-I. D. Cho, "A planar, x-axis, single-crystalline silicon gyroscope fabricated using the extended SBM process," in the Proceeding of *17th IEEE International Conference on Micro Electro Mechanical Systems (MEMS)*, Maastricht, The Netherlands, 2004, pp. 556-559.

[36] S. Lee, S. Park, J. Kim, S. Lee, and D.-I. Cho, "Surface/bulk micromachined single-crystalline-silicon micro-gyroscope," *Journal of Microelectromechanical Systems,* vol. 9, pp. 557-567, 2000.

[37] T. D. Hudson, S. W. Hol, P. Ruffin, M. Kranz, J. McKee, M. Whitley, M. Buncick, and E. Tuck, "High-performance microfabricated angular rate sensor," *Journal of Micro/Nanolithography, MEMS, and MOEMS,* pp. 043006-1-8, 2005.

[38] X. S. Liu, Z. C. Yang, X. Z. Chi, J. Cui, H. T. Ding, Z. Y. Quo, B. Lv, and G. Z. Yan, "An x-axis micromachined gyroscope with doubly decoupled oscillation modes," in the Proceeding of *IEEE 21st International Conference on Micro Electro Mechanical Systems(2008)*, Tucson, Arizona, USA, 2008, pp. 860-863.

[39] H. Johari and F. Ayazi, "High-frequency capacitive disk gyroscopes in (100) and (111) silicon," in the Proceeding of *Micro Electro Mechanical Systems, 2007. MEMS. IEEE 20th International Conference on*, 2007, pp. 47-50.

[40] A. R. Schofield, A. A. Trusov, C. Acar, and A. M. Shkel, "Anti-Phase Driven Rate Gyroscope with Multi-Degree of Freedom Sense Mode," in the Proceeding of *International Solid-State Sensors, Actuators and Microsystems Conference (TRANSDUCERS)*, Lyon, France, 2007, pp. 1199-1202.

[41] ADXRS150/300 (Analog Device, Inc.)

[42] M. S. Weinberg and A. Kourepenis, "Error sources in in-plane silicon tuning-fork MEMS gyroscopes," *Microelectromechanical Systems, Journal of,* vol. 15, pp. 479-491, 2006.

[43] J.-H. Weng, W.-H. Chieng, and J.-M. Lai, "Structural design and analysis of micromachined ring-type vibrating sensor of both yaw rate and linear acceleration," *Sensors and Actuators A: Physical,* vol. 117, pp. 230-240, 2005.

[44] M. Esmaeili, M. Durali, and N. Jalili, "Ring Microgyroscope Modeling and Performance Evaluation " *Journal of Vibration and Control,* vol. 12, pp. 537-553 2006.

[45] R. D. Blevins, *Formulas for Natural Frequency and Mode Shape* Krieger Pub Co 1995.

[46] S. Timoshenko, D. H. Young, and W. J. Weaver, *Vibration Problems in Engineering* 4th ed.: Jon Wiley & Sons, 1974.

[47] R. A. Becker, *Introduction to Theoretical Mechanics*: McGraw-Hill Book Company, Inc., 1954.

[48] G. B. Thomas, *Calculus and Analytic Geometry*. Menlo Park, California: Addison Wesley, 1972.

[49] W. C. Young and R. G. Budynas, *Roark's Formulas for Stress and Strain* 7th ed.: McGraw-Hill 2002.

[50] T. Namazu and S. Inoue, "Characterization of single crystal silicon and electroplated nickel films by uniaxial tensile test with in situ X-ray diffraction measurement," *Fatigue & Fracture of Engineering Materials & Structures,* vol. 30, pp. 13-20, 2006.

CHAPTER 3

VIBRATION ISOLATION for MEMS

In Chapter 1, we surveyed vibration isolation methods for MEMS and divided them into two categories: (1) device-level suppression using vibration-insensitive device structures and (2) system-level suppression using vibration isolators. In Chapter 2, we analyzed vibration effects on MEMS gyroscopes and investigated the effectiveness of device-level vibration suppression. We demonstrated that even MEMS devices designed to be relatively immune to vibration, such as tuning fork gyroscopes, cannot eliminate all vibration effects due to capacitive nonlinearity in the drive and sense electrodes. Therefore, we are further motivated to explore system-level vibration reduction using added vibration isolators.

This chapter discusses the design and integration of vibration isolators for MEMS devices. We open in Section 3.1 by explaining how a vibration isolator functions as a low-pass-filter (LPF). Section 3.2 further explains how the LPF reduces vibration effects and introduces important design parameters for the LPF. Section 3.3 introduces a model of the LPF integrated with a MEMS device, provides methods to minimize possible side-effects, and presents a quantitative analysis of the vibration reduction for two example gyroscope designs. Section 3.4 further explains the integration of the LPF and Section 3.5 summarizes our findings.

3.1. Benefits of Mechanical Low Pass Filter

Figure 3.1 shows a schematic of a LPF integrated with a MEMS device. A LPF is inserted between the device and the external environment, and it attenuates the amplitude of the vibrations with frequencies substantially greater than the cut-off frequency. We focus on a passive low-pass filter as our isolation method due to the major advantages it possesses over other vibration-isolation methods; refer to Chapter 1.

First, a LPF can be easily fabricated using simple microstructures. A typical LPF microstructure consists of a proof mass, a damper, and a spring as shown in Figure 3.1.

Second, the LPF is effective in suppressing vibrations whose frequencies are higher than the cut-off frequency (f_L) of the LPF, and we can easily optimize the performance of the LPF by adjusting the properties of the mass, damper, or spring. A design process is provided in Section 3.2. If the level of vibration-attenuation is not sufficient, we can employ multiple vibration-isolator platforms, as illustrated in Figure 3.2. The multiple platforms form a multi-order low pass filter and further attenuate vibration. Generalizing, the N-platform filter shown in Figure 3.2b forms a 2*Nth order filter while the single vibration-isolation platform, shown in Figure 3.1, is a second order filter.

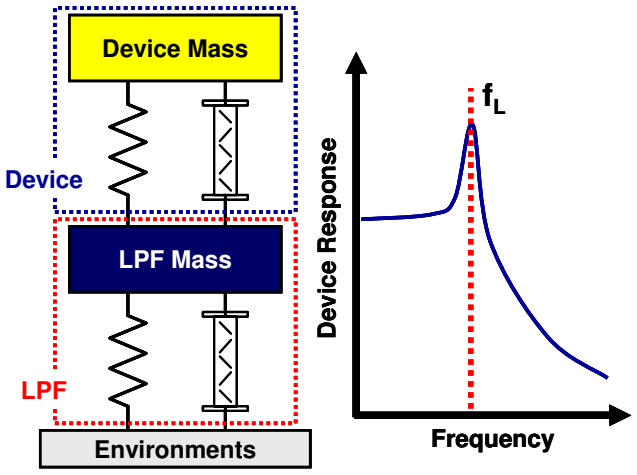

Figure 3.1. Schematic of a LPF integrated with a device and the frequency response of the LPF.

Third, a vibration-isolator remains superior to a vibration absorber. The natural frequency of an absorber is matched to the excitation frequency from a harmonic source. Thus, an absorber can only be used effectively when the environmental excitation is well characterized by a major/known harmonic excitation. This places severe limits on when an absorber can be used. Also, outside of the absorber's resonant frequency, the absorber may even amplify vibration.

Finally an active vibration isolator requires a sensor, a feedback system, and a micromachined actuator. These additional components increase the cost, power consumption, and size of the device, and may generate additional design difficulties. In addition, it is difficult to fabricate a micromachined actuator that can produce large forces and over a sufficiently large bandwidth. For instance, electrostatic actuation cannot generate large forces, piezoelectric actuation requires additional fabrication steps

and magnetic actuation requires a permanent magnet or coil magnet which complicates processing and increases cost. Thermal actuation is obviously too slow to accommodate for vibration attenuation.

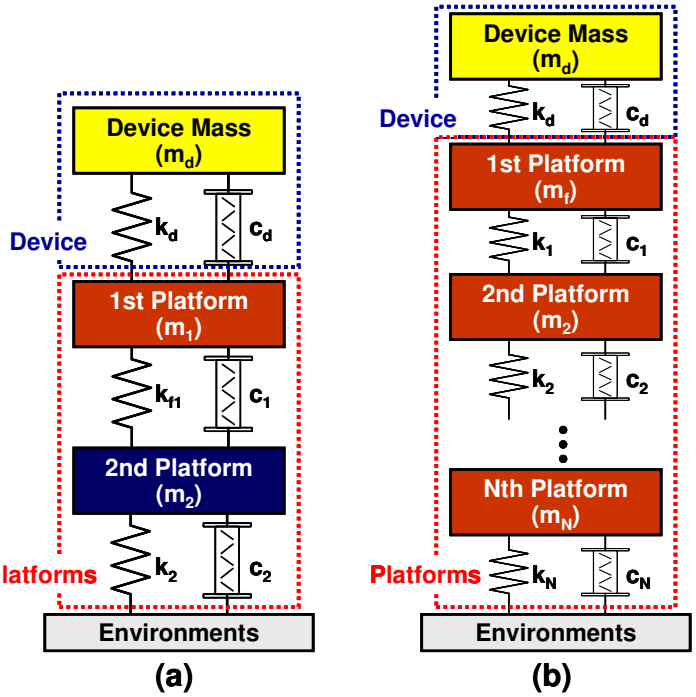

Figure 3.2. Multiple vibration-isolation platforms. (a) Two platforms and (b) N platforms.

3.2. Operation and Design of Low Pass Filter

We elect to demonstrate the effectiveness of the LPF's on MEMS gyroscopes. Gyroscopes are selected because (1) they are sensitive to environmental vibration, and (2) because the LPF method should be an effective counter measure, as explained in Chapter 2. Gyroscopes are known to be very susceptible to vibration due to their high quality factor (Q-factor), which amplifies vibrations at/near the device resonant frequency and increases output signal distortions. Note that the gyro's resonant frequency, which is in a range of 8 kHz to 30 kHz remains substantially larger than the excitation frequencies in most environments; refer to Section 1.2. Therefore, the LPF has significant potential for this application.

The operation of the LPF integrated with a MEMS gyroscope is conceptually shown in Figure 3.3. The LPF attenuates the amplitude of vibrations having frequencies larger than the bandwidth (f_L) of the LPF, and this provides vibration

isolation, provided that f_L is substantially smaller than the gyroscope's resonant frequency (f_0). In essence, the LPF attenuates the frequency response of the gyroscope as shown in the figure.

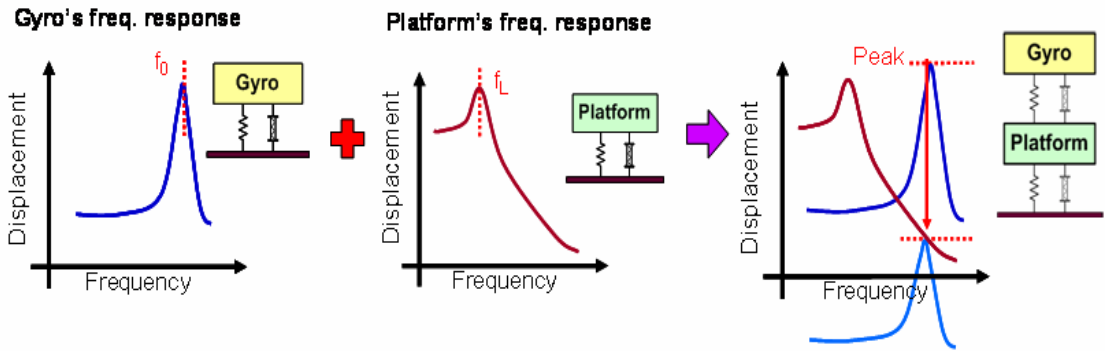

Figure 3.3. Operation of a mechanical low pass filter integrated with a MEMS gyroscope.

The design process for a mechanical low pass filter (LPF) is well known. Details of generic designs are explained in textbooks [1] and several papers already discuss the design process for MEMS-based vibration isolators [2]. Therefore, this chapter briefly review important design parameters to design a LPF-based vibration isolator (or vibration-isolation platform) for MEMS, especially for MEMS gyroscopes, and discusses possible side-effects in Section 3.3.

The first parameter is the resonant frequency (or cut-off frequency) of the LPF. The second parameter is the number of vibration-isolation platforms. As explained in Section 3.1, multiple isolation platforms form a high-order LPF and further reduce vibration amplitude. The third parameter is the damping of the platform. Most mechanical structures are second order filters, so they will have 40dB/dec slope ideally. Finally, the fourth parameter is the difference between the device resonance frequency and the vibration-isolation platform's cut-off frequency. In most cases, this frequency difference or is not crucial but it becomes important for resonating devices such as gyroscopes, resonators, or resonating sensors because small frequency separations were observed to decrease the Q of the devices [3]. The decreased Q derives from the increased energy loss by the vibration-isolation platform.

3.3. Modeling and Design Guidance

Figure 3.4 depicts the model of multiple platforms and the forces acting on each platform and the device. The forces are expressed as functions of the stretch of the device spring (X_d), the stretch of the ith platform spring (i=1,2,…N), and the vibration-induced displacement of the base (X_v). From the figure, we can derive the equations of motion for each platform as follows

$$\text{Device: } m_d\left(X_d'' + X_1'' + X_2'' + \cdots + X_N'' + X_V''\right) = -k_d X_d - c_d X_d' \tag{3.1}$$

$$\text{1st platform: } m_1\left(X_1'' + X_2'' + \cdots + X_N'' + X_V''\right) = \left(k_d X_d + c_d X_d'\right) - \left(k_1 X_1 + c_1 X_1'\right) \tag{3.2}$$

$$\text{2nd platform: } m_2\left(X_2'' + \cdots + X_N'' + X_V''\right) = \left(k_1 X_1 + c_1 X_1'\right) - \left(k_2 X_2 + c_2 X_2'\right) \tag{3.3}$$

$$\vdots$$

$$\text{Nth platform: } m_N\left(X_N'' + X_V''\right) = \left(k_{N-1} X_{N-1} + c_{N-1} X_{N-1}'\right) - \left(k_N X_N + c_N X_N'\right) \tag{3.4}$$

If N=1, these equations reduce to equations (3.1) and (3.2).

A primary characteristic of the vibration-isolation platform is the transmission ratio (TR). The TR is defined as the ratio of the stretch of device spring (X_d) and the vibration-induced displacement of the base (X_v), i.e. X_d/X_v. The TR determines how much vibration is transmitted to the device through the vibration-isolation platform and thus it measures the degree of vibration isolation. Because MEMS gyroscopes are susceptible to vibrations having frequencies are at or near the resonant frequency of the gyroscopes, we will use the TR at the gyroscope's resonance as our criterion.

The integration of the vibration-isolation platform may also results in adverse side-effects. One of them is the reduction of the device's resonant frequency. Figure 3.5 illustrates the frequency spectrum of one sample gyroscope integrated with one or two vibration-isolation platforms. The figure clearly shows that the integration of the platforms reduces the resonance frequency of the gyroscope and this change may be critical for gyroscope performance. However, it should be noted that the reduction does not depend on the number of platforms.

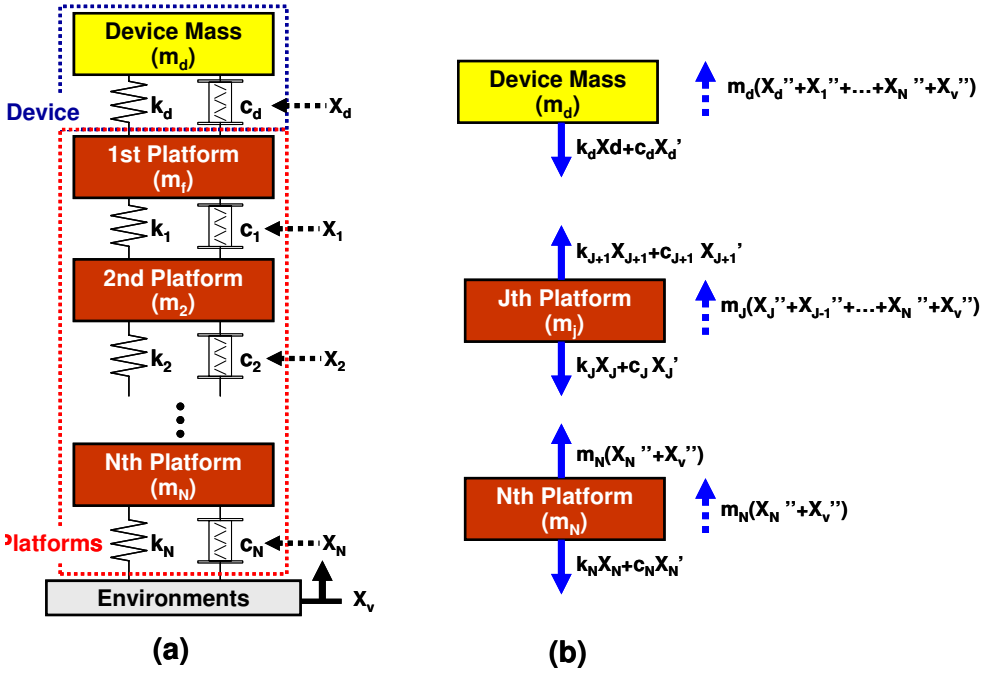

Figure 3.4. Modeling of multiple vibration-isolation platforms. (a) Conceptual view of the multiple platforms, (b) forces involved with the device mass and each platform (J=1,2,…, N-1).

This reduction of gyro's resonant frequency can be understood and also minimized using the following method. Suppose $w_{d,original}$ and $w_{1,original}$ denote the resonant frequency of the device and the 1st vibration-isolation platform before integration.

$$w_{d,original}^2 = \frac{k_d}{m_d}, w_{1,original}^2 = \frac{k_1}{m_1} \tag{3.5}$$

After integration, the resonant frequency of the device becomes:

$$w_{d,new}^2, w_{1,new}^2 = \frac{1}{2}\cdot\left[\frac{k_d}{m_d}+\frac{k_1}{m_1}+\frac{k_d}{m_1} \pm \sqrt{\left(\frac{k_d}{m_d}+\frac{k_1}{m_1}+\frac{k_d}{m_1}\right)^2 - 4\cdot\frac{k_d}{m_d}\cdot\frac{k_1}{m_1}}\right] \tag{3.6}$$
$$= \frac{1}{2}\cdot\left[S \pm \sqrt{(S)^2 - 4\cdot w_{d,old}^2\cdot w_{1,old}^2}\right]$$

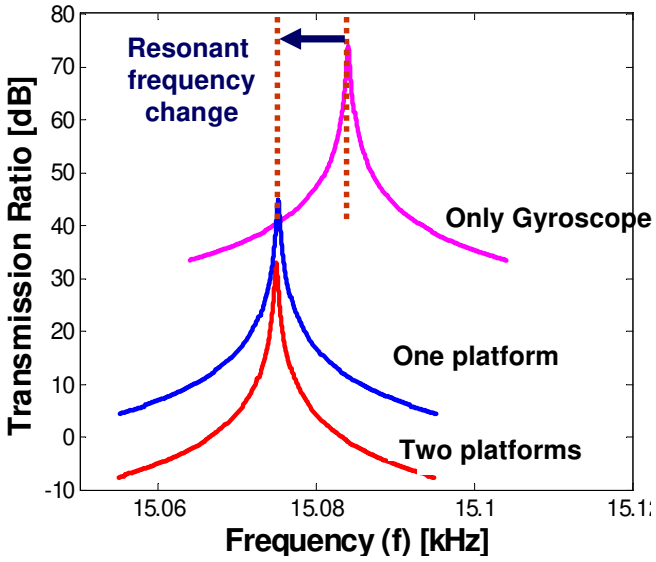

Figure 3.5. Reduction of resonance frequency of the gyroscope due to the integration of vibration-isolation platforms.

where S is defined to be:

$$S = \frac{k_d}{m_d} + \frac{k_1}{m_1} + \frac{k_d}{m_1} = w_{d,original}^2 + w_{1,original}^2 + \frac{k_d}{m_1} \tag{3.7}$$

If,

$$\frac{k_d}{m_d}, \frac{k_1}{m_1} = w_{d,original}^2, w_{1,original}^2 \gg \frac{k_d}{m_1} \tag{3.8}$$

then equation (3.6) can be simplified to

$$w_{d,new}^2, w_{1,new}^2 \cong \frac{1}{2} \cdot \left[\frac{k_d}{m_d} + \frac{k_1}{m_1} \pm \sqrt{\left(\frac{k_d}{m_d} - \frac{k_1}{m_1} \right)^2} \right] = \frac{k_d}{m_d}, \frac{k_1}{m_1} = w_{d,original}^2, w_{1,original}^2 \tag{3.9}$$

and no change occurs to the device resonant frequency.

The way to satisfy equation (3.8) is to maximize the 1st platform's mass (m_1). This fact also explains why there is only a minor difference between the one-platform and two-platform cases in Figure 3.5 because the mass of the 1st platform is the same for the two cases.

Another side-effect of the integration is the reduced Q-factor. If the Q of the

integrated platform is not sufficiently high compared with that of the device, higher energy losses arise and the device Q-factor is accordingly reduced. This reduced Q may critically degrade the performance of MEMS gyroscopes and must be avoided.

To identify the critical parameter determining the Q reduction, several simulations were conducted. First, the damping coefficients of the gyroscope and the platform are calculated using

$$c_d = \frac{\sqrt{m_d k_d}}{Q_d}, c_1 = \frac{\sqrt{m_1 k_1}}{Q_1} \tag{3.10}$$

with fixed Q's of the gyro (Q_d) and the platform (Q_1). Using equations (3.1), (3.2), and (3.10), the transmission ratio is plotted as shown in Figure 3.6. The Q of the gyroscope ($Q_{d,after}$) after integration with the platform is then calculated from

$$Q_{d,after} = \frac{f_{0,new}}{\Delta f_{3dB}}, \quad \Delta f_{3dB} = f_1 - f_2 \tag{3.11}$$

Figure 3.7 demonstrates the relationship between the performance of MEMS gyroscopes (i.e., resonant frequency and quality factor) and the mass and Q of the first vibration-isolation platform. First, the gyro's resonance frequency does not change much once the mass of the first platform becomes sufficiently large. If the first platform has a mass 300 times that of the device mass, only a 2.5 Hz resonant frequency reduction is observed.

Second, the Q of the gyroscope increases by increasing either the first platform's Q (Q_1) or mass (m_1). When m_1 is small ($10*m_d$), a high-Q gyroscope (Q=40k) experienced a minor Q reduction (<1%) when integrated with a high Q platform (Q=2666), but a larger Q reduction (~22%) was observed when the gyro was integrated with a low Q platform (Q=100). However, in any situation, the increased mass of the first platform helps to accommodate the Q reduction, and a platform whose mass is >220 times larger than the device demonstrated a minor Q-reduction with both high-Q and low-Q platforms. Therefore, the most important design recommendation is to increase the mass of the first platform.

Table 3.1 and Table 3.2 summarize the performance of gyroscopes integrated with one or two vibration-isolation platforms. The two gyros in the tables have different resonant frequencies and Q's. In these simulations, we assumed that the gyro and the platforms are vacuum packaged in a single package, and thus, their damping

coefficients are identical. Therefore, the Q of platforms varies depending the resonant frequency and designs, which is different from the simulations in Figure 3.7 where Q as held fixed.

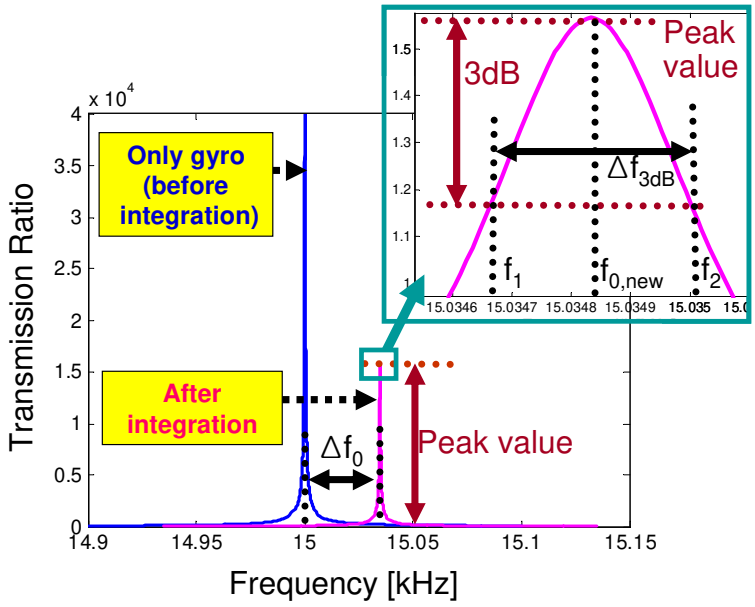

Figure 3.6. Q and Δf_0 calculation after integrating with a platform.

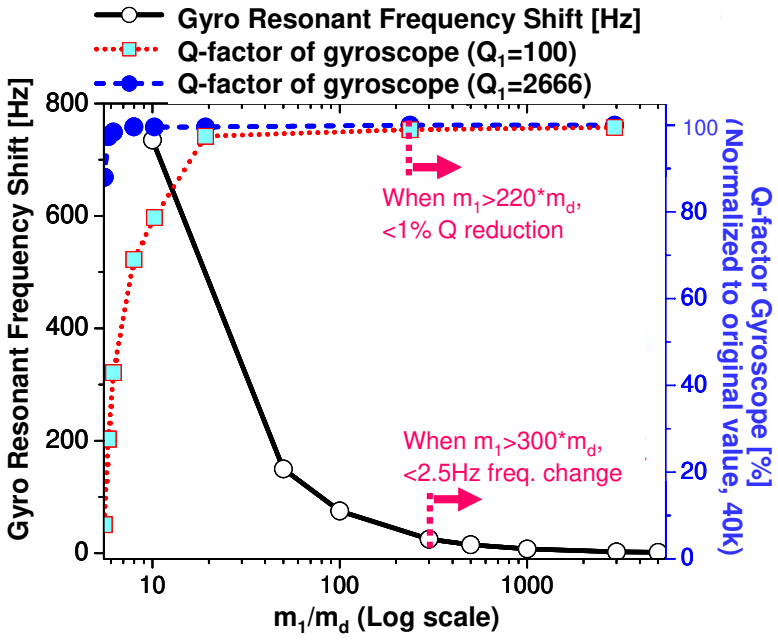

Figure 3.7. The resonant frequency and Q-factor of a gyroscope integrated with a vibration-isolation platform.

Table 3.1. Performance of a gyroscope [4] integrated with one or two vibration-isolation platforms. The gyroscope has a resonant frequency of 15 kHz and a Q of 40,000.

# of platform	Platform mass	Platform resonant freq	Freq. shifting	TR Peak value	TR Peak reduction	Q
	m_1	f_1 [Hz]	Δf_0 [Hz]		Compared to gyro only	
One	m_dx300	0.5k	2.5	44	99.9%	40k
		1k	2.5	177	99.6%	40k
		5k	4.5	4.95k	87.6%	40k
Two	1st: x30 2nd:x300	0.5k	248	0.042	99.9999%	39k
		1k	250	0.71	99.998%	39k
		5k	277	551	98.6%	37k
Two	1st: x10 2nd:x300	1k	735	0.58	99.998%	35k
		5k	812	427	98.9%	35k

The results of these tables reveal three major findings that are consistently observed in both gyroscopes. First, the two most important design parameters are the resonant frequency and the mass of the first platform. By decreasing the resonant frequency of the first platform, we decrease the transmission ratio. By increasing the mass, we can minimize the resonant frequency change and the Q reduction. For example, in Table 3.1, the one-platform design shows that the peak transmission ratio (TR) decreases from 12.4% to 0.1% (when normalized to the TR of the case without any platform) by adjusting the first platform's resonant frequency (f_1) from 5 kHz to 0.5 kHz. Because the TR represents how much vibration is transmitted to the device, as explained in Section 3.3, the decreased TR implies that vibration effects is also reduced by lowering the f_1. In the same table, the two-platform designs demonstrate that larger first-platform mass (m_d x 30) produces a smaller change in both the gyro's resonant frequency (Δf_0) and Q-factor than the smaller first-platform mass (m_d x 10), even though the first platform's resonant frequencies are identical.

Second, the integration of two (or multiple) platforms further reduces vibration effects, as expected. For example, in Table 3.1, the TR of the one-platform design is reduced from 0.4% to 0.002% by employing the second platform when f_1=1 kHz. The amount of the TR reduction is almost the same regardless of the masses of the first and

second platform.

Third, the characteristics of the second platform (or platforms other than the first platform) are not critical compared to those of the first platform because they are not strongly related with the reductions of the TR, Δf_0, and/or Q.

Therefore, the design of the first platform is crucial. All of the behaviors listed above are consistently observed in both Table 3.1 and Table 3.2, despite the resonant frequency and Q of the sample gyroscopes being different. Also, considering the discussions in Chapter 2, the vibration-isolation platforms are most efficient when aligned along the sense direction of gyroscopes.

Table 3.2. Performance of another gyroscope [5, 6] integrated with one or two vibration-isolation platform. The gyroscope has resonant frequency of 8.9 kHz and Q of 4.1k.

# of platform	Platform mass	Platform resonant freq	Freq. shifting	TR Peak value	TR Peak reduction	Q
	m_1	f_1 [Hz]	Δf_0 [Hz]		Compared to gyro only	
One	m_dx300	0.5k	15	13	99.69%	4.07k
		1k	15	52	98.73%	4.07k
		5k	21.6	1.9k	54.68%	4.07k
Two	1st: x30 2nd:x300	0.5k	148	0.037	99.999%	3.92k
		1k	149	0.60	99.985%	3.92k
		5k	214	737	82.03%	3.81k
Two	1st: x10 2nd:x300	0.5k	436	0.03	99.9993%	3.6k
		1k	439	0.48	99.988%	3.61k

3.4. Integration

An isolator designed according to the concepts above has been integrated with a wafer-level, environment-resistant package in Dr. Lee's dissertation as a vertical vibration-isolation platform [7-9]. An upgraded version of the vibration isolator is presented in Appendix A. The same package used in [7] is used, but our method allows us to integrate lateral vibration-isolation platforms or multiple vibration-isolation platforms.

3.5. Design of Gyroscopes and Vibration Isolators by Applications

Although vibration sensitivity is an important gyro parameter, as mentioned in Section 2.6, one might have to compromise vibration sensitivity to meet other specifications in some applications. Therefore, when designing gyroscope structures and vibration isolators, one must consider the application and its requirements. The application then dictates two different sets of design specifications: (1) gyroscope performance and (2) environmental condition. A gyroscope used for an automotive application is used as an example to illustrate the design process.

Based on their performance specifications, gyroscopes can be classified into three classes: rate-grade, tactical-grade, and inertial-grade [10]. For automotive applications, rate-grade gyroscopes are widely employed and require a resolution of ~0.1 deg/sec.

The dominant vibration frequencies in automotive applications (<2 kHz) are much lower than the resonant frequencies of MEMS gyroscopes (Table 1.2), and therefore, do not produce critical vibration-induced errors, as discussed in Chapter 2. However, impact-induced vibration can generate errors. Figure 2.5 shows that a DS-type tuning fork gyroscope generates an error of ~14 deg/sec induced by an 100g impact shock [11]. This impact amplitude falls in the range that automotive sensors can experience (<1000g), as shown in Table 1.1.

The gyroscope described above cannot satisfy the requirements of rate-grade gyroscopes because of large vibration sensitivity. This problem can be solved either by changing the gyro structure, such as DD-type tuning fork or ring gyroscopes, or by integrating vibration-isolation platforms. Especially when the gyro structure cannot be modified because of other specification requirements, it is possible to satisfy rate-grade requirements by adding one isolation platform (f_L=1 kHz, m_l=300*m_d).

3.6. Summary

This chapter reviewed the rationale for using a low-pass mechanical filter method, the design process to optimize this filter, and (3) the design trade-offs and side effects caused by its integration with MEMS gyros. Two example gyroscopes are selected and they both exhibit substantial vibration isolation using the designed LPF's.

Simulation results show that vibration reduction is increased by >99.98% using a single vibration-isolation platform. The results also demonstrate that the most critical design parameter is the mass and the resonant frequency of the first vibration-isolation platform. The designed platform was integrated into a generic environmental isolation package in a follow-up study.

References

[1] D. J. Inman, *Engineering Vibration*, 2 ed.: Prentice Hall, 2000.

[2] T. Braman and O. Grossman, "Designing Vibration and Shock Isolation Systems for Micro Electrical Machined Based Inertial Measurement Units," in the Proceeding of *IEEE/ION Position, Location, And Navigation Symposium (PLANS)*, 2006, pp. 400-404.

[3] J. R. Reid, V. M. Bright, and J. A. Kosinski, "A micromachined vibration isolation system for reducing the vibration sensitivity of surface transverse wave resonators," *Ultrasonics, Ferroelectrics and Frequency Control, IEEE Transactions on,* vol. 45, pp. 528-534, 1998.

[4] M. F. Zaman, A. Sharma, and F. Ayazi, "High Performance Matched-Mode Tuning Fork Gyroscope," in the Proceeding of *IEEE International Conference on Micro Electro Mechanical Systems*, Istanbul, Turkey 2006, pp. 66-69.

[5] I. Song and B. Lee, "MEMS-based angular rate sensors," in the Proceeding of *IEEE Sensors*, Vienna, Austria, 2004, pp. 650-653 vol.2.

[6] S. An, Y. S. Oh, K. Y. Park, S. S. Lee, and C. M. Song, "Dual-axis microgyroscope with closed-loop detection," *Sensors and Actuators A: Physical,* vol. 73, pp. 1-6, 1999.

[7] S. H. Lee, S. W. Lee, and K. Najafi, "A Generic Environment-Resistant Packaging Technology for MEMS," in the Proceeding of *International Solid-State Sensors, Actuators and Microsystems Conference (TRANSDUCERS)*, Lyon, France, 2007, pp. 335-338.

[8] S.-H. Lee, J. Cho, S. W. Lee, M. F. Zaman, F. Ayazi, and K. Najafi, "A Low-power oven-controlled vacuum package technologies for high-performance MEMS " in the Proceeding of *IEEE International Conference on Micro Electro Mechanical Systems*, Sorrento, Italy, 2009.

[9] S.-H. Lee, "Wafer-level packaging for environment resistant microinstruments," Ph.D. Thesis, EECS, University of Michigan, 2009

[10] N. Yazdi, F. Ayazi, and K. Najafi, "Micromachined inertial sensors," *Proceedings of the IEEE,* vol. 86, pp. 1640-1659, 1998.

[11] ADXRS150/300 (Analog Device, Inc.)

CHAPTER 4

NEW SHOCK PROTECTION CONCEPTS: THEORY and DESIGN

Current shock protection concepts for MEMS, as described in Chapter 1, can be divided into two categories: 1) those that minimize stress by optimizing device dimensions, and 2) those that minimize stress through motion-limiting hard shock stops. While both methods can be effective, they also possess major shortcomings. The dimension optimization method cannot decouple device design from shock protection design, and consequently, may compromise device performance. The hard shock stop method leads to secondary shock (i.e., subsequent impact on hard shock stops) that may cause fracture, debris, performance changes, or unwanted oscillation of a device. Therefore, a need remains for superior shock protection methods. This need is critical for high performance devices, which often employ delicate device structures, in vacuum packaging, where we have limited material selection and larger dynamic response, and in harsh environment applications, where we expect higher shock amplitude.

Herein we propose two novel shock protection concepts: (1) nonlinear spring shock stops, and (2) soft coating shock stops. Both concepts are simple and both address problems that can arise from conventional shock-protection methods. In addition, they can be easily integrated with many MEMS devices without major design changes, additional fabrication processes, or extensive increase of device area. They can be implemented in wafer-level and batch fabrication processes, and are compatible with conventional microfabrication techniques.

In this chapter, we discuss the design, simulated performance, and possible applications of these concepts. Section 4.1 summarizes the principles underlying the concepts. Section 4.2 presents the key design parameters for nonlinear spring shock stops and Section 4.4 presents those for soft coating shock stops. Performance trade-offs associated with each parameter are also described. Sections 4.3 and 4.5 present simulation results and demonstrate the impact-force reduction afforded by both concepts. Section 4.6 summarizes our findings, and Section 4.7 discusses possible

applications of our technologies. Section 4.8 closes this chapter by summarizing results and conclusions.

4.1. Underlying Principles

Both design concepts limit the displacement of the device mass as the means to reduce potentially large stresses under shock loading. In addition, they also seek to minimize the impact force (F_{IM}) delivered to the device while it contacts a stop, a force that can becomes excessive for conventional hard shock stops.

The impact force (F_{IM}) can be minimized in two ways: (1) by decreasing the impulse (δ) generated during contact, or (2) by increasing the contact time (Δt). These potential solutions follow from the relation $F_{IM} \propto \delta/\Delta t$. One way to increase the contact time is to increase the compliance of the "stop". One way to decrease the impulse is to maximize the energy dissipation during impact.

The first method utilizes a nonlinear spring formed either by a single microbeam or by a cascade of closely spaced microbeams (Figure 4.1b). The compliance of these beam structures increases the contact time between the device and the stops, and thus reduces the impact force. In addition, the nonlinear hardening stiffness afforded by these structures leads to rapid (nonlinear) increases in the restoring force and decreased travel of the device mass. However, the impact-force reduction by this method is minor because only a small amount of energy is lost through the contact between the device mass and the shock-stop beams.

The second method utilizes a soft thin-film layer on an otherwise hard surface, and utilizes both surface compliance and energy dissipation (Figure 4.1c). The increased compliance extends the contact time, the increased dissipation (i.e. smaller coefficient of restitution) reduces the impulse and thus both effects reduce the impact force. Moreover, the soft coating dissipates energy during impact, and thus serves to reduce both the number of impacts and the settling time following a shock event. This energy absorption at the impact site becomes more attractive particularly in the case of vacuum-packaged MEMS which have virtually no/little air damping. However, simulations reveal that this method is not nearly as effective as the nonlinear spring shock stops in reducing the impact force.

Figure 4.1 shows three different shock stop concepts: (1) a conventional hard shock stop (silicon), (2) a nonlinear-spring shock stop, and (3) a soft thin-film coating

shock stop. Each design seeks to protect the MEMS structure represented here by a device mass supported by a cantilever.

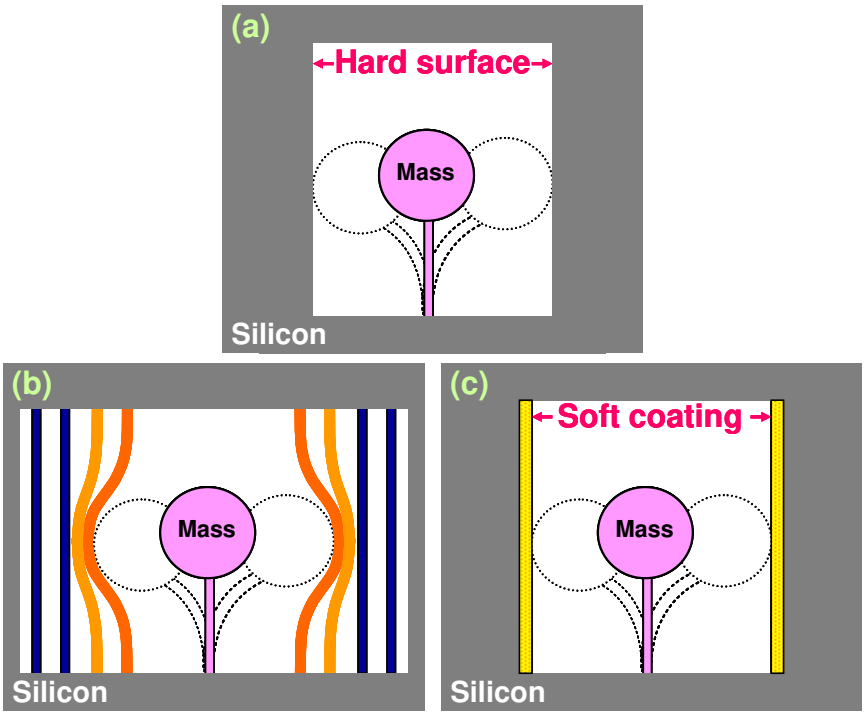

Figure 4.1. Three different shock stops: (a) conventional hard, (b) nonlinear spring, (c) soft thin-film coating.

Figure 4.2 provides a preview of our analysis of these methods which is detailed later in this chapter. This figure depicts the simulated time record of the displacement of a device mass following a large shock (1000 g amplitude) which causes the device mass to impact a shock stop. The three shock stops (hard, nonlinear, and soft coating) produce distinctly different device dynamics and, in particular, very different impact forces (as predicted by the maximum device acceleration during impact).

The overall characteristics of the three methods are reported in Table 4.1. As noted, both concepts are compatible with current microfabrication processes and provide wafer-level and batch fabrication processes. In addition, both permit the control of target shock amplitude by simple design adjustments. More specifically, the performance of the nonlinear spring stops can be adjusted by changing the geometric and material properties (number, separation, stiffness) of the shock stop springs. The characteristics of soft coating stops are determined by the coating material properties and thickness, and by the design of the bumpers (attached to a device mass) contacting the coated surface. These conclusions will be developed in this chapter.

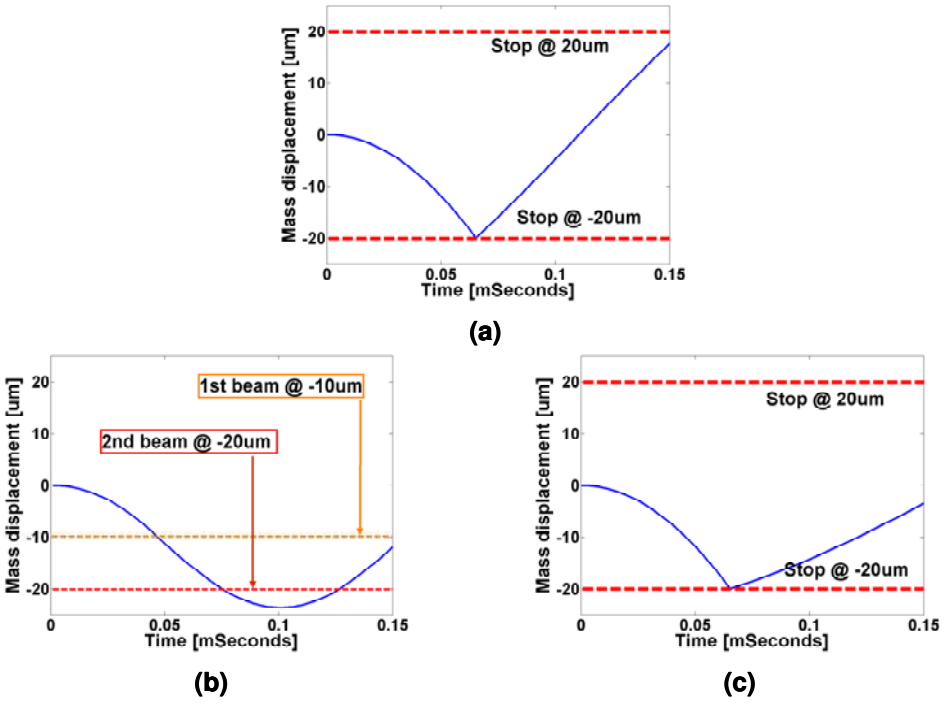

Figure 4.2. Simulated device mass displacement during first impact with (a) conventional hard (silicon) shock stop, (b) nonlinear spring shock stop, (c) soft thin-film coated shock stop.

Table 4.1. Characteristics of the three shock protection methods in Figure 4.1

Features	Hard	Nonlinear Spring	Soft Coating
Impact Force Reduction	Minor	High	
Compliance	Low	High	Moderate
Energy dissipation	Low	Low	High
Preferred direction	Lateral/Vertical	Lateral	Later/Vertical
Additional fabrication Process	No	No	Deposition and definition of soft materials
Increase of device area	No	Minor	No
Microfabrication compatibility	Yes	Yes	
Wafer-level and batch process	Yes	Yes	
Control of target shock amplitude	Provided via gap between device mass and stop	Provided via (1) geometric & (2) material properties of shock springs	Provided via (1) property & thickness of coating and (2) design of bumpers

While both nonlinear spring and soft coating shock stops reduce the impact force, the two differ in several important ways. Both stops utilize compliant stops to reduce the impact force, but the nonlinear spring stops introduce substantially greater compliance than the soft coating stops. The soft coating stops, however, dissipate considerably more energy and hence they further reduce the number of impacts. These two shock protection concepts also differ in the steps required for fabrication and in their preferred direction of protection. For in-plane shock protection, the nonlinear spring stops can be simultaneously fabricated with the MEMS device in a single fabrication steps. Soft coating stops, however, need additional fabrication steps for the deposition of soft materials. For out-of-plane shock protection, the nonlinear spring stops are not convenient because it is difficult to fabricate released micro-springs under a device. By contrast, the soft coating stops can be readily fabricated in both lateral and vertical directions. Moreover, we do not need to expand the area of the device for either concept except perhaps a minor area increase when adding nonlinear springs.

4.2. Design and Analysis I - Nonlinear Spring Shock Stops

4.2.1. Design of Nonlinear Spring Shock Stop

The performance of nonlinear spring shock stops is mainly determined by the design of the beam structure used as shock stops. The addition of one or more beams creates a compliant shock stop that can greatly reduce the impact force when struck by the device mass. The possible penalty paid by the increased travel of the device mass can also be minimized by designing a nonlinear "hardening" spring with rapidly increasing stiffness. This hardening nonlinearity can be introduced through a single beam, either a double-clamped bridge beam or a single-clamped cantilever beam. The nonlinearity of the bridge beam manifests itself in stretching the centerline of the beam, whereas that of cantilever beam stems from the bending of the beam [1]. Alternatively, a hardening nonlinearity can be introduced through a cascade of closely spaced beams wherein the nonlinearity arises from the stepwise increase in stiffness as additional beams are engaged. In either example, the nonlinear growth of the restoring force is an advantage in rapidly but smoothly decelerating the device mass. Figure 4.3 shows, a schematic of these designs with including a cascade of beams (left) and single nonlinear beam (right).

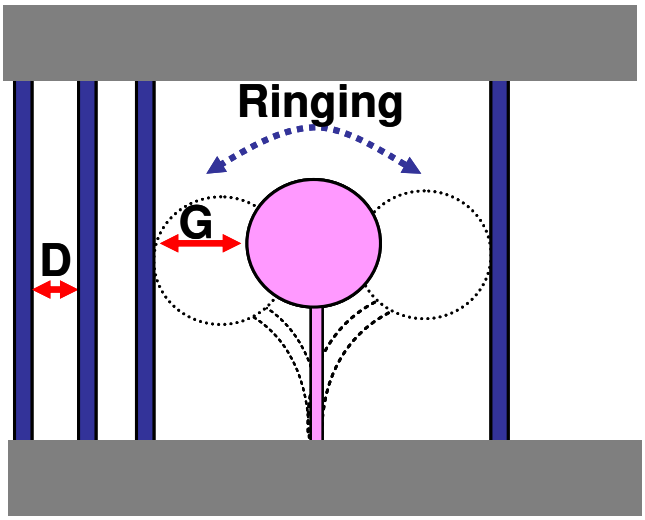

Figure 4.3. Schematic of nonlinear spring shock stop designs. Beam cascade (left) and single nonlinear beam (right).

The design of the beam structures in a nonlinear spring stop requires simultaneous satisfaction of two principal criteria:

- Criterion #1: The maximum stress developed in the device and its stop beams must remain less than that defining failure.
- Criterion #2: The compliance must be maximized to reduce the impact force.

Therefore, the design of the shock stop beam structure should be optimized so that the structure's compliance is maximized (minimize the impact force), while the stresses developed in the device and the shock stop beam structure remain smaller than the fracture stress. The compliance of the shock-stop beam can be easily adjusted by layout-level design changes (i.e., by changing the width or the length of shock stop beams).

We evaluate below three nonlinear spring designs, namely (1) a cascade of beams, (2) a single nonlinear bridge beam, and (3) a single nonlinear cantilever beam. By way of example, we will consider a device that utilizes a cantilevered beam. First, we derive the stiffness of each shock spring design. This stiffness is used to calculate the restoring force from the shock spring structure as a function of the spring stiffness and displacement of the device mass. The calculated restoring force is further used to evaluate whether the shock springs satisfy the two criteria above.

4.2.2. Definitions of Parameters

The parameters used in Sections 4.2 and 4.3 are listed below.

1. Parameters defining the device structure
   - k_d, c_d, m_d : Stiffness, damping coefficient, and mass of the device
   - x_d: Displacement of the device mass
   - σ_{max}: Maximum allowable stress, which is the fracture stress in brittle materials or the yield stress if one considers a ductile material.
   - $d_{allowable}$: Maximum allowable deflection of the device before it fractures (based on σ_{max})
   - d_{amp}: Maximum amplitude of the device mass following shock loading (i.e. the deflection where the velocity of the mass vanishes)

2. Parameters defining shock the shock spring structure
   - w, L, and t: Width, length, and thickness of a shock spring beam
   - F_r: Restoring force from shock beam structure
   - G, D, k_S: Initial gap, spacing, and stiffness of the beams in beam cascade structures
   - N: Number of the shock stop beams engaged by the device mass in a beam cascade structure
   - L_0: Original length of a cantilever shock spring
   - k_L and k_{NL}: Linear and nonlinear stiffness of a single shock beam structure. In our examples, k_L and k_S are identical.

3. Parameters defining the shock environment
   - A_{shock}: Pulse-like acceleration delivered to the device from a shock event

4.2.3. Stiffness and Restoring Force of Shock Spring Structures

4.2.3.1. Stiffness and Restoring Force of Beam Cascade Structures

Consider the piecewise linear system composed of a cascade of closely spaced single beams, as shown in Figure 4.4a. As the figure shows, the springs can be designed with different structures (cantilever or bridge). We assume that the gap

between adjacent beams remains small (one beam thickness or less) and that the stiffness of the beam assembly increases as each beam is deflected in succession (refer to Figure 4.4b). Each beam is considered to be linear, but as more beams are recruited, the total stiffness is the sum of the stiffnesses of the individual beams. If all beams have the same stiffness, the total final stiffness is simply the number of beams recruited times the stiffness of each beam, resulting in piecewise linear behavior.

Following the initial shock input, these springs rapidly but smoothly decelerate the device mass, leading to dramatic reduction in the subsequent impact force compared to a conventional hard shock stop. The effectiveness of this concept is partially offset by the additional deflection of the device mass, but this deflection can be readily adjusted by changing the separation (D) and stiffness (k_S) of the beam assembly, and the number of shock beams recruited during an impact (N).

Figure 4.4 shows that the device mass is located a distance of G from the first shock beam and each shock beam is separated by D. Let the N denote the total number of beams recruited. As shown in Figure 4.4b, the spring constant of the cascaded beams structure increases with the number of beams being recruited. Let x_d denote the displacement of the device mass from its equilibrium position. The restoring force from the cascaded beams $F_r(x_d)$ is the linear superposition of the restoring forces from each shock beam, as shown in Figure 4.5.

When $x_d < G$, no shock beams are contacted by the device mass and the restoring force is zero ($F_r=0$).

When $G+(N-1)\cdot D < x_d < G+N\cdot D$, the first N shock beams are recruited. The restoring force from each beam is given by

$$\text{(1) 1st beam: } F_{r,1st} = k_s\left[x_d - G\right] \tag{4.1}$$

$$\text{(2) 2nd beam: } F_{r,2nd} = k_s\left[x_d - G - D\right] \tag{4.2}$$

$$\vdots$$

$$\text{(N) Nth beam: } F_{r,Nth} = k_s\left[x_d - G - (N-1)D\right] \tag{4.3}$$

Therefore, the total restoring force from the cascades structure is given by

$$F_r = \sum_{i=1}^{N} k_s \left[x_d - G - (i-1)D \right] = k_s \left[(x_d - G)N - D\frac{N(N-1)}{2} \right] \tag{4.4}$$

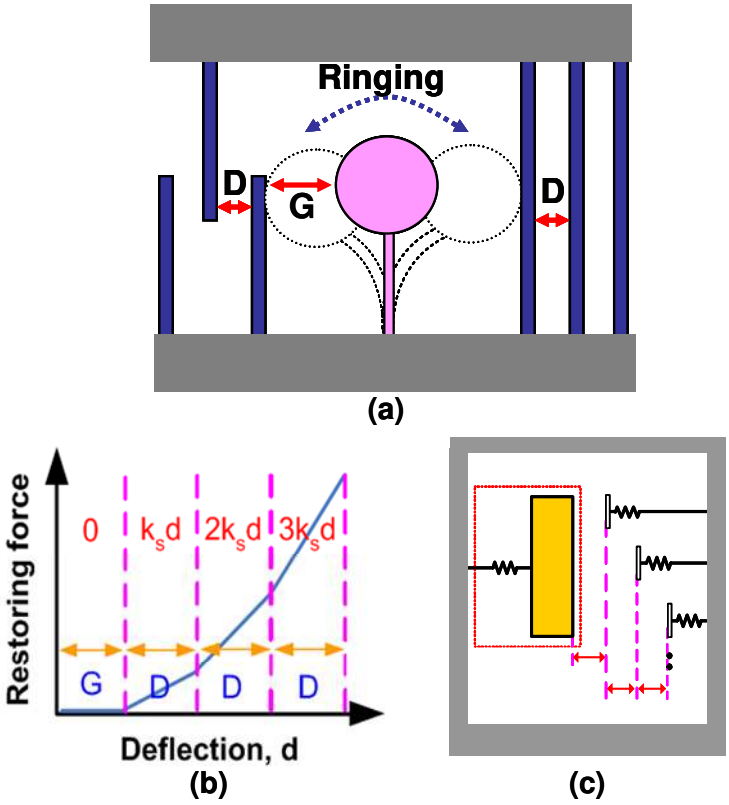

Figure 4.4. Piecewise linear system formed by a cascade of beams. (a) Structure showing three beams separated by a gap of D. Cantilever (left, smaller k_S) and bridge structure (right, larger k_S); (b) restoring force as a function of deflection; (c) simple model of a device and the beam cascade.

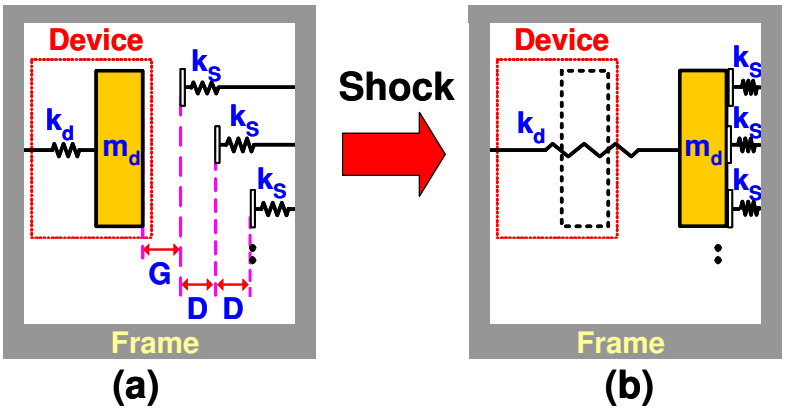

Figure 4.5. Piecewise linear system before (left) and after (right) compression of entire beam cascade.

4.2.3.2. Stiffness of a Single Beam with Nonlinear Hardening Effects

We consider next a nonlinear model for the deflection of a single beam (Figure 4.6).

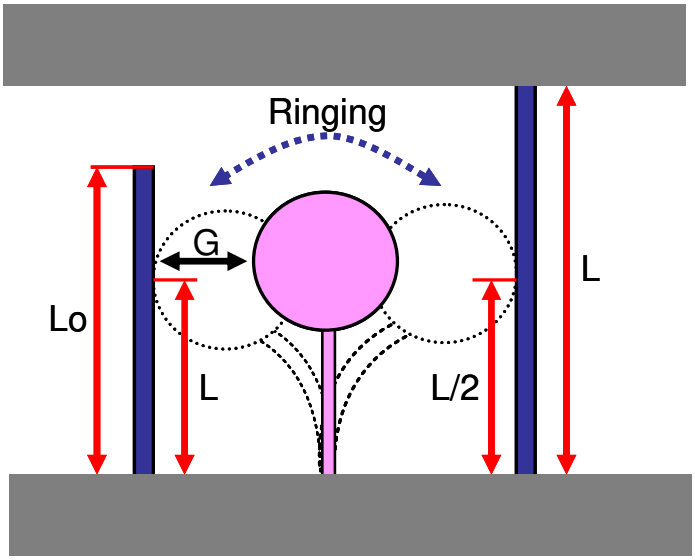

Figure 4.6. Schematic of two nonlinear single beam designs. Single clamped cantilever (left) and double clamped bridge beam (right). Note that in the cantilever case, the length of a beam L is defined as the position where the mass contacts the shock stop, where the overall length of the beam L_0 is larger than L.

As this beam deflects, the centerline must necessarily bend (cantilever and bridge) and stretch (bridge) and both effects manifest themselves as cubic hardening nonlinearities [1]. The restoring force vs. deflection relation is given by equation (4.5) and illustrated in Figure 4.7.

$$F_r = F_L + F_{NL} = k_L d + k_{NL} d^3 \tag{4.5}$$

Here, F_L and k_L denote the linear force and stiffness component, and F_{NL} and k_{NL} denote the nonlinear force and stiffness component. (Equations for each are presented later in this section.) Note that the length L of the cantilever is not the overall beam length L_0 but rather the position where the mass contacts the shock stop, as shown in Figure 4.6.

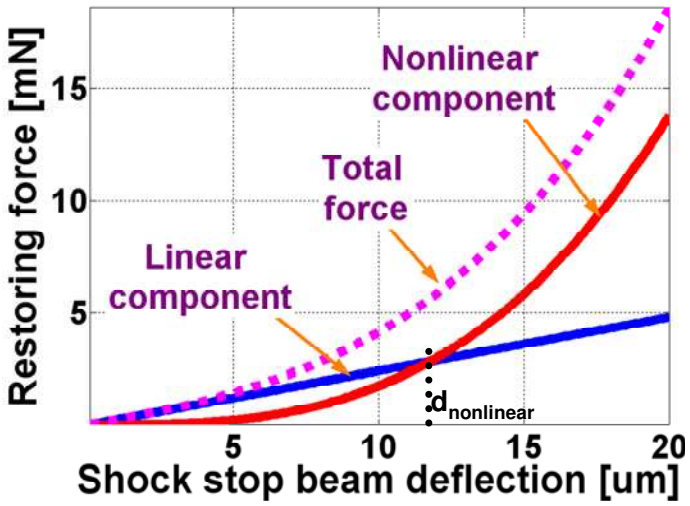

Figure 4.7. Restoring force as a function of deflection in a single beam with nonlinear hardening effects.

Linear and Nonlinear Stiffness of a Cantilever Beam

The nonlinear effect of a single nonlinear cantilever comes mainly from the bending of the beam as given by the differential equation of beam equilibrium (4.6) [1]. Figure 4.8 illustrates the cantilever beam under a force (F_0) applied to its tip.

$$-EI\frac{d^2}{dx^2}\left[v''-\frac{3}{2}(v')^2 v''\right]+F_0\cdot\delta(x-L)=0 \tag{4.6}$$

Here, v(x) is the beam displacement as a function of the spatial coordinate x along the beam centerline. The boundary conditions defining the cantilever are v(0)=0, v'(0)=0, v''(L)=0, v'''(L)=0.

The resulting nonlinear boundary-value problem will be solved using the Ritz method. We start with the solution *w(x)* of the linear problem:

$$-EI\frac{d^2}{dx^2}(w'')+F_0\cdot\delta(x-L)=0 \tag{4.7}$$

Next, we seek a solution to the nonlinear problem in the form $v(x)=\alpha\cdot w(x)$ where α denotes an unknown amplitude. Substituting this solution form into (4.6), multiplying by *w(x)* and then integrating with respect to *x* from 0 to L yields the following results:

$$C_1\cdot\alpha+C_1\cdot\alpha^3+F_0\cdot w(L)=0 \text{ and } d=v(L)=\alpha\cdot w(L) \tag{4.8}$$

$$F_0 = -\frac{C_1}{w^2(L)} \cdot d - \frac{C_2}{w^4(L)} \cdot d^3 = k_L \cdot d + k_{NL} \cdot d^3 \tag{4.9}$$

where C_1 and C_2 are constants. Solving these equations provides the following relationship between the restoring force (F_0= F_r in this situation) and the stiffness and deflection of the device.

$$F_0 = k_L \cdot d + k_{NL} \cdot d^3 = \left(\frac{3 \cdot EI}{L^3}\right) \cdot d + \left(\frac{3^4}{5 \cdot 7} \frac{EI}{L^5}\right) \cdot d^3 = F_r \tag{4.10}$$

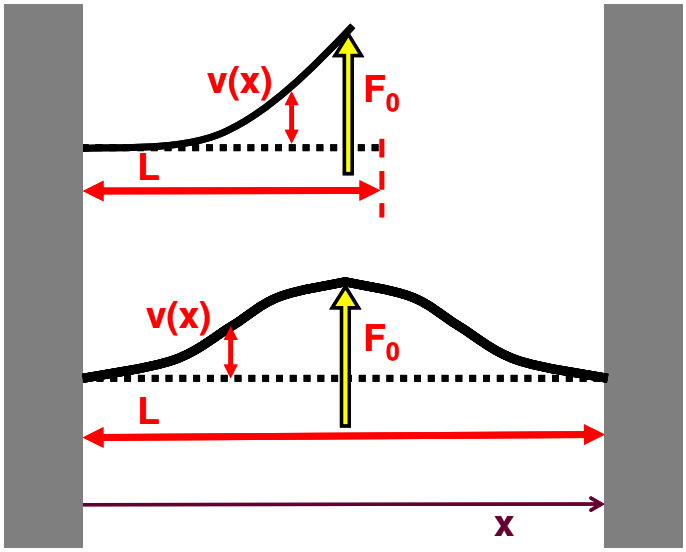

Figure 4.8. Dimensions defining a single clamped cantilever beam (above) and a clamped-clamped bridge beam (below).

Linear and Nonlinear Stiffness in a Bridge Beam

The Ritz method is now applied to the case of a clamped-clamped bridge beam. The bridge beam under a central force (F_0) is illustrated in Figure 4.8. The nonlinear effect for a single bridge beam (shown in Figure 4.6 and Figure 4.8) derives mainly from the stretching, not the bending of the beam. The differential equation of equilibrium is [1]

$$-EI\frac{d^4v}{dx^4} + \frac{EA}{2L}\left[\int_0^L \left(\frac{dv}{d\eta}\right)^2 d\eta\right]\frac{\partial^2 v}{\partial x^2} + F_0 \cdot \delta(x-L) = 0 \tag{4.11}$$

The boundary conditions for the clamped-clamped beam is v(0)=0, v'(0)=0, v(L)=0,

v'(L)=0.

Proceeding with the Ritz method as in the last example leads to cubic equation for the amplitude α. Upon solution for α, one can then obtain the following solutions for the restoring force (F_0=F_r in our model) and the nonlinear stiffness characteristics of a bridge beam:

$$F_0 = k_L \cdot d + k_{NL} \cdot d^3 = \left(\frac{192 \cdot EI}{L^3} \right) \cdot d + \left(\frac{2^5 \cdot 3^2}{5^2} \frac{EA}{L^3} \right) \cdot d^3 \qquad (4.12)$$

Comparison of Nonlinearities in a Cantilever Beam and a Bridge Beam

In summary, the non-linear restoring force of a cantilever beam and a bridge beam is given by equations (4.10) and (4.12) as reproduced here:

(1) Single-clamped cantilever: $k_L d + k_{NL} d^3 = \left(\frac{3 \cdot EI}{L^3} \right) \cdot d + \left(\frac{3^4}{5 \cdot 7} \frac{EI}{L^5} \right) \cdot d^3 \qquad (4.10)$

(2) Double-clamped bridge: $k_L d + k_{NL} d^3 = \left(\frac{192 \cdot EI}{L^3} \right) \cdot d + \left(\frac{2^5 \cdot 3^2}{5^2} \cdot \frac{EA}{L^3} \right) \cdot d^3 \qquad (4.12)$

Consider next the ratios of the linear stiffness and nonlinear stiffness coefficients, respectively for the bridge and cantilever beams as given by

$$\frac{k_{L,Bridge}}{k_{L,Cantilever}} = 64 \qquad (4.13)$$

$$\frac{k_{NL,Bridge}}{k_{NL,Cantilever}} = \left(\frac{2^5 \cdot 7}{3^2 \cdot 5} \cdot \frac{AL^2}{I} \right) \cong 60 \cdot \left(\frac{L}{w} \right)^2 \text{ (in-plane bending)} \qquad (4.14)$$

These results demonstrate that the bridge beam has linear and nonlinear stiffnesses that are substantially larger than those associated with the cantilever as expected.

The hardening nonlinearity for both designs is a distinct benefit in limiting the travel of the device mass. To understand this effect, consider next the ratio of the nonlinear and linear force components as defined by:

$$T = \frac{k_{NL} d^3}{k_L d} = \frac{k_{NL}}{k_L} d^2 \tag{4.15}$$

$$\text{(1) Bridge: } T = 0.06 \cdot \frac{Ad^2}{I} \geq 1 \rightarrow d \geq \sqrt{\frac{I}{0.06 \cdot A}} = d_{nonlinear,bridge} \cong 1.18 \cdot w \tag{4.16}$$

$$\text{(2) Cantilever: } T = \frac{3^3}{5 \cdot 7} \cdot \frac{d^2}{L^2} \geq 1 \rightarrow d \geq \sqrt{\frac{5 \cdot 7 \cdot L^2}{3^3}} = d_{nonlinear,cantilever} \cong 1.14 \cdot L \tag{4.17}$$

Setting T=1 yields the beam deflection $d_{nonlinear}$ for which the nonlinear force component equals the linear force component thereby doubling the total restoring force over a purely linear model; refer to Figure 4.7. Note further that $d_{nonlinear}$ is simply a function of the beam dimensions. For example, for a bridge beam, the restoring force doubles due to the nonlinearity for a deflection that is a mere 18% larger than the beam thickness (w) in the bending direction. For a cantilever beam, a similar effect is realized but only when the beam deflection is 14% larger than the beam length L. Thus, the nonlinear restoring effect is significantly greater for the bridge beam than the cantilever beam as expected.

4.2.4. Design Considerations for Nonlinear Spring Shock Stops

The linear/nonlinear stiffness and restoring forces derived in Section 4.2.3 are used to satisfy the design criteria given in Section 4.2.1. Those two criteria are:

- Criterion #1: The maximum stress developed in the device and its stop beams must remain less than that defining failure.
- Criterion #2: The compliance must be maximized to reduce the impact force.

Criterion #1 can be easily checked in reference to the results of Figure 4.9. This figure shows (1) the maximum allowable deflection ($d_{allowable}$) of the device mass before either the device beam or the shock stop beams fracture, and (2) the maximum amplitude of the deflection (d_{amp}) of the device mass after shock loading, as a function of the applied shock. The region where $d_{allowable}$ exceeds d_{amp} defines the allowable range of shock protection for a design. To increase the allowable shock range, one can stiffen the shock beams and thereby further reduce d_{amp}. Note also that the

nonlinearity considered for this single beam can be readily extended for each of the beams in the beam cascade resulting in additional stiffness of the shock beam structure and further reduction of the travel of the device mass. While increasing the stiffness of the beam structures increases the ability to meet Criterion #1, reducing the stiffness increases the ability to meet Criterion #2.

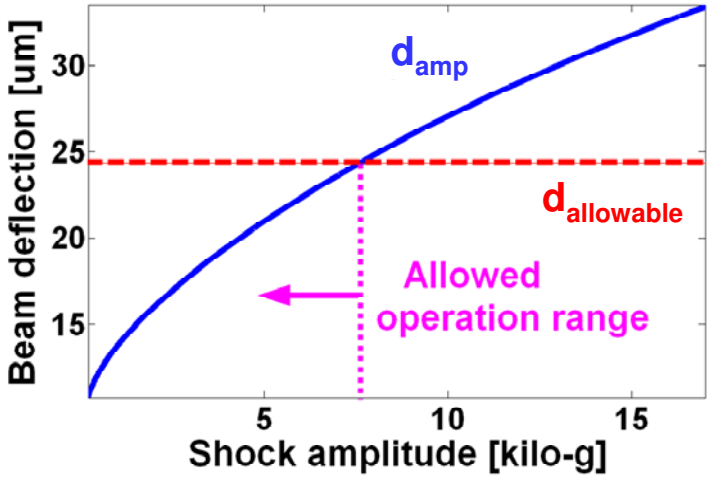

Figure 4.9. Range of shock protection offered by a device with a single nonlinear beam.

4.2.4.1. Beam Cascade Structure

From Newton's law, the device mass under shock load (amplitude of A_{shock}) can be expressed by the following equation of motion when the number of shock beams touched by the device mass is N.

$$m_d\ddot{x}_d = \sum \text{Forces} = F_{shock} - F_{r,device} - F_{r,shockbeam} = m_d A_{shock} - k_d x_d - \sum_{i=1}^{N} k_s\left[x_d - G - (i-1)D\right] \quad (4.18)$$

$$= m_d A_{shock} - k_d x_d - k_s\left[(x_d - G)N - D\frac{N(N-1)}{2}\right] \qquad \text{when} \quad G+(N-1)D < x_d < G+ND$$

The impact force generated while the device mass maintains contact with the shock stop can be calculated from the stiffness terms in the above equation.

Application of work/energy to this system leads to the following result for d_{amp}. Assuming no device dissipation, one can compute an upper bound estimate of d_{amp} by equating the work done by F_{shock} to the work done by the beam cascade between the equilibrium state $x_d = 0$ and the rest state when $x_d = d_{amp}$. These two work integrals

are

$$\int_0^{d_{amp}} F_{shock}\,dx = \int_0^{d_{amp}} \left(m_d A_{shock}\right)dx = m_d A_{shock} d_{amp} \tag{4.19}$$

where A_{shock} denotes the average acceleration induced by the external shock and

$$\int_o^{d_{amp}} \left[F_{device\_beam}(x) + F_{beam\_cascade}(x)\right]dx = \int_0^{d_{amp}} \left(k_d x\right)dx + \sum_{i=1}^{N}\left[\int_{G+(i-1)D}^{d_{amp}} k_s\left[x - \left\{G + (i-1)D\right\}\right]dx\right] \tag{4.20}$$

Equating (4.19) and (4.20) yields the following quadratic equation for solution of $d_{\min}$

$$0 = {d_{amp}}^2\left(\frac{k_S N}{2} + \frac{k_d}{2}\right) + d_{amp}\left\{k_S N\left(\frac{D}{2} - G - \frac{ND}{2}\right) - m_d A_{shock}\right\} + \frac{Nk_S}{2}\left\{-DG + G^2 + DGN + \frac{D^2(N-1)(2N-1)}{6}\right\} \tag{4.21}$$

The maximum allowable deflection $d_{allowable}$ of any beam is determined from the maximum allowable stress σ_{max}, which, for simplicity, we will take to be either the fracture strength (for brittle materials) or the yield strength (for ductile materials). Then $d_{allowable}$ is determined as the minimum of the maximum deflections of the device beam and the stop beam as given by:

$$\begin{aligned} d_{allowable} &= \min(d_{allowable,stop} + G,\, d_{allowable,device}) \\ &= \min\left(\frac{{L_{stop}}^2}{24 \cdot E_{stop} w_{stop}}\sigma_{\max,stop} + G,\, \frac{2}{3}\frac{{L_{device}}^2}{E_{device} w_{device}}\sigma_{\max,device}\right) > d_{amp} \end{aligned} \tag{4.22}$$

To satisfy Criterion #1, $d_{allowable}$ must be larger than d_{amp}, and this condition can be satisfied by adjusting the geometric and material properties of the stop beams.

4.2.4.2. Single Beam with Nonlinear Hardening Effects

Following the same development above, we begin with the equation of motion of the device mass subject to a shock load (average amplitude of A_{shock}) and contacting a single nonlinear beam

$$m_d \ddot{x}_d = \sum Forces = F_{shock} - F_{r,device} - F_{r,shockbeam}$$
$$= m_d A_{shock} - k_d x_d - \left[k_L \left(x_d - G \right) + k_{NL} \left(x_d - G \right)^3 \right] \quad (4.23)$$

Using work/energy again applied between the positions $x = 0$ and $x = d_{amp}$ yields

$$\int_0^{d_{amp}} mA_{shock} = \int_0^{d_{amp}} \left(k_d x \right) dx + \int_G^{d_{amp}} \left[k_L \left(x - G \right) + k_{NL} \left(x - G \right)^3 \right] dx \quad (4.24)$$

$$mA_{shock} d_{amp} = \left(\frac{k_d d_{amp}^{\ 2}}{2} + \frac{k_L (d_{amp} - G)^2}{2} + \frac{k_{NL} (d_{amp} - G)^4}{4} \right) \quad (4.25)$$

This quartic equation yields d_{amp} as a function of: (1) the device spring constant (k_d), (2) the linear and nonlinear spring constants of the stop (k_L, k_{NL}), (3) the device mass (m_d), and (4) the applied shock amplitude (A_{shock}).

As before, a maximum allowable deflection of the stop ($d_{allowable,stop}$) before the device or the shock beam structure fractures is defined by equations (4.26) and (4.27). In equation (4.26), the maximum allowable force $F_{allowable,stop}$ producing $d_{allowable,stop}$ determined by shock-beam design and maximum allowable stress ($\sigma_{max,shock}$). From the $F_{allowable,stop}$, we can calculate the maximum allowable deflection ($d_{allowable,stop}$) of the shock beams using equation (4.27). To satisfy Criterion #1, the $d_{allowable,stop}$ must yield a solution that is greater than d_{amp} as defined by (4.28).

Bridge: $F_{allowable,stop} = \frac{2}{3} \frac{w^2 t}{L} \sigma_{\max,stop}$, Cantilever: $F_{allowable,stop} = \frac{1}{6} \frac{w^2 t}{L} \sigma_{\max,stop}$ (4.26)

$$F_{allowable,stop} = k_L (d_{allowable,stop}) + k_{NL} (d_{allowable,stop})^3 \quad (4.27)$$

$$d_{allowable} = \min(d_{allowable,stop} + G, d_{allowable,device} = \frac{2}{3} \frac{L^2}{Ew} \sigma_{\max,device}) > d_{amp} \quad (4.28)$$

4.3. Simulation Results I – Nonlinear Spring Shock Stops

The shock performance of the nonlinear spring shock stop designs is assessed by direct numerical simulation of the previous equations of motion using MATLAB and SIMULINK under equivalent input conditions. Each simulation considers the

response of the device mass following a prescribed acceleration pulse of 1000 g over a short time interval of 0.06 milliseconds. This acceleration is close to the shock amplitude used in the reliability tests of a commercial MEMS gyroscope (~1200g) [2] and the shock range required in several automotive applications including knocking sensors (1000g) [3]. The impact force generated upon the first impact with the shock stop and the maximum displacement of the device mass is then computed. The computed impact force is then normalized by the impact force produced on a conventional hard stop, which serves as a benchmark.

The simulations, which reveal the merits and demerits of each concept, are also founded on several other assumptions. We neglect energy dissipation by friction and assumed high vacuum conditions (damping factor=10^{-5}). Inclusion of these effects would otherwise further reduce the impact force and the settling time. We also assume a representative device mass m_d=1 mg. In the case of nonlinear spring shock stops, we select a representative gap of 10 μm between the device mass and the first shock beam (G=10 μm). This gap can, of course, be smaller (<5 μm) depending on the application.

4.3.1. Nonlinear Spring I - Beam Cascade

We begin with a simulation of the device mass restrained by the beam cascade design. Figure 4.10 summarizes the computed results over a wide range of beam cascade designs. Shown are the (normalized) impact force and the maximum displacement as functions of the stiffness of an individual beam in the cascade and for two different beam spacings of 5 and 10 μm. Overall, the considerable compliance offered by the beam cascade leads to a dramatic reduction of the impact force by over 90% relative to a hard stop for all possible designs shown in Figure 4.10. This impact force decreases gradually with decreasing beam stiffness and increasing beam spacing, both of which render the beam cascade more compliant in support of Criterion #2. However, the additional benefit afforded by the added compliance is rather modest when compared to the dramatic reduction relative to a hard stop. Similarly, increasing the beam stiffness and decreasing the beam separation lead to an overall stiffer beam cascade, and therefore, both changes result in reductions in the maximum deflection of the device mass.

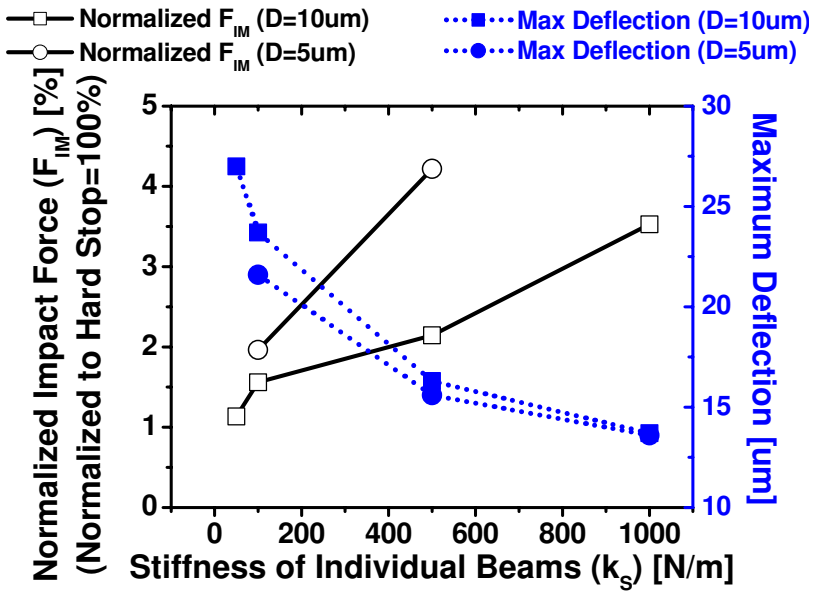

Figure 4.10. Impact force reduction and maximum displacement due to beam cascade as functions of beam stiffness (k_S) and spacing (D=5 or 10 μm). Two shock-stop beams are considered.

4.3.2. Nonlinear Spring II - Single Nonlinear Beam

Consider next the performance of a stop composed of a single nonlinear beam forming either a bridge or a cantilever.

4.3.2.1. Single Nonlinear Bridge

For a single nonlinear bridge beam Figure 4.11 illustrate resulted obtained using equations (4.24)-(4.28). The results show the maximum allowable shock (acceleration magnitude) as a function of beam width for polysilicon beams having two lengths and an aluminum (Al) beam. Inspection of these results reveals that the maximum allowable shock is largely controlled by 1) the beam width and, 2) Young's modulus, and is only weakly dependent on beam length. In reference to Criterion #1, the maximum allowable shock reported in this figure derives from fracture for the polysilicon beam and by yielding for the aluminum beam. In reference to Criterion #2, and the previous results for the beam cascade, it is obvious that the additional compliance afforded by the aluminum beam reduces the impact force over that produced by the polysilicon beam.

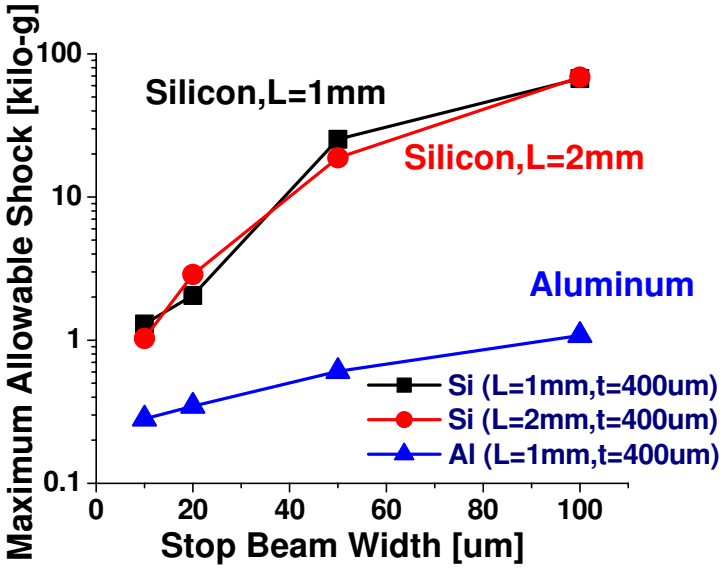

Figure 4.11. Maximum allowable shock as a function of the width and length of shock-stop beams made of both polysilicon and aluminum.

We now consider the dynamic response of the device mass upon impacting the single nonlinear bridge beam shock stop. For this calculation, we simulate the same shock event considered above for the beam cascade. Figure 4.12 shows that the computed impact force magnitude and maximum beam displacement as functions of the linear stiffness of the single beam (k_L). For reference, we also include data from Figure 4.10 for a beam cascade composed of linear beams of the same (polysilicon) material with spacing D=10 μm. For this comparison, k_S in Figure 4.10 and k_L in Figure 4.12 are identical.

Overall, the impact force reduction afforded by a single nonlinear bridge beam is dramatic when compared to that induced by hard shock stops (over 90% reduction for all designs considered in the figure). As expected, the impact force decreases as the linear stiffness decreases but at the expense of increased maximum deflection. Compared with the beam cascade, the single nonlinear bridge beam is slightly better at reducing the impact force because of its greater compliance. This difference is modest however when compared to the large impact force reduction afforded by both designs compared to hard shock stops. Note that the nonlinear stretching of each beam in the beam cascade, which can readily be incorporated in an analysis, will yield a slightly stiffer shock stop and thus a modest increase in the predicted impact force.

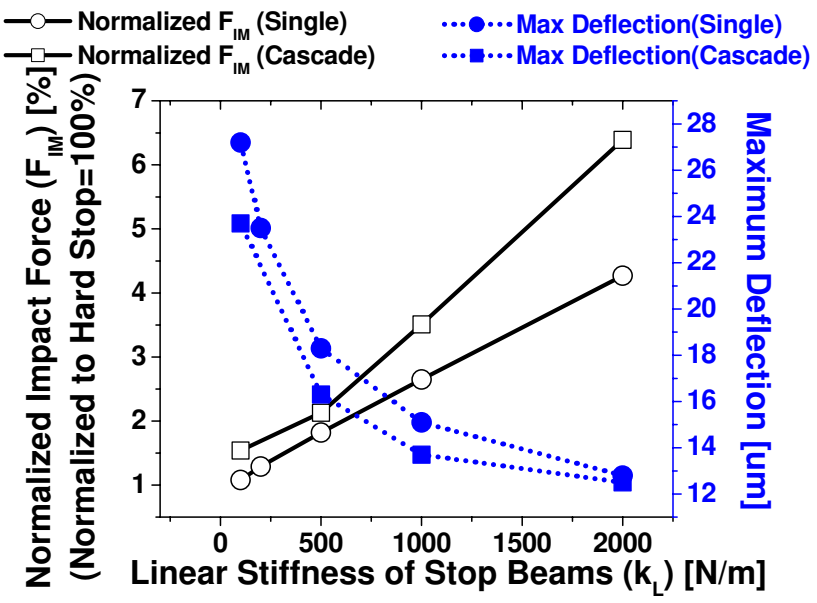

Figure 4.12. Impact force reduction and maximum deflection for a single nonlinear beam (w=20 μm) as functions of the linear beam stiffness k_L. Results for a beam cascade (N=2, D=10 μm, w=20 μm) from Figure 4.10 are shown as a reference.

4.3.2.2. Single Nonlinear Cantilever

We now present analogous results for a shock stop formed by a single nonlinear cantilever based on equations (4.13) and (4.14). Figure 4.13 summarizes the performance of this design as a function of beam length L, while the range of linear stiffness is adjusted to be similar to that considered in Figure 4.10 and Figure 4.12.

The results are consistent with the previous designs. In particular, longer beam length yields a more compliant stop which then decreases the impact force but increases the maximum deflection. As expected from equations (4.13) and (4.14), a cantilever is more compliant than a bridge having the same dimensions and materials. Thus, as observed in the results of Figure 4.13, a cantilever is superior in reducing the impact force but inferior in reducing the maximum deflection as compared to the nonlinear bridge (Figure 4.12). As the beam becomes longer, there is little difference in the impact force reduction, but the difference in maximum deflection remains. This difference is much larger than that of Figure 4.12, which reveals a greater performance difference between the nonlinear bridge and the cantilever beam than between the nonlinear bridge and the linear beam cascade.

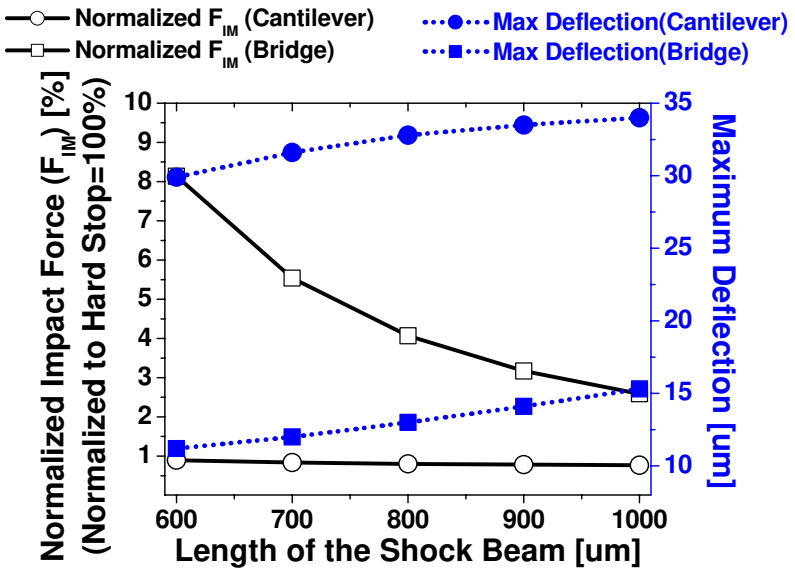

Figure 4.13. Impact force reduction and maximum deflection for a single nonlinear bridge and cantilever (w=20 μm, t=50 μm) as functions of the shock-beam length (L). Used beam lengths are selected to make similar linear stiffness (k_L), which is used in Figure 4.12.

4.4. Design and Analysis II – Soft Coating Shock Stops

4.4.1. Design of Soft Coating Shock Stops

The second concept for shock protection is to add a thin compliant layer to an otherwise hard (conventional) shock stop. This layer not only serves to reduce the secondary impacts on the stop, but also dissipates energy and hence reduces the number of collisions as well as the settling time following a shock event.

The performance of the soft coatings is mainly determined by the viscoelastic property of the coating material. The viscoelasticity can be simply modeled as a combination of a damper and a spring (Maxwell or Voigt model [4]). The damper's properties depend on the coefficient of restitution (COR) of the coating material. The spring's properties can be derived from elastic modeling of thin films and are determined by both coating material and device design.

Soft coating shock stops should be designed to satisfy the following criterion.

- Criterion: The compliance/damping of the soft material must be maximized to reduce the impact force.

4.4.2. Damping in Soft Coating

The coefficient of restitution (COR) is the ratio of velocities just before and after an impact event. The COR as a concept, though quite approximate, is a generally accepted means to characterize impacts [5]. For an object impacting a stationary object, such as a coated shock stop, the COR simplifies to

$$COR = -\frac{v_{after}}{v_{before}} \tag{4.29}$$

where v_{before} and v_{after} denote the velocity of the device mass immediately before and after impact on the coated shock stop. The COR also determines the energy loss during the impact because kinetic energy is proportional to the square of the velocity. The impulse delivered to the device mass is given by [6]

$$\left|m \cdot \Delta v\right| = \left|m\left(v_{after} - v_{before}\right)\right| = m\left|v_{before}\right|(1 + COR) \tag{4.30}$$

The soft coating concept capitalizes on the fact that the coating material reduces the COR and thus reduces the impulse delivered to the device mass during impact with the coated shock stop. Unfortunately, most conventional MEMS materials have relatively large COR (Si: 0.7, oxide: 0.96), resulting in little/no shock protection [7-9]. However, effective shock protection can be achieved by employing significantly softer coatings like copper, gold (COR=0.22), and various polymers. Table 4.2 shows the COR of MEMS-compatible coating materials.

Table 4.2. COR and Mohs hardness for candidate coating materials [7-9] (Maximum Mohs hardness=10)

	Material	COR	Hardness	Material	COR	Hardness
Hard	Si	0.7	7.0	Oxide, Glass	0.96	
	Cr		9.0			
Soft	Al		2-2.9	Cu	0.22	2.5-3
	In		1.2	Ag		2.5-4
	Au	0.22	2.5-3	Pb	0.16	1.5

We further note that the COR scales with the material's Mohs hardness. The soft materials shown in the table are therefore attractive since the resulting smaller COR

reduces the impulse and thus dissipates more energy during impact.

4.4.3. Elasticity in Soft Coating

The stiffness of a thin-film layer was analyzed utilizing simple but reliable models suggested in a previous study [10]. These models have been experimentally validated with minor corrections and referenced in many studies [11-13]. The models describe the deflection of a thin film (d_{film}) in response to a load (P_{load}) applied by an indenter as a function of the indenter's shape and dimensions. Figure 4.14 depicts three shapes of the indenter and defines pertinent variables. The film is assumed to be perfectly bonded to a semi-infinite substrate. The stiffness of the layer can be deduced from the relationship between P_{load} and d_{film} which is given as follows for three different indenter shapes:

Flat-ended indenter (Figure 4.14-a): $$P_{load} = (\zeta_i \cdot a) \cdot d_{film} \tag{4.31}$$

Conical indenter (Figure 4.14-b): $$P_{load} = (\zeta_i \cdot \tan\alpha) \cdot d_{film}^2 \tag{4.32}$$

Spherical indenter (Figure 4.14-c): $$P_{load} = \left(\frac{2}{3}\zeta_i \cdot \sqrt{R}\right)^{3/2} \cdot d_{film}^{3/2} \tag{4.33}$$

Here, ζ_i is defined to be $\zeta_i = 4*E_i/(1-\nu_i)$ where E_i is Young's modulus and ν_i is Poisson's ratio. Note that a film's indentation is related to its contact area, not to its total surface area. This behavior is similarly observed for both purely elastic and elastic-plastic indentations, as reported in other papers [11, 12]. On the other hand, when the film thickness approaches infinity, E_i and ν_i approach those of the thin film material (i=1). When the film thickness approaches zero, E_i and ν_i approach those of a hard substrate material (i=2). Therefore, a thicker soft film decreases ζ_i, and thus reduces the film's stiffness. This reduced stiffness leads to a smoother deceleration and longer contact time during impacts, and eventually decreases the impact force generated when a device collides with the shock stop. In the later simulations, we used the ζ of a coating material assuming an infinite film thickness.

In summary, the stiffness of a thin-film layer has the following characteristics. First, it depends only on the contact area not on the total surface area. Second, it is determined by both (1) the coating material's mechanical properties (E_1, ν_1), and

thickness, and (2) by the shape of the indenter (or "bumper" on device mass). In short, the compliance of the coating layer increases (1) as ζ_1, which is proportional to the stiffness of a layer, decreases; (2) as the thickness of the coating material increases; and (3) the area of layer contacted by bumpers decreases. However, the coating material's thickness and bumper designs are limited by fabrication challenges and limitations.

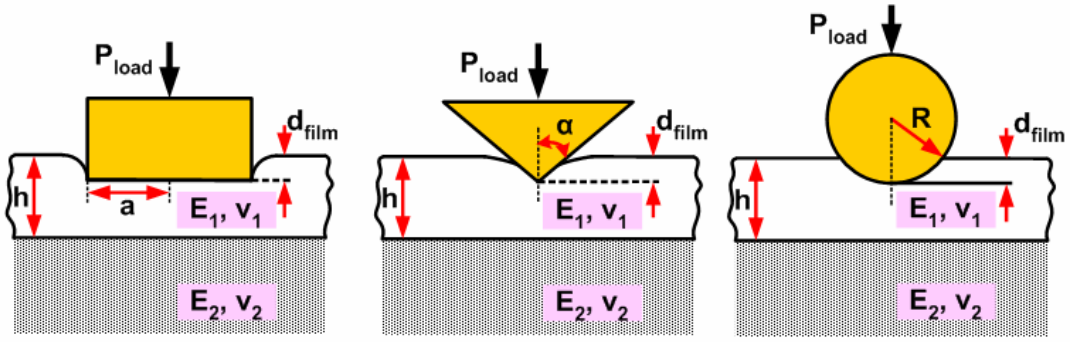

Figure 4.14. A thin film layer on a semi-infinite substrate indented by (a) a rigid flat-ended indenter, (b) a conical indenter, or (c) a spherical indenter [10].

4.5. Simulation Results II – Soft Coating Shock Stops

4.5.1. Simulation Results Demonstrating Damping Properties

Deposition of a thin film soft coating on an otherwise hard shock stop provides both impulse (and impact force) reduction and energy dissipation following the contact of the device mass with the stops. To characterize energy dissipation, we used the number of impacts between the device mass and its stops as a determinant.

Figure 4.15 summarizes our findings for three different coatings (glass/oxide, silicon, and gold/copper) and compares the impulse (magnitude) and the number of impacts following the same shock event considered in all studies above.

Both the impulse magnitude and the number of impacts are normalized with respect to those obtained using a perfectly rigid stop having COR=1 (100%). Overall, we note the significant (40%) reduction in impulse magnitude and the significant (>90%) decrease in number of collisions are predicted for a gold/copper coating, compared to the glass/oxide.

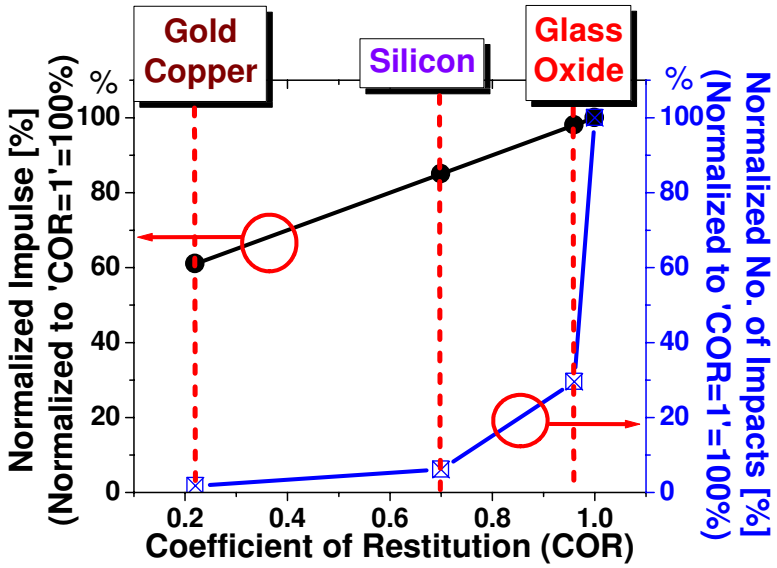

Figure 4.15. Impulse reduction and impact number reduction as function of COR – Results shown for three coatings: glass /oxide, silicon and gold/copper.

4.5.2. Simulation Results Demonstrating Stiffness Properties

Figure 4.16 shows the elastic energy vs. deflection of a thin Parylene film (ζ is calculated to be 20 GPa from Parylene's E=3 GPa, v=0.4 [14]) for a device mass (~1 mg) with four bumper designs shaped like the indenters in Figure 4.14. Also, the initial kinetic energy of the device mass following a 1000g shock load (prior to the device mass impacting the shock stop) is shown by the solid line labeled as threshold. When the device mass impacts the thin film, it compresses the film until the work done by the film (stiffness and damping forces) equals the initial kinetic energy of the device mass. When this occurs, the film is maximally compressed and the device mass is momentarily at rest. If one ignores the work done by damping, then one can readily predict an upper bound estimate of this maximum compression (equivalently, an upper bound estimate of the film thickness) needed to absorb the impact. These estimates are illustrated in Figure 4.16 as the intersection of the "threshold" line (the initial kinetic energy of the device mass) and the elastic energy of the thin film for each design.

Figure 4.17 shows the time record of (a) the displacement of the device mass and (b) the impact force involved during this movement. The motion of the device mass is initiated by a 1000-g shock load. From these figures, we can characterize the impact by (1) the contact time (Figure 4.17-a), and 2) the maximum impact force (Figure 4.17-b). Clearly, the shock performance of the stops depends upon the coating material

properties and thickness as well as and the bumper design (shape and dimensions). Consequently, a soft coating shock stop can likely be designed to accommodate a wide range of incident shock loads.

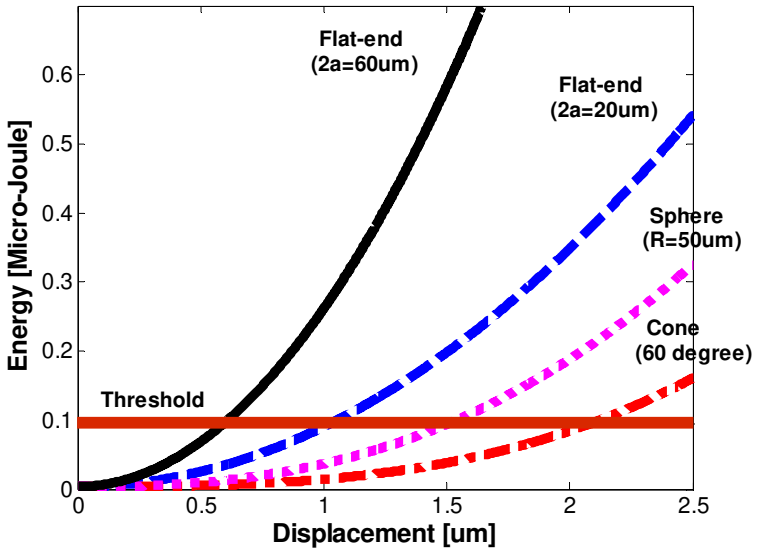

Figure 4.16. Elastic energy vs. deflection of a Parylene film (ζ_i is assumed to be 20 GPa) for a device mass that has one bumper of different shapes. The energy produced by a 1000-g shock applied to a device mass is shown as the solid line, which is labeled as threshold.

Focusing now on a spherical bumper, we employed the models of Section 4.4.3 to compute the average impact force and the maximum impact force of both Parylene coated (soft) shock stops and silicon (hard) shock stops. The simulations in the Figure 4.17 are conduced using the Young's modulus and the Poisson's ratio of Parylene (E=3 GPa, v=0.4) and silicon (E=160 GPa, v=0.23). From the simulation results, we conclude that Parylene coated stops provide significant reductions in both the average impact force (78% reduction) and the maximum impact force (78% reduction) relative to hard silicon shock stops. These substantial reductions explain why soft coating stops yield much higher device survival rates in the drop test experiments of Chapter 5. Further reductions are also likely due to the large damping that Parylene provides relative to that afforded by silicon; refer to Section 4.5.1.

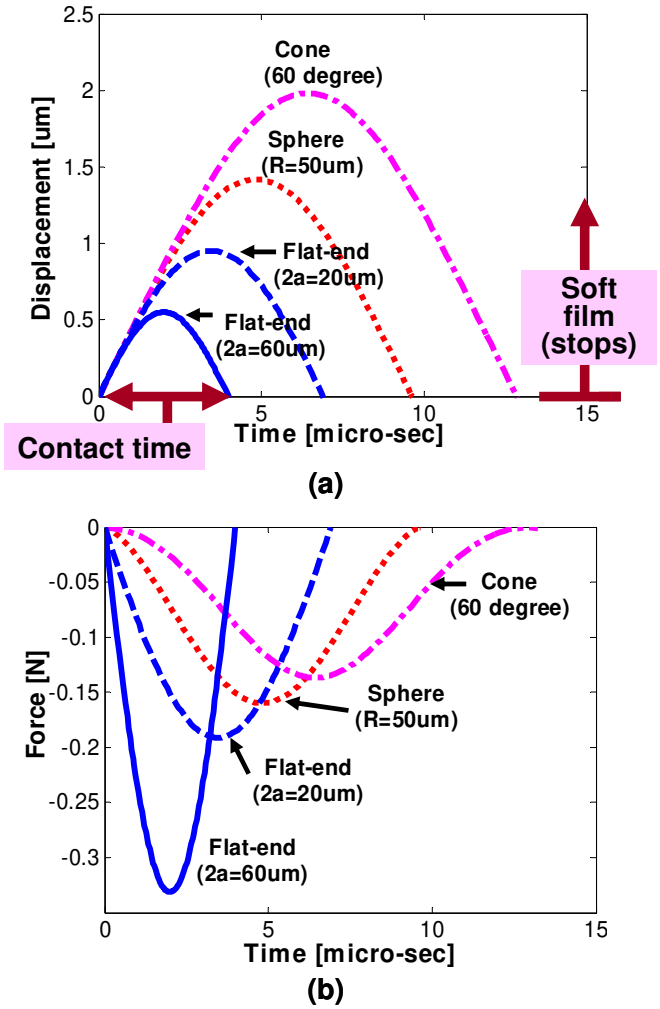

Figure 4.17. The time record of (a) the displacement of a device mass and (b) the involved impact force during this movement.

4.6. Limit of Proposed Approaches

Because of fabrication limitations, the approaches proposed and discussed above are not appropriate for devices that have large resonant frequencies (>100 kHz). These devices include resonators, resonating pressure sensors, and resonating accelerometers. For shock stops to be effective, devices must be able to deflect enough to impact the shock stop, but not break before they impact the stop. For high frequency devices it is difficult to do this since they are typically stiff, which causes their maximum stress to exceed fracture stress after deflection.

4.7. Summary

In this chapter, we described the concept, design, and analysis of two concepts for shock protection of MEMS using nonlinear springs and soft coatings. The two concepts (nonlinear springs and soft coatings) could improve shock protection by reducing the impact force generated between a moveable MEMS device and its shocks stops and by dissipating its energy in a reliable manner. We analyze the merits and demerits of each concept using simulations, and ranges of shock design parameters to enhance performance are suggested.

The two concepts above demonstrate considerable promise for reducing the impact force when the device impacts the shock stop following a shock event. Table 4.3 provides an overall summary of the relative performance of three shock stop designs for a single MEMS device (mass=~1 mg, device spring constant=~200 N/m).

Table 4.3. Comparison of shock protection afforded by the three designs shown in Figure 4.1. Cascade-beam and single-bridge designs have the same linear stiffness.

Criteria	Hard wall	Nonlinear spring		Soft coating	
	Hard silicon	Cascading beams	Single nonlinear bridge	Gold coating	Parylene coating
Impact force	100%	~2.4%	~1.5%	<60%	<22%
Max deflection	20μm	20.8μm	21.5μm	~20μm	~20μm
Collision number reduction	Minor	Small		>90% reduction	N/A

The considerable compliance afforded by both the beam cascade and the single nonlinear beam leads to tremendous reductions in the impact, and additional deflection of the device mass is a modest penalty paid for such a drastic impact force reduction. The soft gold coating allows no additional device mass deflection but produces a significant reduction of impact force (40%) and the notable decrease in number of impacts (>90%), compared to an uncoated (hard) stop. Moreover, these benefits are amplified by using flexible polymers, such as Parylene, for which the simulation results indicate a 78% reduction in impact force. The reductions realized in practice may well

be larger than those predicted here due to the simultaneous benefits of coating compliance and damping.

References

[1] N. C. Perkins, *Nonlinear systems, overview*: Academic Press, 2001.

[2] ADXRS150/300 (Analog Device, Inc.)

[3] J. D. Turner and A. L. Austin, "Sensors for automotive telematics," *Measurement Science and Technology,* vol. 11, pp. R58-R79, 2000.

[4] R. J. Young and P. A. Lovell, *Introduction to Polymers*: Champman & Hall, 1991.

[5] R. M. Brach, *Mechanical Impact Dynamics*: Wiley, 1991.

[6] T. W. Burkhardt, "of a randomly accelerated particle: recent results for partially absorbing and inelastic boundaries," *Physica A,* vol. 306, pp. 107-116 2002.

[7] X. Li, P. F. Dunn, and R. M. Brach, "Experimental and Numerical STudies of Microsphere Oblique Impact with Planar Surface," *Journal of Aerosol Science,* vol. 31, pp. 583-594, 2000.

[8] J. H. Twelvers, "Physics of Law Enforcement," in the Proceeding of *Ontario Association of Physics Teachers Annual Conference*, Ontario, Canada, 2003, p. 16.

[9] D. R. Lide, *CRC Handbook of Chemistry and Physics*, 73 ed.: CRC Press, 2002.

[10] H. Y. Yu, S. C. Sanday, and B. B. Rath, "The effect of substrate on the elastic properties of films determined by the indentation test -- axisymmetric boussinesq problem," *Journal of the Mechanics and Physics of Solids,* vol. 38, pp. 745-764, 1990.

[11] S. M. Han, R. Saha, and W. D. Nix, "Determining hardness of thin films in elastically mismatched film-on-substrate systems using nanoindentation," *Acta Materialia,* vol. 54, pp. 1571-1581, 2006.

[12] X. Chen and J. J. Vlassak, "Numerical study on the measurement of thin film mechanical properties by means of nanoindentation," *Journal of Materials Research,* vol. 16, pp. 2974-2982, 2001.

[13] P. M. Ramsey, H. W. Chandler, and T. F. Page, "Modelling the contact response of coated systems," *Surface and Coatings Technology,* vol. 49, pp. 504-509, 1991.

[14] T. A. Harder, Y. Tze-Jung, H. Qing, S. Chi-Yuan, and T. Yu-Chong, "Residual stress in thin-film parylene-c," in the Proceeding of *The Fifteenth IEEE International Conference on Micro Electro Mechanical Systems*, Las Vegas, NV 2002, pp. 435-438.

CHAPTER 5

NEW SHOCK PROTECTION CONCEPTS: EXPERIMENTS and DISCUSSIONS

The advantages of the novel shock protection technologies were analyzed in Chapter 4. To demonstrate three of these advantages of: (1) improved shock protection, (2) convenient integration with many devices and (3) easy design modification, we fabricated and tested devices having nonlinear spring or soft coating shock stops, and present these in Chapter 5.. The fabricated devices were tested with a drop test machine, and test results are compared with benchmark devices with conventional hard stops.

The test results verify that both of our technologies provide superior shock protection over hard stops in our test conditions. Device survival rate of nonlinear spring devices (88%) and that of soft coating devices (94%) are more than twenty times higher than the rate of hard stop devices (4%). The test devices were fabricated with two fabrication methods (Silicon-on-glass and highly-doped LPCVD polysilicon processes), and demonstrated that our technologies can provide a generic and batch approach compatible with conventional microfabrication techniques. In addition, every device was fabricated at wafer level. Moreover, we found an interesting device fracture behavior in the tests, and discuss this device fracture mechanism by high bending stress induced by impact force.

Section 5.1 describes available shock test methods and our drop test setup. Section 5.2 explains the design of test devices used in our shock experiments, and Section 5.3 explains fabrication processes and shows fabricated test devices. Section 5.4 demonstrates our shock test results, and Section 5.5 discusses about device fracture mechanism by impact force. Finally, Section 5.6 summarizes our results and discussions.

5.1. Design of Shock Test Setup

We designed and manufactured a setup to conduct shock tests. Various shock

test methods are explained in Section 5.1.1. We decided to use a drop machine to meet the requirements listed in Section 5.1.2. Finally, we present the performance of our test setup in Section 5.1.3.

5.1.1. Shock Test Methods

Various shock test methods are used in a macro-world and in a micro-world. The methods are shaker table, impact hammer, Hopkinson bar, ballistic tests, and drop machine. Table 5.1 shows the advantages and disadvantages of the shock test methods.

Table 5.1. Characteristics of shock test methods

Test method	Shock amplitude	Direction control	Repeata -bility	Convenient setup manufacture & installation
Shaker Table	Low (<100 g) (<500 g in an extreme case)	Provided	Yes	Easy
Impact hammer	Low-Mid	Need additional equipment		Easy
Hopkins bar	High (5,000-40,000 g) (<200,000 g in an extreme case)	Provided	Yes	Hard
Ballistic test	High (up to 100,000 g)	No	No	Hard
Drop Machine	Mid-High (<~4,000g w/o pull-down) (up to 30,000g w/ pull-down)	Provided	Yes	Easy

5.1.1.1. Shaker Table

A shaker table is a table oscillating in a sinusoidal manner that is commonly used for vibration testing. Several shaker tables can also be operated to generate a sharp impulse of acceleration (i.e. instantaneous shock) [1]. A shaker table can also control shock direction and amplitude, provide repeatable tests and afford convenient installation because test devices are simply attached to the top of the table. However, the maximum shock amplitude produced by the shaker table is low. Most shaker

tables provide small shock amplitudes of <100 g [2-4]; a giant table (3500kg weight) could generate 500g shock [5].

5.1.1.2. Impact Hammer

Impact hammer is a hammer with a fine tip that hits a device to generate shock. The fine tip restricts the shock generation to a single contact point for better control. The hammer can provide directed and repeatable shock if used with additional direction-guidance equipment [6]. Many impact hammers have implanted shock accelerometers inside them so that we can measure the applied shock. The implanted accelerometer cannot measure the shock really experienced by the test device, however, because the hammer and the device experience the same force but different acceleration because of their different masses.

5.1.1.3. Hopkinson Bar

The Hopkinson bar, first suggested by Bertram Hopkinson in 1914, is an apparatus for testing the dynamic stress-strain response of materials. As shown in Figure 5.1 [7], the Hopkinson bar consists of (1) a metal bar designed to minimize energy loss, (2) impacting object to apply shock to one end of the bar, and (3) measurement devices detecting shock at the other end of the bar. The impacting object produces a mechanical shock wave at one end of the metal bar and the bar guides the wave to propagate through a metal bar with minimized energy loss. Therefore, the Hopkinson bar works as an ideal guide for a mechanical wave.

Multiple metal bars are used in a split Hopkinson bar, a refined version of the Hopkinson bar, but will not be dealt with in this dissertation. The impacting object commonly uses a pendulum or an air gun (shooting a metal ball through the air barrel) [1, 7]. Measurement devices include laser vibratometers (L.V. in the figure) or accelerometers. Sometimes, a more complex control system is also used for better control of shock [1, 8].

Hopkinson bars can generate high shock amplitude in a controlled and repeatable manner. A Hopkinson bar controlled by complex feedback systems generated high shock from 5,000 to 10,000g with accurate amplitude control (<7.1 % error) [8]. Without the fine amplitude control, higher shock (>30,000g) was generated from the same bar. This Hopkinson bar was used in several experiments using MEMS devices

and generated shock amplitudes from 5,000 g to 40,000 g [9-11]. One paper reported that a Hopkinson bar could produce very high shock amplitudes up to 200,000 g [11].

Despite these advantages, we did not use Hopkinson bars because they require complex control systems and are difficult to manufacture and install.

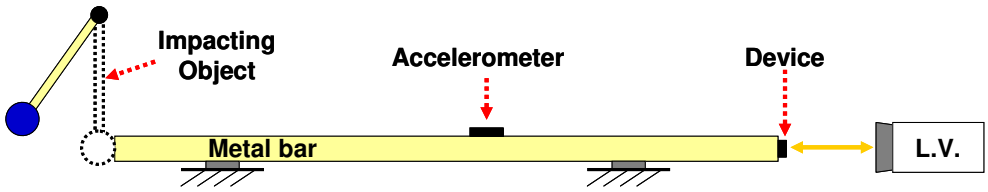

Figure 5.1. Conceptual view of a Hopkinson bar [7].

5.1.1.4. Ballistic Test

In this method, a test device is mounted inside a projectile, which will be launched and shot at targets. Figure 5.2 shows the conceptual view of the ballistic test [12]. This method can easily generate high shock amplitudes up to 100,000 g but cannot be repeated or controlled. The target is important in determining the shock amplitude. High shock amplitudes from 50,000 g to 100,000 g were produced when the projectile was fired at hard targets such as concrete or rock [12], but lower shock of 42,000 g was measured when softer targets, such as a sawdust catch , were used [13]. MEMS-based safety and aiming devices were mounted inside a bullet and fired by an MK19 machine gun and produced > 42,000 g [13].

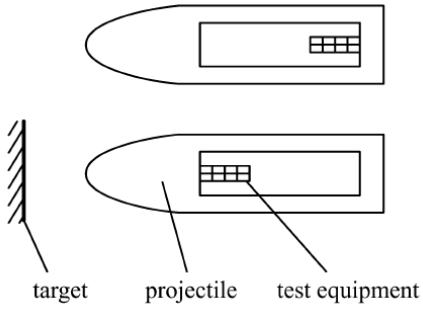

Figure 5.2. Conceptual view of ballistic tests [12].

5.1.1.5. Drop Machine (Drop Test)

In drop tests, we mount test devices on a metal plate and drop the plate from a known height to a hard surface. Sometimes the plate is pulled downward so that

higher shock amplitude is generated. This drop test can easily provide controlled and repeatable shock direction and amplitude. For better shock control, we sometimes use a sharp surface like a chisel as the surface hit by the metal dropping plate. Figure 5.3 shows a sample drop test machine (IMPAC66 HVA) developed in the Army Research Laboratory [14]. In some drop machines, the metal plate was dropped on the test device [15].

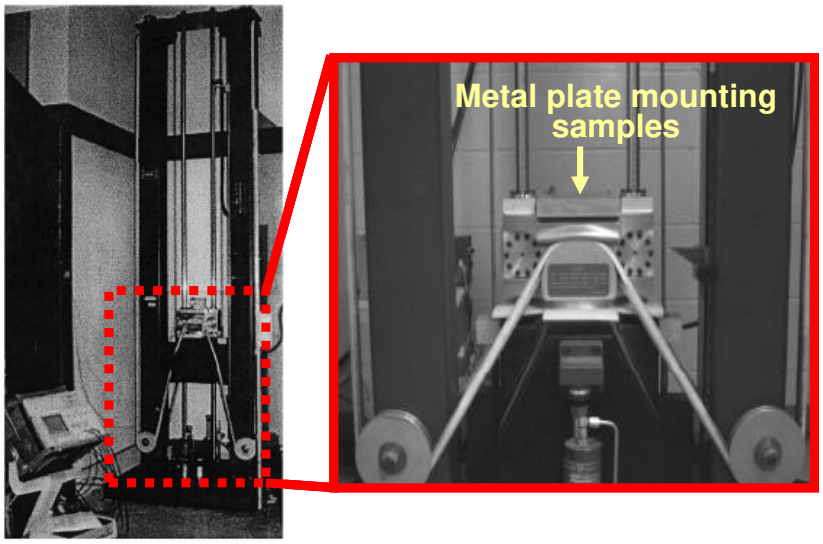

Figure 5.3. IMPAC66 HVA drop test machine.

This drop test is widely used in testing many devices including MEMS [16-18] and electronic devices [15, 19]. A drop machine without a pull-down option generated mid-range shock amplitudes up to 4200 g when the plate was dropped from 1.5-m height [15]. Anther drop machine employed the pull-down option and sharp contact-surface [14], and achieved higher shock amplitudes up to 30,000 g [16-18].

5.1.2. Design of Shock Test Machine

We defined four requirements in the design of our shock test machine. They are: (1) controlled shock direction, (2) repeatable shock amplitude, (3) wide selection of shock amplitudes, and (4) convenient manufacture and installation.

First, we need to control shock so that it is applied along a single direction. Our devices, which will be shown in later sections, are shock-protected to only one lateral direction but not to other directions. Second, we need to repeatedly generate the shock amplitudes because we will conduct many tests using multiple devices. Third, we need to produce a wide range of shock amplitudes by our shock machine to mimic the

many environmental shock conditions listed in Chapter 1. Thus, our machine needs to produce up to at least mid-range shock amplitudes. Finally, we need to easily manufacture and install our shock machine to reduce test costs.

Table 5.2 compares our requirements with the shock test methods shown in Table 5.1. As this table shows, the drop machine (drop test) is selected because it meets all of our four requirements.

Table 5.2. Shock test methods (in Table 5.1) compared with our requirements

Test method	Shock amplitude	Direction control	Repeata -bility	Convenient setup manufacture & installation
Shaker Table	~~Low (<100 g) (<500 g in an extreme case)~~	Provided	Yes	Easy
Impact hammer	~~Low-Mid~~	Need additional equipment		Easy
Hopkins bar	High (5,000-40,000g) (<200,000g in an extreme case)	Provided	Yes	~~Hard~~
Ballistic test	High (up to 100,000 g)	~~No~~	~~No~~	~~Hard~~
Drop Machine (Drop test)	Mid-High (<~4,000g w/o pull-down) (up to 30,000g w/ pull-down)	Provided	Yes	Easy
Our requirement	**Must be up to at least mid-range**	**Must be provided**	**Must be yes**	**Must be easy**

5.1.3. Manufactured Drop Test Machine

Figure 5.4 shows the conceptual view and photograph of our drop test machine. In this machine, samples are attached to a steel plate using thin epoxy, and dropped from a known height (H_d) guided by long aluminum guides to produce directional shocks. The steel plate collides with a steel rail at the foot of the drop test track. The sharp tip of the rail confines shock generation to a single point on the steel dropping plate and permits better control of the shock. We determined the contact time between

the steel plate and the steel rail by applying a 5V signal between the plate and the rail, and by measuring the time during which electrical contact is first achieved between the two. This critical contact time (ΔT) is shown in Figure 5.5 and ranged from ~200 to ~800 μSeconds, depending on H_d because the higher H_d generally produced smaller ΔT.

The ΔT and the dropping height (H_d) determine the shock amplitude applied to the test devices. While the steel plate contacts the steel rail, we assumed that a constant shock amplitude of A_{AV} (average shock amplitude) is generated and applied to our test devices. The meaning of the 'average' amplitude will be explained in the next section. This average shock amplitude (A_{AV}) can be estimated based on the computed velocity change during this time interval as shown in Equation 5.1 [15, 20].

$$A_{AV} = \frac{(COR+1)\cdot\sqrt{2\cdot 9.8\cdot H_d}}{\Delta T} \tag{5.1}$$

Here, COR is coefficient of restitution of steel. We also assumed that the test devices experience the same shock as they are firmly attached to the steel plate. Also, we assumed that the energy losses due to friction and the epoxy layer are negligible. Based on these assumptions and the dimensions of the setup, our drop tests could produce a maximum average shock of >2500 g when the steel plate is dropped from a height of ~8 feet (~2.4m).

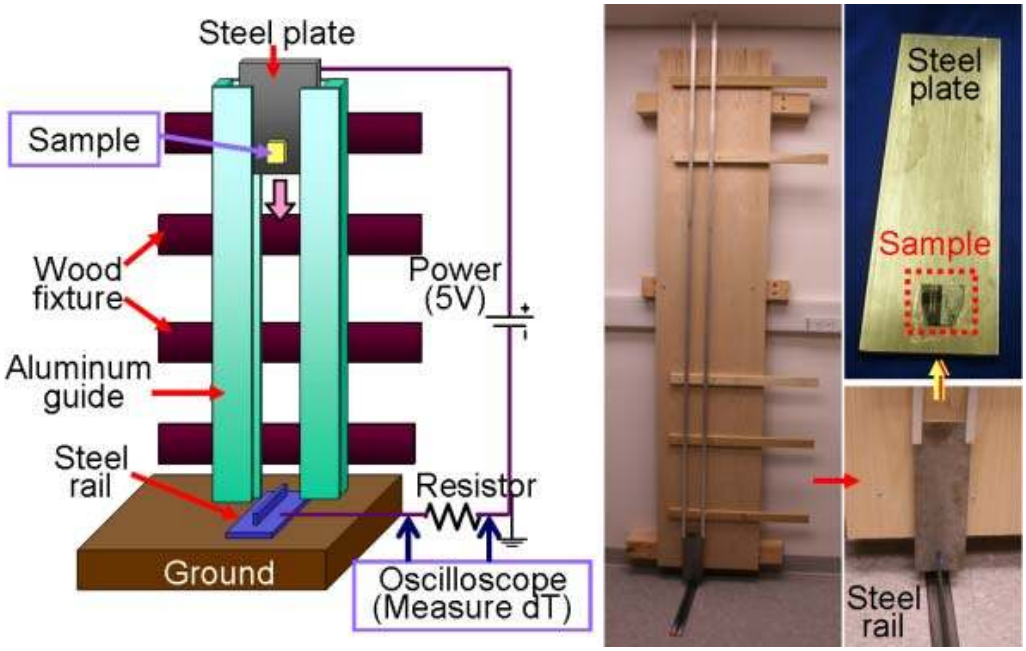

Figure 5.4. Our drop test machine (left: conceptual view, right: manufactured machine).

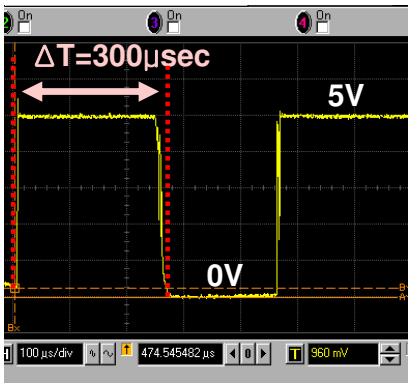

Figure 5.5. Time record of the contact time (ΔT) between the steel plate and the steel rail in our drop test machine in Figure 5.4.

5.1.4. Average and Peak Shock Load

The average shock amplitude (F_{AV} in force, A_{AV} in acceleration) used in Section 5.1.3 is expressed by $F_{AV} = \delta/T_{shock}$. Here, δ is impulse and T_{shock} is shock duration (e.g., ΔT in Section 5.1.3). The average shock amplitude assumes that a constant amplitude of F_{AV} is applied during the duration of shock. However, as Figure 5.6 illustrates, shock in a real environment varies by time and has a peak value of F_{PK}. The momentum of F_{AV} and that of F_{PK} are the area underneath each line and are the same based on conservation of momentum. The F_{PK} was frequently observed to be 2.2-3.5 times larger than the F_{AV}, as reported in several publications [21-23].

Shock amplitudes generated by our drop machine are expressed using average values (F_{AV} or A_{av}) in Section 5.1.3 and in following sections, and thus, the real peak shock amplitudes are larger than those values.

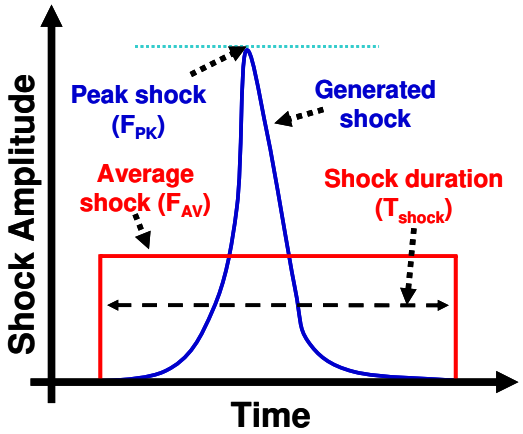

Figure 5.6. Conceptual illustration of (a) shock generated in a real environment and its peak value (F_{PK}) and (b) average shock (F_{AV}).

5.2. Design of Shock-Test Devices

Our shock tests aim to investigate the effect of the impact force. Therefore, our test devices must be flexible enough to touch their shock stops, but their bending stress must remain smaller than fracture stress so that no damage occurs by excessive bending stress. Also, to demonstrate the necessity of shock stops, the shock load used in our tests should generate sufficient bending stress to damage our test devices without any shock stops.

Before starting design, we first need to define fracture stress in silicon-based microstructures because the stress varies widely by test conditions. Section 5.2.1 surveys measured fracture stress in silicon structures and defines standard fracture stress for our situation. In Section 5.2.2, we use the defined stress and the maximum shock amplitude of our drop machine in Section 5.1.3 to design test devices. Section 5.2.3 and 5.2.4 describe the design of our nonlinear spring shock stops and soft coating shock stops.

5.2.1. Fracture Stress of Silicon-based Microstructures

The measured fracture stress of bulk single crystal silicon or thin-film polysilicon shows wide variations depending on many conditions, including the orientation of the silicon, the direction of the external load, the treatment of the specimen, and the measurement methods [21, 24-29]. Therefore, to define fracture stress for our purpose, we selected the situation the most similar to our study, that of load tests using a silicon beam fabricated from a wafer using dry etching methods.

Two papers presented load tests using RIE fabricated beams [9, 24]. One paper measured fracture stress using many (>400) cantilever beams [24]. The beams were fabricated from double-polished (100) wafers and have a width of 100 μm, a length of either 300 or 400 μm, and a thickness of 18-30 μm. The beams were defined by RIE and thinned down to their thickness with KOH backside etching. Using a custom-built loading stage, the cantilevers were then subjected to either vertical or lateral loading until they fractured. The paper summarized results by the direction of loading, i.e. vertical or lateral directions, and by the plane of fracture, i.e. (110) and (111) crystal planes.

The test results led to two major observations. The first one was that cantilever beams subjected to lateral loading tend to fracture at lower stress than those subjected to

vertical loading because of side-wall surface roughness created by the RIE process. The rough surface had more crack-initiation points than the polished surface, and thus fractures more easily. The second observation was that cantilever beams fracture more easily along (111) plane than along (110) plane. The planes are shown in Figure 5.7. This is because (111) crystal plane of silicon has the lowest surface energy to resist crack propagation. The fracture stress under lateral loading is 0.7-2 GPa along {111} plane and 1.4-3.1 GPa along z plane [30]. In contrast, the fracture stress by vertical loading is 0.7-5 GPa from frontside loading [30]. However, there was still huge variation in the measured fracture stress despite we narrowed test conditions.

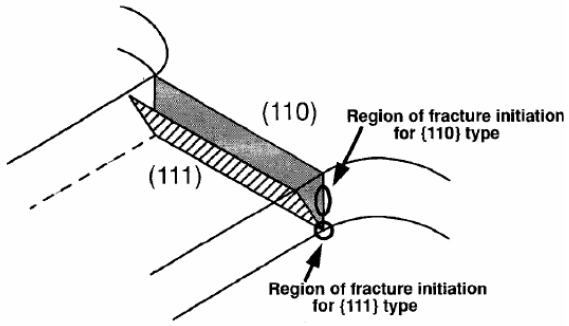

Figure 5.7. Schematic of fracture planes at the anchor of a micro-beam [24].

The second paper provides more detailed demonstration of the (111) plane fracture [9]. Cantilever beams were fabricated using a silicon wafer thinned down to 100 μm by KOH etching and patterned by deep RIE. The beams had a length of 1-7 mm and a width of 50-200 μm. After incident shocks, the beams fractured at their anchor because of high bending stress along with a (111) plane. Figure 5.8 clearly shows a micro-cantilever beam fractured along (111) planes.

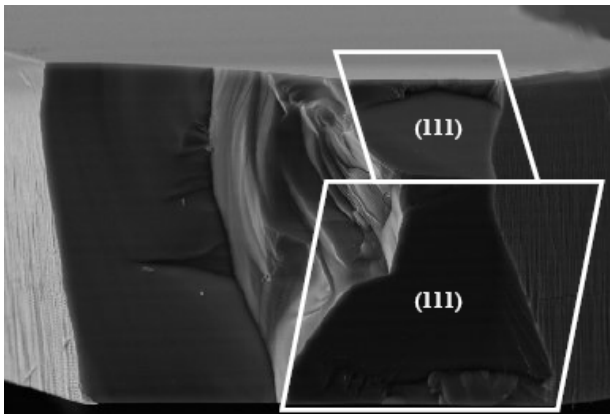

Figure 5.8. Fracture plane at the anchor of a micro-cantilever beam [9].

This fracture along the weakest (111) plane was also presented in another paper providing a more detailed study of the orientation dependence [25]. This paper used the more classic method of three-point bending (Figure 5.9). A silicon beam patterned by dicing was placed on the knife-edge supports and a load was applied on the bar. The silicon beam has a width of 2.7-2.8 mm and a thickness of 380-400 μm, and diced aligned with the direction of <100> and <110> using (100) wafer, and with the direction of <111> using (110) wafer. The test results compare the stress inducing (100), (110) and (111) plane fracture, and fracture stress applied to the (111) is the lowest, consistent with results presented in the first paper. The test was conducted using 30 samples per direction. All planes had average fracture stress of ~0.51 GPa along (111), ~0.68 GPa along (110) and 0.78 GPa along (100) planes. These values are slightly lower than but not significantly different from previous observations.

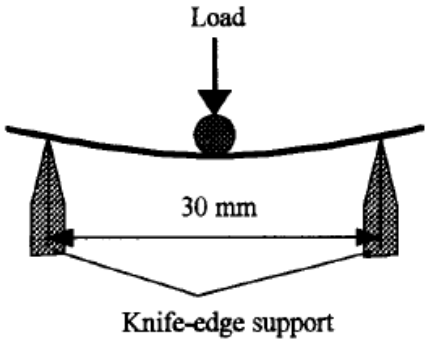

Figure 5.9. Three point test to measure bending stress [25].

Our situation is that a micro-structure fabricated using a (100) wafer is subjected to side loading. Both (110) and (111) fracture can happen in our situation. In our test-device design, we decided to choose the worst case, i.e. lowest fracture stress along (111) plane, as our standard and it is 0.5-0.7 GPa. This is a bit lower than 0.8-1 GPa, the value that is generally accepted in designing shock protection for MEMS, as described in Chapter 1.

We designed our test structures to meet the three following requirements.

(1) The device's bending stress must be significantly lower than 0.7 GPa when the device mass touches its shock stops.

(2) The device must touch its shock stops under the shock load generated by our shock test setup

(3) The device's bending stress must be larger than 0.7 GPa when the device

without shock stops is subjected to the shock load generated by our test setup.

All our test devices were confirmed to meet the three requirements and ensured to exclude shock-induced damages by excessive bending stress from excessive device displacement.

5.2.2. Design of Test Devices

Our test devices are designed to meet the three criteria listed in Section 5.2.1. The dimensions of the designed devices are listed in Table 5.1. Every device has a 10-μm gap between the device mass and each shock-stop design. The devices were fabricated using silicon wafers having a thickness of 100 μm or 475 μm.

Table 5.3. Designed test devices and their characteristics

Design	Mass	Thick-ness	Beam width	Beam stiffness	Res. freq.	Displace-ment by 1000g static load	Max. bending stress	
							10μm bending	No stops (1000g)
SOG-A	0.97mg	100μm	50μm	111 N/m	1.70 kHz	86μm	70 MPa	0.9 GPa
SOG-B	0.97mg	100μm	30μm	105 N/m	1.66 kHz	91μm	150 MPa	1.8 GPa
SOG-C	0.97mg	100μm	50μm	79 N/m	1.44 kHz	120μm	60 MPa	1.0 GPa
SOG-D	0.97mg	100μm	50μm	203 N/m	2.30 kHz	47μm	120 MPa	0.8 GPa
Piezo	5.1mg	400μm	50μm	188 N/m	1.00 kHz	266μm	50 MPa	1.8 GPa
Our require-ments						**> 10 μm**	**< 500 MPa**	**> 0.7 GPa**

First, when bent by 10 μm, our devices experience the maximum bending stress of 50 M-150 MPa developed at their anchor. The maximum bending stress is at least three times smaller than our standard fracture stress (0.5-0.7 GPa) discussed in Section 5.2.1. By rule of thumb, we have 2-3 times the margin of stress necessary to ensure that no fracture will occur by bending stress in our devices. No previous work reported this low fracture stress. Therefore, our devices, no matter what sort of shock stops they have, should not be damaged by bending stress. This absence of damage was verified using beam theory [31], FEM simulation, and static loading experiments. We applied static loading by bending the mass of the test device in the lateral direction until the mass touches its shock stops, and found that no devices were damaged. In the vertical direction, where there are no shock stops, every device was broken at its anchor,

where the maximum bending stress was created (Figure 5.10). We integrated shock stops along only one direction to protect against applied shocks in along with one direction, but stops for other directions can be also fabricated.

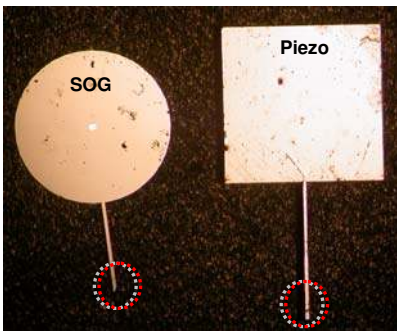

Figure 5.10. Test devices damaged by static loading in the vertical direction, where no shock stops exist. As expected, both SOG and piezoresistive (Piezo) devices were damaged at their anchors (highlighted).

Second, all devices touch the 10-μm-distance shock stops when a static loading of 1000 g is applied. This factor is designed to take into consideration the fact that our shock test setup can apply shock amplitude larger than 1000 g.

Third, all devices suffer 0.8-1.8 GPa bending stress when no shock stops are integrated and a 1000-g shock is applied. This bending stress is larger than our standard fracture stress (0.5G-0.7 GPa) and therefore, all devices without shock stops will fracture.

Therefore, our designed test devices meet all three criteria discussed above.

5.2.3. Design of Nonlinear Spring Shock Stops

We conducted two experiments using nonlinear spring shock stops. The first experiment aimed to compare the shock performance of nonlinear spring stops with that of hard shock stops. In this experiment, shock beams forming shock springs were designed to be rather stiff to survive large shock amplitude of >5000 g (average shock, A_{AV}). In contrast, the second experiment was designed to include several shock-beam designs having various maximum allowable shock amplitudes. These custom-made shock beams were designed to survive up to 300 g, 570 g, 900 g, 1900 g, and >5000 g. The shock springs are expected to fracture at shock amplitudes larger than their designed values. The dimensions of the designed shock-stop beams are listed in Table

5.4.

Table 5.4. Physical dimensions of designed shock beams

Target shock	Shock beam width	Shock beam length	Number of shock beams
~300g	10 μm	2000 μm	1
~570g	20 μm	3300 μm	1
~900g	20 μm	1300 μm	1
~1900g	30 μm	1300 μm	1
> 5000g	50 μm	1000 μm	3

5.2.4. Design of Soft Coating Shock Stops

Parylene is selected as the coating material due to its conformal coverage and room-temperature deposition [32, 33]. In addition, Parylene is chemically stable [34]. Therefore, we can minimize possible device damage by the Parylene deposition process. The thickness of Parylene is selected to be sufficient so that a device mass is not deflected to the point of touching the hard surface underneath the Parylene film by the maximum shock amplitude of our machine. One the basis of the analysis and simulation in Chapter 4, we decided to coat our test devices with a 3-μm-thick Parylene film.

This 3-μm thickness is not suitable for several MEMS devices that have narrow gaps (<3μm). The soft coating shock stops can be integrated with narrow-gap devices by one of two methods. In the first method, can one simply reduce Parylene thickness. However, this method also reduces the sustainable shock amplitude. In the second method, one can simply use selective etching of Parylene through a silicon shadow mask [35], [36]. This selective Parylene etching can also be used to expose critical parts, such as metal pads.

5.3. Test Device Fabrication

Both shock stops can be conventionally integrated with many MEMS devices without excessive area expansion. In addition, nonlinear spring stops do not need additional fabrication processes. Moreover, both shock stops are compatible with current MEMS fabrication processes, and provide wafer-level and batch process. We demonstrated these benefits by fabricating test devices.

5.3.1. Devices with Nonlinear Spring Shock Stops

We integrated nonlinear shock stops with two micromachined devices with different sensing mechanisms and made by different processes. One is a capacitive accelerometer using the Silicon-On-Glass (SOG) process (Figure 5.12) [37]. The other is a piezoresistive accelerometer using highly-doped LPCVD polysilicon piezoresistors (Figure 5.13) [38].

Figure 5.11a shows the SOG process flow. A Pyrex glass wafer is recessed. Then a shield metal layer is deposited and patterned (a-1), which is used to prevent the footing effect generated by deep reactive ion etching (DRIE). Next, a 100-µm-thick, double-polished silicon wafer is anodically bonded to the glass wafer (a-2), and contact-pad metal is deposited and patterned (a-3). Finally, a through-wafer-etch is preformed using DRIE to form the device and shock stops (a-4).

Figure 5.11b shows the piezoresistive device's process flow. We used a 475-µm--thick double-polished silicon wafer. First, we deposit LPCVD nitride (1000 Å), and then deposit high-boron-doped polysilicon (1 µm) using LPCVD (b-1). Next, piezoresistors and contact pads are formed using RIE (b-2). Finally, the device and stops are defined using DRIE (b-3: 400-µm front etch, b-4: 75-µm backside etch), and mounted on glass slides.

Note that, in both cases, the device and the shock stops are fabricated in a single step and made of the same material (silicon). This simplifies fabrication and integration. It is also possible to fabricate shock stops using other materials as needed.

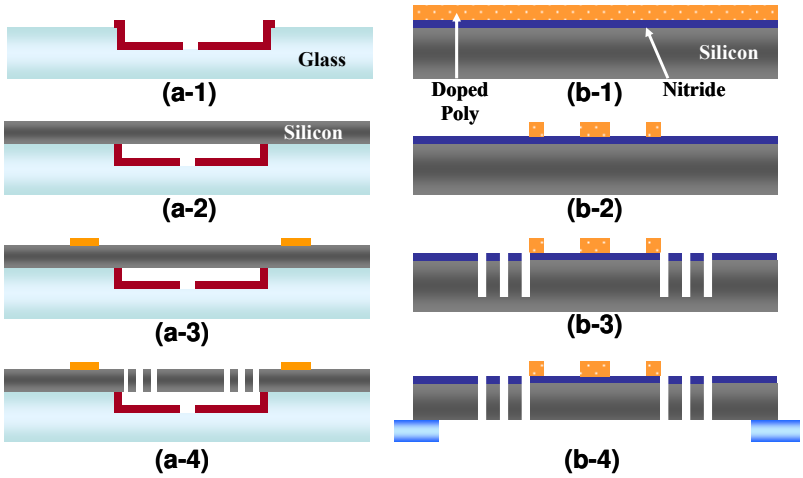

Figure 5.11. Fabrication process flow of (a) Silicon-On-Glass (SOG) capacitive and (b) high-doped polysilicon piezoresistive devices.

Figure 5.12 and Figure 5.13 show the fabricated devices and shock stops. Shock stop beams are fabricated by deep silicon etching for different etch depths (Figure 5.12: 100 μm, Figure 5.13: 400 μm), and both show uniform beam widths (46-49 μm) and gaps (Figure 5.12: 10 μm, Figure 5.13: 21-24 μm). Figure 5.13 also shows fabricated piezoresistors, having ~15k-Ω original resistance.

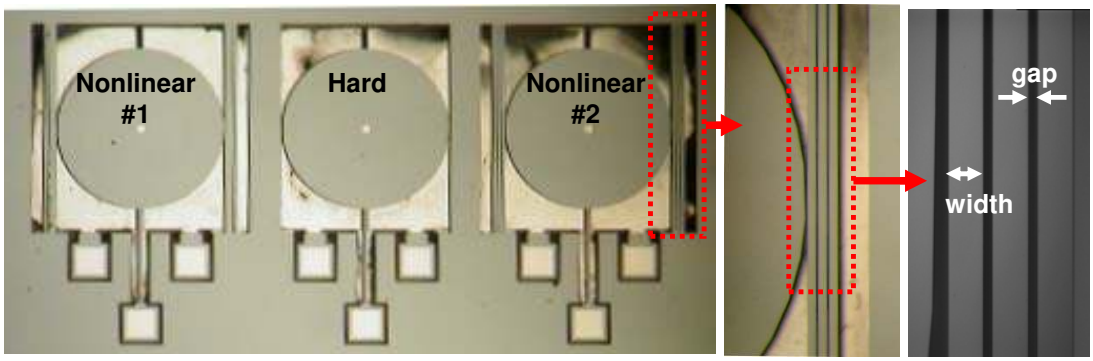

Figure 5.12. Fabricated capacitive accelerometer integrated with nonlinear spring shock stops using SOG process.

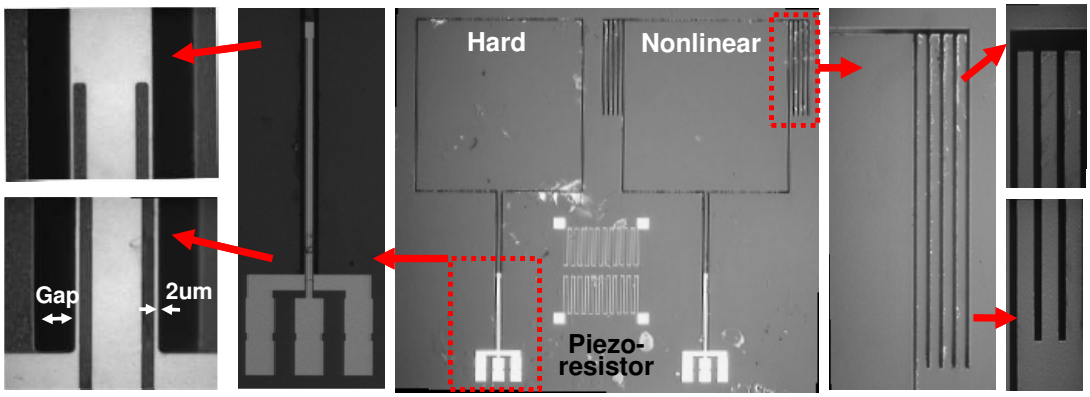

Figure 5.13. Fabricated piezoresistive accelerometer integrated with nonlinear spring shock stops using highly doped polysilicon.

5.3.2. Devices with Soft Coating Shock Stops

Soft-coating-shock-stop test devices were fabricated using the modified SOG process flow is shown in Figure 5.14. We first create a recess (10 μm) in a Pyrex glass wafer and pattern a shield metal layer (Figure 5.14a), and then the glass wafer is halfway diced to form scribe lines. The glass wafer is anodically bonded to a 100-μm-thick, double-polished silicon wafer; and then contact pad metal is deposited and patterned (Figure 5.14b). A DRIE through-wafer-etch is preformed to form the device

and shock stops (Figure 5.14c). Finally, some samples are coated with a 3-μm-thick Parylene film to form soft coating shock stops (Figure 5.14d), while some samples are completed without this coating to make hard shock stops. Figure 5.15 shows fabricated hard (silicon) and soft coated (Parylene) shock stops and devices.

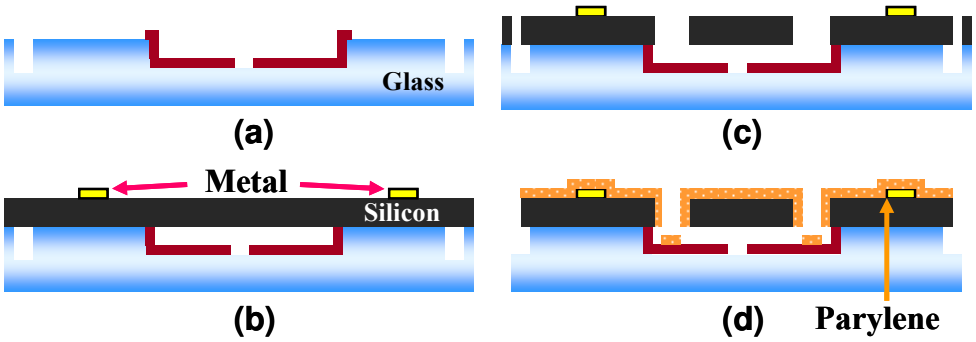

Figure 5.14. Fabrication process flow of soft-coating test devices and Parylene coated shock stops.

We first create a recess (10 μm) in a Pyrex glass wafer and pattern a shield metal layer (Figure 5.14a), and then the glass wafer is halfway diced to form scribe lines. The glass wafer is anodically bonded to a 100-μm-thick, double-polished silicon wafer; and then contact pad metal is deposited and patterned (Figure 5.14b). A DRIE through-wafer-etch is preformed to form the device and shock stops (Figure 5.14c). Finally, some samples are coated with a 3-μm-thick Parylene film to form soft coating shock stops (Figure 5.14d), while some samples are completed without this coating to make hard shock stops. Figure 5.15 shows fabricated hard (silicon) and soft coated (Parylene) shock stops and devices.

Figure 5.16 shows SEM views of suspended microbeams covered with a 3-μm-thick layer of Parylene, demonstrating the excellent step coverage of Parylene without damaging the released structure.

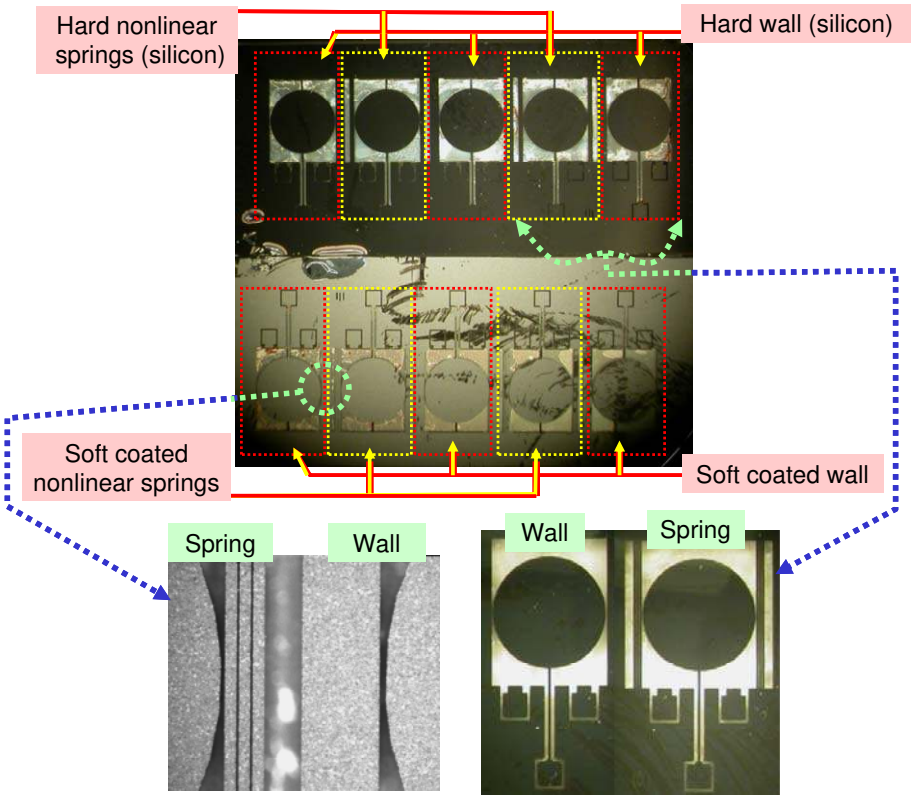

Figure 5.15. Top views of the fabricated hard (silicon) and soft coated (Parylene) devices. Each sample has three wall and two nonlinear spring devices.

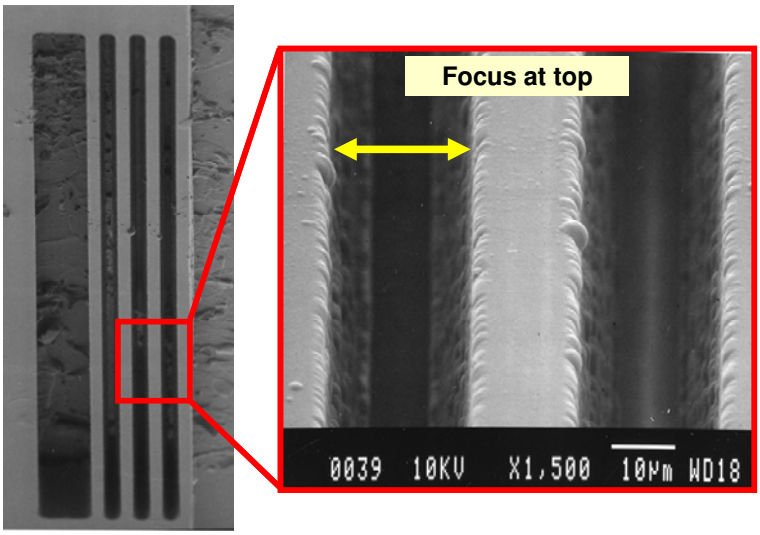

Figure 5.16. SEM of the top view of suspended micro-beams after Parylene deposition. It shows excellent step coverage.

5.4. Shock Test Results

5.4.1. Shock Test Process

Multiple shock tests were conducted using multiple devices from different wafers. During a test, for a fair comparison, all devices used in the test were fabricated on the same wafer and had identical dimensions. Nonlinear-spring devices were fabricated on the same die as the hard-stop devices serving as a benchmark. Soft-coating devices, also fabricated from the same wafer, have larger gaps than the hard-stop devices to compensate for the gap decrease resulting from Parylene deposition. Because the Young's modulus and the thickness of Parylene (3 GPa, 3μm) are smaller that those of silicon (160 GPa, 100μm), the change of device characteristics by Parylene deposition is negligible. Calculations using a multi-layer model [39] show that only minor changes occur in both the stiffness (<0.1%) and mass (<5%) of the test device.

Shock loading was applied initially using an impact hammer (PCB-86B03), and later, using our drop machine explained in Section 5.1.3. For a fair comparison, all of the different test devices were mounted together on a PC board (for the hammer test) or on a steel plate (for the drop test). Applying a shock load to the entire PC board (or the steel plate) ensured that each design is subjected to the same shock.

5.4.2. Shock Test I – Comparison of Nonlinear-Spring-Stop Devices to Hard-Stop Devices

The two nonlinear spring devices were fabricated on the same die as the hard stop device serving as a benchmark, as shown in Figure 5.12 and Figure 5.13. After several impacts, all devices with hard stops failed, but those protected by the nonlinear spring shock stops survived without damage, as shown in Figure 5.17. We conducted subsequent tests with substantially higher shock levels, and again observed that almost all devices with the nonlinear shock stops survived. In summary, 22 out of 25 devices were survived (88% survival rate).

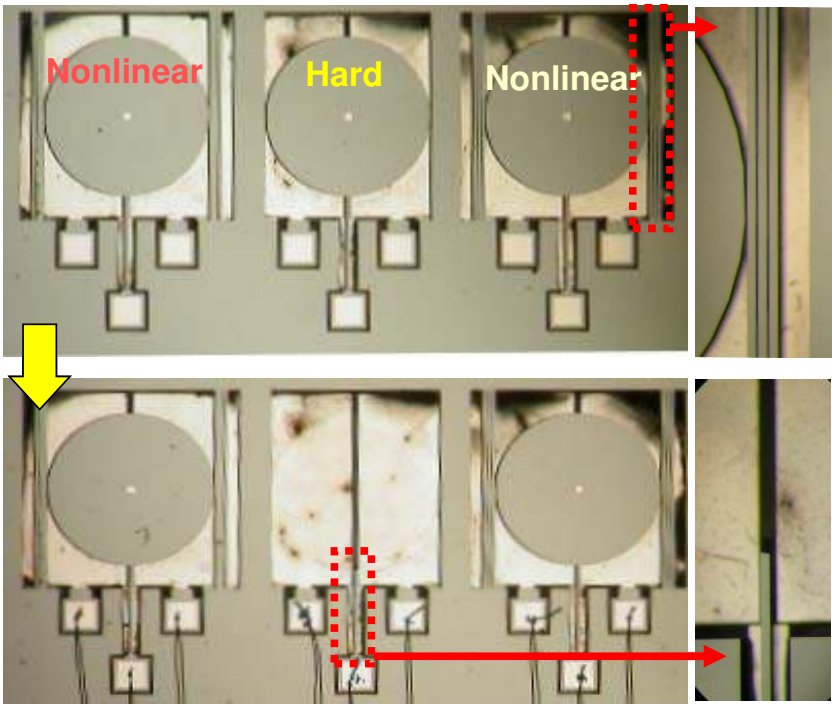

Figure 5.17. Nonlinear spring stops and hard stops after several impacts. Only a device with hard stops was damaged at the tip close to the device mass.

5.4.3. Shock Test II – Comparison of Soft-Coating-Stop Devices to Hard-Stop Devices

Figure 5.18 is a series of photographs of the hard wall and soft coating shock stop devices (shown in Figure 5.13) following drop tests. Testing started with the application of a small shock to the test devices. We then applied increasingly larger shocks by dropping the test devices from higher distances. Shocks under ~640 g produced no observable damage to either hard-shock-stop or soft-shock-stop devices (Figure 5.13a). When a shock of ~840 g was applied, one hard stop device broke (Figure 5.13b). The two remaining hard stop devices were damaged after a shock of ~940g (Figure 5.13c). No damage was observed on any soft stop devices for shocks up to ~1300g (Figure 5.13d). We conducted this series of experiments four times, using four different samples, each containing several hard and soft shock stops. Total of 17 devices were tested and 16 were survived (94% survival rate). This result was consistent with the result in Section 5.4.2; our shock technology has superior device survival rate compared with conventional hard shock stops in our test conditions.

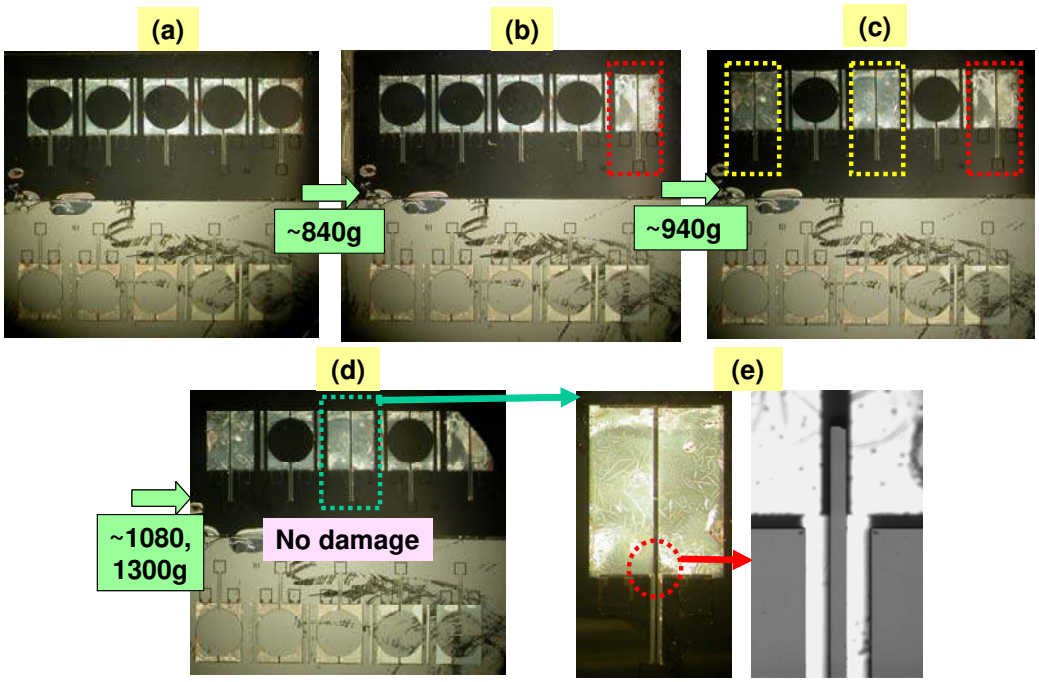

Figure 5.18. A series of photographs of the test samples containing both hard wall and soft coating shock stops following each drop test for the device shown in Figure 5.15. All hard stops were damaged at the tip close to the device mass.

5.4.4. Summary of Shock Tests Comparison with Hard Shock Stops

Table 5.5 summarizes our findings both from the analysis in Chapter 4 and from the experiments in Chapter 5. The table clearly shows that both the nonlinear spring shock stops and the soft coating shock stops provide shock protection superior to conventional hard shock stops in our test situations. For shocks ranging from ~100 g to 2500 g, only 4% of the hard shock stop devices survived all impacts, compared to 88% of nonlinear spring devices and 94% of soft coating devices.

It is interesting to note that in the majority of the damaged devices with hard stops, the support beam failed quite close to the proof mass (i.e., tip of the device beam), not at the anchor where the maximum stress due to bending occurs. In addition, we verified that the maximum bending stress of the device at the anchor is indeed lower than the fracture stress of silicon based on beam theory, FEM simulation, and static loading experiments, as described in Section 5.2.2. Therefore, the damage of our hard-shock-stop devices occurred by a mechanism different from previously known ones, and we discuss a new fracture mechanism induced by impact force in Section 5.5.

The test devices presented here are designed solely to compare shock-survival rates between the two new shock protection concepts and conventional hard shock stops,

and thus, have simpler structures than real MEMS devices. To implement our concepts into a real device, our shock stops will be used at only the critical parts of the device. This implementation can be realized in various ways. One possibility is to use comb fingers as shock stops, as presented in a previous work where several comb fingers were fabricated to have smaller gaps than other fingers to act as motion-limit stops [40]. Another possibility is to use shock stop beams attached to the mass and frame of a device [41].

Table 5.5. Summary of tests results comparing three shock-protection methods

			Conventional	Nonlinear spring		Soft Coating	
Simulation	Criteria		Hard wall	Beam cascade	Single beam	Parylene coating	Gold coating
	Impact force		100%	2.38%	1.52%	<24%	<60%
	Max. deflection		20 μm	20 μm	20 μm	~20 μm	20 μm
	Collision number		Minor change	Small reduction		> 90% reduction	
Experiments	Sample number	Max. shock	Survival/Total	Survival/Total		Survival/Total	
	SOG, 1-4	2500g	0/10	12/15			
	Piezo-1		1/3	2/2			
	SOG, 5-8		0/10	6/6		16/17	
	SOG, 9		0/4	2/2			
	Summary		*1/27 (4%)*	*22/25 (88%)*		*16/17 (94%)*	*N/A*

5.4.5. Shock Test III – Tailor-Made Nonlinear Spring Shock Stops

In Chapter 4, we claimed that the design of the nonlinear spring shock stops should be optimized. The compliance of the shock-stop springs (i.e. beams) should be maximized to minimize the generated impact force; however, the compliance is upper limited because the maximum bending stress developed in the device and shock-stop beams must remain less than the fracture stress. Therefore, the shock-stop beams must be stiff enough not to fracture by the excessive bending stress. To verify this claim, several experiments were conducted.

We designed and fabricated nonlinear spring stops having different target-shock amplitudes, i.e., shock-beam structures having various dimensions, as described in Table 5.4. Figure 5.19 shows the fabricated devices and their target-shock amplitudes. Two types of test devices were designed with almost the same mass/stiffness but

different beam width/length (Designs SOG-A and SOG-B in Table 5.3 and Figure 5.19). Each nonlinear spring shock stop was designed to fracture at shock amplitudes of 300 g, 570 g, 900 g, 1900 g, and >5000 g, using theories in our previous works [42, 43] and using an average of fracture stress [24]. Each design had one SOG- A and one SOG-B device (total two devices). Four hard-stop devices (two of each type) were also included as a benchmark. All devices were fabricated and tested together.

Shock was applied, starting at the lowest value, using our drop machine illustrated in Figure 5.4. No damages were observable up to 140 g. But when a larger shock was applied, the devices and/or the shock stops began to fail, as expected. Figure 5.20 shows the damaged devices and shock beams. The devices and shock beams in the figure were designed to be durable up to 300 g and 570 g. All 300-g devices were fractured by 520-g and 620-g shocks, and one of the 570-g devices was damaged by a 620-g shock.

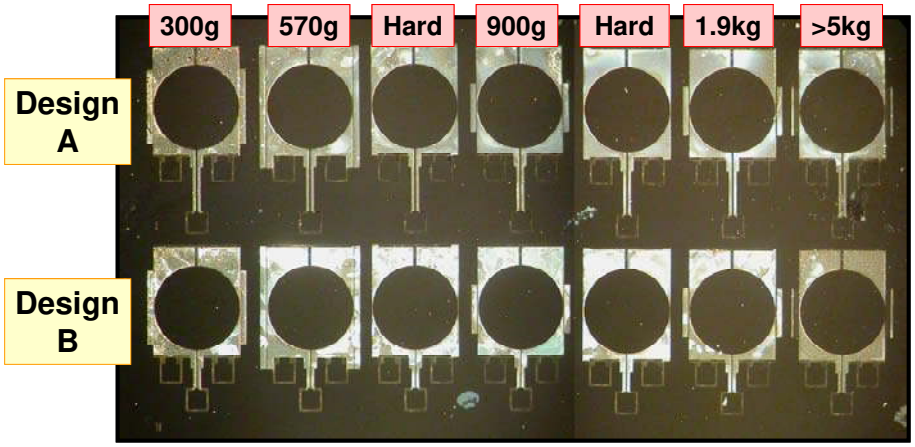

Figure 5.19. Fabricated shock-stops designed to have different target-shock amplitudes. Hard stops are also fabricated as a benchmark.

It is interesting that the damaged devices failed both at their shock-stop beams and at the tip of the device beams. It is likely that the device first fractured at the shock beams, then it collided with the hard stops made by the substrate, and was consequently damaged by the impact force as happened in hard-stop devices in Sections 5.4.1 to 5.4.3.

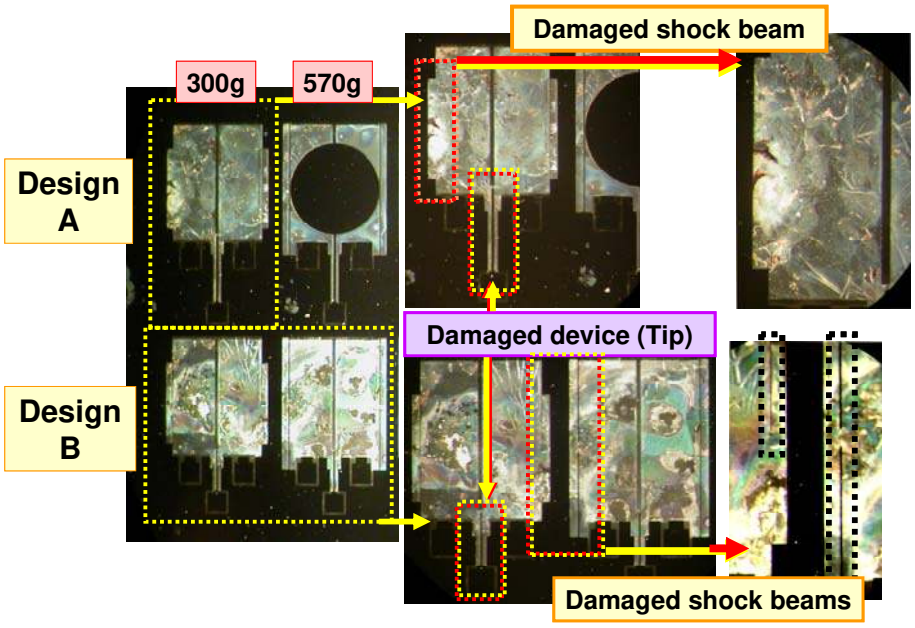

Figure 5.20. Fractured device and shock-stop beams after shocks.

Figure 5.21 summarizes the test results. The shock-survival range for each device is designated by the bar. In the figure, the applied shock amplitudes are listed only when at least one device failed, even though other shock amplitudes were also applied. For example, one of the four hard-stop devices was damaged by a ~240-g shock, and the rest of them broke at ~520g. One of the 300-g devices was damaged by a ~520-g shock, and the other was damaged by a ~620g. All devices designed to survive >5k-g survived after an application of 2.5k-g shock.

Figure 5.21 clearly shows that each shock-stop-beam design failed at or above its target-shock amplitude. In addition, as a device's target-shock-amplitude increased, the shock-amplitude fracturing the device also increased, excluding one exception (one of 570-g devices failed at 1.9kg). These results verify that optimization of shock-beam designs is required to maximize shock protection and that the shock beams must be stiff enough to survive a target shock amplitude in each application.

The beam-fracturing shock amplitude was slightly different in theoretical and experimental values; one possible reason can be the wide variation of fracture stress (described in Section 5.2.1), which is extremely diverse.

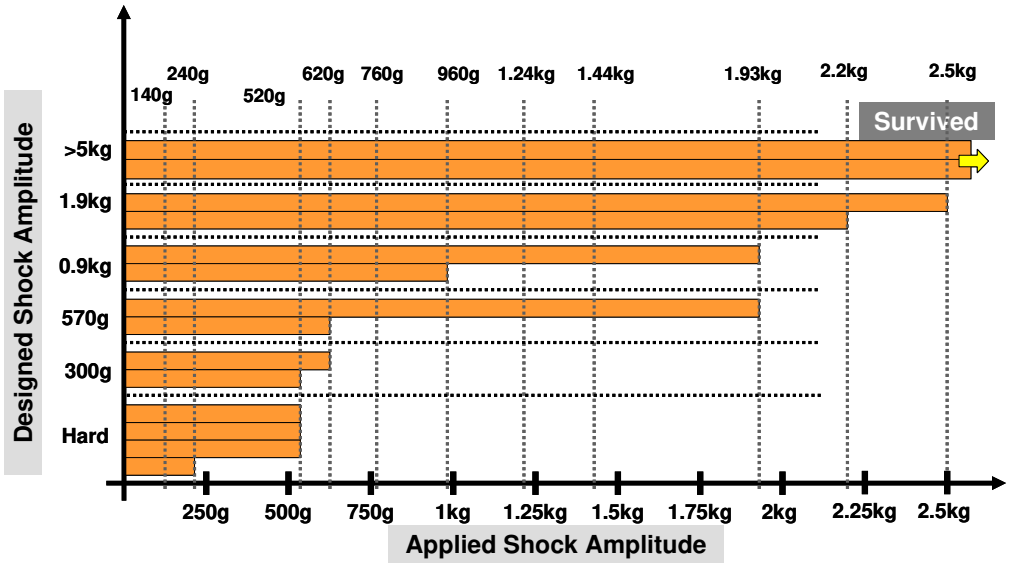

Figure 5.21. Test results of the nonlinear spring shock stops in Figure 5.19.

5.5. Fracture Mechanism by Impact Force

In our shock test results, we repeatedly observed a device-fracture phenomenon different from previously reported shock-test results. Previous shock tests [9, 11, 24] showed that fractured devices failed at the anchor point of their supporting beams. This occurs because the anchor is the location of the maximum bending stress, and shock studies in the MEMS field have focused on limiting this bending stress. However, a majority of our test devices failed at the support beam quite close to the proof mass, not at the anchor point of the beam, even though our devices were designed to experience the maximum bending stress at their anchor points, as explained in Section 5.2. Therefore, we concluded that the damaging mechanism of our test devices was induced by impact force generated from the hard shock stops in our test conditions.

5.5.1. Impact-Force-Induced Fracture in Our Test Devices

The fracture at the tip of device-beam can be explained by considering dynamic behavior of the proof mass after impact. Figure 5.22 explains how the impact force (F_{IM}) generates high stress at the tip of the beam. The movement of each part of the device is shown with a dot -arrow. In response for the external shock, the device mass begins to move to the right side (Figure 5.22a) and eventually comes to contact with the

shock stop. Before contact, the center of the device mass and each part of the device beam move in the same direction, as shown with the dot-arrows. At the instant of impact, the device mass is 'stopped' by the hard shock stop (Figure 5.22b) and begins to accelerate in the opposite direction (i.e., left side). However, the beam, which has its own inertia, continues to move in the original direction (i.e., right side). This produces a large beam curvature at the tip of the beam connected to the device mass, which is highlighted in Figure 5.22c. Starting with the tip, the large curvature propagates through the beam to the anchor. This implies that a huge bending stress is generated, since the bending stress σ_B is proportional to the beam curvature κ by the following equation [31].

$$\sigma_B \propto \kappa \tag{5.2}$$

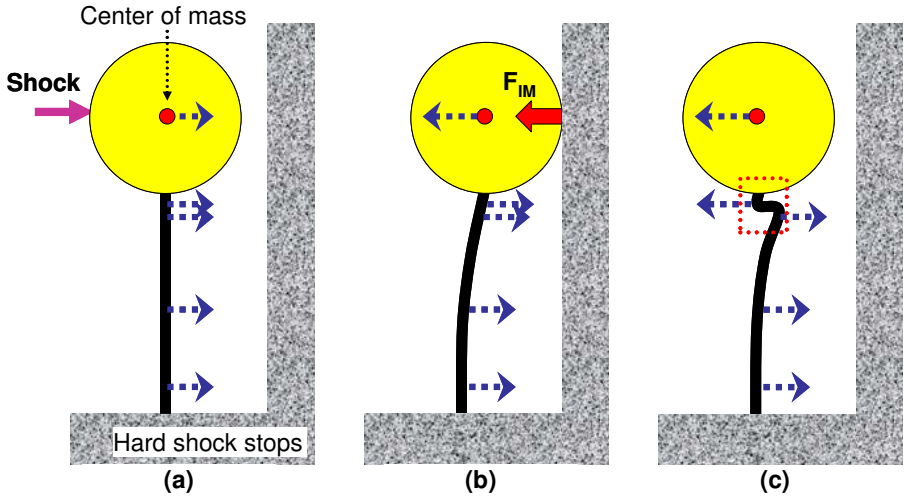

Figure 5.22. Device facture mechanism by impact force (F_{IM}) generated from the contact between the device mass and its hard shock stops. A device with cantilever beam is used in our shock tests.

As shown in Figure 5.22, the maximum bending stress by the impact force is initially generated at the tip of the beam, and then gradually propagates through the beam to the anchor. Therefore, the tip of the device beam first experiences high stress and fails if the impact-force-induced bending stress goes over the fracture stress of silicon.

This bending stress induced by the impact force explains the previously undiscussed fracture phenomenon that we observed in our test devices. This

phenomenon and mechanism have rarely considered in previous MEMS researches. Previous works analyzed the detailed motion of a flexible beam (that has its own inertia) subjected to external impact using a Euler-Bernoulli beam equation [44, 45].

This phenomenon explains the behavior at our devices but may also be extended to outer structures.

5.5.2. Impact-Force-Induced Fracture in Clamped-Clamped Beam Structure

The same phenomenon is observed in many other MEMS designs other than the cantilever beam structure shown in Figure 5.22. Clamped-clamped beam structure is another commonly used structure in MEMS. When a clamped-clamped beam is subjected to a side shock loading (Figure 5.23), it experiences the same mechanism that occurred in cantilever beam structures described in Section 5.5.1. Because of the impact force from the hard shock stops, a large curvature is generated at the tip of the beam and gradually propagates through the beam to its anchor. Therefore, we can expect that this clamped-clamped beam structure will also fracture at its tip, not at its anchor.

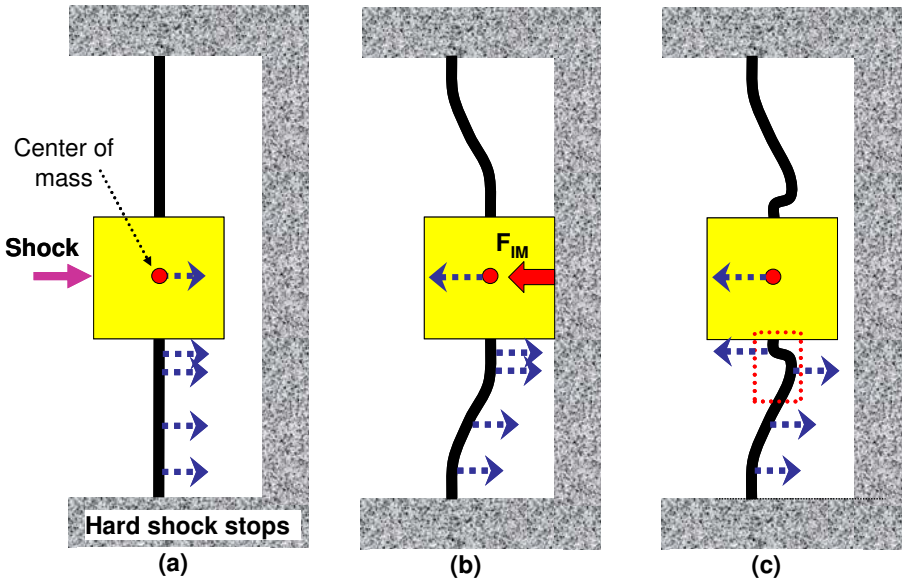

Figure 5.23. Impact-force induced fracture mechanism in another device with clamped-clamped beam structure.

5.6. Summary

In this chapter, we fabricated and tested two novel shock protection technologies

we developed and designed in Chapter 4. These technologies employ either nonlinear spring structure or soft coating as shock stops and overcome some drawbacks of previously reported shock-protection techniques. The proposed shock stops reduce the impact force generated when a device contacts its shock stops as well as decouple the shock-protection design from the device design. Moreover, they allow wafer-level and batch fabrication processes compatible with current MEMS fabrication.

The test devices of nonlinear spring shock stops were fabricated using silicon micro-beams, and the soft coating shock stops were made using a Parylene-film coating. Silicon beams were selected to demonstrate that the nonlinear spring shock stops can be simultaneously fabricated with the device in a single step, and thus no additional fabrication steps or masks are required. Parylene was selected as coating material due to its conformal coverage, room-temperature deposition, and chemical stability. Both devices could be easily integrated with MEMS devices without excessive area expansion.

The fabricated devices and benchmark devices (hard-shock-stop devices) were selected from the same wafer and mounted together on a test platform to maintain the same test conditions. The mounted devices were tested using either an impact hammer or a drop machine we built. The test results show that the device-survival rate of both nonlinear spring (88%) and soft coating (94%) shock stops are considerably superior to conventional hard stops (4%).

It is interesting that most damaged devices were fractured at the tip of the device beam close to the device mass, not at the anchor of the beam. This phenomenon reveals that a device can fail even though the maximum bending stress at the device anchor is limited, because the stress induced by the impact force becomes more critical in our test devices and test conditions.

The effect of the impact-force-induced stress has not been significantly emphasized or comprehensively understood in conventional shock-protection technologies for MEMS. Therefore, we have analyzed the device-fracture mechanism using the dynamic response of a flexible beam subjected to an impact, and identified that a huge impact-force-induced stress is developed at the device beam's tip.

In addition, devices having shock stops with different target-shock amplitudes were fabricated and tested. The results verified that the design of shock-stop beam should be optimized.

References

[1] H.-J. v. Martens, A. Taubner, W. Wabinski, A. Link, and H.-J. Schlaak, "Traceability of vibration and shock measurements by laser interferometry," *Measurement,* vol. 28, pp. 3-20, 2000.

[2] F. D. Coninck, W. Desmet, P. Sas, and D. Vaes, "Multisine shock and vibration testing using a high-frequency 6-DOF shaker table," in the Proceeding of *International Congres on Sound and Vibration*, Stockholm, Sweden, 2003.

[3] M. Karshenas, M. W. Dunnigan, and B. W. Williams, "Adaptive inverse control algorithm for shock testing," *IEE Proceedings of Control Theory and Applications,* vol. 147, pp. 267-276, 2000.

[4] Type 4809 (Bruel & Kjaer)

[5] Shock testing of shipboard equipment (Center of Mechanical and Maritime Structures, Thales Naval Nederland, Netherlands)

[6] M. J. Carre and S. J. Haake, "An examination of the Clegg impact hammer test with regard to the playing performance of synthetic sports surfaces " *Sports Engineering,* vol. 7, pp. 121-129, 2004.

[7] J. Knapp, E. Altmann, J. Niemann, and K. D. Werner, "Measurement of shock events by means of strain gauges and accelerometers," *Measurement,* vol. 24, pp. 87-96, 1998.

[8] AACS Shock Calibrator, Model 2973A (ENDEVCO)

[9] M. Sheehy, M. Reid, J. Punch, S. Goyal, and G. Kelly, "The failure mechanisms of micro-scale cantilevers in shock and vibration Stimuli," in the Proceeding of *Symposium on Design, Test, Integration and Packaging of MEMS & MOEMS*, 2008.

[10] D. M. Tanner, J. A. Walraven, K. Helgesen, L. W. Irwin, F. Brown, N. F. Smith, and N. Masters, "MEMS reliability in shock environments," in the Proceeding of *IEEE International Reliability Physics Symposium*, 2000, pp. 129-138.

[11] M. A. Duesterhaus, V. I. Bateman, and D. A. Hoke, "Shock testing of surface micromachined MEMS devices," in the Proceeding of *Auunual Fuze Conference*, New Orleans, LA, USA, 2003.

[12] X. Peng, Z. Jing, and L. Zu-Seng, "The study of buffer structure of on-board test's circuit module in high shock," *Instrumentation and Measurement, IEEE Transactions on,* vol. 53, pp. 1224-1226, 2004.

[13] C. H. Robinson, R. H. Wood, T. Q. Hoang, and D. Hollingsworth, "Development and demonstration of a MEMS-based safety and arming device for the 20-mm OICW fuze," in the Proceeding of *NDIA Joint Services Small Arms Conference*, Atlantic City, NJ, USA, 2002.

[14] M. A. Childers, "Evaluation of the IMPAC66 Shock Test Machine, Serial Number 118," 2002.

[15] T. Y. Tee, H. S. Ng, C. T. Lim, E. Pek, and Z. Zhong, "Impact life prediction modeling of TFBGA packages under board level drop test," *Microelectronics and Reliability,* vol. 44, pp. 1131-1142, 2004.

[16] J. K. Yee, H. H. Yang, and J. W. Judy, "Shock resistance of ferromagnetic micromechanical magnetometers," *Sensors and Actuators A: Physical,* vol. 103, pp. 242-252, 2003.

[17] R. G. Azevedo, J. G. Debbie, A. V. Jog, J. Babak, D. R. Myers, C. Li, X.-a. Fu, M. Mehregany, W. B. J. Muthu, and A. P. Pisano, "A SiC MEMS Resonant Strain Sensor for Harsh Environment Applications," *Sensors Journal, IEEE,* vol. 7, pp. 568-576, 2007.

[18] T. G. Brown, B. Davis, D. Hepner, J. Faust, C. Myers, C. Muller, T. Harkins, M. Holis, and B. Placzankis, "Strap-down microelectromechanical (MEMS) sensors for high-g munition applications," *Magnetics, IEEE Transactions on,* vol. 37, pp. 336-342, 2001.

[19] C. T. Lim and Y. J. Low, "Investigating the drop impact of portable electronic products," in the Proceeding of *Electronic Components and Technology Conference*, 2002, pp. 1270-1274.

[20] S. W. Yoon, S. Lee, N. C. Perkins, and K. Najafi, "Shock protectiong using soft coating as shock stops," in the Proceeding of *A Solid State Sensors, Actuators and Microsystems Workshop (Hilton Head)*, Hilton Head Island, SC, USA, 2006, pp. 396-399.

[21] C. J. Wilson, A. Ormeggi, and M. Narbutovskih, "Fracture testing of silicon microcantilever beams," *Journal of Applied Physics,* vol. 79, pp. 2386-2393, 1996.

[22] Y.-H. Chang, C. M. Hamerski, and R. Kram, "Applied horizontal force increases impact loading in reduced-gravity running," *Journal of Biomechanics,* vol. 34, pp. 679-685, 2001.

[23] S. Wang, "Experimental investigation of the mechanics of vibratory finishing," Thesis, Thesis of Master of Applied Science, 1999

[24] C. J. Wilson and P. A. Beck, "Fracture testing of bulk silicon microcantilever beams subjected to a side load," *Journal of Microelectromechanical Systems,* vol. 5, pp. 142-150, 1996.

[25] T. Ando, K. Sato, M. Shikida, T. Yoshioka, Y. Yoshikawa, and T. Kawabata, "Orientation-dependent fracture strain in single-crystal silicon beams under uniaxial tensile conditions," in the Proceeding of *International Symposium on Micromechatronics and Human Science*, 1997, pp. 55-60.

[26] C. L. Muhlstein, S. B. Brown, and R. O. Ritchie, "High-cycle fatigue of single-crystal silicon thin films," *Journal of Microelectromechanical Systems,* vol. 10, pp. 593-600, 2001.

[27] K. Yasutake, M. Iwata, K. Yoshii, M. Umeno, and H. Kawabe, "Crack healing and fracture strength of silicon crystals," *Journal of Materials Science,* vol. V21, pp. 2185-2192, 1986.

[28] J. Vedde and P. Gravesen, "The fracture strength of nitrogen doped silicon wafers," *Materials Science and Engineering B,* vol. 36, pp. 246-250, 1996.

[29] K. Sato, M. Shikida, T. Yoshioka, T. Ando, and T. Kawabata, "Micro tensile-test of silicon film having different crystallographic orientations," in the Proceeding of *International Conference on Solid State Sensors and Actuators (TRANSDUCERS)*, Chicago, USA, 1997, pp. 595-598 vol.1.

[30] K. Azgin, Y. Temiz, and T. Akin, "A Novel In-Operation High g-Survival MEMS Gyroscope," in the Proceeding of *IEEE Sensors Conference*, Atlanta, GA, USA, 2007, pp. 111-114.

[31] R. J. Roark, *Formulas for stress and strain*. New York: McGraw-Hill, 1965.

[32] L. Morisset, "Conformal Coating Through Gas Phase Polymerisation " *OnBoard Technology,* pp.

32-34, 2003.

[33] H. Kim and K. Najafi, "Characterization of low-temperature wafer bonding using thin-film parylene," *Journal of Microelectromechanical Systems,* vol. 14, pp. 1347-1355, 2005.

[34] A. Campbell and J. Scialdone, "Outgassing Data for Selecting Spacecraft Materials," *NASA Reference Publication,* 1990.

[35] C.-Y. Shih, "Temperature-controlled microchip liquid chromatography system," PhD Thesis, Electrical Engineering, Caltech, 2006

[36] E. Meng and Y.-C. Tai, "Parylene etching techniques for microfluidics and bioMEMS " in the Proceeding of, Miami, USA, 2005, pp. 568- 571.

[37] S. W. Yoon, N. Yazdi, J. Chae, N. C. Perkins, and K. Najafi, "Shock protection using integrated nonlinear spring shock stops," in the Proceeding of *IEEE International Conference on Micro Electro Mechanical Systems (MEMS)*, Istanbul, Turkey, 2006, pp. 702-705.

[38] K. Kwon and S. Park, "Three axis piezoresistive accelerometer using polysilicon layer," in the Proceeding of *International Conference on Solid State Sensors and Actuators (TRANSDUCERS)*, Chicago, IL 1997, pp. 1221-1224 vol.2.

[39] E. P. Popov, *Engineering mechanics of solids*: Prentice-Hall 1990.

[40] J. M. Tsai and G. K. Fedder, "Mechanical noise-limited CMOS-MEMS accelerometers," in the Proceeding of *IEEE International Conference on Micro Electro Mechanical Systems (MEMS)*, 2005, pp. 630-633.

[41] S. Huang, X. Li, Y. Wang, J. Jiao, X. Ge, D. Lu, L. Che, K. Zhang, and B. Xiong, "A piezoresistive accelerometer with axially stressed tiny beams for both much increased sensitivity and much broadened frequency bandwidth," in the Proceeding of *International Conference on Solid-State Sensors, Actuators and Microsystems (TRANSDUCERS)*, 2003, pp. 91-94 vol.1.

[42] S. W. Yoon, N. Yazdi, N. C. Perkins, and K. Najafi, "Novel integrated shock protection for MEMS," in the Proceeding of *International Conference on Actuators and Microsystems Solid-State Sensors (TRANSDUCERS)*, 2005, pp. 396-400 Vol. 1.

[43] S. W. Yoon, N. Yazdi, N. C. Perkins, and K. Najafi, "Micromachined integrated shock protection for MEMS," *Sensors and Actuators A: Physical,* vol. 130-131, pp. 166-175, 2006.

[44] D. J. Wagg and S. R. Bishop, "Application of non-smooth modeling techniques to the dynamics of a flexible impacting beam " *Journal of Sound and Vibration,* vol. 256, pp. 803-820, 2002.

[45] D. J. Wagg, "A note on using the collocation method for modelling the dynamics of a flexible continuous beam subject to impacts," *Journal of Sound and Vibration,* vol. 276, pp. 1128-1134, 2004.

CHAPTER 6

CONCLUSION

Vibration and shock have profound impact on MEMS, and induce degraded performance and distorted reliability. This dissertation (1) analyzes the performance-degradation mechanisms and (2) develops methods to protect MEMS devices against them. We present our conclusion with a brief achievement summary in Section 6.1 and suggest future researches in Section 6.2.

6.1. Conclusion

Vibration produces short-lived device output errors that can generate critical systemic problem in sensor systems. The errors are unpredictable and hard to correct using electronics.

Chapter 2 analyzes the unpredictable output errors in MEMS devices, especially in MEMS gyroscopes. The gyroscopes are selected because of their high vibration susceptibility. We classified reported MEMS gyroscopes into several categories, i.e. degenerate gyroscopes, non-degenerate tuning fork gyroscopes (TFGs), and non-degenerate non-TFGs. Vibration effects on each design were analyzed.

The results showed that all gyroscope designs we analyzed are sensitive to vibration. Briefly, in the non-TFG designs, vibration-induced errors stem from the dynamics of the mechanical structure of the gyroscopes and increase in proportion to the Q of the gyros. Unlike the non-TFG designs, the TFG and degenerate gyro designs are known to be relatively vibration-insensitive because of their differential operation in the case of TFGs and because of the decoupled vibration modes in the case of degenerate gyros. However, we demonstrated that the TFGs can completely eliminate vibration effects in specific situations, even though the amount of error is much smaller than that of the non-TFG cases, whereas the degenerate gyroscopes are vibration-insensitive. The errors in the TFGs stem not from the dynamics of the gyro structures, but from the nonlinearity at drive and sense electrodes of the gyros. Among the specific situations, the sense-directional vibration is the most dominant

because it is involved with all error sources. Moreover, because of the difference among the designs in regard to the degree of decoupling, some designs (Type-DD tuning fork gyros and ring gyros) showed substantially smaller (>99%) vibration-induced errors than the other designs (Type-CP and Type-DS tuning fork gyros). This difference results from the difference dominant error source. However, all of the three errors do not occur in ring gyroscopes, the most general degenerate gyroscope, because their resonant frequencies of vibration-induced modes are >10 kHz smaller than their operation-mode frequencies.

On the basis of the analysis in Chapter 2, Chapter 3 proposes a vibration isolator based on a mechanical low pass filter (LPF). The LPF can be formed by either a single or multiple vibration-isolation platforms. We demonstrated the vibration-suppression performance using the platforms integrated with a sample gyroscope and identified important design parameters to control the performance. The most critical parameter is the mass of the first platform in the multiple vibration-isolation platforms. Increasing the mass beyond certain level (>300 times larger than gyro mass in our analysis) minimizes the gyroscopes' performance degradation, including resonant frequency change and Q reduction.

Unlike vibration, shock damages MEMS device structures. Most shock-protection methods are focused on limiting displacement of device mass so that we can also limit the maximum bending stress in the structure. One common method to achieve this goal is utilizing motion-limiting hard shock stops. Despite their many advantages, the hard stops can generate a secondary shock source by sequential impacts on the shock stops. The force generated by the impacts (i.e., impact force) can damage device structures in several applications, and therefore, we proposed two novel technologies to resolve this problem.

Chapter 4 presents the concept, designs, and simulations of the two novel shock protection technologies, named nonlinear spring shock stops and soft coating shock stops. Both technologies are compatible with current microfabrication techniques and can be integrated with many MEMS devices without major change in device design and fabrication. Simulation results showed that both technologies dramatically reduce the impact force by an order of magnitude compared with the hard stops. The shock performance of the two technologies can be readily adjusted by changing several parameters of the mechanical structures used as shock stops. The parameters include physical dimensions and material properties of shock-beam structures, material

properties and thickness of soft coating film, and the shapes of bumper contacting the coated shock stops. We also explained the design guidance to optimize the design parameters and to minimize any side-effects.

Chapter 5 demonstrates the design, fabrication, and results of shock tests to validate the improvement in shock protection and establish the feasibility of fabrication. We fabricated test devices either by silicon-on-glass (SOG) processes using 100μm-thick silicon wafers or by highly doped polysilicon processes using 475μm-thick silicon wafers. For soft-coating devices, the fabricated silicon devices were coated using 3μm-thick Parylene. The fabricated devices were tested using a drop machine we built. The machine applied multiple high-g shocks (more than 2500g) to >70 devices from different wafers. Test results demonstrated that the device-survival rates for both new technologies (88% in nonlinear spring and 92% in soft coating shock stops) are more than twenty times better than that of conventional hard stops (4%). Moreover, both technologies allow wafer-level, generic, and batch fabrication processes to protect MEMS devices from shock.

Subsequently, the mechanical protection technologies (shock protection and vibration isolation) developed in this thesis have now been integrated into environmental isolation packages being developed for high-performance micromachined gyroscopes.

6.2. Suggestions For Future Work

There are several potential improvements to the work presented in this dissertation. Vibration-isolation methods other than the mechanical low pass filter are needed in several applications. More shock experiments will be beneficial in achieving better understanding of our new shock-protection technologies and device-fracture mechanism.

6.2.1. Advanced Vibration Suppression Methods

The vibration-isolation methods presented in this dissertation are based on the mechanical low pass filter. The methods are effective for high frequency vibration, but several devices and applications were observed to be also susceptive to low frequency vibration. For example, MEMS resonators showed phase noise induced by

vibrations whose frequencies (<1 kHz) are much lower than the resonant frequency of the resonators (>100 kHz). Therefore, we need to develop advanced methods to suppress those low frequency vibrations. In addition, it will be worthwhile to introduce materials used in macro-scale vibration isolators but not in microfabrication. Electrorheological fluid is an attractive candidate because the mechanical properties of the fluid can be controlled using electrical energy. Moreover, it is also possible to utilize force-balancing schemes or active control to further suppress vibration effects.

6.2.2. Shock-Induced Device Fracture

In Chapter 4, we discussed the ways to adjust the shock-protection performance of soft coating shock stops by changing the material thickness or the design of bumpers contacting the stops. Experimental verification of these discussions will allow us further validation of our technologies. Also, to investigate the effects of rough RIE etched side-wall surfaces, shock experiments using vertical-directional shock stops are also beneficial.

APPENDIX A

Micromachined Multi-Axis Vibration-Isolation Platform

Vibration has profound impact on the performance and reliability of MEMS devices by inducing unwanted output errors [1]. These vibration–induced problems can be dominated especially by vibrations whose frequencies are at/near the resonant frequency of a device since the Q-factor will amplify the amplitude of the vibration. To suppress the vibration-induced problems, one of the commonly used method is a mechanical low pass filter (LPF) using mass-spring-damper system.

We presented a new concept for a vibration isolator based on micromachined mass-spring-damper system which is schematically depicted in Figure A.1. The vibration-isolation platform consists of vertical feedthroughs (VFT), isolation springs, and bonding pads. The isolation springs are micromachined from a 475μm-thick silicon wafer. This spring not only acts as mechanical isolator, but also as an electrical interconnection.

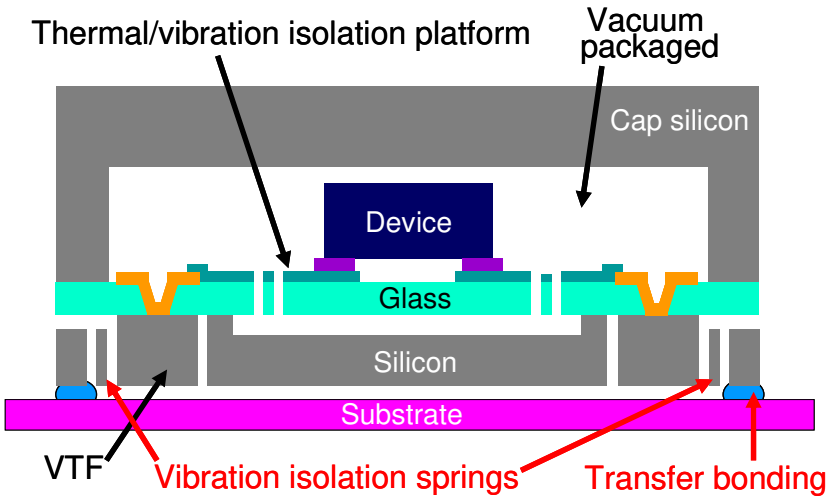

Figure A.1. Schematic of the micromachined vibration isolator integrated to a vacuum package previously presented [2].

Unlike other approaches, the proposed vibration-isolation platform is integrated with a wafer-level package, and thus, enables vibration isolation without adding additional volume or vertical profile. The complete fabrication of the system uses

standard micromachining technology in wafer-level and batch process. Furthermore, this technology provides the capability for simultaneous fabrication of multi-axis isolators in lateral, vertical and torsional directions and is also compatible with vacuum packaging technology in a previous work [2]. The package in the work has an internal vertical vibration-isolation platform, and therefore our technology can provide multiple isolators cascaded (i.e., a multi-order low pass filter) to achieve dramatic vibration suppression.

Our new technologies can integrate both lateral and vertical vibration isolators. The lateral isolator uses clamped beams as springs, whereas the vertical isolator employs torsion beams [3]. Due to the direction of operation and the thickness of the silicon wafer used for isolation springs, FEM simulations, shown in Figure A.2, demonstrate that the fundamental resonant frequency of the lateral design (~0.8 kHz) is relatively low compared to that of the vertical deign (~3.6 kHz). Regardless, both resonant frequencies are substantially smaller than gyroscopes' resonant frequencies, and thus, high vibration suppression is expected.

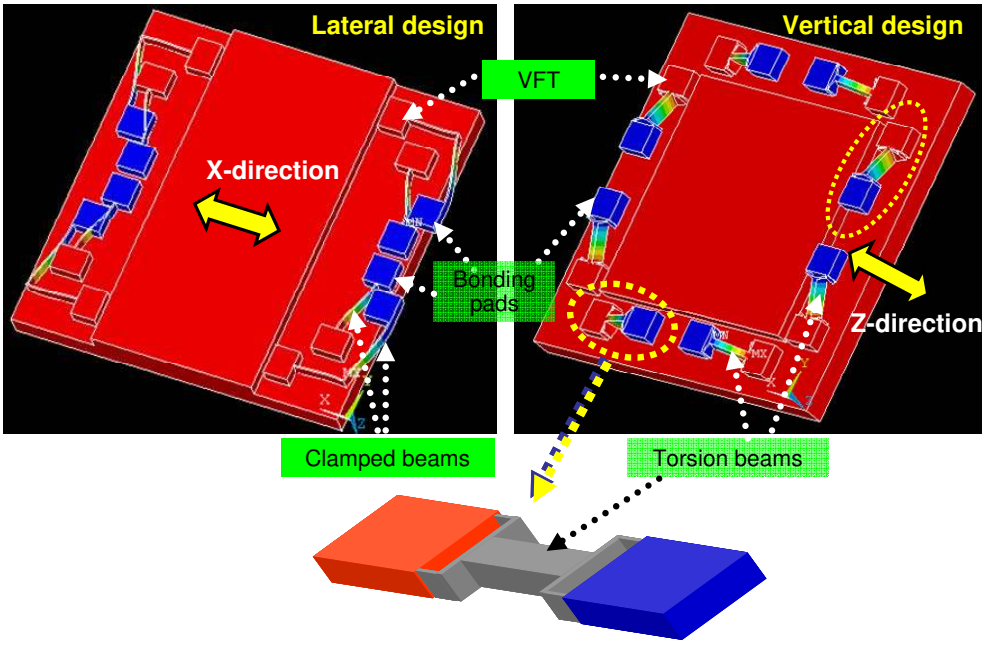

Figure A.2. FEM simulation results showing the fundamental resonant frequencies of lateral and vertical isolator designs. The lateral design has ~0.8 kHz resonance, whereas vertical design has ~3.6 kHz.

The fabrication of the isolation platform without the vacuum package is shown in Figure A.3. First, a 2-4 μm recess on the platform silicon wafer was etched (Figure

A.3a), which was then anodically bonded to a glass wafer (Figure A.3b). Next, a through-wafer DRIE was preformed to create the VFTs, isolation springs, and bonding pads. Following this, Ti/Au was deposited and finally the wafer was diced (Figure A.3c). On the substrate wafer, a DRIE etched island (7-8 μm tall) was formed and conformally coated with PECVD oxide for electrical insulation (Figure A.3d). To form metal interconnections, Ti/Au was deposited and patterned. Then, NiCr/In/Au was deposited and patterned to form transient liquid phase (TLP) [4] bonding material (Figure A.3d) and the two wafers were then bonded (Figure A.3e) using a guide wafer. The final structure is shown in Figure A.3f. The gold deposited on the vibration isolator has two main purposes; as TLP bonding material (for bonding pads) and to lower electrical resistance (for vibration beams).

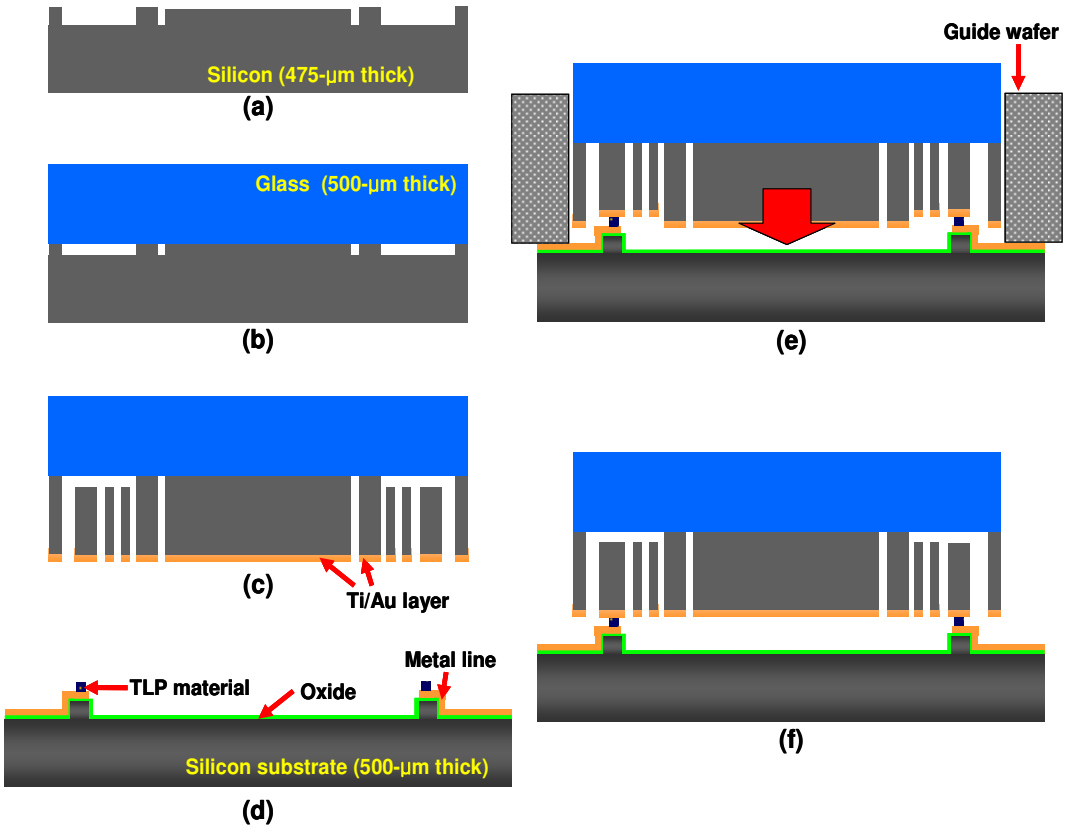

Figure A.3. The fabrication process for the vibration-isolation platform. The platform and the substrate wafer are processed separately and boned together using TLP bonding.

The isolation springs and bonding pads on the platform wafer were successfully released and suspended. Figure A.4 demonstrates that both lateral and vertical

vibration-isolation platforms were successfully bonded on the same substrate. To investigate the bond quality, a vertical-isolation platform was intentionally detached as shown in Figure A.5. A number of devices were tested for bond quality and all showed a good quality bond as the bonding pads were still attached to the substrate even though all vibration beams are broken. The size of the isolation platform is 12.2 x 12.2 mm^2, and the contact resistance between the VTFs and the bond pads ranges from 4 to11 Ω depending on the spring design.

The performance of a lateral vibration-isolation platform was characterized using a shaker table (B&K, 4809) and a laser Doppler vibrometer (Polytech, OFV-3001/OFV 303). The initial test results in Figure A.6 showed that vibration suppression is achieved at vibration frequencies higher than >~2.1 kHz.

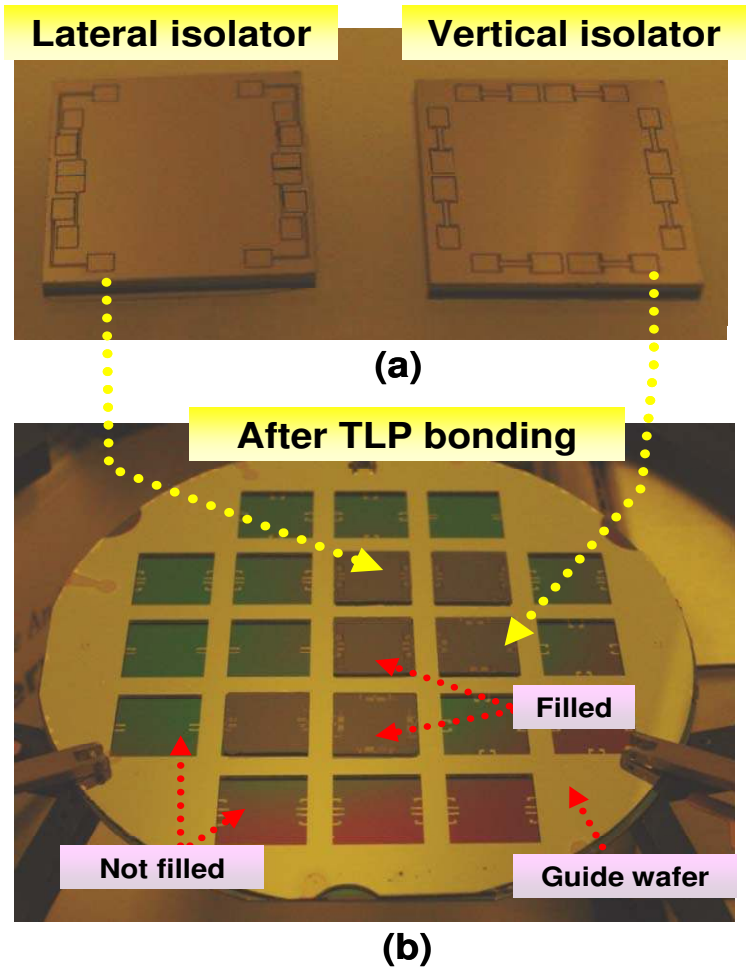

Figure A.4. (a) Fabricated lateral and vertical vibration isolator, (b) Isolation platform after TLP bonding on a substrate.

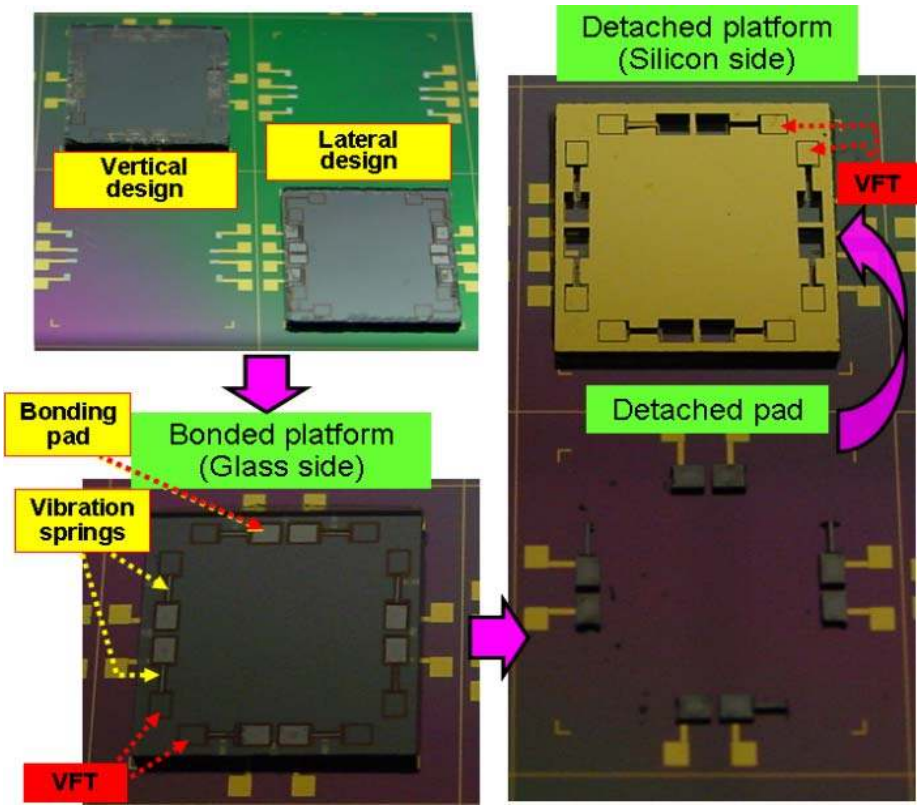

Figure A.5. Fabricated vibration-isolation platforms (on a single wafer) and detached vertical design showing good bonding quality and released vibration springs.

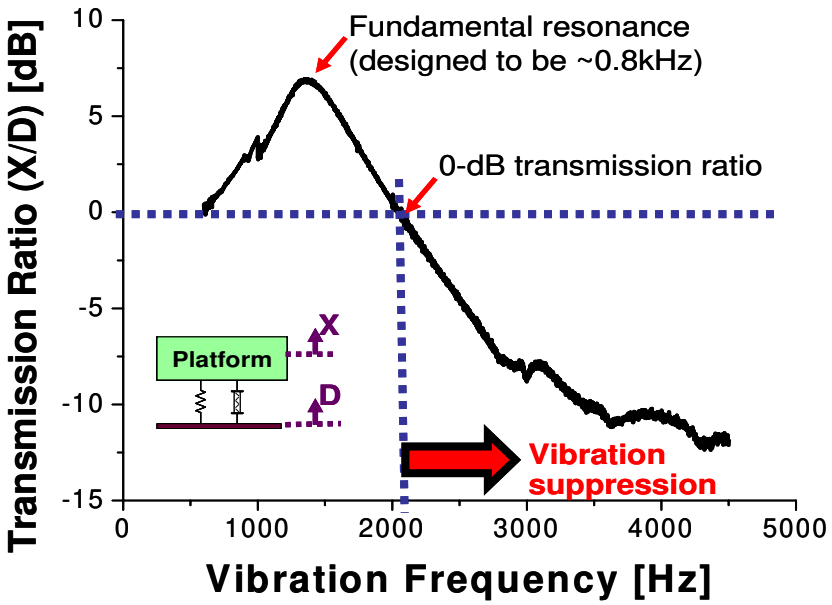

Figure A.6. The frequency response of the lateral vibration isolator. This design shows vibration suppression after ~2.1k Hz vibration frequency.

References

[1] S. W. Yoon, S. W. Lee, N. C. Perkins, and K. Najafi, "Vibration Sensitivity of MEMS Tuning Fork Gyroscopes," in *the Proceeding of IEEE SENSORS 2007 Conference* Atlanta, Georgia, USA, 2007, pp. 115-119.

[2] S. H. Lee, S. W. Lee, and K. Najafi, "A Generic Environment-Resistant Packaging Technology for MEMS," in *the Proceeding of International Solid-State Sensors, Actuators and Microsystems Conference (TRANSDUCERS)*, Lyon, France, 2007, pp. 335-338.

[3] S. Lee, J. Cho, and K. Najafi, "Fabrication of vertical comb electrodes using selective anodic bonding," in *the Proceeding of IEEE International Conference on Micro Electro Mechanical Systems (MEMS)*, Kobe, Japan, 2007, pp. 349-352.

[4] W. C. Welch and K. Najafi, "Nickel-Tin Transient Liquid Phase (TLP) Wafer Bonding for MEMS Vacuum Packaging," in *the Proceeding of International Solid-State Sensors, Actuators and Microsystems Conference (TRANSDUCERS)*, Lyon, France, 2007, pp. 1327-1328.

APPENDIX B

MATLAB Codes to Generate Figures in Section 2.4

B.1. MATLAB Code (General Usage)

```
%% Impulsive vibration %%
clear all

%%%% Setup
fsample=-1; fL=50;    filter_order=2;
%if fL is too small, like 10, the response is too long.

%%% Not used but maybe required in future
phase_demod=pi/2;

%%%% Structure - electrode
gd=1.6e-6; gs=1.6e-6; %gap of drive/sense electrode
lamda=5e-6; %drive electrode' overlaping length

%%%% Structure - sense beam
h=4e-6; %thickness of beam

%%%% Driving electrode
Vac=6; Vdc=6;

%%%% Sense electrode
Vs=1.5; As=h*500e-6;

%%%% General constant
etha=8.85e-12; n=50; h=4e-6;

%%%% Constants
Fd_constant=n*etha*h/gd; Fes_const=2*gs*Vs^2*etha*As;
Fed_const_ax=n*etha*h*gd; Cap_ratio=etha*As*2;

%%%%%%%%%%%%%%%%%%%%%%%%%%%%%%%%%%%%%%%%%%%%%%%%%%%%%%%%
```

```
%%%%%%%%%%%%%%%%%%%%%%%%%%%%%%%%%%%%%%%%%

%%%%% DS-type
Fc_on=1; Fes_on=0; Fed_on=1; k3s_on=0; k3d_on=0;
ay_on=1; ax_on=1;

delay_Fc=0.05; delay_x=0.12; delay_y=0.12;

%%%%% Parameter Type-DS    %%%%%
%%%% Sense mass
msense=0.2e-9*2; Qsense=45; fsense=14e3;
ksense=(2*pi*fsense)^2*msense;
csense=sqrt(ksense*msense)/Qsense;

%%%% Drive mass
md=0.2e-9; Qd=45; fd=fsense;
kd=(2*pi*fd)^2*md;
cd=sqrt(kd*md)/Qd;
wd=2*pi*fd;

%%%% Rotation %%%%
omega_dh=100*3600; %rotation amplitude, [deg/hr]
omega=omega_dh/180*pi/3600; %rotation amplitdue, [rad/sec]

%%%% Changing constant %%%%
Fc_const=2*md*omega;

%%%% Vibration %%%%
Ax=100*9.8; % X-axis vibration's amplitude
Ay=100*9.8; % Y-axis vibration's amplitude
duration_x=3e-3; duration_y=3e-3;

sim('VibGyro_TypeDS_impulse',0.25)
% save
save('RUN1.mat', 't', 'CoutF', 'Cout', 'xdR', 'vib_x','yL', 'yR', 'drive');

%%%%%%%%%%%%%%%%%%%%%%%%%%%%%%%%
%%%%% 2nd run. DD-type    %%%%%
Fc_on=1; Fes_on=0; Fed_on=1; k3s_on=0; k3d_on=0;
ay_on=1; ax_on=1;
```

```
delay_Fc=0.05; delay_x=0.12; delay_y=0.12;

%%%%% Parameter Type-DD    %%%%%
%%%% Sense mass
msense=0.2e-9; Qsense=45; fsense=14e3;
ksense=(2*pi*fsense)^2*msense;
csense=sqrt(ksense*msense)/Qsense;

%%%% Drive mass
md=0.2e-9*2; Qd=45; fd=fsense;
kd=(2*pi*fd)^2*md;
cd=sqrt(kd*md)/Qd;
wd=2*pi*fd;

%%%% Rotation %%%%
omega_dh=100*3600; %rotation amplitude, [deg/hr]
omega=omega_dh/180*pi/3600; %rotation amplitdue, [rad/sec]

%%%% Changing constant %%%%
Fc_const=2*md*omega;

%%%% Vibration %%%%
Ax=100*9.8; % X-axis vibration's amplitude
Ay=100*9.8; % Y-axis vibration's amplitude
duration_x=3e-3; duration_y=3e-3;

sim('VibGyro_TypeDD_impulse',0.25)
save('RUN2.mat', 't', 'CoutF', 'Cout', 'yL', 'yR','drive');

%%%%% 3rd run. CP-type
Fc_on=1; Fes_on=0; Fed_on=1; k3s_on=0; k3d_on=0;
ay_on=1; ax_on=1;

delay_Fc=0.05; delay_x=0.12; delay_y=0.12;

%%%%% Parameter Type-CP    %%%%%
%%%% Sense mass
msense=0.2e-9*2; Qsense=45; fsense=14e3;
ksense=(2*pi*fsense)^2*msense;
```

```
csense=sqrt(ksense*msense)/Qsense;

%%%% Drive mass
md=msense; Qd=45; fd=fsense;
kd=(2*pi*fd)^2*md;
cd=sqrt(kd*md)/Qd;
wd=2*pi*fd;

%%%% Rotation %%%%
omega_dh=100*3600; %rotation amplitude, [deg/hr]
omega=omega_dh/180*pi/3600; %rotation amplitdue, [rad/sec]

%%%% Changing constant %%%%
Fc_const=2*md*omega;

%%%% Vibration %%%%
Ax=100*9.8; % X-axis vibration's amplitude
Ay=100*9.8; % Y-axis vibration's amplitude
duration_x=3e-3; duration_y=3e-3;

sim('VibGyro_TypeDS_mpulse',0.25)
save('RUN3.mat', 't', 'CoutF', 'Cout', 'xdR', 'yL', 'yR', 'drive');

% END MATLAB
return;
```

B.2. SIMULINK Model (General Usage)

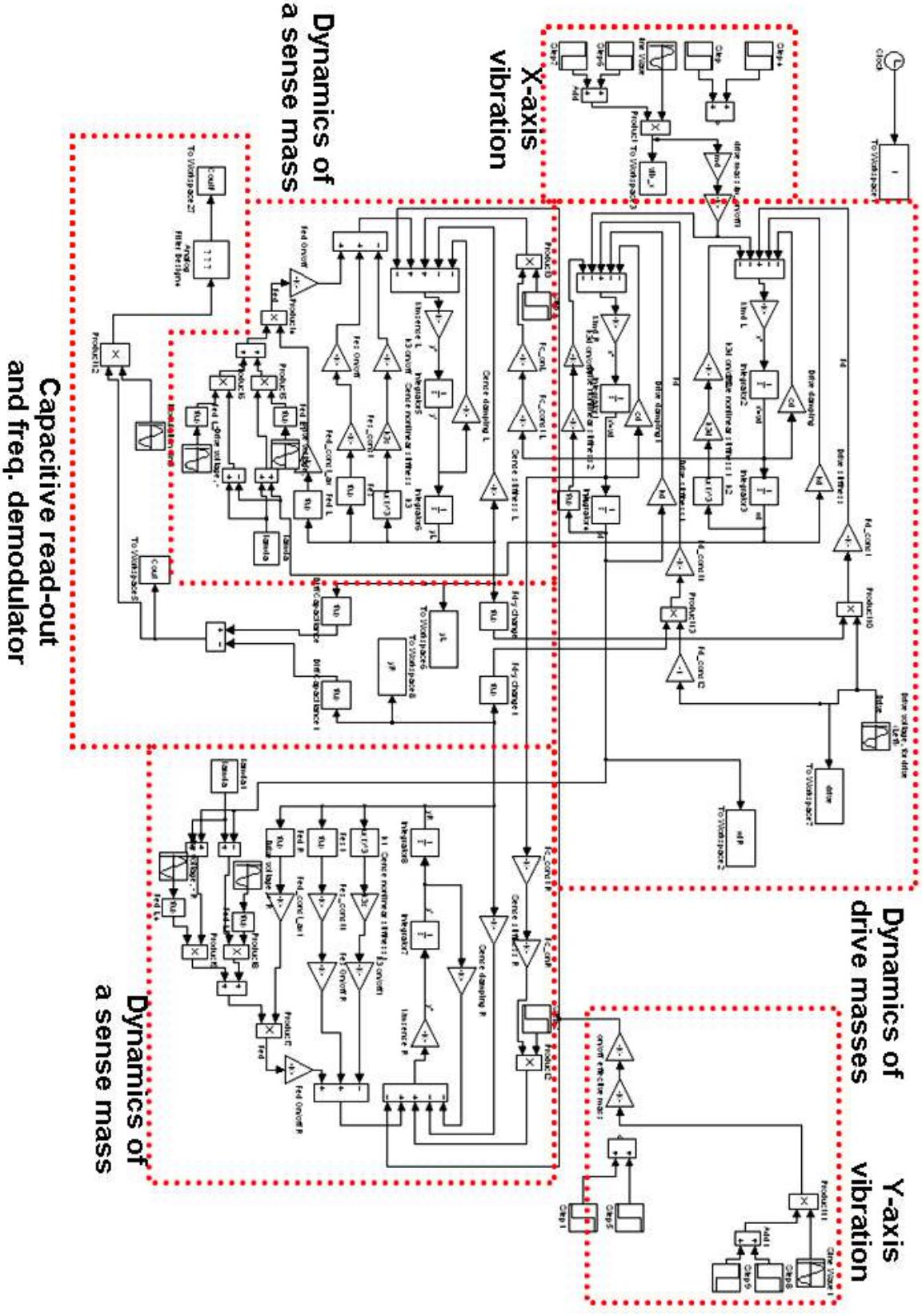

Figure B.1. SIMULINK model for Type-CP and Type-DS gyroscopes.

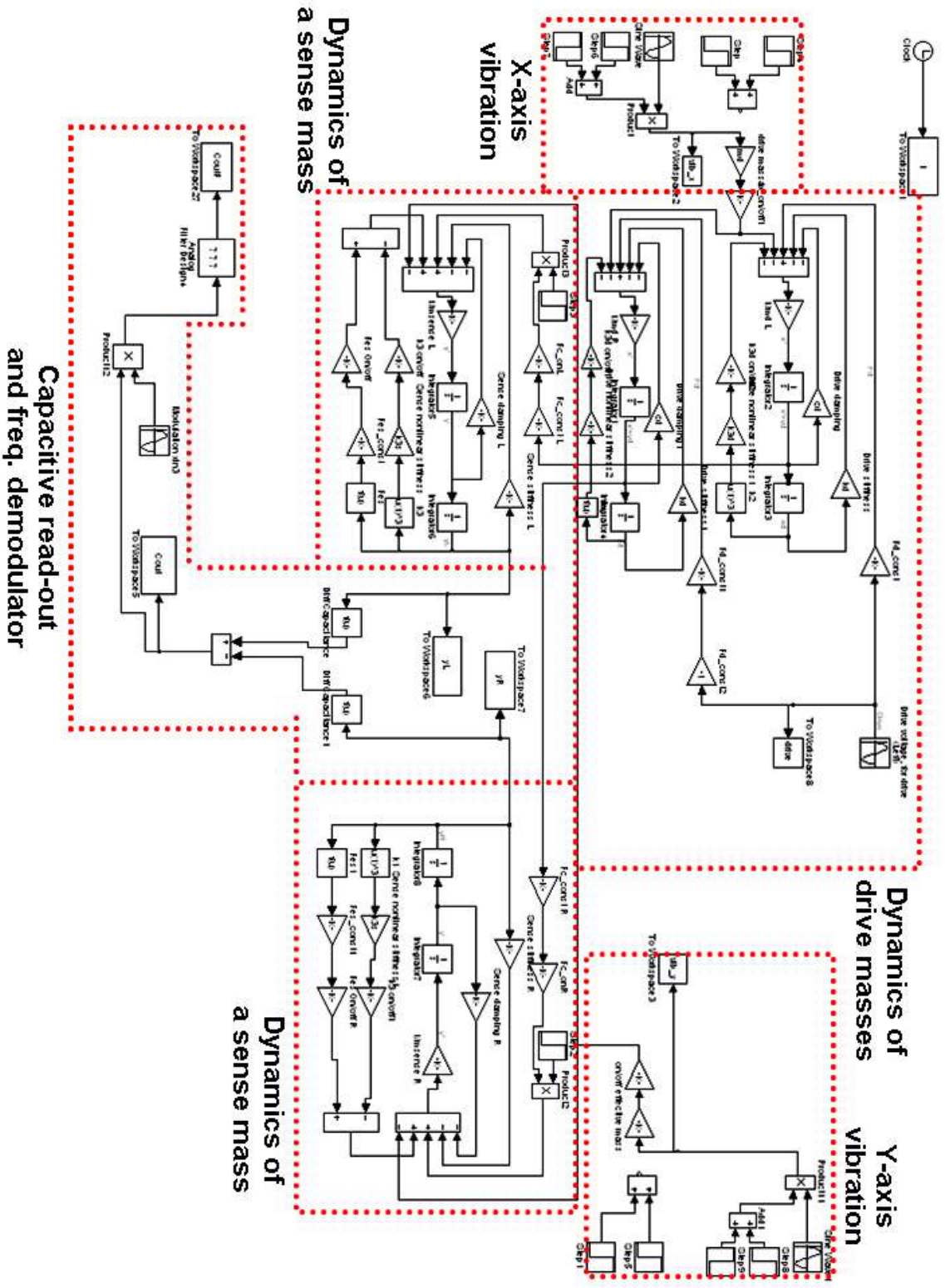

Figure B.2. SIMULINK model for Type-DD gyroscopes.

APPENDIX C

MATLAB Codes to Generate Figures in Chapter 4

C.1. MATLAB Code for Nonlinear Spring Shock Stops

```
clear all
close all

m=1e-6;
k=200;
b=1e-4;

fs=10e6;
ks=50;
gap=10e-6; d=10e-6;

shock_amplitude=9.8*1e3;    %1000g shock
shock_start_time=0; shock_time=1e-4; % Shock duration in seconds.
restitution=0.7;
%%%%%%%%%%%%%%%%%%%%

N=3;
state=0; next_state=0; prev_vel=0;
no_change=0; %0=State changes, 1=No change state.
dummy_wait=15;

%%%%%%%%%%%%%%%%%%%%
As=[-1*b/m -1*k/m; 1 0]; Bs=[-1; 0]; Cs=[1 0;0 1];    Ds=[0; 0];
Be=[1; 0]; Ce=[1 0;0 1]; De=[0; 0];
%%%%%%%%%%%%%%%%%%%%

sim('Nonlinear_s',[0 0.002])

% first stage %

up_x1=min(find((output(:,2))>=gap))-1;    %Should substract 1 to get 'previous' one
```

```
down_x1=min(find((output(:,2))<=-1*gap))-1;

if (length(up_x1)==0)
    if (length(down_x1)==0)          %No touch
        ini_c=output(end,:);
        save_output=output;
        prev_vel=output(end,1);

    else                                        %No up touch, but down touch
        ini_c=output(down_x1,:);
        save_output=output(1:down_x1,:);
        prev_vel=output(down_x1,1);

    end

    elseif (length(down_x1)==0)    %No down touch, but up touch
        ini_c=output(up_x1,:);
        save_output=output(1:up_x1,:);
        prev_vel=output(up_x1,1);


    elseif up_x1 >= down_x1 %Down touch is faster than up touch
        ini_c=output(down_x1,:);
        save_output=output(1:down_x1,:);
        prev_vel=output(down_x1,1);


    else
        ini_c=output(up_x1,:);
        save_output=output(1:up_x1,:);
        prev_vel=output(up_x1,1);

end

state=1;
 %%%%%%%%% End of 1st stage %%%%%%%%%%%%
 %%%%%%%%% Start of 2nd stage %%%%%%%%%%%%
   %if prev_vel > 0, moving up. <, moving down
 if prev_vel >= 0,
        next_state=2;
```

```
    else
        next_state=3;
 end

Ae=[-1*b/m -1*(k+ks)/m; 1 0]; %Anycase, Ae is same, 2,3
in=ks*gap/m;

for i=1:N,

    %%%%%%%%%%%%%%%%%%%%%%%%%%%%%%%%%%%%%%%%%%%%%%%%%%%%%%%%
    %   Next State determination
    if no_change==1, %no state change
        next_state=state;
    else
        if state == 1 % -gap < < gap
            if prev_vel >= 0,
                next_state=2;
            else
                next_state=3;
            end
        end

        if state == 2 % gap < < gap + d
            if prev_vel >= 0,
                next_state=4;
            else
                next_state=1;
            end
        end

        if state == 3 % -gap-d < < -gap
            if prev_vel >= 0,
                next_state=1;
            else
                next_state=5;
            end
        end

        if state == 4 % gap+d < < gap+2*d
            if prev_vel >= 0,
```

```
            next_state=6;
        else
            next_state=2;
        end
end

if state == 5 % -gap-2*d < < gap-d
        if prev_vel >= 0,
            next_state=3;
        else
            next_state=7;
        end
end

if state == 6 % gap+2*d < < gap+3*d
        if prev_vel >= 0,
            next_state=8;
        else
            next_state=4;
        end
end

if state == 7 % -gap-3*d < < -gap-2*d
        if prev_vel >= 0,
            next_state=5;
        else
            next_state=9;
        end
end

if state == 8 % -gap < < gap
        if prev_vel >= 0,
            next_state=8;
        else
            next_state=6;
        end
end

if state == 9 % -gap < < gap
        if prev_vel > 0,
```

```
                next_state=7;
            else
                next_state=9;
            end
        end
    end
    no_change=0; %off

    %%%%%%%%%%%%%%%%%%%%%%%%%%%%%%%%%%%%%%%%%%%%%%%%%%
%%
    %%% Asignment
    if next_state==1
        Ae=[-1*b/m -1*k/m; 1 0]; %Anycase, Ae is same
        in=0; %Free motion
        up_limit=gap;
        down_limit=-1*gap;
    end

    if next_state==2
        Ae=[-1*b/m -1*(k+ks)/m; 1 0]; %Anycase, Ae is same
        in=ks*gap/m;
        up_limit=gap+d;
        down_limit=gap;
    end

    if next_state==3
        Ae=[-1*b/m -1*(k+ks)/m; 1 0]; %Anycase, Ae is same
        in=ks*gap/m;
        up_limit=-1*gap;
        down_limit=-1*gap-d;
    end

    if next_state==4
        Ae=[-1*b/m -1*(k+2*ks)/m; 1 0]; %Anycase, Ae is same
        in=ks*(2*gap+d)/m;
        up_limit=gap+2*d;
        down_limit=gap+d;
    end

    if  next_state==5
```

```
    Ae=[-1*b/m -1*(k+2*ks)/m; 1 0]; %Anycase, Ae is same
    in=ks*(2*gap+d)/m;
    up_limit=-1*gap-d;
    down_limit=-1*gap-2*d;
end

if next_state==6
    Ae=[-1*b/m -1*(k+3*ks)/m; 1 0]; %Anycase, Ae is same
    in=ks*(3*gap+3*d)/m;
    up_limit=gap+3*d;
    down_limit=gap+2*d;
end

if next_state==7
    Ae=[-1*b/m -1*(k+3*ks)/m; 1 0]; %Anycase, Ae is same
    in=ks*(3*gap+3*d)/m;
    up_limit=-1*gap-2*d;
    down_limit=-1*gap-3*d;
end

if next_state==8 | next_state==9
    Ae=[-1*b/m -1*(k+3*ks)/m; 1 0]; %Anycase, Ae is same
    in=ks*(3*gap+3*d)/m;
    ini_c=save_output(end,:);
    ini_c(1)=-1*restitution*ini_c(1);
    up_limit_2=gap+3*d;
    down_limit_2=-1*gap-3*d;
end

state=next_state;    %% state change
%*******************************%
%%% Running
sim('Nonlinear_e',[0 0.0002])
x_velocity=output2(:,1);
x_displace=output2(:,2);

if next_state==8 | next_state==9      %%%%% Bouncing
    if next_state==8 %upper limit
        target_up_x1=min(find((x_displace(dummy_wait:end))>=up_limit_2))-1;
        target_up_x1=target_up_x1+dummy_wait; % Return to original number
```

```
            ini_c=save_output(target_up_x1,:);
            save_output=[save_output; output2(2:target_up_x1,:)];
            prev_vel=ini_c(1);
        elseif next_state==9
            target_down_x1=min(find((x_displace(dummy_wait:end))<=down_limit_2))-1;
            target_down_x1=target_down_x1+dummy_wait; % Return to original number
            ini_c=output2(target_down_x1,:);
            save_output=[save_output; output2(2:target_down_x1,:)];
            prev_vel=ini_c(1);
        end
    else
        target_up_x1=min(find((x_displace(dummy_wait:end))>=up_limit))-1;    %Should substract 1
to get 'previous' one
        target_down_x1=min(find((x_displace(dummy_wait:end))<=down_limit))-1;
        target_up_x1=target_up_x1+dummy_wait;    % Return to original number
        target_down_x1=target_down_x1+dummy_wait;
        if (length(target_up_x1)==0)
            if (length(target_down_x1)==0)          %No touch
                ini_c=output2(end,:);
                save_output=[save_output; output2(2:end)];
                prev_vel=ini_c(end,1);      %%%%%%%******* 1
                no_change=1;
            else                                    %No up touch, but down touch
                ini_c=output2(target_down_x1,:);
                save_output=[save_output; output2(2:target_down_x1,:)];
                prev_vel=output2(target_down_x1,1);
            end

        elseif (length(target_down_x1)==0)    %No down touch, but up touch
            ini_c=output2(target_up_x1,:);
            save_output=[save_output; output2(2:target_up_x1,:)];
            prev_vel=output2(target_up_x1,1);

        elseif target_up_x1 >= target_down_x1 %Down touch is faster than up touch
            ini_c=output2(target_down_x1,:);
            save_output=[save_output; output2(2:target_down_x1,:)];
            prev_vel=output2(target_down_x1,1);

        else    %target_up_x1 < target_down_x1 %Up touch is faster than down touch
            ini_c=output2(target_up_x1,:);
```

```
                save_output=[save_output; output2(2:target_up_x1,:)];
                prev_vel=output2(target_up_x1,1);
            end
        end

end


%*****************************%
time=[1:length(save_output)]/fs;

valid_num=max(find(time<0.151));
disp=save_output(:,2);
vel=save_output(:,1);

plot(time(1:valid_num)*1e3,disp(1:valid_num)*1e6)
xlabel('Time [mSec]')
ylabel('Displacement fo the mass [um]')
axis([0 0.15 -30 30])

max_displace=min(disp(1:valid_num));
abs(max_displace)

max_point=(find(disp==max_displace));

data(1)=abs(vel(max_point-2)-vel(max_point-3));
data(2)=abs(vel(max_point-1)-vel(max_point-2));
data(3)=abs(vel(max_point)-vel(max_point-1));
data(4)=abs(vel(max_point+1)-vel(max_point));
data(5)=abs(vel(max_point+2)-vel(max_point+1));
data(6)=abs(vel(max_point+3)-vel(max_point+2));

dv=max(data)
```

C.2. MATLAB Code for Soft Coating Shock Stops

```
clear all

m=1e-6; k=200; b=1e-4;
```

```
fs=10e6; restitution=0.7;

shock_amplitude=9.8*1e3;    %1000g shock
shock_start_time=0;
shock_time=1e-4;
%%%%%%%%%%%%%%%%%%%%

collision=0; N=200; %% large dummy number
flag_still_shock=1; %initialize. If 0, loop ends
shockstop_up_x1=20e-6;
shockstop_down_x1=-20e-6;

%%%%%%%%%%%%%%%%%%%%
A1=[-1*b/m -1*k/m; 1 0]; B1=[-1; 0]; C1=[1 0;0 1];    D1=[0; 0];

A2=A1;    C2=C1;    D2=D1; B2=[0; 0];

%%%%%%%%%%%%%%%%%%%%

sim('SoftStop_s',[0 0.002])

%%%%%%%%%%%%%%%%%%%%
% first stage %

target_up_x1=min(find((output(:,2))>=shockstop_up_x1))-1;    %Should substract 1 to get 'previous' one
target_down_x1=min(find((output(:,2))<=shockstop_down_x1))-1;

if (length(target_up_x1)==0
    if (length(target_down_x1)==0)          %No touch
        ini_c=output(end,:);
        save_output=output;
        %time=output/fs;
    else                                    %No up touch, but down touch
        ini_c=output(target_down_x1,:);
        ini_c(1)=-1*restitution*ini_c(1);
        save_output=output(1:target_down_x1,:);
        collision=collision+1;
        %time=[1:target_down_x1]'/fs;
    end
```

```
    elseif (length(target_down_x1)==0)    %No down touch, but up touch
        ini_c=output(target_up_x1,:);
        ini_c(1)=-1*restitution*ini_c(1);
        save_output=output(1:target_up_x1,:);
        collision=collision+1;
        %time=[1:target_up_x1]'/fs;

    elseif target_up_x1 >= target_down_x1 %Down touch is faster than up touch
        ini_c=output(target_down_x1,:);
        ini_c(1)=-1*restitution*ini_c(1);
        save_output=output(1:target_down_x1,:);
        collision=collision+1;
        %time=[1:target_down_x1]'/fs;

    else    %target_up_x1 < target_down_x1 %Up touch is faster than down touch
        ini_c=output(target_up_x1,:);
        ini_c(1)=-1*restitution*ini_c(1);
        save_output=output(1:target_up_x1,:);
        collision=collision+1;
        %time=[1:target_up_x1]'/fs;
end

  %%%%%%%% End of 1st stage %%%%%%%%%%%

  %%%%%%%% Calibrate %%%%%%%%%%%%%
for i=1:N,

    sim('SoftStop_e',[0 0.0002])

    target_up_x1=min(find((output2(:,2))>=shockstop_up_x1))-1;      %Should substract 1 to get
'previous' one
    target_down_x1=min(find((output2(:,2))<=shockstop_down_x1))-1;

    if (length(target_up_x1)==0)
        if (length(target_down_x1)==0)          %No touch
            ini_c=output2(end,:);
              save_output=[save_output; output2];

          else                                  %No up touch, but down touch
```

```
            ini_c=output2(target_down_x1,:);
            ini_c(1)=-1*restitution*ini_c(1);
            save_output=[save_output; output2(1:target_down_x1,:)];
            collision=collision+1;

        end

        elseif (length(target_down_x1)==0)    %No down touch, but up touch
            ini_c=output2(target_up_x1,:);
            ini_c(1)=-1*restitution*ini_c(1);
            save_output=[save_output; output2(1:target_up_x1,:)];
            collision=collision+1;


        elseif target_up_x1 >= target_down_x1 %Down touch is faster than up touch
            ini_c=output2(target_down_x1,:);
            ini_c(1)=-1*restitution*ini_c(1);
            save_output=[save_output; output2(1:target_down_x1,:)];
            collision=collision+1;


        else    %target_up_x1 < target_down_x1 %Up touch is faster than down touch
            ini_c=output2(target_up_x1,:);
            ini_c(1)=-1*restitution*ini_c(1);
            save_output=[save_output; output2(1:target_up_x1,:)];
            collision=collision+1;
    end
end

time=[1:length(save_output)]/fs;

plot(time,save_output(:,2)*1e6)
xlabel('Time [Seconds]')
ylabel('Displacement of the mass [um]')
```

C.3. SIMULINK Model for Nonlinear Spring Shock Stops

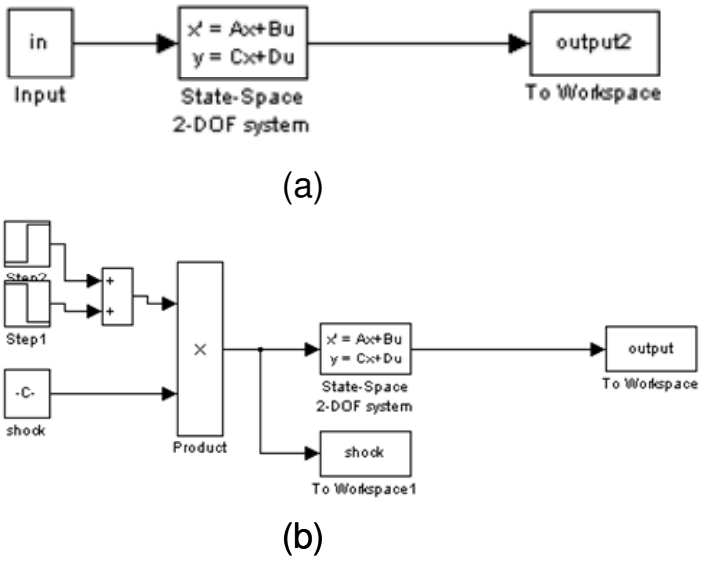

Figure C.1. SIMULINK model for nonlinear spring and soft coating shock stop simulations. (a) Nonlinear_e.mdl and SoftStop_e.mdl, (b) Nonlinear_s.mdl and SoftStop_s.mdl.

APPENDIX D

Derivation of Kinetic Energy of Ring Gyroscopes in Section 2.5.4

Terms in equation (2.53) are substituted to equation (2.54)

$$
\begin{aligned}
|\vec{v}|^2 &= \left[\left(\dot{u}_x\right)^2 + \left(\dot{u}_y\right)^2\right] \\
&+ \left[2\Omega_z\left(u_x\dot{u}_y - \dot{u}_x u_y\right)\right] \\
&+ \left[\left(u_x\right)^2\left(\Omega_y^2 + \Omega_z^2\right)\right] + \left[\left(u_y\right)^2\left(\Omega_x^2 + \Omega_z^2\right)\right] \\
&+ \left[u_x u_y\left(-2\Omega_x\Omega_y\right)\right] \\
&+ \left[u_x x_p\left(2\Omega_y^2 + 2\Omega_z^2\right) + u_x y_p\left(-2\Omega_x\Omega_y\right) + u_y y_p\left(2\Omega_x^2 + 2\Omega_z^2\right) + u_y x_p\left(-2\Omega_x\Omega_y\right)\right] \\
&+ \left[u_x\left(2v_{oy}\Omega_z - 2v_{oz}\Omega_y\right) + u_y\left(-2v_{ox}\Omega_z + 2v_{oz}\Omega_x\right) + \dot{u}_x\left(2v_{ox}\right) + \dot{u}_y\left(2v_{oy}\right)\right] \\
&+ \left[\dot{u}_x y_p\left(-2\Omega_z\right) + \dot{u}_y x_p\left(2\Omega_z\right)\right]
\end{aligned}
\tag{2.53}
$$

$$
T_{kinetic} = \frac{1}{2}\int_V \rho|\vec{v}|^2\, dV \tag{2.54}
$$

to produce

$$
\begin{aligned}
T_{kinetic} &= \frac{1}{2}\int_V \rho\left[\left(\dot{u}_x\right)^2 + \left(\dot{u}_y\right)^2\right]dV \\
&+ \frac{1}{2}\int_V \rho\left[2\Omega_z\left(u_x\dot{u}_y - \dot{u}_x u_y\right)\right]dV \\
&+ \frac{1}{2}\int_V \rho\left[\left(u_x\right)^2\left(\Omega_y^2 + \Omega_z^2\right)\right]dV + \frac{1}{2}\int_V \rho\left[\left(u_y\right)^2\left(\Omega_x^2 + \Omega_z^2\right)\right]dV \\
&+ \frac{1}{2}\int_V \rho\left[u_x u_y\left(-2\Omega_x\Omega_y\right)\right]dV \\
&+ \frac{1}{2}\int_V \rho\left[u_x x_p\left(2\Omega_y^2 + 2\Omega_z^2\right) + u_x y_p\left(-2\Omega_x\Omega_y\right) + u_y y_p\left(2\Omega_x^2 + 2\Omega_z^2\right) + u_y x_p\left(-2\Omega_x\Omega_y\right)\right]dV \\
&+ \frac{1}{2}\int_V \rho\left[u_x\left(2v_{oy}\Omega_z - 2v_{oz}\Omega_y\right) + u_y\left(-2v_{ox}\Omega_z + 2v_{oz}\Omega_x\right) + \dot{u}_x\left(2v_{ox}\right) + \dot{u}_y\left(2v_{oy}\right)\right]dV \\
&+ \frac{1}{2}\int_V \rho\left[\dot{u}_x y_p\left(-2\Omega_z\right) + \dot{u}_y x_p\left(2\Omega_z\right)\right]dV
\end{aligned}
\tag{E.1}
$$

These terms will be substituted by equations (2.31) and (2.32).

$$u_x = \Phi_{x1}^T q_1^T + \Phi_{x2}^T q_2^T + \Phi_{x1}^F q_1^F + \Phi_{x2}^F q_2^F \tag{2.31}$$

$$u_y = \Phi_{y1}^T q_1^T + \Phi_{y2}^T q_2^T + \Phi_{y1}^F q_1^F + \Phi_{y2}^F q_2^F \tag{2.32}$$

which are represented by equations (2.43)-(2.46). Note that they are sometimes reported as multiple of the expressions, as explained using equations (2.37) and (2.39). To simplify the equation (E.1), we will use the orthogonality of the mode shapes and because of the symmetry of the ring structure and the mode shapes. Because of the orthogonality,

$$\int_V \left[\Phi_1^T \Phi_2^T\right] dV = \int_V \left[\Phi_{x1}^T \Phi_{x2}^T + \Phi_{y1}^T \Phi_{y2}^T\right] dV = 0 \tag{E.2}$$

$$\int_V \left[\Phi_1^T \Phi_1^F\right] dV = \int_V \left[\Phi_{x1}^T \Phi_{x1}^F + \Phi_{y1}^T \Phi_{y1}^F\right] dV = 0 \tag{E.3}$$

$$\int_V \left[\Phi_1^T \Phi_2^F\right] dV = \int_V \left[\Phi_{x1}^T \Phi_{x2}^F + \Phi_{y1}^T \Phi_{y2}^F\right] dV = 0 \tag{E.4}$$

$$\int_V \left[\Phi_2^T \Phi_2^F\right] dV = \int_V \left[\Phi_{x2}^T \Phi_{x2}^F + \Phi_{y2}^T \Phi_{y2}^F\right] dV = 0 \tag{E.5}$$

$$\int_V \left[\Phi_1^F \Phi_2^T\right] dV = \int_V \left[\Phi_{x1}^F \Phi_{x2}^T + \Phi_{y1}^F \Phi_{y2}^T\right] dV = 0 \tag{E.6}$$

$$\int_V \left[\Phi_1^F \Phi_2^F\right] dV = \int_V \left[\Phi_{x1}^F \Phi_{x2}^F + \Phi_{y1}^F \Phi_{y2}^F\right] dV = 0 \tag{E.7}$$

The mode shapes and position vector ($\vec{r}_p$) of a ring structure are given by linear combinations of sine and cosine as shown in equations (2.43)-(2.46) and following.

$$\vec{r}_p = (x_p, y_p) = \left(R_{ring} \cos\theta, R_{ring} \sin\theta\right) \tag{E.8}$$

Note that

$$dV = \left(R_{ring} W_{ring} h_{ring}\right) d\theta \tag{E.9}$$

where R_{ring}, W_{ring}, and h_{ring} are radius, width and thickness of the ring structure. Also note that

$$\int_0^{2\pi}\left[\sin(m\theta)\sin(n\theta)\right]d\theta=\int_0^{2\pi}\left[\sin(m\theta)\cos(n\theta)\right]d\theta=\int_0^{2\pi}\left[\cos(m\theta)\cos(n\theta)\right]d\theta=0 \tag{E.10}$$

when $m\neq n$ (m and n are integers.) For further simplification, we assumed that

$$\Omega_x=\Omega_y=0 \tag{E.11}$$

Equation (E.1) has seven lines of terms. After the substitution, because of the orthogonality, the terms at the first line are simplified to

$$\frac{1}{2}\int_V\rho\left[\left(\dot{u}_x\right)^2+\left(\dot{u}_y\right)^2\right]dV=\frac{1}{2}M_1^T\left(\dot{q}_1^T\right)^2+\frac{1}{2}M_2^T\left(\dot{q}_2^T\right)^2+\frac{1}{2}M_1^F\left(\dot{q}_1^F\right)^2+\frac{1}{2}M_2^F\left(\dot{q}_2^F\right)^2 \tag{E.12}$$

where

$$M_1^T=\int_V\rho\left[\left(\Phi_{x1}^T\right)^2+\left(\Phi_{y1}^T\right)^2\right]dV=\int_V\rho\left[\left(\Phi_{r1}^T\right)^2+\left(\Phi_{\theta1}^T\right)^2\right]dV \tag{2.57}$$

$$M_2^T=\int_V\rho\left[\left(\Phi_{x2}^T\right)^2+\left(\Phi_{y2}^T\right)^2\right]dV=\int_V\rho\left[\left(\Phi_{r2}^T\right)^2+\left(\Phi_{\theta2}^T\right)^2\right]dV \tag{2.58}$$

$$M_1^F=\int_V\rho\left[\left(\Phi_{x1}^F\right)^2+\left(\Phi_{y1}^F\right)^2\right]dV=\int_V\rho\left[\left(\Phi_{r1}^F\right)^2+\left(\Phi_{\theta1}^F\right)^2\right]dV \tag{2.59}$$

$$M_2^F=\int_V\rho\left[\left(\Phi_{x2}^F\right)^2+\left(\Phi_{y2}^F\right)^2\right]dV=\int_V\rho\left[\left(\Phi_{r2}^F\right)^2+\left(\Phi_{\theta2}^F\right)^2\right]dV \tag{2.60}$$

. The terms at the second line becomes

$$\frac{1}{2}\int_V\rho\left[2\Omega_z\left(u_x\dot{u}_y-\dot{u}_xu_y\right)\right]dV=\Omega_z\left[\gamma^T\left(q_1^T\dot{q}_2^T-\dot{q}_1^Tq_2^T\right)+\gamma_1^F\left(q_1^F\dot{q}_2^F-\dot{q}_1^Fq_2^F\right)\right] \tag{E.13}$$

where

$$\gamma^T=\int_V\rho\left[\Phi_{x1}^T\Phi_{y1}^T\right]dV,\ \gamma_1^F=\int_V\rho\left[\Phi_{x1}^F\Phi_{y2}^F-\Phi_{x2}^F\Phi_{y1}^F\right]dV \tag{2.61}$$

because of the symmetry of mode shapes.

The terms at the third line are simplified to

$$\begin{aligned}&\frac{1}{2}\int_V \rho\left[\left(u_x\right)^2\left(\Omega_y^2+\Omega_z^2\right)\right]dV+\frac{1}{2}\int_V \rho\left[\left(u_y\right)^2\left(\Omega_x^2+\Omega_z^2\right)\right]dV \\ &=\frac{1}{2}\Omega_z^2\alpha_1^T\left(q_1^T\right)^2+\frac{1}{2}\Omega_z^2\beta_2^T\left(q_2^T\right)^2+\frac{1}{2}\Omega_z^2\mu_1^F\left(q_1^F\right)^2+\frac{1}{2}\Omega_z^2\mu_2^F\left(q_2^F\right)^2\end{aligned} \tag{E.14}$$

where

$$\alpha_1^T=\int_V \rho\left(\Phi_{x1}^T\right)^2dV,\ \beta_2^T=\int_V \rho\left(\Phi_{y2}^T\right)^2dV \tag{2.62}$$

$$\mu_1^F=\int_V \rho\left[\left(\Phi_{x1}^F\right)^2+\left(\Phi_{y1}^F\right)^2\right]dV=M_1^F,\ \mu_2^F=\int_V \rho\left[\left(\Phi_{x2}^F\right)^2+\left(\Phi_{y2}^F\right)^2\right]dV=M_2^F \tag{2.63}$$

because of the symmetry of mode shapes and the assumption in equation (E.11).

The terms at the fourth line become

$$\frac{1}{2}\int_V \rho\left[u_x u_y\left(-2\Omega_x\Omega_y\right)\right]dV=0 \tag{E.15}$$

because of the symmetry of mode shapes and the assumption in equation (E.11).

The terms at the fifth line become

$$\begin{aligned}&\frac{1}{2}\int_V \rho\left[u_x x_p\left(2\Omega_y^2+2\Omega_z^2\right)+u_x y_p\left(-2\Omega_x\Omega_y\right)+u_y y_p\left(2\Omega_x^2+2\Omega_z^2\right)+u_y x_p\left(-2\Omega_x\Omega_y\right)\right]dV \\ &=\left[\Omega_z^2\cdot\delta_{x1}^F-\Omega_x\Omega_y\cdot\delta_{y1}^F\right]q_1^F+\left[\Omega_z^2\cdot\delta_{y2}^F-\Omega_x\Omega_y\cdot\delta_{x2}^F\right]q_2^F\end{aligned} \tag{E.16}$$

where δ_{x1}^F, δ_{y1}^F, δ_{x2}^F, δ_{y2}^F are constants. These terms become zero or constants after Lagrange equation, and thus, do not contribute the resonant excitation of a ring gyroscope. Therefore, terms in equation (E.14) are ignored.

The terms at the sixth line become

$$\begin{aligned}&\frac{1}{2}\int_V \rho\left[u_x\left(2v_{oy}\Omega_z-2v_{oz}\Omega_y\right)+u_y\left(-2v_{ox}\Omega_z+2v_{oz}\Omega_x\right)+\dot{u}_x\left(2v_{ox}\right)+\dot{u}_y\left(2v_{oy}\right)\right]dV \\ &=\left(v_{oy}\Omega_z\right)\eta_1^T q_1^T-\left(v_{ox}\Omega_z\right)\eta_2^T q_2^T+\left(v_{ox}\right)\eta_1^T\dot{q}_1^T+\left(v_{oy}\right)\eta_2^T\dot{q}_2^T\end{aligned} \tag{E.17}$$

where

$$\eta_1^T = \int_V \rho\left[\Phi_{x1}^T\right]dV,\ \eta_2^T = \int_V \rho\left[\Phi_{y2}^T\right]dV \tag{2.64}$$

The terms at the seventh line become

$$\begin{aligned}&\frac{1}{2}\int_V \rho\left[\dot{u}_x y_p\left(-2\Omega_z\right) + \dot{u}_y x_p\left(2\Omega_z\right)\right]dV \\ &= \Omega_z\left(\delta_{x2}^F + \delta_{y2}^F\right)\dot{q}_2^F\end{aligned} \tag{E.18}$$

where δ_{x2}^F, δ_{y2}^F are constants. These are ignored because they become zero after Lagrange equation.

APPENDIX E

Derivation of Potential Energy from Drive Electrodes of Ring Gyroscopes

C_n in equation (2.82) can be rewritten as

$$\begin{aligned} C_n = {} & C_s + f_{1n}^T q_1^T + f_{2n}^T q_2^T + f_{1n}^F q_1^F + f_{2n}^F q_2^F \\ & + g_{1n}^T \left(q_1^T\right)^2 + g_{2n}^T \left(q_2^T\right)^2 + g_{1n}^F \left(q_1^F\right)^2 + g_{2n}^F \left(q_2^F\right)^2 \\ & + 2h_{1\,2\,n}^{TT} \left(q_1^T q_2^T\right) + 2h_{1\,1\,n}^{TF} \left(q_1^T q_1^F\right) + 2h_{1\,2\,n}^{TF} \left(q_1^T q_2^F\right) \\ & + 2h_{2\,1\,n}^{TF} \left(q_2^T q_1^F\right) + 2h_{2\,2\,n}^{TF} \left(q_2^T q_2^F\right) + 2h_{1\,2\,n}^{FF} \left(q_1^F q_2^F\right) \end{aligned} \tag{E.1}$$

where

$$C_s = \frac{\varepsilon R_{ring} h_{ring}}{g_0} \Delta\theta_n \tag{E.2}$$

$$\begin{aligned} f_{1n}^T &= \frac{\varepsilon R_{ring} h_{ring}}{g_0^2} \int_{\theta_n - \frac{\Delta\theta_n}{2}}^{\theta_n + \frac{\Delta\theta_n}{2}} \left(\Phi_{r1}^T\right) d\theta, \quad f_{2n}^T = \frac{\varepsilon R_{ring} h_{ring}}{g_0^2} \int_{\theta_n - \frac{\Delta\theta_n}{2}}^{\theta_n + \frac{\Delta\theta_n}{2}} \left(\Phi_{r2}^T\right) d\theta, \\ f_{1n}^F &= \frac{\varepsilon R_{ring} h_{ring}}{g_0^2} \int_{\theta_n - \frac{\Delta\theta_n}{2}}^{\theta_n + \frac{\Delta\theta_n}{2}} \left(\Phi_{r1}^F\right) d\theta, \quad f_{2n}^F = \frac{\varepsilon R_{ring} h_{ring}}{g_0^2} \int_{\theta_n - \frac{\Delta\theta_n}{2}}^{\theta_n + \frac{\Delta\theta_n}{2}} \left(\Phi_{r2}^F\right) d\theta \end{aligned} \tag{E.3}$$

$$\begin{aligned} g_{1n}^T &= \frac{\varepsilon R_{ring} h_{ring}}{g_0^3} \int_{\theta_n - \frac{\Delta\theta_n}{2}}^{\theta_n + \frac{\Delta\theta_n}{2}} \left(\Phi_{r1}^T\right)^2 d\theta, \quad g_{2n}^T = \frac{\varepsilon R_{ring} h_{ring}}{g_0^3} \int_{\theta_n - \frac{\Delta\theta_n}{2}}^{\theta_n + \frac{\Delta\theta_n}{2}} \left(\Phi_{r2}^T\right)^2 d\theta, \\ g_{1n}^F &= \frac{\varepsilon R_{ring} h_{ring}}{g_0^3} \int_{\theta_n - \frac{\Delta\theta_n}{2}}^{\theta_n + \frac{\Delta\theta_n}{2}} \left(\Phi_{r1}^F\right)^2 d\theta, \quad g_{2n}^F = \frac{\varepsilon R_{ring} h_{ring}}{g_0^3} \int_{\theta_n - \frac{\Delta\theta_n}{2}}^{\theta_n + \frac{\Delta\theta_n}{2}} \left(\Phi_{r2}^F\right)^2 d\theta \end{aligned} \tag{E.4}$$

$$\begin{aligned} h_{1\,2\,n}^{TT} &= \frac{\varepsilon R_{ring} h_{ring}}{g_0^3} \int_{\theta_n - \frac{\Delta\theta_n}{2}}^{\theta_n + \frac{\Delta\theta_n}{2}} \left(\Phi_{r1}^T \Phi_{r2}^T\right) d\theta, \quad h_{1\,1\,n}^{TF} = \frac{\varepsilon R_{ring} h_{ring}}{g_0^3} \int_{\theta_n - \frac{\Delta\theta_n}{2}}^{\theta_n + \frac{\Delta\theta_n}{2}} \left(\Phi_{r1}^T \Phi_{r1}^F\right) d\theta, \\ h_{1\,2\,n}^{TF} &= \frac{\varepsilon R_{ring} h_{ring}}{g_0^3} \int_{\theta_n - \frac{\Delta\theta_n}{2}}^{\theta_n + \frac{\Delta\theta_n}{2}} \left(\Phi_{r1}^T \Phi_{r2}^F\right) d\theta, \quad h_{2\,1\,n}^{TF} = \frac{\varepsilon R_{ring} h_{ring}}{g_0^3} \int_{\theta_n - \frac{\Delta\theta_n}{2}}^{\theta_n + \frac{\Delta\theta_n}{2}} \left(\Phi_{r2}^T \Phi_{r1}^F\right) d\theta, \\ h_{2\,2\,n}^{TF} &= \frac{\varepsilon R_{ring} h_{ring}}{g_0^3} \int_{\theta_n - \frac{\Delta\theta_n}{2}}^{\theta_n + \frac{\Delta\theta_n}{2}} \left(\Phi_{r2}^T \Phi_{r2}^F\right) d\theta, \quad h_{1\,2\,n}^{FF} = \frac{\varepsilon R_{ring} h_{ring}}{g_0^3} \int_{\theta_n - \frac{\Delta\theta_n}{2}}^{\theta_n + \frac{\Delta\theta_n}{2}} \left(\Phi_{r1}^F \Phi_{r2}^F\right) d\theta \end{aligned} \tag{E.5}$$

Equation (2.83) can be rewritten as

$$U_{drive} = -\sum_{\theta_n=0,180^0} \frac{1}{2}\left[V_{DC} - V_{AC}\sin(w_0 t)\right]^2 C_n \qquad \text{(E.6)}$$
$$= -\sum_{\theta_n=0,180^0} \frac{1}{2}\left[\left(V_{DC}{}^2 + \frac{V_{AC}{}^2}{2}\right) - \frac{V_{AC}{}^2}{2}\cos(2w_0 t) - 2V_{DC}V_{AC}\sin(w_0 t)\right] C_n$$

After substituting equation (E.1) to equation (2.83), equation (E.7) is generated.

$$U_{drive} = -\frac{1}{2}\left(V_{DC}{}^2 + \frac{V_{AC}{}^2}{2}\right)\sum_{\theta_n=0,180^0}\left[\begin{array}{l} C_s + f_{1n}^T q_1^T + f_{2n}^T q_2^T + f_{1n}^F q_1^F + f_{2n}^F q_2^F \\ + g_{1n}^T\left(q_1^T\right)^2 + g_{2n}^T\left(q_2^T\right)^2 + g_{1n}^F\left(q_1^F\right)^2 + g_{2n}^F\left(q_2^F\right)^2 \\ + 2h_{1\ 2n}^{TT}\left(q_1^T q_2^T\right) + 2h_{1\ 1\ n}^{TF}\left(q_1^T q_1^F\right) + 2h_{1\ 2\ n}^{TF}\left(q_1^T q_2^F\right) \\ + 2h_{2\ 1\ n}^{TF}\left(q_2^T q_1^F\right) + 2h_{2\ 2\ n}^{TF}\left(q_2^T q_2^F\right) + 2h_{1\ 2\ n}^{FF}\left(q_1^F q_2^F\right) \end{array}\right]$$
$$+ \frac{V_{AC}{}^2}{4}\cos(2w_0 t)\sum_{\theta_n=0,180^0}\left[\begin{array}{l} C_s + f_{1n}^T q_1^T + f_{2n}^T q_2^T + f_{1n}^F q_1^F + f_{2n}^F q_2^F \\ + g_{1n}^T\left(q_1^T\right)^2 + g_{2n}^T\left(q_2^T\right)^2 + g_{1n}^F\left(q_1^F\right)^2 + g_{2n}^F\left(q_2^F\right)^2 \\ + 2h_{1\ 2n}^{TT}\left(q_1^T q_2^T\right) + 2h_{1\ 1\ n}^{TF}\left(q_1^T q_1^F\right) + 2h_{1\ 2\ n}^{TF}\left(q_1^T q_2^F\right) \\ + 2h_{2\ 1\ n}^{TF}\left(q_2^T q_1^F\right) + 2h_{2\ 2\ n}^{TF}\left(q_2^T q_2^F\right) + 2h_{1\ 2\ n}^{FF}\left(q_1^F q_2^F\right) \end{array}\right]$$
$$+ V_{DC}V_{AC}\sin(w_0 t)\sum_{\theta_n=0,180^0}\left[\begin{array}{l} C_s + f_{1n}^T q_1^T + f_{2n}^T q_2^T + f_{1n}^F q_1^F + f_{2n}^F q_2^F \\ + g_{1n}^T\left(q_1^T\right)^2 + g_{2n}^T\left(q_2^T\right)^2 + g_{1n}^F\left(q_1^F\right)^2 + g_{2n}^F\left(q_2^F\right)^2 \\ + 2h_{1\ 2n}^{TT}\left(q_1^T q_2^T\right) + 2h_{1\ 1\ n}^{TF}\left(q_1^T q_1^F\right) + 2h_{1\ 2\ n}^{TF}\left(q_1^T q_2^F\right) \\ + 2h_{2\ 1\ n}^{TF}\left(q_2^T q_1^F\right) + 2h_{2\ 2\ n}^{TF}\left(q_2^T q_2^F\right) + 2h_{1\ 2\ n}^{FF}\left(q_1^F q_2^F\right) \end{array}\right] \qquad \text{(E.7)}$$

This equation is very complex, but by applying the observations listed in Section 2.5.7, it is reduced to

$$U_{drive} = -\frac{1}{2}\left(V_{DC}{}^2 + \frac{V_{AC}{}^2}{2}\right)\sum_{\theta_n=0,180^0}\left[\begin{array}{l} g_{1n}^T\left(q_1^T\right)^2 + g_{2n}^T\left(q_2^T\right)^2 + g_{1n}^F\left(q_1^F\right)^2 + g_{2n}^F\left(q_2^F\right)^2 \\ + 2h_{1\ 2n}^{TT}\left(q_1^T q_2^T\right) + 2h_{1\ 1\ n}^{TF}\left(q_1^T q_1^F\right) + 2h_{1\ 2\ n}^{TF}\left(q_1^T q_2^F\right) \\ + 2h_{2\ 1\ n}^{TF}\left(q_2^T q_1^F\right) + 2h_{2\ 2\ n}^{TF}\left(q_2^T q_2^F\right) + 2h_{1\ 2\ n}^{FF}\left(q_1^F q_2^F\right) \end{array}\right] \qquad \text{(E.8)}$$
$$+ V_{DC}V_{AC}\sin(w_0 t)\sum_{\theta_n=0,180^0}\left[f_{1n}^T q_1^T + f_{2n}^T q_2^T + f_{1n}^F q_1^F + f_{2n}^F q_2^F\right]$$

In our analysis, θ_n of the drive electrodes are 0^0 and 180^0. Therefore,

$$\sum_{\theta_n=0,180^0} f_{1n}^T = \sum_{\theta_n=0,180^0} f_{2n}^T = \sum_{\theta_n=0,180^0} f_{2n}^F = 0 \qquad \text{(E.9)}$$

$$\sum_{\theta_n=0,180^0} h_{1\ 2\ n}^{TT} = \sum_{\theta_n=0,180^0} h_{1\ 1\ n}^{TF} = \sum_{\theta_n=0,180^0} h_{1\ 2\ n}^{TF}$$
$$= \sum_{\theta_n=0,180^0} h_{2\ 1\ n}^{TF} = \sum_{\theta_n=0,180^0} h_{2\ 2\ n}^{TF} = \sum_{\theta_n=0,180^0} h_{1\ 2\ n}^{FF} = 0 \tag{E.10}$$

By equations (E.9) and (E.10), equation (E.8) is further reduced to

$$\begin{aligned} U_{drive} &= -\frac{1}{2}\left({V_{DC}}^2 + \frac{{V_{AC}}^2}{2} \right) \sum_{\theta_n=0,180^0} \left[g_{1n}^T \left(q_1^T\right)^2 + g_{2n}^T \left(q_2^T\right)^2 + g_{1n}^F \left(q_1^F\right)^2 + g_{2n}^F \left(q_2^F\right)^2 \right] \\ &\quad + V_{DC} V_{AC} \sin(w_0 t) \sum_{\theta_n=0,180^0} \left[f_{1n}^F q_1^F \right] \\ &= -\frac{1}{2}\left({V_{DC}}^2 + \frac{{V_{AC}}^2}{2} \right) \begin{bmatrix} \chi_{g2}\left(\chi_{d3} + \chi_{d1}\right)\left(q_1^T\right)^2 + \chi_{g2}\left(\chi_{d3} - \chi_{d1}\right)\left(q_2^T\right)^2 \\ + \chi_{g2}\left(4\chi_{d3} + 2\chi_{d2}\right)\left(q_1^F\right)^2 + \chi_{g2}\left(4\chi_{d3} - 2\chi_{d2}\right)\left(q_2^F\right)^2 \end{bmatrix} \\ &\quad + \left(V_{DC} V_{AC}\right)\left(4\chi_{g1}\chi_{d1}\right)\sin(w_0 t) q_1^F \end{aligned} \tag{E.11}$$

where

$$\chi_{g1} = \frac{\varepsilon R_{ring} h_{ring}}{g_0^2},\ \chi_{g2} = \frac{\varepsilon R_{ring} h_{ring}}{g_0^3}$$
$$\chi_{d1} = \sin(\Delta\theta_n),\ \chi_{d2} = \sin(2\Delta\theta_n),\ \chi_{d3} = \Delta\theta_n \tag{2.85}$$

As explained, they can be also reported as multiple of the expressions depending on the selection of mode shapes.